

**UCLA**

**UCLA Electronic Theses and Dissertations**

**Title**

Development of a Complexity-Reduced, Collisional-Radiative Model for Multiphysics Plasma Simulations

**Permalink**

<https://escholarship.org/uc/item/2g11z2bq>

**Author**

Abrantes, Richard Jun Espino

**Publication Date**

2018

Peer reviewed|Thesis/dissertation

UNIVERSITY OF CALIFORNIA  
Los Angeles

Development of a Complexity-Reduced, Collisional-Radiative Model  
for Multiphysics Plasma Simulations

A dissertation submitted in partial satisfaction  
of the requirements for the degree  
Doctor of Philosophy in Aerospace Engineering

by

Richard June Espino Abrantes

2018

© Copyright by  
Richard June Espino Abrantes  
2018

# ABSTRACT OF THE DISSERTATION

Development of a Complexity-Reduced, Collisional-Radiative Model  
for Multiphysics Plasma Simulations

by

Richard June Espino Abrantes

Doctor of Philosophy in Aerospace Engineering

University of California, Los Angeles, 2018

Professor Ann R. Karagozian, Chair

The influence of plasma physics on modern technology spans many disciplines beyond the fields of physics and engineering. The fundamental operation of forthcoming plasma physics devices are becoming increasingly complex, producing transient plasma structures and instabilities that can affect any of these devices' nominal performance conditions. One set of underlying physical phenomenon that can impact the plasma evolution in these devices derives from the atomic kinetics. A fully-resolved numerical simulation of these plasma systems involves solving the time-dependent atomic kinetics using a collisional-radiative model. However, a plasma simulation that includes such an atomic model exacerbates the problem's dimensionality because of the resolution of the atomic structure and number of atomic levels that must be resolved. The goal of this dissertation is to develop and implement state-of-the-art complexity reduction techniques to accurately simulate the atomic kinetics in reasonable computational times, without restricting the model to any atomic species or any single application. This approach will enable researchers to assess and analyze complex features of new plasma devices and experiments impacted by atomic kinetics.

The collisional-radiative model's rate equations were first extended to include energy equations to study laser-induced breakdown events. This study was used to verify processes affected by energy transfers due to the energy equations' coupling to the atomic state densities' rate equations. Here, multiphoton ionization and inverse Bremsstrahlung were used as

the laser source terms to simulate laser-induced breakdown events similar to experimental conditions found in the literature. Once the simulations were deemed sufficient to capture the atomic kinetics observed in breakdown experiments, the entire kinetics model was used as the foundation to implement and investigate the effect of complexity-reduction algorithms. The techniques explored in this work included the quasi-steady-state (QSS) solution, uniform grouping, and Boltzmann grouping. These techniques were then tested against isothermal and Planckian irradiation test cases; amongst all of the reduction algorithms, the Boltzmann grouping technique was found to hold the most promise for its flexible representation of atomic state distributions across a wide range of plasma regimes.

The collisional-radiative model's symbiotic connection with atomic codes additionally allows these models to become tools to be used for spectroscopic analysis. Spectral images of chlorine generated for the NLTE-10 workshop verified high-density, high-temperature spectral data obtained from a newly-constructed spectrometer called OHREX. Accurate comparisons were observed among the present findings, results from other collisional-radiative models in the scientific community, and the OHREX experimental data presented at the workshop. Additionally, spectral comparisons between the model and a low-density, low-temperature inductively-coupled argon plasma at the Air Force Research Laboratory were attempted. It was found that spectral comparisons were poorly matched as a result of the preferential disposition of atomic codes for high- $Z$  ions. Hence, additional analysis is needed to properly capture detailed atomic kinetics for low- $Z$  applications.

The dissertation of Richard June Espino Abrantes is approved.

Robert Martin

Raymond Mitchell Spearrin

George J Morales

Xiaolin Zhong

Ann R. Karagozian, Committee Chair

University of California, Los Angeles

2018

*“Wisdom is the principal thing: Therefore get wisdom.*

*And with all thy getting get understanding.”*

*- Proverbs 4:7*

## TABLE OF CONTENTS

<b>1</b>	<b>Introduction</b>	<b>1</b>
1.1	Applications	3
1.1.1	Electric Propulsion	3
1.1.2	Laser-Plasma Interactions	6
1.2	Objective and Outline	10
<b>2</b>	<b>Governing Equations and Concepts</b>	<b>12</b>
2.1	Theoretical Framework	12
2.2	Plasma Equilibria	17
2.2.1	Maxwell Distribution	19
2.2.2	Boltzmann Distribution	20
2.2.3	Saha Distribution	21
2.2.4	Planck Distribution	22
2.3	Departing from Equilibrium	23
<b>3</b>	<b>The Collisional-Radiative Model</b>	<b>25</b>
3.1	Elementary Processes and Detailed Balancing	27
3.1.1	Collisional Excitation/Deexcitation	29
3.1.2	Collisional Ionization and Three-Body Recombination	30
3.1.3	Bound-Bound Radiative Processes	31
3.1.4	Bound-Free Radiative Processes	32
3.1.5	Elastic Processes	33
3.1.6	Bremsstrahlung	34
3.2	Rate Equations	35

3.3	Argon Atomic Data Sets . . . . .	37
3.4	Chlorine Atomic Data Sets . . . . .	41
3.5	Preliminary Code Validation and Analysis . . . . .	43
<b>4</b>	<b>Laser-Induced Breakdown Modeling of Argon . . . . .</b>	<b>52</b>
4.1	Introduction . . . . .	52
4.2	Modeling the Breakdown . . . . .	54
4.2.1	Multiphoton Ionization . . . . .	55
4.2.2	Inverse Bremsstrahlung . . . . .	57
4.3	Comparative Results and Analysis . . . . .	58
4.4	Summary . . . . .	75
<b>5</b>	<b>Complexity Reduction Techniques for Atomic Plasmas . . . . .</b>	<b>79</b>
5.1	Introduction . . . . .	79
5.2	Collisional-Radiative Model . . . . .	80
5.2.1	Atomic and Cross-Sectional Data . . . . .	80
5.2.2	Kinetic Processes and Rates . . . . .	81
5.3	Level Grouping Strategies . . . . .	83
5.3.1	Quasi-Steady-State (QSS) Solution . . . . .	83
5.3.2	Uniform Grouping . . . . .	84
5.3.3	Boltzmann Grouping . . . . .	84
5.4	Isothermal Heating . . . . .	86
5.5	Planckian Irradiation . . . . .	95
5.6	Summary . . . . .	100
<b>6</b>	<b>Spectroscopic Modeling . . . . .</b>	<b>102</b>

6.1	Spectroscopic Construction . . . . .	103
6.2	Chlorine Spectra from the ORION laser facility . . . . .	108
6.3	Inductively-coupled Argon Spectra from the Bell Jar Device . . . . .	123
6.3.1	Experimental Setup . . . . .	123
6.3.2	Spectral Comparisons and Analysis . . . . .	125
6.4	Summary . . . . .	134
<b>7</b>	<b>Conclusions &amp; Future Work . . . . .</b>	<b>136</b>
<b>A</b>	<b>Rate Calculation Adjustment: Change of Variable . . . . .</b>	<b>141</b>
<b>B</b>	<b>Construction of the Source Terms and Jacobian Matrix . . . . .</b>	<b>143</b>
B.1	Terms due to change in species density . . . . .	143
B.2	Terms due to change in energy of heavy species . . . . .	145
B.3	Terms due to change in electron energy . . . . .	146
<b>C</b>	<b>Ordinary Differential Equation (ODE) Solvers . . . . .</b>	<b>149</b>
C.1	Backward Euler . . . . .	149
C.2	Radau5 . . . . .	150
C.2.1	Implementation . . . . .	151
	<b>References . . . . .</b>	<b>155</b>

## LIST OF FIGURES

1.1	Plasma Regimes . . . . .	2
1.2	Field-Reversed Configuration (FRC) thruster concept . . . . .	4
1.3	Field-Reversed Configuration (FRC) plasmoid features . . . . .	4
1.4	Laser wakefield accelerator concept . . . . .	7
1.5	Direct and indirect drive ICF devices . . . . .	8
1.6	ICF implosion for a direct-drive target . . . . .	9
3.1	Various excitation rates for Ar+0 from ground state . . . . .	40
3.2	Ionization rates from Ar+0's ground state to the first 3 levels of Ar+1 . . . . .	41
3.3	Ar Charge Fraction Comparison between FLYCHK and CR Model for $N_e = 10^{22}$ m <sup>-3</sup> . . . . .	45
3.4	Ar Charge Fraction Comparison between FLYCHK and CR Model for $N_e = 10^{25}$ m <sup>-3</sup> . . . . .	47
3.5	Effect of High-n Shells on Charge Distribution from CRETIN . . . . .	49
3.6	Ar Charge Fraction Comparison between FLYCHK and CR Model for $N_e = 10^{28}$ m <sup>-3</sup> . . . . .	50
3.7	Mean Ar Charge Comparison with NLTE-4 and 7 as a Function of Temperature	51
4.1	Generic Laser-Induced Breakdown Setup with Spectroscopic Analysis . . . . .	53
4.2	Laser-Induced Breakdown Schematic of Aluminum Target . . . . .	54
4.3	Comparison of Threshold Breakdown Intensities between Experiments and CR Model . . . . .	61
4.4	Threshold Breakdown Intensity from picosecond Experiment by Krasnyuk et al. . . . .	64
4.5	Threshold Breakdown Intensity from picosecond Experiment by Dewhurst . . . . .	64
4.6	Threshold Breakdown Intensity from Rosen et al.'s Experiment . . . . .	65

4.7	Modified Threshold Breakdown Intensity for a CR Model without Multiphoton Ionization . . . . .	67
4.8	Sensitivity of Ionization Fraction for Simulations without MPI . . . . .	69
4.9	Density Evolution of Ions and Respective Excited States during LIB . . . . .	70
4.10	Electron Temperature Evolution during LIB . . . . .	72
4.11	Energy Deposition by Laser for P = 117 Torr Rosen Case . . . . .	73
4.12	Energy Deposition by Laser for P = 1276 Torr Rosen Case . . . . .	74
4.13	Plasma Radiation Loss for P = 1276 Torr Rosen Case . . . . .	76
4.14	Electron Power Transfer for P = 1276 Torr Rosen Case . . . . .	77
5.1	Boltzmann Plots of Ar+9 for Different $N_{Ar}$ at Steady State, $T_e = 50$ eV . . . . .	88
5.2	Boltzmann Plots for Ar+8 under Various Reduction Schemes at Steady State, $N_{Ar} = 10^{19}$ cm <sup>-3</sup> and $T_e = 100$ eV . . . . .	89
5.3	Mean Ion Charge Evolution for Multiple Reduction Schemes, $N_{Ar} = 10^{19}$ cm <sup>-3</sup> and $T_e = 100$ eV . . . . .	90
5.4	Radiation Rates for Multiple Reduction Schemes, $N_{Ar} = 10^{19}$ cm <sup>-3</sup> and $T_e = 100$ eV	91
5.5	Argon Group Temperatures Evolution under Ionic Excitation Configuration for $T_e = 100$ eV . . . . .	92
5.6	Boltzmann Plots for Ar+2 under Various Reduction Schemes at $t \sim 90$ $\mu$ secs, $N_{Ar} = 10^{12}$ cm <sup>-3</sup> and $T_e = 100$ eV . . . . .	93
5.7	Spontaneous Emission Rates for Multiple Reduction Schemes, $N_{Ar} = 10^{12}$ cm <sup>-3</sup> and $T_e = 100$ eV . . . . .	94
5.8	Configuration-Based Spectral Plots for Ar+2 at $t \sim 90$ $\mu$ secs under Conditions $N_{Ar} = 10^{12}$ cm <sup>-3</sup> and $T_e = 100$ eV . . . . .	95
5.9	DCA-based Boltzmann Plots of Ar+5 to Ar+14 at Steady State for $N_{Ar} = 10^{19}$ cm <sup>-3</sup> with $T_{rad} = 50$ eV. . . . .	96

5.10	Temporal Evolution of Electron and Group Temperatures for $N_{Ar} = 10^{19} \text{ cm}^{-3}$ with $T_{rad} = 50 \text{ eV}$ . . . . .	97
5.11	Radiation Rates for Full, Conservative Boltzmann, and Boltzmann IE for $N_{Ar} = 10^{19} \text{ cm}^{-3}$ with $T_{rad} = 50 \text{ eV}$ . . . . .	98
5.12	Total Ionic Spontaneous Emission Rates under Different Grouping Conditions: DCA levels, Boltzmann - IE, Boltzmann (conservative groupings) . . . . .	99
6.1	Gaussian, Lorentz, and Voigt Line Profiles . . . . .	107
6.2	Maxwellian Gaunt Factor Approximation . . . . .	109
6.3	Contributions to Spectral Reconstruction for Cl at 400 eV, $10^{21} \text{ cm}^{-3}$ . . . . .	113
6.4	Comparisons of Cl spectra at 400 eV and $10^{21} \text{ cm}^{-3}$ at NLTE-10 . . . . .	114
6.5	Generated Spectra for Cl at 400 eV with $N_e = 10^{21} \text{ cm}^{-3}$ , $10^{22} \text{ cm}^{-3}$ , $10^{23} \text{ cm}^{-3}$	115
6.6	Generated Spectra for Cl at 500 eV with $N_e = 10^{21} \text{ cm}^{-3}$ , $10^{22} \text{ cm}^{-3}$ , $10^{23} \text{ cm}^{-3}$	116
6.7	Generated Spectra for Cl at 600 eV with $N_e = 10^{21} \text{ cm}^{-3}$ , $10^{22} \text{ cm}^{-3}$ , $10^{23} \text{ cm}^{-3}$	117
6.8	Zoom on Edge Broadening Effect on Cl Spectra at 600 eV with $N_e = 10^{23} \text{ cm}^{-3}$	118
6.9	Spectral Comparison between ACRE and OHREX at 450 eV and $N_e = 3.0 \times$ $10^{21} \text{ cm}^{-3}$ . . . . .	119
6.10	Spectral Comparison between ACRE and OHREX at 450 eV and $N_e = 2.8 \times$ $10^{22} \text{ cm}^{-3}$ without Stark Broadening . . . . .	120
6.11	Spectral Comparison between ACRE and OHREX at 400 eV and $N_e = 3.0 \times$ $10^{21} \text{ cm}^{-3}$ . . . . .	121
6.12	Spectral Comparison between ACRE and OHREX at 500 eV and $N_e = 3.0 \times$ $10^{21} \text{ cm}^{-3}$ . . . . .	122
6.13	Bell Jar Schematic for ICP Plasmas . . . . .	124
6.14	Inductively-coupled plasma generated using the Bell Jar's induction coil . . . . .	125
6.15	Inductively-coupled plasma generated downstream due to port coupling . . . . .	126

6.16 Spectra of Inductively-Coupled Argon Plasma at 75 mTorr with NIST Reference	127
6.17 Spectra of Inductively-Coupled Argon Plasma at 50 mTorr . . . . .	129
6.18 Spectra of Inductively-Coupled Argon Plasma at 75 mTorr with LANL Reference	131
7.1 Adapted schematic of physical models that may be necessary for a plasma fluid simulation . . . . .	139
C.1 Stability Regions for Backward Euler and Radau5 . . . . .	152

## LIST OF TABLES

3.1	Rate coefficients in the collisional-radiative model. . . . .	28
3.2	Argon atomic data sets found in the LANL database. . . . .	38
3.3	Ar+0 atomic levels found in the LANL database. . . . .	39
3.4	Ar+1 atomic levels found in the LANL database. . . . .	39
3.5	Ar+2 atomic levels found in the LANL database. . . . .	40
3.6	Chlorine atomic data sets found in the LANL database. . . . .	42
3.7	Cl+14 atomic levels found in the LANL database. . . . .	42
3.8	Cl+15 atomic levels found in the LANL database. . . . .	43
4.1	Argon LIB Parameters from Several 532 nm Experiments . . . . .	58
6.1	Ar+0 Energy Level Comparisons (LANL & NIST) . . . . .	132
6.2	Ar+0 Wavelength Emission Comparisons . . . . .	133
6.3	Ar+0 Oscillator Strength Comparisons . . . . .	134

## Nomenclature

### Acronyms

AC	Alternating Current
AI	Autoionization
BB	Bound-Bound
BF	Bound-Free
CRM	Collisional-Radiative Model
CSD	Charge State Distribution
DCA	Detailed Configuration-Averaged
DLA	Detailed-Level Accounting
DR	Dielectronic Recombination
EEDF	Electron Energy Distribution Function
EP	Electric Propulsion
FRC	Field-Reversed Configuration
HET	Hall-Effect Thrusters
HWHM	Half-Width at Half-Maximum
ICF	Inertial Confinement Fusion
ICP	Inductively-Coupled Plasma
IE	Ionic Excitation
LANL	Los Alamos National Laboratory

LIB	Laser-Induced Breakdown
LPI	Laser-Plasma Interactions
LTE	Local Thermodynamic Equilibrium
LWFA	Laser Wakefield Acceleration
MPD	Magnetoplasmadynamic
ODE	Ordinary Differential Equation
OHREX	Orion High-Resolution X-Ray Spectrometer
QSS	Quasi-Steady-State
RMF	Rotating Magnetic Field
VDF	Velocity Distribution Function

### Greek Symbols

$\alpha$	Forward Reaction Rate
$\beta$	Backward Reaction Rate
$\Delta\nu$	Half-width at Half-Maximum
$\epsilon_0$	Permittivity of Free Space
$\hat{\eta}$	Elementary Occupation
$\nu$	Frequency
$\phi_\nu$	Line Profile
$\rho_s$	Mass Density
$\sigma$	Cross Section
$\epsilon_s$	Thermal Energy

## Roman Symbols

<b>B</b>	Magnetic Field
<b>E</b>	Electric Field
<b>j</b>	Charge Current Density
$\mathcal{Z}$	Partition Function
$\bar{\mathbf{P}}_s$	Total Stress Tensor
$\bar{v}$	Thermal Velocity
$f_s$	Distribution Function
$j_\nu$	Emissivity (per frequency)
$k_B$	Boltzmann's Constant
$m_s$	Particle Mass of Species 's'
$n$	Orbital Shell
$N_s$	Number Density
$c$	Speed of Light
$g$	Degeneracy
$h$	Planck's Constant
<b>Kn</b>	Knudsen Number
<b>Ry</b>	Rydberg Constant
<b>T</b>	Temperature
<b>Z</b>	Charge Number

## ACKNOWLEDGMENTS

There are many people to whom I owe a great amount of gratitude for accomplishing this dissertation. First, I would like to thank my advisor, Prof. Karagozian, for her wonderful guidance and inspiration, having been a part of my academic life since my undergraduate studies. It is a truly great privilege to be under her tutelage for my academic career and am very much indebted to my advisor for this opportunity and experience.

I am also thankful for the other professors of my committee, all of whom have and will continue to impact my research endeavours: to Prof. Zhong for teaching gas dynamics and showing me a glimpse of its importance in fluid simulations; to Prof. Morales for encouraging my growth in plasma physics knowledge and guidance in many other respects; and to Prof. Spearrin for his breadth in spectroscopy and advising. I have also had the amazing opportunity to tap into the knowledge of other professors outside of my committee, including Prof. Jeff Eldredge and Prof. Joseph Teran.

I would like to express my gratitude to Dr. Jean-Luc Cambier, whose vision and wide scope in plasmas have nurtured my desire to continually expand my knowledge in academia. I am also immensely grateful to Dr. Hai P. Le for his amazing mentorship and the amount of time that he has invested in developing my knowledge base to tackle many plasma physics problems. I also had the unique chance to improve my work thanks to the insights of Stephanie Hansen, Howard Scott, Yuri Ralchenko, Hyun Kyung Chung, and Evgeny Stambulchik.

I have also been fortunate enough to work with an excellent group of researchers at AFRL (termed AFRL family): to Dr. Justin Koo for being an effective leader and guiding the group to new (plasma) pastures; to Dr. Robert Martin for such an amazing breadth of knowledge and being a part of my committee; and to Dr. David Bilyeu for continually challenging my developing precepts. I am also thankful to Drs. Carl Lederman, Éder Sousa, Daniel Eckhardt, Jun Araki, Michelle Scharfe, Michael Holmes for teaching me extra experimental know-how, as well as Robert Lilly and Jon Tran.

I would also like to acknowledge my supportive colleagues: Takeshi-kun, Ayaboe, Chris,

Morad, (mi) Elisa, Danny, Ze-Yu, Eric W., Chen Kang, Thamine, Alexandra L., Minh, John B., Dario, Levon, and many more, all of whom have stimulated my neurons and progress in research. I also thank my friends for revitalizing my research mentality: Raturaj, Szu-Chieh, Abe M., Nataly, Edward L., Sarkis, Szu-Kai, Beatrice, Rafael, Kaushik, Daniel A., Austin, Shaival, and so many others.

My family has always been a great source of encouragement and motivation in my academic pursuits. I thank my early role model and father, Richard (Sr.), for instilling a sense of curiosity for the sciences in my childhood, my mother, Cynthia, for teaching me her unyielding faith in all that I do, my sister, Donna, for constantly striving and making me proud, and my brother, Bryan, for teaching me lessons beyond what I thought life could offer. I also thank my late grandparents, especially my maternal grandmother, Crisanta, for molding my life into what it has become.

This research was supported by the Air Force Office of Scientific Research (AFOSR) laboratory tasks 14RQ05COR & 17RQCOR463 (PM: Dr. Jason Marshall), ERC, Inc. under subcontract PS150008, and the UCLA MAE Department teaching assistant and graduate fellowship programs.

## VITA

- 2013 B.S. in Aerospace Engineering,  
University of California, Los Angeles, CA
- 2013–2014 Member of the Technical Staff, Aerospace Corp.  
El Segundo, CA
- 2013–2014 MAE Teaching Assistant  
University of California, Los Angeles, CA
- 2014 M.S. in Aerospace Engineering  
University of California, Los Angeles, CA
- 2014–present Research Co-op, ERC Inc.  
Air Force Research Laboratory, Edwards AFB, CA.

## PUBLICATIONS

**R.J.E. Abrantes**, A.R. Karagozian, D. Bilyeu, H.P. Le, Complexity Reduction Effects on Transient Atomic Plasmas, *Journal of Quantitative Spectroscopy and Radiative Transfer* (May, 2018) (online)

# CHAPTER 1

## Introduction

Widely regarded as the fourth state of matter, plasmas comprise more than 99.9% of the universe's ordinary matter, a definition which includes other forms of matter composed of protons and neutrons, i.e. solids, liquids, and gases. Despite the ubiquitous nature of plasmas within the known universe, plasma physics still presents many challenges in the scientific community's efforts to understand its abundant complexities. Current plasma physics studies can be primarily categorized into two branches: naturally-occurring plasmas, such as astrophysical plasmas and auroras stemming from solar-atmospheric interactions, and artificially-produced plasmas resulting from advancements in recent technology. The plasma regimes occupied by these naturally- or artificially-produced plasmas are shown in Figure 1.1. Between both branches of plasma physics, plasmas can be supported in a wide variety of systems that spans order of magnitudes in temperature or density. Although the relevant temporal and spatial scales of these different plasma systems vary considerably, the fundamental physics concepts governing the formation or sustenance of these plasmas remain common between these systems.

One important aspect in the understanding of plasma physics is the plasma makeup and kinetics between participating species; this will be referred to as the *plasma chemistry*. Plasma chemistry is a broad term which goes beyond the atomic reactions considered in this work. Examples of such topics that are categorized under plasma chemistry include molecular plasmas and plasma-material interactions (PMI). Ignoring the widespread coverage of plasma chemistry that also includes solid and liquid interactions, the sole consideration of atomic plasmas already presents many unsolved challenges to overcome within the field. Considering a 0-dimensional plasma alone leads to a whole range of plasma conditions that are governed

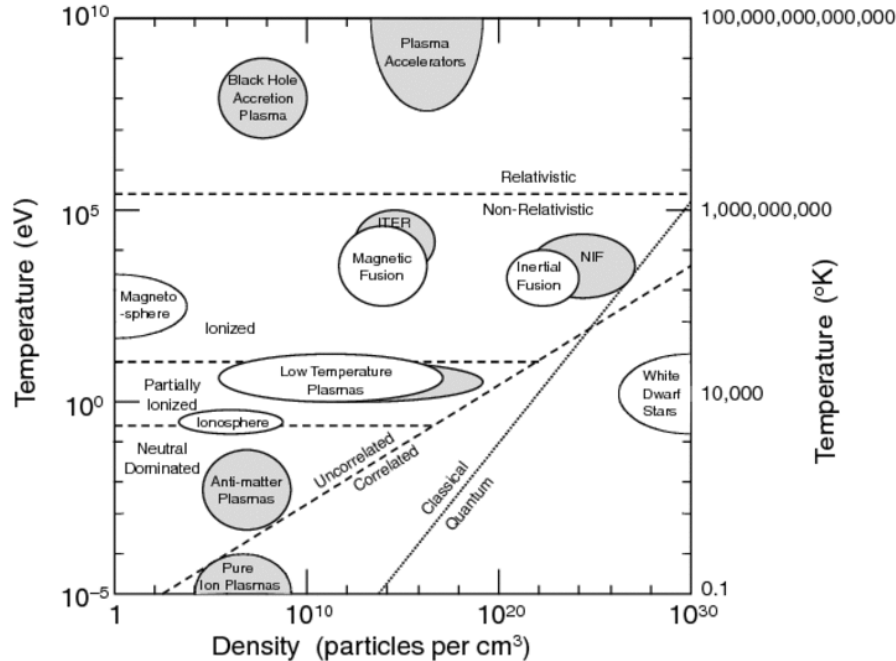


**Figure 1.1:** Various plasma regimes and topics. New areas of study since 1990 are indicated by the gray bubbles. (Taken from Plasma Science: Advancing Knowledge in the National Interest (NRC) [1])

by parameters such as electron density, temperatures, mean ionic charge, and possible non-/equilibrium characteristics. Macroscopic plasma parameters such as density, temperature, and ionic charge immediately correlate to fluid-based variations; but, non-equilibrium kinetics can further compound the complexity of the microscopic plasma dynamics that eventually magnify to the fluid, or transport scales, making these reactions an important consideration in the plasma's evolution.

This forward and backward coupling between the plasma chemistry and fluid scales introduces an additional level of complexity in many modern plasma applications. In fact, this interwoven characteristic between chemistry and transport also extends to other governing physical equations such as radiation transport and Maxwell's equations. It is through these coupled systems of equations that at least one of the many plasma-based nonlinearities, or even instabilities, manifests itself in these complex systems. One should therefore recognize the potential adverse or suppressive effect that plasma chemistry has on any given system's

instabilities. In order to motivate this idea, several applications under different plasma conditions with different scientific and practical objectives will now be discussed to shed more light on the relevance and necessity of resolving these microscopic processes.

## 1.1 Applications

As the community’s understanding of plasmas continues to grow and expand, the list of artificially-constructed plasma devices also grows and diversifies. Some of these devices at the forefront of technology present several engineering obstacles that simultaneously requires further insight and an increased understanding of plasma physics as they tie to the operation of the device. Two such applications are the fields of electric propulsion (EP) and laser-plasma interactions (LPI). Representative devices within each field will be discussed below to elaborate on the growing complexities of these systems.

### 1.1.1 Electric Propulsion

As one of the primary means of spacecraft locomotion, electric propulsion involves accelerating plasma particles under various electrostatic or magnetic configurations to produce thrust. Electric propulsion, specifically plasma-based propulsion, is unique from chemical propulsion as expended power becomes as another propulsion “knob” which must be optimized. In addition to thrust and specific impulse, the stored power used to convert the propellant into a plasma must be utilized efficiently. The onboard electrical power on spacecrafts is also used to drive the electromagnetic systems used for propulsion, as well as other subsystems. Some thrusters that fall under the category of plasma propulsion devices include Hall-effect thrusters (HET), grid-based ion thrusters, and magnetoplasmadynamic (MPD) thrusters. [2] Naturally, these thrusters are a hotbed for plasma kinetics as the particles undergo many transitions prior to being ejected from the thruster channels.

Amongst the growing list of electric propulsion concepts, one example of a thruster being explored for its efficient-handling of power while providing sufficient thrust capabilities is the field-reversed configuration (FRC) thruster. With the FRC plasmoid concept being

identified as early as the 1950s, the concept was taken by Slough et al. and modified into a propulsive device. [3] In Slough et al.'s FRC device (see Fig. 1.2), the plasmoid is generated by a rotating magnetic field (RMF) that is formed by alternating, external loop antennae and free electrons produced from a pre-ionization stage.

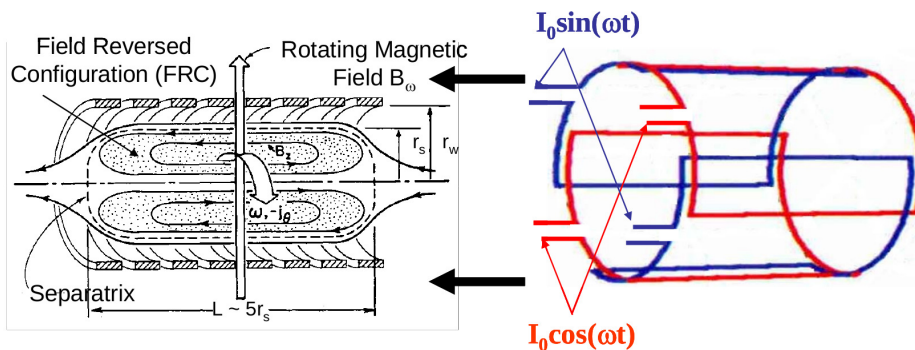


**Figure 1.2:** The superposition of antennae over the Field-Reverse Configuration (FRC) channel allows the preionized electrons to spool subject to the rotating magnetic field's (RMF) frequency,  $\omega$ . (Taken from Slough [3])

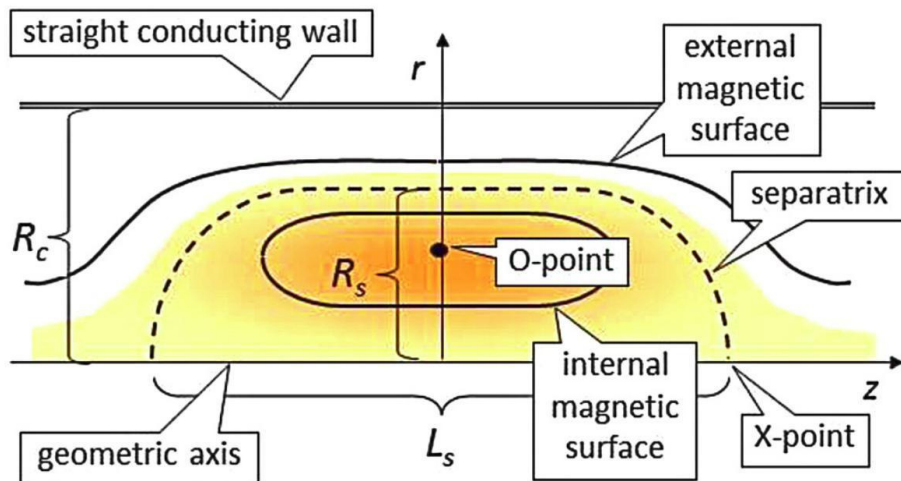


**Figure 1.3:** The FRC plasmoid's features are seen here. In the thruster configuration, the enveloped plasmoid defined by the separatrix is ejected by sequencing several, external magnets that will produce the necessary force in a timely manner. (Taken from Steinhauer [4])

The RMF current leads to further ionization of the plasma as the electrons revolve around the axis of the FRC plasmoid. The revolutions of the increasing electron density induces

a secondary magnetic field which confines the ionizing plasma. Once the fields are well-developed, a relatively distinguishable separatrix forms and defines the plasmoid. This plasmoid may finally be ejected by a series of external magnets whose fields are timed so as to push the plasmoid and produce thrust.

There are several significant advantages outlined by FRC progenitors as the basis for a new plasma propulsion device. First, the absence of electrodes makes this concept an attractive choice for thruster lifetime. Electrodes exposed to plasmas are subject to deterioration due to the high-impact collisions between the particles and the electrode surfaces. This feature of electrode-dependent thrusters limits the full capabilities of current electric propulsion technology. Second, the FRC plasmoid can be conceivably generated from a variety of propellants which would be subject to the ionization mechanisms mentioned above. Therefore, other atomic elements or even molecules may be used for this thruster, an atypical feature when compared with many of today's flight-ready thrusters. One should note that many electric propulsion thrusters currently operate optimally with noble gases as opposed to other chemical species. The FRC device's efficiency ratings are also unattainable by current electric propulsion devices because of the FRC's ability to condense much of the expended energy into the plasmoid. These features make the FRC thruster a highly-valued prospect in the line of new electric propulsion devices.

On the other hand, the use of strong magnetic fields to form and eject the plasmoid demands large power banks to supplement each transient cycle of the FRC thruster. [5] The FRC thruster's transient mode of operation along with imperfections in the device can also lead to plasmoid asymmetries, nonequilibrium conditions, and possible instabilities. [6] Scenarios such as a depleted ionization rate or variations in overall ionic charge can fundamentally alter the performance characteristics of the device. All of these problems beckon for an exploration of the FRC physics during the pre-ionization stage and the subsequent cascade ionization caused by the collisions between the heavy particles and spooling electron current. Amongst all of the possible scenarios that can affect the nominal operation of the thruster, plasma chemistry remains a common, but critical feature to resolve the FRC physics.

### 1.1.2 Laser-Plasma Interactions

Another prominent plasma field that is filled with many types of kinetic processes is laser-plasma interactions. When supplied with a sufficient amount of power, lasers can produce distinct features and characteristics when interacting with any of the four phases of matter. In addition to the laser's photon interactions with particles such as ionization or dissociation, the plasma has inherent wave-like characteristics that can interfere with the laser's electromagnetic waves. These particle-particle, particle-wave, and wave-wave interactions produce a whole variety of plasma physics phenomena that are unique to LPI systems. Altogether, there is an inherently coupled set of events involving the changes in the macroscopic plasma parameters caused by the atomic kinetics, such as mean ionic charge, and the laser-plasma structure that ensues. Therefore, these types of plasmas are not immune to changes in the plasma makeup caused by the irradiating laser, making plasma chemistry an important feature in these systems as well.

One laser-plasma concept that is pushing towards smaller timescales (fsecs) and higher electron energies (GeV) is the study of laser wakefield acceleration (LWFA). Laser wakefield acceleration takes advantage of the residual electric wakefield induced by a ponderomotive blowout to accelerate particles towards relativistic velocities. This accelerative capability opens possibilities towards better innovations such as X-ray imaging/spectroscopy and nuclear resonance fluorescence. [7] An image of the LWFA concept is shown in Fig. 1.4.

Laser wakefield acceleration requires driving an ultrashort and ultra-intense laser pulse into a plasma to create the wakefield. As the laser pulse travels through the plasma, electrons are blown outward due to the ponderomotive force induced by the laser's propagating electric field; in contrast, the ions remain stationary relative to the electrons' motion due to the inertial difference between the two particles. In the wake of the laser, the electrons spatially oscillate transverse to the axis of laser propagation. However, the separation of the electrons and ions in the longitudinal direction creates strong, axial electric fields. Therefore, these pockets in the wake of the laser pulse become ideal locations to seed particles for acceleration, whether by active injection of other ions or passive injection by recycling the electrons seen

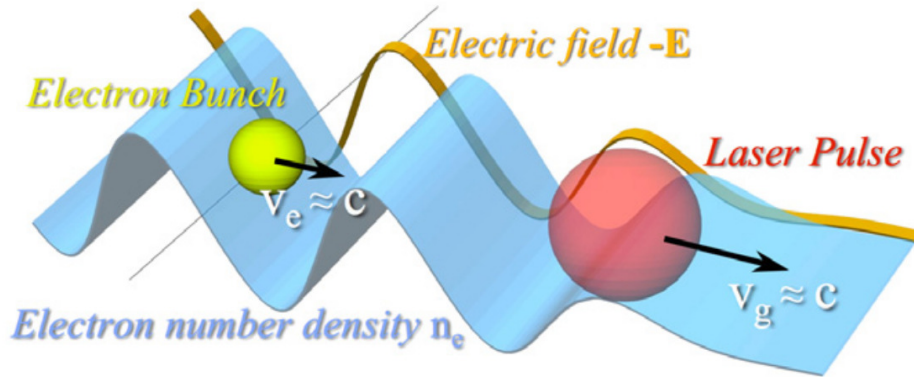


**Figure 1.4:** The laser wakefield accelerator (LWFA) operates through the use of a short, yet high-powered, laser pulse. The laser pulse’s large electric field leads to a ponderomotive blowout of the plasma’s electrons. The electron blowout subsequently produces a wake filled with regions of high, longitudinal electric fields due to species separation. The formation of these electric fields are the basis for particle acceleration. [7]

in Fig. 1.4.

Although laser wakefield acceleration is currently making grand leaps in its development, there are still some difficulties, computational and experimental, with realizing the goals of LWFA, such as the efficient injection of particles into the bubble accelerator. [8] For instance, the plasma can effect lensing properties which are then observed by the laser pulse, distorting the nominal laser characteristics sought in the investigated region. This field of nonlinear optics adds another level of complexity in laser-plasma interactions which has many challenges and complications in its current status.

Another laser-plasma application is the field of inertial confinement fusion, or ICF. A study aimed at achieving nuclear ignition, the approach for ICF devices differs from the more commonly-known field of magnetic confinement fusion. Although both mechanisms are capable of driving the plasma to very high temperatures, and possibly achieving similar plasma temperatures, ICF conditions tend towards higher pressure conditions and much lower timescales of operation unlike magnetically-confined fusion devices. [9] As mentioned, the ICF venture is primarily focused on fusion ignition which, in and of itself, is a difficult task in the field. Since ignition is not a steady-state operation, plasma conditions in ICF studies tend to be transient with several other challenges that differ from its magnetically-confined

counterpart. Despite these differences, both concepts hope to provide different avenues for realizing fusion-based energy.

There are currently two subdivisions in inertial confinement fusion seeking achieve the goal of ignition: direct-drive and indirect-drive. Direct-drive targets utilize direct laser impingement onto a spherical capsule housing fusion-specific fuel that is typically Deuterium-Deuterium (DD) or Deuterium-Tritium (DT). The fuel is enclosed by an ablative shell that interacts with the laser field. In this class of ICF devices, laser deposition is highly dominated by inverse Bremsstrahlung and supplemented by other more secondary collective processes. [10] Indirect-drive, on the other hand, places the capsule within a hohlraum; the hohlraum acts as the bridge for energy transfer from the laser to the capsule. The purpose of indirect-drive's hohlraum heating via lasers is to produce secondary emissions in the form of X-rays which ultimately becomes the primary source of heating in the fusion ignition process. The advantage of using indirect-drive in spite of the device's increased complexity and losses associated with the energy conversion through the hohlraum is the suppression or aversion of the hydrodynamic instabilities usually observed in direct-drive ICFs.<sup>1</sup> [11] Nonetheless, both approaches lead to the same implosion phenomena within the capsule.

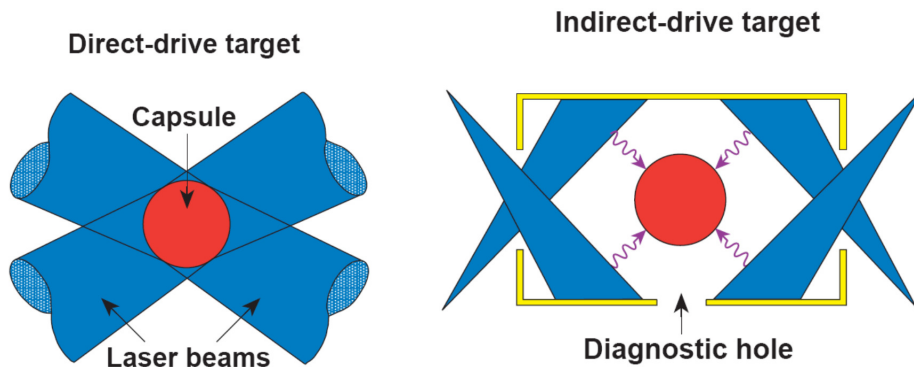


**Figure 1.5:** Two currently explored methods of ICF. Direct-drive targets (left) involve direct laser deposition on the capsule. Indirect-drive targets (right) use hohlraums to spur secondary radiative emissions onto the capsules. [9]

---

<sup>1</sup>These hydrodynamic instabilities can vary in magnitude between both approaches and are heavily driven by the interplay between the radiation field and plasma that forms along the capsule's ablative shell. The direct-drive laser pulse incident upon the capsule would have an optical mean free path that can considerably differ from the value one would obtain from the secondary emissions originating from the hohlraum.

A visual representation of fuel compression in an ICF device is shown in Fig. 1.6. The implosion phenomena begins with laser energy deposition onto the capsule's ablative shell. The ablative shell then begins two simultaneous processes: the outer layer of the shell begins blowoff due to the laser's energy deposition. Second, the momentum balance causes pressure waves to be driven towards the center of the capsule as a consequence of Newton's 2nd Law, collapsing into a shock structure that propagates through the fuel. This causes the fuel to compress, creating high pressure and temperature conditions that are sought for fusion ignition conditions.

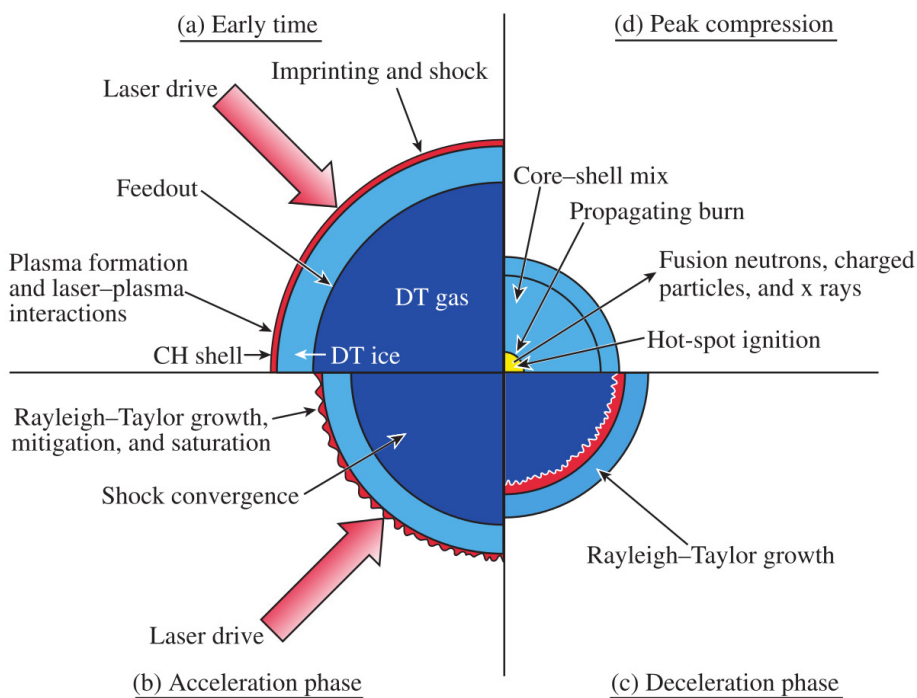


**Figure 1.6:** The ICF device shown here is the direct-drive approach. The shock instantiated by the laser drive propagates inward by balancing the blowout velocity of the shell. As the shock drives inward, the fluid structure eventually reflects, reaches the inner shell layer, resulting in a deceleration phase. Heating and further compression occurs, thereafter, leading to the ignition of the fuel in the capsule. [10]

Unfortunately, inertial-confinement fusion devices are not without their obstacles and challenges. The formation of a spherically symmetric shock that propagates through the plasma demands high precision with minimal perturbations that can amount to the formation of these instabilities. When these instabilities are not hindered, the subsequent asym-

metric ablation front that eventually interacts with the nominal laser drive effects other (nonlinear) features that makes the ICF difficult to control. From an experimental standpoint, the sensitivity of these devices to imperfections, whether they stem from the hohlraum or the laser, must be investigated to determine whether these challenges are true barriers to achieving ignition. However, the expenses associated with performing these experiments can be bypassed by conducting simulations that can help resolve the plasma dynamics and elucidate the sources of instabilities within these systems.

## 1.2 Objective and Outline

The plasma concepts described above all have their respective challenges. The type of instabilities, plasma timescales and spatial scales, laser conditions in the case of LPI, and many other qualities vary substantially so as to create the numerous hurdles associated with plasma-based applications. In the case of electric propulsion devices, the choice of propellant at the onset affects the performance parameters that impact any satellite's ability to move through space. The species makeup in laser wakefield accelerators are impacted by changes in the ionization energy gap, electron-ion dynamics, and potential radiation/laser-coupling. Within inertial confinement fusion devices, the gradients imposed by an spherically-asymmetric plasma composition can dictate the severity or benign nature of instabilities that align the capsule's shell, thereby requiring proper chemistry resolution. A thorough understanding of how the chemistry couples to the entire system is required to grasp the plasma kinetics' effects on the efficiency and operation of these devices.

There are three prominent directions one can undertake to validate the scientific community's theoretical underpinnings behind plasma physics and its applications: further theoretical exploration, experiments, and computational methods or simulations. Although the procedure and execution between these three directions differ, the objective to verify and assert the theory behind the operation of these plasma devices are achievable using any of these methods. In fact, these methods should proceed in synergy to concretely validate our theoretical understanding. In this work, the approach will be primarily computational to

develop the plasma chemistry model.

The plasma chemistry model which will be developed in this study is called a collisional-radiative model, or CRM. In the 0-dimensional setting, the CRM is a state-to-state model that uses an ordinary differential equation (ODE) solver on rate equations designed to temporally evolve the atomic state densities, as well as thermodynamic variables when necessary. These atomic state densities can be evolved based on a variety of the possible collisional and radiative processes that can be accounted for in the set of rate equations. The collisional-radiative model will then be used to investigate its impact in a wide range of applications by using several test cases that have implications for multiple plasma regimes. Since the goal of simulating an entire plasma system is a long venture, the objectives in this work are to demonstrate the significance of plasma chemistry in these systems, explore reduced-order models for atomic kinetics within large-scale plasma simulations, and potentially forecast the effect of complexity-reduced CRMs in a large, coupled framework.

The outline of this dissertation is as follows: Chapter 2 will be an overview of the governing equations used to describe these plasma systems. Chapter 3 will then discuss the construction of the collisional-radiative model, followed by some validation work. Initial studies using the CR model are discussed in Chapter 4, where the CRM was extended to laser-induced breakdown (LIB) simulations. In anticipation of coupled physics modules, complexity reduction capabilities were added to the CR model to make large-scale simulations more feasible, which is discussed in Chapter 5. The CRM's spectroscopic capabilities will then be shown in Chapter 6. The conclusions and a quick discussion of future work will then follow.

## CHAPTER 2

### Governing Equations and Concepts

The impact of atomic kinetics on plasma physics can be appreciated from a theoretical standpoint. An overview of the relevant plasma physics equations is provided in this chapter. It is from these equations that source terms pertaining to the collisional-radiative model can be extracted. These terms will be elaborated upon throughout this dissertation to highlight physical processes that are crucial for determining the plasma's makeup or identity. The key concepts fundamental to plasma kinetics and definitions used to interpret the collisional-radiative model's results will be discussed.

#### 2.1 Theoretical Framework

Plasmas are comprised of a variety of particles including charged species, neutral species, atoms, electrons, and molecules. Each one of these particles interacts with other particles individually and collectively through different kinetic processes such as reactions and transport. Tracking each individual particle would be a daunting task if one sought to fully simulate the plasma to determine its space-time evolution. In a computational framework, the amount of memory required to monitor each particle's motion and interactions becomes very costly if all of the scales are to be captured. However, a simplification can be made if one considers each plasma species as global ensembles in both spatial and velocity dimensions.<sup>1</sup> This leads to the well-known kinetic, or Boltzmann, equation shown in Eq. 2.1.

---

<sup>1</sup>This simplification assumes molecular chaos, where the velocities of the particles in the fluid are uncorrelated and independent of position. [12]

$$\frac{\partial}{\partial t} f_s + \mathbf{v} \cdot \frac{\partial}{\partial \mathbf{r}} f_s + \mathbf{a} \cdot \frac{\partial}{\partial \mathbf{v}} f_s = \left( \frac{\partial f}{\partial t} \right)_{coll} \quad (2.1)$$

The kinetic equation is a description of the temporal evolution of a species' distribution function,  $f_s$ , in 6-dimensional space, 3 of which are physical space variables and the other 3 being variables from velocity space (3-D, 3-V). On the LHS of the equation, the first term represents the temporal derivative and the next two terms of the kinetic equation are two convective terms, one in physical space ( $\partial/\partial \mathbf{r}$ ) and another in velocity space ( $\partial/\partial \mathbf{v}$ ). The first of the two convective terms corresponds to the particles' momenta being convected through space, if one considers including the mass of particle in the formulation. The momentum of the particles may also change due to the forces acting on the plasma, which is captured by the term containing the velocity derivative of the distribution function. Finally, the RHS term of the kinetic equation is of great relevance to this work because it encapsulates all of the collisions between all species. When considering interactions between different portions of the distribution from the same or different fluid species, the distribution function may alter as a result of these collisions.

The acceleration induced upon the plasma particles may stem from several, external sources. However, plasmas have self-generated electric ( $\mathbf{E}_M^2$ ) and magnetic fields ( $\mathbf{B}$ ) caused by the motion of the charged particles. Therefore, the presence and motion of these particles is enough to exert electromagnetic forces in the plasma, leading at very least to some small-scale structures even without externally applied fields. In order to capture the electromagnetic variations in the plasma, the kinetic equation should be coupled to Maxwell's equations shown below in cgs form.

---

<sup>2</sup>The subscript **M** for 'Maxwell' is used to distinguish from solving the electrostatic electric field strictly with Poisson's equation. Maxwell's equations allow one to fully capture the coupled nature of the electric and magnetic fields.

$$\text{Faraday's Law: } \nabla \times \mathbf{E}_M = -\frac{1}{c} \frac{\partial}{\partial t} \mathbf{B} \quad (2.2)$$

$$\text{Gauss's Law: } \nabla \cdot \mathbf{E}_M = 4\pi\rho_c \quad (2.3)$$

$$\text{Ampère's law: } \nabla \times \mathbf{B} = 4\pi\mathbf{j} + \frac{1}{c} \frac{\partial}{\partial t} \mathbf{E}_M \quad (2.4)$$

$$\text{Law for "no magnetic monopoles": } \nabla \cdot \mathbf{B} = 0 \quad (2.5)$$

Together, the kinetic and Maxwell's equations constitute the theoretical foundation to understand and investigate any plasma system. The 0-D collisional-radiative model can be isolated from the equations by focusing only on the collisional terms. Although the fundamental nature of plasmas can be captured through the kinetic and Maxwell's equations, this system of equations are computationally demanding when numerically implemented because of the 6-dimensional nature of the kinetic equation. Instead, one opts to extract the CRM from the plasma's fluid representation without an outstanding loss of generalization in the collision terms.<sup>3</sup>

The fluid plasma equations consist of equations that conserve mass, momentum, and energy, each of which can be obtained through integrated moments of the kinetic equation. The system of equations shown here follow Braginskii's derivation of the fluid equations from kinetic theory. [13] Equation 2.6, shown below, expresses the fluid's first equation: the conservation of mass. The equation is obtained by integrating the 0<sup>th</sup>-order moment of the kinetic equation over the velocity distribution function, or VDF.

$$\partial_t \rho_s + \nabla_{\mathbf{r}} \cdot (\rho_s \mathbf{u}_s) = \left( \frac{\partial \rho_s}{\partial t} \right)_{coll} \quad (2.6)$$

The subscript,  $s$ , denotes the inclusion of multiple fluid species in the plasma, such as

---

<sup>3</sup>This work will focus on a 0-D implementation and study of the collisional-radiative model. Even though the collisional and radiative terms will be reduced to effective rates based solely on macroscopic temperature descriptions, the plasma chemistry rates can always be adjusted to account for specific non-equilibrium scenarios when other non-equilibrium, physical models are introduced. This is briefly discussed in the collisional-radiative model (see Chapter 3).

electrons and atoms for example. While the LHS represents the conservation of mass  $s$  through space-time, the collisional term on the RHS represents the addition or loss of species density due to reactions of the species in question. This collisional term will be particularly relevant in a latter part of this sequence to construct the collisional-radiative model. The next set of equations obtained is a 1<sup>st</sup>-order integrated moment of the kinetic equation, the conservation of momentum. Similarly, multiple momentum conservation equations can be included for the multiple fluid species present in a multi-fluid system.

$$\partial_t(\rho_s \mathbf{u}_s) + \nabla_{\mathbf{r}} \cdot (\rho_s \mathbf{u}_s \mathbf{u}_s) = n_s \mathbf{F}_s - \nabla_{\mathbf{r}} \cdot \bar{\mathbf{P}}_s + (\dot{\mathbf{P}}_s)_{coll} \quad (2.7)$$

The equation describes the fluid's change of momentum due to the sum of forces, including gravity or electromagnetic acceleration, a total stress tensor,  $\bar{\mathbf{P}}_s$ , and collisional processes represented by the agglomerate term  $(\dot{\mathbf{P}}_s)_{coll}$ . One complication resulting from the derivation of the fluid equations is the requirement of higher-order closure terms. For example, the pressure matrix obtained from the kinetic equation requires a higher-order equation to close the current system and occurs ad infinitum for the next set of moments. In these situations, a Chapman-Enskog method is employed to close the system of equations, for which the reader is referred to Braginskii's closure models. While these are necessary considerations in a fluid framework, i.e. multi-dimensional simulation, the objective of developing the CR model detracts from the fluid model's implementation of the closure terms and will be reserved for future work.

Lastly, the equation dictating energy conservation is obtained by integrating the kinetic equation's 2<sup>nd</sup>-order moment ( $\frac{1}{2}v^2$ ) over the VDF. This 2<sup>nd</sup>-order moment integration produces additional variables that also require higher-order closures as observed in the momentum equation. The energy conservation equation accounts for changes in the internal energy,  $\varepsilon$ , the heat flux vector,  $\mathbf{q}_s$ , energy exchange processes due to microscopic collisions,  $Q_{st}$ , and frictional heating,  $\mathbf{R}_{st} \cdot \mathbf{u}_s$ . Note that while joule heating is present due to contributions from

the electric field, the magnetic field's effect does not factor into this derivation.

$$\partial_t(\varepsilon_s + \frac{1}{2}\rho_s \mathbf{u}_s \cdot \mathbf{u}_s) + \nabla_{\mathbf{r}} \cdot [(\varepsilon_s + \frac{1}{2}\rho_s \mathbf{u}_s \cdot \mathbf{u}_s + \bar{\mathbf{P}}_s) \cdot \mathbf{u}_s] + \nabla_{\mathbf{r}} \cdot \mathbf{q}_s = \mathbf{j}_s \cdot \mathbf{E} + \sum_t (Q_{st} + \mathbf{R}_{st} \cdot \mathbf{u}_s) \quad (2.8)$$

Having derived the plasma fluid description, there are several restrictions associated with using the fluid notion to discuss the plasma's unique kinetic features. One of the limitations of the plasma's fluid description is the obstacle of exploring the wave-particle interactions. The waves in the plasma are capable of forming structures such as instabilities because of the resonances that can evolve between the waves and the plasma particles' wave-like properties. Many of these kinetic aspects are lost as a result of the kinetic equation's moment integrations. However, one can bypass the kinetic resolution if the phase velocities of the waves are much less or much greater than the thermal velocity of the distribution, i.e.  $v_p = \omega/k \ll \bar{v}$  or  $v_p \gg \bar{v}$ . These regions of wave-particle interactions for both scenarios in the plasma's distribution function are termed "adiabatic" and "inertial", respectively. But, between these two conditions, which is also known as the "resonant" region, the interactions can be significant enough to alter the plasma dynamics such that these effects cannot be ignored.

Another criterion that is important in the hydrodynamic description is the Knudsen number,  $Kn$ , which is the ratio of the collisional mean free path to the characteristic length scale of the plasma system. The collisionality of the species distribution is paramount to the fluid description because the hydrodynamic representation is incapable of capturing drastic deviations away from the Maxwellian distribution, a term that will be described in the following section. In fact, the increased collisionality within the plasma can lead to a more accurate representation of the plasma by reinforcing the coupling between the plasma chemistry and the fluid description in a Maxwellian context. Additionally, simulating a plasma becomes simpler when the entire system of equations being solved can be reduced to a Maxwellian distribution assumption. However, when the plasma begins to deviate from this equilibrium condition, these departures become a focal point in collisional-radiative processes, which feeds back to the kinetic or fluid evolution of the plasma. Therefore, it is

important to recognize and define these non-equilibrium conditions in the collisional-radiative model which can have an impact at larger plasma scales.

## 2.2 Plasma Equilibria

Achieving total equilibrium throughout an entire plasma is difficult because of the many possible conditions that are likely to prevent its occurrence. Considering the issue of plasma confinement alone can lead to multiple non-equilibrium conditions: for example, devices such as magnetic confinement fusion devices require constant provisions of energy lest the system becomes cold due to various losses. These sources can be rapidly counterbalanced or overcome by sink terms such as walls that can collect particles away from the plasma or simply by radiation losses from the system, both of which can create thermal and density gradients along the plasma's periphery. In reality, there are many natural and artificial imperfections that are not accounted in plasma simulations that lead to non-equilibrium phenomena. All of these possibilities can force the plasma into a non-equilibrium state in spite of any plasma system's attempt to realign into an equilibrium distribution.

The scenario above exemplifies the ease with which plasmas depart from a state of thermodynamic equilibrium (TE), where all thermodynamic processes are balanced including spatial considerations. In thermodynamic equilibrium, the plasma is easily described by quantities such as density, temperature, and plasma composition amongst other variables. In non-equilibrium conditions, these variables are insufficient descriptions of the plasma, requiring an increased number of parameters that must be monitored to analyze the deviation away from equilibrium. Although many more quantitative variables can be used to quantify these conditions, a list of definitions describing equilibrium structures will be used in their stead to recognize when the plasma departs from equilibrium.

It is well known that the equations describing equilibria can be derived from statistical mechanics using concepts like entropy and the H-theorem. [14] Since these equilibria are well-described by mathematical descriptions, the intuition for non-equilibrium scenarios can be developed by observing the correlations of the plasma systems to these descriptions. The

concept of thermal equilibrium begins with the *principle of microscopic reversibility*, which states that the probability of a particle leaving a quantum state by a particular process is counterbalanced by an inverse process driving a particle to the same quantum state. This idea of symmetry at the quantum level must be translated into a macroscopic understanding of the elementary processes. By enforcing thermal equilibrium and using the H-theorem to justify these claims, the following equation indicating that the number of forward and backward reactions are equal holds,

$$k_{for}N_xN_y = k_{bac}N_{x'}N_{y'} \quad (2.9)$$

where  $k$  corresponds to the forward and backward reaction rates and  $N$  refers to the participating species in the reaction with features  $x$ ,  $x'$ ,  $y$ , and  $y'$ . [15] The example shown here is for a binary species reaction; but, this also extends to reactions involving more than two participating reactants. This equation corresponds to the *principle of detailed balance*. Naturally, the concept of microscopic reversibility allows one to enforce the principle of detailed balanced at the macroscopic level, from which a quantum level description of the reaction may also be ascertained,

$$\hat{\eta}_X\hat{\eta}_Y = \hat{\eta}_{X'}\hat{\eta}_{Y'} \quad (2.10)$$

In the quantum description,  $\hat{\eta}$  is the elementary occupation, or the number of particles within each quantum state ( $\hat{\eta} = N/g$ ), with properties pertaining to states  $X$ ,  $X'$ ,  $Y$ , and  $Y'$ . More interesting to note is the absence of a rate coefficient in the quantum description. This result is a consequence of the *elementary mass action law* which describes how particles change between quantum states; this is the basis from which detailed balancing and microscopic reversibility naturally relate the macroscopic and elementary description of the reactions. These principles will now be used to obtain four known equilibrium distributions fundamental to plasmas and collisional-radiative models: Maxwell, Boltzmann, Saha, and Planck. A more in-depth discussion of these distributions and their use may be found in van der Mullen's paper. [16]

### 2.2.1 Maxwell Distribution

The Maxwell distribution describes an equilibrium condition attained through an exchange of energy with elastic collisions. This distribution, along with the other equilibrium definitions that follow, can be derived by considering collisions between similar or different species, whose choice merely alters the rate at which equilibrium is attained. For the case of the Maxwell distribution, one begins with the elastic exchange of energy between particles  $X_i$  and  $Y_j$ ,

$$X_i(\varepsilon) + Y_j(\varepsilon') \rightleftharpoons X_i(\varepsilon - \Delta) + Y_j(\varepsilon' + \Delta). \quad (2.11)$$

$\Delta$  in the equation corresponds to the amount of energy exchanged between species  $i$  and  $j$ . The subscripts are used to denote the internal states meaning that energy is transferred from the translational energies rather than the internal energies. In the quantum description, the resulting equation is

$$\hat{\eta}_X(i, \varepsilon)\hat{\eta}_Y(j, \varepsilon') = \hat{\eta}_X(i, \varepsilon - \Delta)\hat{\eta}_Y(j, \varepsilon' + \Delta) \quad (2.12)$$

which can be reorganized into the following equation

$$\frac{\hat{\eta}_X(i, \varepsilon)}{\hat{\eta}_X(i, \varepsilon - \Delta)} = \frac{\hat{\eta}_Y(j, \varepsilon' + \Delta)}{\hat{\eta}_Y(j, \varepsilon')} = H(\Delta). \quad (2.13)$$

This reorganization is important as it highlights the relationship's sole dependence on  $\Delta$ , regardless of  $\varepsilon$  or  $\varepsilon'$ . This term is derived in many statistical mechanics books where  $H$  has an exponential expression:

$$H(\Delta) = e^{\theta\Delta} \quad \text{where } \theta = 1/k_B T \quad (2.14)$$

If one considers an energy distribution function, this exchange of energy can occur between any pair of bins lying in the distribution. Instead of  $H$ , the variable  $\Delta$  will now be represented by  $E$  to signify this energy exchange.

From statistical mechanics, the relation between the quantum mechanical density  $\hat{\eta}$  and

macroscopic density variable  $\eta$  is as follows

$$\hat{\eta}_X(i, E) = \eta_X(i) \frac{h^3}{(2\pi m_X k_B T)^{3/2}} e^{-E/k_B T} \quad (2.15)$$

where the fraction represents the average volume of a quantum state. Taking the equation above and multiplying it by the number density of kinetic states per energy range, i.e.  $dG/dE = 2^{5/2} \pi m_X^{3/2} E^{1/2} / h^3$ , to obtain the Maxwellian energy distribution function normalized by the number of particles per unit volume,  $\eta$ , one gets the Maxwell distribution function

$$f^M(E) = \frac{1}{\eta(i)} \frac{d\eta(i)}{dE} = \frac{2\sqrt{E}}{\sqrt{\pi}(k_B T)^{3/2}} e^{-E/k_B T} \quad (2.16)$$

When the entire fluid reaches equilibrium based solely on the transfer of translational energy, the Maxwellian distribution function represents the fluid's characteristics in equilibrium. In a multi-fluid framework, each fluid is characterized by its own temperature. Since the derivation generalizes to any group of identical particles, this assumption dictates that a single Maxwellian temperature will only be established at equilibrium. This concept becomes important when considering elastic collisions between vastly different particles, such as electrons and ions where there is a large difference in mass.

### 2.2.2 Boltzmann Distribution

The rest of the equilibria definitions are related to the inelastic set of collisions that occur within plasmas. The Boltzmann distribution is based on excitation processes within an ion distribution and can be obtained by considering the following process



In the equation above, the reaction proceeds such that the amount of energy,  $\Delta$ , is the energy gap that must be overcome to take particle  $Y$  from state  $j$  to state  $k$ . Although this distribution may be rewritten to account for the additional change in particle  $Y$ 's translational energy, the Boltzmann distribution is a reflection of the overall plasma's energy or

temperature, rather than discrete translational energy values. This is a consequence of the principle of detailed balance which involves the concept of equilibrium in its definition. The Boltzmann balance leads to the following microscopic reversibility statement

$$\hat{\eta}_X(i, \varepsilon)\hat{\eta}_Y(j, \varepsilon') = \hat{\eta}_X(i, \varepsilon - \Delta)\hat{\eta}_Y(k, \varepsilon') \quad (2.18)$$

Following the derivation of the Maxwell distribution, the equation above leads to the following exponential statement

$$\frac{\hat{\eta}_Y(j)}{\hat{\eta}_Y(k)} = e^{\Delta/k_B T} \quad (2.19)$$

which is the well-known Boltzmann relation. At equilibrium, all particles within an ionic distribution follow Boltzmann's relation. This is also defined as Boltzmann equilibrium. One can see that the particles do not distinguish between the resolution of the atomic levels from fine-structure levels, where all quantum numbers are deemed to be "good" or uniquely descriptive, to detailed-configuration averaged (DCA) states. This aspect of the Boltzmann relation will be used when considering grouping of atomic states for reduced-order modeling.

### 2.2.3 Saha Distribution

The next set of inelastic collisions that leads to the Saha distribution is the balance of ionization processes and its inverse three-particle, or 3-body, recombination. This reaction balance is given by the following equation

$$X_i(\varepsilon) + Y_j(\varepsilon') \rightleftharpoons X_i(\varepsilon - \Delta) + Y_k^+(\varepsilon'') + e(\Delta - (\varepsilon'' - \varepsilon')). \quad (2.20)$$

Here, the ionization energy is given by  $I = \varepsilon'' - \varepsilon'$  and  $\Delta$  is a particular amount of energy that exceeds the ionization threshold. As before, microscopic reversibility gives

$$\hat{\eta}_X(i, \varepsilon)\hat{\eta}_Y(j, \varepsilon') = \hat{\eta}_X(i, \varepsilon - \Delta)\hat{\eta}_{Y^+}(k, \varepsilon'')\hat{\eta}_e(\Delta - I) \quad (2.21)$$

which is rearranged into

$$\frac{\hat{\eta}_X(i, \varepsilon)}{\hat{\eta}_X(i, \varepsilon - \Delta)} = \frac{\hat{\eta}_Y(j, \varepsilon')}{\hat{\eta}_{Y^+}(k, \varepsilon'')\hat{\eta}_e(\Delta - I)} = e^{\Delta/k_B T} \quad (2.22)$$

The electron variable in this Saha expression may still be expanded. The mean occupation number for electrons is normalized by the ionization energy as expected, i.e.  $\eta_e(\Delta - I) = \frac{1}{2}N_e\lambda_e^3e^{-(\Delta-I)/k_B T}$  with  $\lambda_e$  being the electron's thermal de Broglie wavelength. Substituting this expression into the Saha equation yields a more well-known form of the equation:

$$\frac{\hat{\eta}_Y(j)}{\hat{\eta}_{Y^+}(k)N_e} = \frac{1}{2}\lambda_e^3e^{I/k_B T} \quad (2.23)$$

Although the derivation above bears similarities to the derivation of the Boltzmann distribution, the connection between states across ionization gaps requires the inclusion of the electron elementary occupation. On atomic distributions incorporating all relevant ionization stages, this electron contribution results in a ‘‘Saha jump’’ at the ionization threshold as termed by van der Mullen. One may expect these ionization events to disrupt the Boltzmann balance, but the similarities in the microscopically-reversible Boltzmann and Saha relations suggest that these processes are more cooperative than being mutually disruptive.

#### 2.2.4 Planck Distribution

The last equilibrium distribution pertaining to the plasma's interactions with the radiation field is the Planck distribution. Deriving the Planck distribution is particularly unique from the previous definitions because of the additional presence of stimulated radiation processes. The bremsstrahlung emission process shown below can be used to define the photons' equilibrium distribution.

$$X_i(\varepsilon) + Y_e(\varepsilon') \rightleftharpoons X_i(\varepsilon) + Y_e(\varepsilon' - h\nu) + \gamma(\nu). \quad (2.24)$$

The above reaction leads to the quantum description below with one caveat: an extra  $(1 + \hat{\eta}_p(\nu))$  factor must be included because of the total contribution from spontaneous and stimulated photon emissions.

$$\hat{\eta}_X(i, \varepsilon)\hat{\eta}_e(\varepsilon')[1 + \hat{\eta}_p(\nu)] = \hat{\eta}_X(i, \varepsilon)\hat{\eta}_e(\varepsilon' - h\nu)\hat{\eta}_p(\nu) \quad (2.25)$$

The quantum mechanical description of the reaction's balance is rearranged once more into a familiar expression seen in the previous derivations.

$$\frac{1 + \hat{\eta}_p(\nu)}{\hat{\eta}_p(\nu)} = \frac{\hat{\eta}_e(\varepsilon' - h\nu)}{\hat{\eta}_e(\varepsilon')} = e^{h\nu/k_B T} \quad (2.26)$$

The mean occupation number of a photon state is found to be

$$\hat{\eta}_p(\nu) = \frac{1}{e^{h\nu/k_B T} - 1} \quad (2.27)$$

For photons, the degeneracy is given by  $g(\nu) = V8\pi\nu^2c^{-3}$ . Combining the degeneracy with the mean occupation number of a photon state leads to the following Planck distribution equation

$$N(\nu) = \frac{8\pi\nu^2}{c^3} \frac{1}{e^{h\nu/k_B T} - 1} \quad (2.28)$$

## 2.3 Departing from Equilibrium

The equilibrium distributions of Maxwell, Boltzmann, Saha, and Planck present a variety of conditions that a plasma may depart from, thereby leading to many combinations of non-equilibrium conditions. In the case of the Maxwell distribution, the imbalance in fluid energy or transport is sufficient to leave Maxwell equilibrium. The collisional-radiative aspects of the plasma can also distort the Boltzmann and Saha distribution, as well as push the system towards or away from the Planck distribution. All of these distributions are distinct by their

energy exchange mechanisms, but each particle in the plasma participates in all of these processes. It is then foreseeable that a perturbation in one measure of equilibrium affects another equilibrium distribution. Therefore, the kinetic processes should be captured as these microscopic deviations propagate to large scales.

There are several more concepts that can be defined to classify non-equilibrium plasmas. A few of those definitions will be discussed here. One of the easiest departures from equilibrium concerns a radiating plasma due to photon emissions. Considering an infinitesimal volume of plasma, the radiation from this plasma can alter the energy content in neighboring plasma volumes. But if this radiation transfer does not dramatically change the equilibrium descriptions of Maxwell, Boltzmann, and Saha in each plasma volume, equilibrium may be defined in a *local* sense, i.e. local thermodynamic equilibrium. Further departures might occur when collisional-radiative processes begin to distort portions of the distribution functions. When equilibrium is sustained in parts of a particular distribution function, the definition of a *partial* equilibrium may be applied. While this concept is explored in this work, explicit usage of the definition will be abstained because of the partly subjective nature of its identification. However, the reader is invited to refer to the work of van der Mullen for an extended discussion on plasma equilibria conditions. Instead, the more widely used non-local thermodynamic equilibrium, or non-LTE, definition, which characterizes systems that are simply out of LTE conditions, will be used to describe these instances in a broader sense.

Using the concepts and definitions in this chapter as the foundation for modeling and understanding the plasma chemistry, one can now construct the chemistry model used to simulate elastic, inelastic, collisional, and radiative processes in plasmas. The collisional-radiative model is particularly convenient for many non-equilibrium plasma investigations because of the numerical model's state-to-state approach. This state-to-state quality allows each atomic state to be solved based on forward and inverse rates which couples the entire set of accounted levels. These characteristics make the collisional-radiative model a premier candidate for exploring these highly-detailed features.

## CHAPTER 3

### The Collisional-Radiative Model

The numerical model used to simulate the plasma chemistry in this work is the collisional-radiative model. One of the advantages of using the CR model is its applicability in multiple plasma regimes. As mentioned in the introduction, the collisional-radiative model has been used to investigate astrophysical phenomena, atmospheric reentry vehicles, nuclear fusion, and many other applications. Whether the module's function is to investigate the theoretical impact of the chemical kinetics on plasma flows or support experimental or natural observations through spectroscopy, the CR model serves a multitude of plasma needs. In many ways, the collisional-radiative model can be considered a bridge in the plasma universe because of the interconnected network that surrounds plasma chemistry and the CR model's ability to create those connections.

The collisional-radiative model's master equation can be obtained by simplifying Braginskii's set of equations and retaining the terms relevant to a 0-dimensional construct. Since the master equation will operate 0-dimensionally, many of the spatial terms will be removed; as a result, the momentum-conservation equations are absent from the collisional-radiative model because of its operation in multi-dimensional physical space. A plasma physics simulation based solely on the collisional-radiative model would be inaccurate if the momentum effects such as diffusion have a large impact on the flux of particles into or out of the plasma. Since the focus of this work is the development of the CRM, one of the two following assumptions may be considered: that all particles remain in a simulated volume of space or that the entire simulation space is void of spatial gradients or variations, i.e. a uniformly evolving plasma. This leaves the mass and energy-conservation equations to consider.

In the mass-conservation equation, the mass-convection term is removed in the 0-D con-

text, leaving the temporal derivative and collisional terms. Although the word “collisional” is used, it also encompasses radiative and other kinetic effects that can interact with the atomic and ionic species in the system. The mass conservation equation is as follows

$$\partial_t N_s = \left( \frac{\partial N_s}{\partial t} \right)_{coll} \quad (3.1)$$

where  $N_s$  is the number density for species  $s$ , instead of the mass density used previously in the Braginskii equation. Using the equation above as the baseline for the master equation, the size of the CRM’s system of equations increases for each state that the user adds and seeks to resolve. As one state is added to the list of reacting states, the corresponding rates of reactions must also be included as RHS terms to the equation.

The next equation that can be added to the master equation is the energy equation. The energy equation monitors the multi-temperature variations of the plasma, which can affect the rate coefficients of the collisional-radiative model. The energy equation can be modified into a 0-D framework ( $\varepsilon_s = m_s E_s$  and  $Q_{st} = m_s \mathcal{Q}_{st}$ ) by removing terms that involve bulk velocities and spatial derivatives, leading to the collisional-radiative model’s energy equation below.

$$\partial_t E_s = \sum_t \mathcal{Q}_{st} \quad (3.2)$$

Including an energy equation for each atomic state in the system is computationally expensive. This can be avoided by if one considers the equilibration times between particles of similar masses. For example, in many applications, the equilibration rates tend to differ between electron-electron collisions and collisions between similar atoms or molecules. Therefore, one might consider a 2-temperature model to account for changes in the plasma’s overall energy, which will be the extent of the energy equations’ inclusion in this work. Without these energy equations, the collisional-radiative model can be used in a steady-state setting or an isothermal context.

The collisional-radiative model’s ability to capture the reactive dynamics in the plasma is dependent on the RHS terms of the mass and energy conservation equations. Insufficient accountability of chemical processes and particle states can lead to inaccurate representations

in the plasma parameters such as ionic charge and plasma density. The rest of this chapter will focus on the inclusion of these collisional-radiative reactions as well as the atomic states and data used in this study.

### 3.1 Elementary Processes and Detailed Balancing

The rates corresponding to each collisional and radiative process must be calculated in the CR model to simulate the evolution of the atomic state densities. As an example, the macroscopic reaction rate for a collision from state 1 to 2 caused by a colliding free electron takes the following form

$$k_{12} = n_1 n_e \int_{v_o}^{\infty} d^3\mathbf{v} |\mathbf{v}| \sigma_{1e}(\mathbf{v}) f_e(\mathbf{v}) \quad (3.3)$$

The integral in the expression above describes the interaction between an atomic state in question and the distribution inducing the transitions, which is due to the electrons in this scenario. The velocity,  $\mathbf{v}$ , is typically the relative velocities between the participating reactants; in many cases, this velocity may be assumed as the electron thermal velocity as is the case in this work. The cross section,  $\sigma$ , which is a function of the relative velocity between the particles represents the likelihood of the transition to proceed.

The term  $f_e$ , which is the electron energy distribution function (EEDF), is important for calculating the collisional rates for the model. The current assumption for the electron distribution is a Maxwellian distribution function. However, there are instances where non-Maxwellian characteristics in the distribution function lead to variations in the reaction rate, altering the overall reaction dynamics in the CR model. This scenario requires solving the EEDF which ties directly into the rate calculations of the CR model, making up a coupled set of physics models. The construction of this coupled CR-EEDF model is currently being pursued and will be addressed in future. However, the reader is encouraged to refer to other sources on the construction of this system. [17] [18] For a Maxwellian EEDF, the macroscopic

reaction rate may be rewritten as follows:

$$k(T) = \frac{\bar{v}}{(kT)^2} \int_{E_0}^{\infty} \sigma(E) E e^{-E/k_B T} dE \quad (3.4)$$

where  $E_0$  is the threshold energy required for the reaction to occur and  $\bar{v} = \left(\frac{8k_B T}{\pi\mu}\right)^{1/2}$  is the mean thermal velocity with  $\mu$  as the reduced mass between both particles.

Rate coefficient	Process at ion stage $+k$
$\alpha_{(m n)}^{+k,e}$	Collisional excitation by an electron ( $n \rightarrow m$ )
$\beta_{(n m)}^{+k,e}$	Collisional deexcitation by an electron ( $m \rightarrow n$ )
$\alpha_{(+,j n)}^{+k,e}$	Collisional ionization by an electron ( $n \rightarrow j$ )
$\alpha_{(m n)}^{+k,0}$	Collisional excitation by a ground state atom ( $n \rightarrow m$ )
$\beta_{(n m)}^{+k,0}$	Collisional deexcitation by a ground state atom ( $m \rightarrow n$ )
$\alpha_{(+,j n)}^{+k,0}$	Collisional ionization by a ground state atom ( $n \rightarrow j$ )
$\beta_{(n +,j)}^{+k,e}$	Three body recombination ( $j \rightarrow n$ )
$\alpha^{+k,e}$	Elastic collisions between an ion and electron
$\Lambda_{nm}$	Bound-bound optical escape factor
$A_{(m n)}^{+k}$	Bound-bound transition (Einstein coefficient)
$\Lambda_{n +,j}$	Bound-free optical escape factor
$R_{(+,j n)}^{+k}$	Radiative recombination
$R_{E;(+,j n)}^{+k}$	Radiative recombination (Energy transfer rate)

**Table 3.1:** Rate coefficients in the collisional-radiative model.

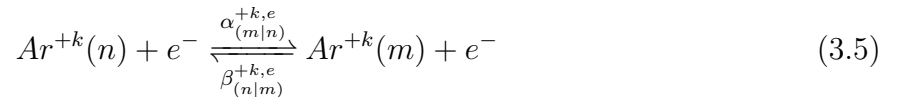
Rate calculations must be performed for processes that involve a distribution of particles or photons that can induce atomic transitions. Table 3.1 lists the rates which will be calculated for the simulations presented. The coefficient's subscript,  $(m|+,n)$ , denote the final and initial states, respectively, where  $+$  denotes the ionization stage corresponding to the specified state. The rates are integrated over the distribution and respective cross sections using an adaptive mesh integration scheme developed by Genz et al. [19]

For the scenarios explored in this work, the rates corresponding to ion-ion interactions have not been included in the simulation. The electron-atom processes are currently assumed

to be the dominant mechanisms of the evolving plasma system. However, one should note the importance of ion-ion interactions for many systems, such as mechanically-shocked flows where these processes are significant for generating priming electrons, as noted by Kapper and Cambier. [20] In this instance, if one were to model the chemical kinetics, the formation of the plasma may be diminished or non-existent if processes that lead to the production of electrons were excluded. In the case of laser-plasma interactions, the laser dominates the set of atomic kinetics, where ensuing accurate electron-ion interactions become more critical. This allows one to ignore the previously-mentioned ion-ion interactions, which also occur at relatively longer timescales.

### 3.1.1 Collisional Excitation/Deexcitation

The first atomic process considered for this model is collisional excitation, which is a result of free electron collisions with an atomically-bound electron. Collisional excitation can also occur between atoms, but will be neglected as previously mentioned. The inverse process to this forward reaction is called collisional deexcitation. The equation representing this set of collisional processes is shown below.



For a particular excitation event, the transition occurs between two states,  $m$  and  $n$ , for a particular ionization stage,  $+k$ . For consistency, state  $m$  is assumed to be greater than state  $n$  in this reaction and the others that follow. The lower state's density rate equation for this set of collisional processes is:

$$\frac{dN_n^{+k}}{dt} = \dot{\omega}_n^{+k} = -\alpha_{(m|n)}^{+k,e} N_e N_{+k,n} + \beta_{(n|m)}^{+k,e} N_e N_{+k,m} \quad (3.6)$$

The first term in equation 3.6 represents the destruction rate of the  $n^{th}$  state due to electronic excitation, while the second term is the production rate resulting from electronic deexcitation. The excitation rate coefficient will be calculated using equation 3.4, while the

backward, or inverse, rate coefficient is calculated using detailed balance.

A system in Boltzmann equilibrium means that the density ratio between any two states is represented by the Boltzmann relation, seen in equation 5.2. Under this condition, one should also recognize that  $\dot{\omega}_n^{+k} = 0$  since the states are in equilibrium. Therefore, the backward rates can be obtained from this equilibrium relation; this is the application of the principle of detailed balance.

$$\frac{\alpha_{(m|n)}^{+k,e}}{\beta_{(n|m)}^{+k,e}} = \frac{N_{+k,m}}{N_{+k,n}} = \frac{g_m^{+k}}{g_n^{+k}} e^{-E_{nm}/k_B T_e} \quad (3.7)$$

Here,  $g$  is the degeneracy of the specified state and  $E_{nm}$  is the energy gap between the two states in the excitation system.

### 3.1.2 Collisional Ionization and Three-Body Recombination

When the electrons have a sufficient amount of energy, the collisions between atoms and electrons can lead to ionization. This atomic process is called collisional ionization. The backward process which involves the loss of energy by an electron due to an electron-electron collision resulting in subsequent recombination of the low-energy electron is called three-body recombination. This set of processes are captured in the following equation:

$$Ar^{+k}(n) + e^- \xrightleftharpoons[\beta_{(n|+,j)}^{+k,e}]{\alpha_{(+,j|n)}^{+k,e}} Ar^{+(k+1)}(j) + e^- + e^- \quad (3.8)$$

The rate equation for collisional ionization and three-body recombination is shown in equation 3.9. The first term corresponds to the reduction of the atomic state density due to electron-impact ionization; the second term is associated with the increase in atomic state density from three-body recombination events.

$$\dot{\omega}_n^{+k} = -\alpha_{(+,j|n)}^{+k,e} N_e N_{+k,n} + \beta_{(n|+,j)}^{+k,e} N_{+(k+1),j} N_e^2 \quad (3.9)$$

Again, the forward ionization rate is calculated by Eq. 3.4. Unlike the collisional excita-

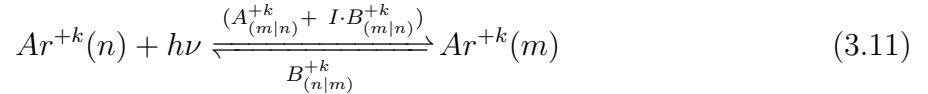
tion case, the backward recombination rate is obtained by applying the principle of detailed balance using the Saha equilibrium assumption. The constant relating the ionization and recombination rates is obtained from the Saha equation, given by the second equality in Eq. 5.3. [16]

$$\frac{\alpha_{(+,j|n)}^{+k,e}}{\beta_{(n|+,j)}^{+k,e}} = \frac{N_{+(k+1),j}N_e}{N_{+k,n}} = \frac{g_{+,j}}{g_n} \frac{2(2\pi m_e k_B T_e)^{3/2}}{h^3} e^{-I_n/k_B T_e} \quad (3.10)$$

where  $I_n$  is the ionization energy. The involvement of the electron's partition function can be seen in the inverse rate calculation due to Saha equilibrium.

### 3.1.3 Bound-Bound Radiative Processes

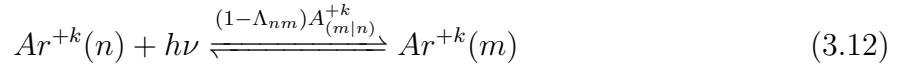
In addition to the collisional processes in the plasma, the plasma is also capable of absorbing or emitting photons due to radiative processes. We will first consider the radiation field's interaction with the atomic particles that lead towards photon-based excitation and deexcitation.



The reaction above contains three radiative processes: spontaneous emission, stimulated emission, and photon absorption, the first which is represented by the Einstein  $A$  coefficient and the latter two given by the Einstein  $B$  coefficients. One should bear in mind that the reaction set requires a specific photon frequency to excite the atom to the final state of the transition. Conversely, the same photon frequency will be released by the atom in an emission event. For a wide range of states and transitions considered, a wide spectrum of frequencies must also be considered to account for as much of the radiation absorption as possible. This requires solving the radiation transport equation which calculates the transported distribution of photons in space. This calculation is computationally expensive as each photon bin is solved in a domain spanned by frequency, angular trajectory, and physical space. This work will not be pursued here as the reader is encouraged to refer to Mihalas et al. for details on its implementation. [21]

For the meantime, solving the radiation transport equation can be avoided by assuming

an optical escape factor, which was denoted as  $\Lambda$  in table 3.1. For the case of 0-dimensional CR kinetics, this is a localized assumption. However, in the multi-dimensional scenario, any form of transport that interacts at scales comparable to the radiation transport scales, such as the optical mean free path and any scale length corresponding to transport, renders this approximation inaccurate. The modified reaction set that uses the optical escape factor is shown below.



The use of optical escape factors simplifies the system of equations immensely by avoiding radiation transport solves. The escape factor value ranges from 0 to 1. A value of 0 characterizes an optically-thick system, while a value of 1 corresponds to the optically-thin case. The density rate of change for ionic stage  $+k$  with state  $n$  due to bound-bound emissions is given by Eq. 3.13. Given in the following equation is the spontaneous emission coefficient which also related to the oscillator strength between the participating states,  $f_{mn}$ .

$$\dot{\omega}_n^{+k} = -\Lambda_{nm}A_{(m|n)}^{+k}N_n^{+k} \quad (3.13)$$

$$A_{(m|n)}^{+k} = \left( \frac{8\pi^2 e^2}{m_e c^2} \right) \frac{g_n}{g_m} f_{nm} \quad (3.14)$$

The remaining Einstein coefficients are related to each other through detailed balance as before:

$$g_n^{+k} B_{(m|n)}^{+k} = g_m^{+k} B_{(n|m)}^{+k} \quad (3.15)$$

$$\frac{A_{(n|m)}^{+k}}{B_{(n|m)}^{+k}} = \frac{2h\nu^3}{c^2} \quad (3.16)$$

### 3.1.4 Bound-Free Radiative Processes

The next set of radiation-based reactions involves bound-free atomic processes induced by photon interactions. This set of processes includes photoionization and radiative recombination induced by photons, similar to the collisional reaction set which instead depends on

electrons. However, an additional process in the form of stimulated recombination is also included in this set of equations, much akin to the bound-bound radiation processes. As before, we avoid solving for radiation transport for this set of processes, thereby leading to the following equation which relies mainly on the radiative recombination rate coefficient.

$$Ar^{+k}(n) + h\nu \xrightleftharpoons{(1-\Lambda_{n|+,j})R_{(+,j|n)}^{+k}} Ar^{+(k+1)}(j) + e^- \quad (3.17)$$

Note that the equation also uses an escape factor, which in the photorecombinative case is called the bound-free optical escape factor. The density rate of change for state  $n$  with ionization stage  $+k$  is given by equation 3.18. The notation has been modified to denote transitions to a lower ionic stage at state  $j$ .

$$\dot{\omega}_n^{+k} = -\Lambda_{(-,j|n)}R_{(-,j|n)}^{+k}N_n^{+k}N_e \quad (3.18)$$

The capture of an electron also changes the overall electron energy of the system. Separate electron energy rates must be tabulated in order to account for the change in the overall electron energy distribution. These energy rate coefficients can be obtained by calculating a  $2^{nd}$ -order energy moment for the rate calculation. This radiative recombination rate coefficient is used to modify the electron energy equation shown in the following equation.

$$R_E(T) = \frac{\bar{v}}{(k_B T)^2} \int_{E_0}^{\infty} \sigma(E) E^2 e^{-E/k_B T} dE \quad (3.19)$$

$$\dot{\omega}_{E_e} = -\Lambda_{(-,j|n)}R_E(T)N_n^{+k}N_e \quad (3.20)$$

### 3.1.5 Elastic Processes

Many of the processes listed so far are known as inelastic collisions where part of the energy results in the alteration of the internal energy state. However, elastic collisions can also occur, which is captured in the 0-D model with the separation of the electron and heavy atom energies; these collisions drive the overall system towards the aforementioned Maxwellian

equilibrium where an exchange of translational energy takes place. Eq. 3.21 expresses the interaction between the electrons and atomic species during the elastic collision.

$$\dot{\omega}_{E_h} = -\dot{\omega}_{E_e} = \frac{2m_e}{m_{Ar}} N_e \frac{3}{2} k_B (T_e - T_h) \sum_{k,j} \bar{\alpha}^{+k,e} N^{+k}, \quad N^{+k} = \sum_j N_j^{+k} \quad (3.21)$$

The summation within the equation captures the electron-neutral and Coulomb collisions, both of which can differ by several orders of magnitude. Both processes are currently included in the CR model. The formulation for the Coulomb collision rate is taken from Mitchner. [22]

$$\bar{\alpha}^{+k,e} = \bar{v}_e \sigma_{e,+k}, \quad \sigma_{e,+k} = 5.58 \times 10^{-10} \frac{\ln \Lambda}{T_e^2} [m^2], \quad \text{where } k > 0 \quad (3.22)$$

### 3.1.6 Bremsstrahlung

Lastly, Bremsstrahlung is an electron emission event that occurs due to radiative phenomena that can occur during any electron's interactions with other particles in the system. This phenomenon occurs as a result of the charge and mass differences between the electron and a secondary particle, such as an ion. In this case, the Coulombic force between the electron and ion causes the electron to undergo an acceleration event, during which radiative emission can occur. This radiation event is captured in the following equation

$$e^-(\varepsilon_1) + h\nu \rightleftharpoons e^-(\varepsilon_2) \quad (3.23)$$

where  $\varepsilon_2 > \varepsilon_1$ . Because of the electrons' high mobility and inertia, much of the radiation loss due to Bremsstrahlung is attributed to the electrons rather than the heavy species.

The free-free transitions associated with Bremsstrahlung emission has also been included in the collisional-radiative model. Assuming a Maxwellian distribution of electrons, the model equation for this process was formulated by Kramer. The representative energy loss is given in the equation below. [23]

$$\dot{\omega}_{E_{e,B}} = \frac{-32\pi}{3\sqrt{3}} \left( \frac{2\pi k_B T}{m} \right)^{1/2} \frac{k^2 e^6}{m c^3 h} N_{+k} N_e = -1.42 \times 10^{-40} k^2 T_e^{1/2} N_{+k} N_e [J \cdot m^{-3} \cdot s^{-1}] \quad (3.24)$$

## 3.2 Rate Equations

All of the collisional, radiative, elastic, and inelastic collisions were compiled into a rate calculation module that is used by the collisional-radiative model to include in the master equation. The entire system of ODEs solves for the density rate equations that includes all of the states under consideration. A multi-temperature set of equations in the form of electron and atomic energy equations can also be evolved in the model. An equation solving for the electron number density is also included in the model; this equation is necessary when individual plasma volumes are not under quasineutral assumptions. However, in this 0-dimensional framework, the quasineutral assumption is upheld and the electron number density equation is not necessary.

The entire collisional-radiative system of equations are shown in Eq. 3.25 to 3.28. This system of ODEs is heavily coupled as a result of the number of transitions that relate various atomic states between one another. An explicit time-marching scheme would involve eigenvalues that correspond to the fastest rate of reactions, meaning that the system would require large amounts of computational time to complete in order to resolve the fastest reactions. Therefore, an implicit scheme is necessary to take larger time steps while maintaining numerical stability. In the current iteration of the CRM, two implicit schemes were used for time-dependent simulations of the plasma. The first numerical scheme is a low-order method in backward Euler. For more accurate simulations, a 3-stage, 5<sup>th</sup>-order Radau5 method was included in the simulation. The difference in implementation of the explicit and implicit scheme requires a Jacobian for implicit time-marching. A discussion of the numerical schemes and the Jacobian construction may be found in the appendices. Further details of Radau5 may be found in Hairer and Wanner’s book on stiff ODE solvers. [24]

## Generalized ionic/excited state

$$\begin{aligned}
\dot{\omega}_n^{+k} = & - \sum_{m>n} \alpha_{(m|n)}^{+k,e} N_e N_{+k,n} + \sum_{m>n} \beta_{(n|m)}^{+k,e} N_e N_{+k,m} + \sum_{m>n} \Lambda_{nm} A_{(n|m)}^{+k} N_{+k,m} \\
& + \sum_{m<n} \alpha_{(n|m)}^{+k,e} N_e N_{+k,m} - \sum_{m<n} \beta_{(m|n)}^{+k,e} N_e N_{+k,n} - \sum_{m<n} \Lambda_{nm} A_{(m|n)}^{+k} N_{+k,n} \\
& - \sum_j \alpha_{(+,j|n)}^{+k,e} N_e N_{+k,n} + \sum_j \beta_{(n|+,j)}^{+k,e} N_{+(k+1),j} N_e^2 \\
& - \sum_j \Lambda_{(-,j|n)} R_{(-,j|n)}^{+k} N_n^{+k} N_e + \sum_j \Lambda_{(n|+,j)} R_{(n|+,j)}^{+(k+1)} N_n^{+(k+1)} N_e^2
\end{aligned} \tag{3.25}$$

## Electron number density

$$\begin{aligned}
\dot{\omega}_e = & \sum_{k,j,n} \alpha_{(+,j|n)}^{+k,e} N_e N_{+k,n} - \sum_{k,j,n} \beta_{(n|+,j)}^{+k,e} N_{+(k+1),j} N_e^2 \\
& - \sum_{k,j,n} \Lambda_{(n|+,j)} R_{(n|+,j)}^{+(k+1)} N_n^{+(k+1)} N_e^2
\end{aligned} \tag{3.26}$$

## Energy equation for heavy particles

$$\begin{aligned}
\dot{\omega}_{E_h} = & \frac{2m_e}{m_{Ar}} \sum_k \alpha^{+k,e} [E_e N^{+k} - N_e E_h] = \frac{2m_e}{m_{Ar}} N_e \frac{3}{2} k_B (T_e - T_h) \sum_{k,j} \bar{\alpha}^{+k,e} N^{+k} \\
& N^{+k} = \sum_j N_j^{+k}
\end{aligned} \tag{3.27}$$

## Energy equation for electrons

$$\begin{aligned}
\dot{\omega}_{E_e} = & \sum_{k,n} \sum_{m>n} E_{nm}^{+k} \left( -\alpha_{(m|n)}^{+k,e} N_{+k,n} N_e + \beta_{(n|m)}^{+k,e} N_{+k,m} N_e \right) \\
& + \sum_{k,n} \sum_j I_{n,j}^{+k} \left( \beta_{(n|+,j)}^{+k,e} N_{+(k+1),j} N_e^2 - \alpha_{(+,j|n)}^e N_{+k,n} N_e \right) \\
& - \sum_{k,n,j} I_{n,j}^{+k} \Lambda_{(-,j|n)} R_{(-,j|n)}^{+k} N_n^{+k} N_e - \sum_{k,n} \sum_{m<n} E_{nm}^{+k} \Lambda_{nm} A_{(m|n)}^{+k} N_{+k,n} \\
& - \frac{2m_e}{m_{Ar}} \sum_k \alpha^{+k,e} [E_e N^{+k} - N_e E_h] \\
& - \frac{32\pi}{3\sqrt{3}} \left( \frac{2\pi k_B T}{m} \right)^{1/2} \sum_{k,n} \frac{k^2 e^6}{m c^3 h} N_{+k,n} N_e
\end{aligned} \tag{3.28}$$

### 3.3 Argon Atomic Data Sets

A comprehensive simulation that captures the plasma's detailed kinetics of the atomic states requires a sufficient set of atomic information to use the collisional-radiative model. In addition to the atomic levels, the relevant transitions across all of the included atomic and their associated reaction cross sections must also be known. The Los Alamos National Laboratory's (LANL) atomic physics codes fulfill this need, having generated the desired data for several atomic elements; amongst the data sets, atomic and transitional data for Ar+0 to Ar+17 have been extracted for this work's modeling objectives. [25] Argon is not only relevant to electric propulsion devices as a commonly-used propellant, but is also present in many other plasma applications.

The data were first generated and published to model the effect of impurities in multiple planned and constructed fusion devices. The purpose of the atomic data was to generate spectroscopic data in light of matching the experimental data; comparing results generated from the CR model did not only verify the presence of reactive processes and validate the conditions of the plasma systems, but also provided critical information concerning the role of impurities, which was found to quench the fusion process in these devices. [26] Due to the widespread pursuit of fusion energy, the accuracy and reliability of the cross sectional data is highly desired. Therefore, the atomic data from the LANL database has been compared with multiple experiments in the fusion regime, along with comparisons against other computationally-determined results. [27] [28]

The atomic data is obtained by performing calculations based in atomic theory. Calculation of the atomic structure in the LANL database involves the use of the Hartree-Fock method which is elaborated by R. D. Cowan in his book regarding atomic structure theory. [29] The Hartree-Fock method is used to calculate the time-dependent Schrödinger's equation to extract the quantum states. [30] These methods involve interdependencies between the nuclear potential and electron shells' contributions to the potential, making the calculations non-trivial. Several atomic levels of argon are shown in tables 3.3, 3.4, and 3.5. While the energy and degeneracy provides a certain measure of the level's information, the

Ion Level	Levels	CE	PI/CI	Ion Level	Levels	CE	PI/CI
Ar +0	347	27284	40483	Ar +9	279	831	20675
Ar +1	841	113260	147454	Ar +10	554	5485	39227
Ar +2	1388	285572	274700	Ar +11	668	9900	36134
Ar +3	1472	336500	228628	Ar +12	564	11070	18199
Ar +4	1104	197157	97490	Ar +13	291	4245	4278
Ar +5	2003	196119	67759	Ar +14	98	925	933
Ar +6	283	9133	3114	Ar +15	97	285	789
Ar +7	258	1273	3357	Ar +16	31	30	73
Ar +8	89	88	3862	Ar +17	16	15	16

**Table 3.2:** Argon atomic data sets found in the LANL database.

Argon sets include information about the atomic levels and the cross sections relevant for state to state transitions. CE: electron-impact (collisional) excitation; PI/CI: photo/electron-impact (collisional) ionization.

uniqueness of each level ultimately stems from the atomic structure given in LS notation in the atomic data, where  $L$ ,  $S$ , and  $J$  are used to describe each subshell's momenta.  $L$  is the total orbital angular momentum,  $S$  is the total spin angular momentum, and  $J$  is the total angular momentum contributed by  $L$  and  $S$ . These three quantum numbers prescribe a unique level; a fourth good quantum number is needed to purely define a unique spin state. However, splittings from such calculations are considered to be more significant under the presence of electromagnetic fields which are currently not being considered in the CR calculations. [31] Descriptions of the energy, degeneracy, and structure of each level are described in the following tables. The description of the orbital and spin angular momenta for the specific subshell are given in the parentheses, while the coupling description to the inner subshells are shown thereafter.

Using the information on the levels obtained with the Hartree-Fock method, transitions can be determined between each of the atomic levels, leading to further information such as energy gaps and likelihood of transitions to proceed. Rates or cross-sectional values as functions of impact energy must be calculated to construct the collisional-radiative rate matrix that relates one atomic state density to another. For the case of electronic excitation, these values can be calculated using the distorted-wave (DW) approximation or first-order many-body perturbation theory (FOMBT). [32] [27] As perturbation/approximation techniques,

n	E(n) [eV]	$g_n$	$nl(^{2S+1}L_J)$	n	E(n) [eV]	$g_n$	$nl(^{2S+1}L_J)$
1	-0.388	1	[Mg]3p <sup>6</sup>	12	13.043	3	3p <sup>5</sup> ( <sup>2</sup> P) <sup>2</sup> P 4p <sup>1</sup> ( <sup>2</sup> P) <sup>1</sup> P <sub>1.0</sub>
2	11.352	5	3p <sup>5</sup> ( <sup>2</sup> P) <sup>2</sup> P 4s <sup>1</sup> ( <sup>2</sup> S) <sup>3</sup> P <sub>2.0</sub>	13	13.056	5	3p <sup>5</sup> ( <sup>2</sup> P) <sup>2</sup> P 4p <sup>1</sup> ( <sup>2</sup> P) <sup>1</sup> D <sub>2.0</sub>
3	11.417	3	3p <sup>5</sup> ( <sup>2</sup> P) <sup>2</sup> P 4s <sup>1</sup> ( <sup>2</sup> S) <sup>3</sup> P <sub>1.0</sub>	14	13.076	3	3p <sup>5</sup> ( <sup>2</sup> P) <sup>2</sup> P 4p <sup>1</sup> ( <sup>2</sup> P) <sup>3</sup> P <sub>1.0</sub>
4	11.517	1	3p <sup>5</sup> ( <sup>2</sup> P) <sup>2</sup> P 4s <sup>1</sup> ( <sup>2</sup> S) <sup>3</sup> P <sub>0.0</sub>	15	13.250	1	3p <sup>5</sup> ( <sup>2</sup> P) <sup>2</sup> P 4p <sup>1</sup> ( <sup>2</sup> P) <sup>1</sup> S <sub>0.0</sub>
5	11.595	3	3p <sup>5</sup> ( <sup>2</sup> P) <sup>2</sup> P 4s <sup>1</sup> ( <sup>2</sup> S) <sup>1</sup> P <sub>1.0</sub>	16	13.626	1	3p <sup>5</sup> ( <sup>2</sup> P) <sup>2</sup> P 3d <sup>1</sup> ( <sup>2</sup> P) <sup>3</sup> P <sub>0.0</sub>
6	12.724	3	3p <sup>5</sup> ( <sup>2</sup> P) <sup>2</sup> P 4p <sup>1</sup> ( <sup>2</sup> P) <sup>3</sup> S <sub>1.0</sub>	..	.....	..	.....
7	12.854	7	3p <sup>5</sup> ( <sup>2</sup> P) <sup>2</sup> P 4p <sup>1</sup> ( <sup>2</sup> P) <sup>3</sup> D <sub>3.0</sub>	343*	72.090(7)	1	3s <sup>0</sup> 3p <sup>6</sup> ( <sup>1</sup> S) <sup>1</sup> S 3d <sup>2</sup> ( <sup>3</sup> P) <sup>3</sup> P <sub>0.0</sub>
8	12.870	5	3p <sup>5</sup> ( <sup>2</sup> P) <sup>2</sup> P 4p <sup>1</sup> ( <sup>2</sup> P) <sup>3</sup> D <sub>2.0</sub>	344*	72.091(2)	3	3s <sup>0</sup> 3p <sup>6</sup> ( <sup>1</sup> S) <sup>1</sup> S 3d <sup>2</sup> ( <sup>3</sup> P) <sup>3</sup> P <sub>1.0</sub>
9	12.920	3	3p <sup>5</sup> ( <sup>2</sup> P) <sup>2</sup> P 4p <sup>1</sup> ( <sup>2</sup> P) <sup>3</sup> D <sub>1.0</sub>	345*	72.092(3)	5	3s <sup>0</sup> 3p <sup>6</sup> ( <sup>1</sup> S) <sup>1</sup> S 3d <sup>2</sup> ( <sup>3</sup> P) <sup>3</sup> P <sub>2.0</sub>
10	12.929	5	3p <sup>5</sup> ( <sup>2</sup> P) <sup>2</sup> P 4p <sup>1</sup> ( <sup>2</sup> P) <sup>3</sup> P <sub>2.0</sub>	346*	72.208	9	3s <sup>0</sup> 3p <sup>6</sup> ( <sup>1</sup> S) <sup>1</sup> S 3d <sup>2</sup> ( <sup>1</sup> G) <sup>1</sup> G <sub>4.0</sub>
11	13.025	1	3p <sup>5</sup> ( <sup>2</sup> P) <sup>2</sup> P 4p <sup>1</sup> ( <sup>2</sup> P) <sup>3</sup> P <sub>0.0</sub>	347*	73.023	1	3s <sup>0</sup> 3p <sup>6</sup> ( <sup>1</sup> S) <sup>1</sup> S 3d <sup>2</sup> ( <sup>1</sup> S) <sup>1</sup> S <sub>0.0</sub>

**Table 3.3:** Ar+0 atomic levels found in the LANL database.

Listed here are the range of levels considered, corresponding energies, degeneracy, and structure of the 2 outermost subshells in LS (Russell-Saunders) notation. The ‘\*’ indicates 3 of the outermost subshells have been described for the level’s structure.

n	E(n) [eV]	$g_n$	$nl(^{2S+1}L_J)$	n	E(n) [eV]	$g_n$	$nl(^{2S+1}L_J)$
1	-1.392	4	[Mg]3p <sup>5</sup> ( <sup>2</sup> P) <sup>2</sup> P <sub>1.5</sub>	12	16.966	2	3p <sup>4</sup> ( <sup>3</sup> P) <sup>3</sup> P 4s <sup>1</sup> ( <sup>2</sup> S) <sup>2</sup> P <sub>0.5</sub>
2	-1.229	3	[Mg]3p <sup>5</sup> ( <sup>2</sup> P) <sup>2</sup> P <sub>0.5</sub>	13	17.028	10	3p <sup>4</sup> ( <sup>3</sup> P) <sup>3</sup> P 3d <sup>1</sup> ( <sup>2</sup> D) <sup>4</sup> F <sub>4.5</sub>
3	13.490	3	3s <sup>1</sup> ( <sup>2</sup> S) <sup>2</sup> S 3p <sup>6</sup> ( <sup>1</sup> S) <sup>2</sup> S <sub>0.5</sub>	14	17.089	8	3p <sup>4</sup> ( <sup>3</sup> P) <sup>3</sup> P 3d <sup>1</sup> ( <sup>2</sup> D) <sup>4</sup> F <sub>3.5</sub>
4	15.954	8	3p <sup>4</sup> ( <sup>3</sup> P) <sup>3</sup> P 3d <sup>1</sup> ( <sup>2</sup> D) <sup>4</sup> D <sub>3.5</sub>	15	17.134	6	3p <sup>4</sup> ( <sup>3</sup> P) <sup>3</sup> P 3d <sup>1</sup> ( <sup>2</sup> D) <sup>4</sup> F <sub>2.5</sub>
5	15.971	6	3p <sup>4</sup> ( <sup>3</sup> P) <sup>3</sup> P 3d <sup>1</sup> ( <sup>2</sup> D) <sup>4</sup> D <sub>2.5</sub>	16	17.164	4	3p <sup>4</sup> ( <sup>3</sup> P) <sup>3</sup> P 3d <sup>1</sup> ( <sup>2</sup> D) <sup>4</sup> F <sub>1.5</sub>
6	15.988	4	3p <sup>4</sup> ( <sup>3</sup> P) <sup>3</sup> P 3d <sup>1</sup> ( <sup>2</sup> D) <sup>4</sup> D <sub>1.5</sub>	..	.....	..	.....
7	16.000	2	3p <sup>4</sup> ( <sup>3</sup> P) <sup>3</sup> P 3d <sup>1</sup> ( <sup>2</sup> D) <sup>4</sup> D <sub>0.5</sub>	837*	81.639	8	3s <sup>0</sup> 3p <sup>5</sup> ( <sup>2</sup> P) <sup>2</sup> P 3d <sup>2</sup> ( <sup>3</sup> F) <sup>2</sup> F <sub>3.5</sub>
8	16.412	6	3p <sup>5</sup> ( <sup>2</sup> P) <sup>3</sup> P 4s <sup>1</sup> ( <sup>2</sup> S) <sup>4</sup> P <sub>2.5</sub>	838*	83.792	2	3s <sup>0</sup> 3p <sup>5</sup> ( <sup>2</sup> P) <sup>2</sup> P 3d <sup>2</sup> ( <sup>3</sup> P) <sup>2</sup> P <sub>0.5</sub>
9	16.506	4	3p <sup>4</sup> ( <sup>3</sup> P) <sup>3</sup> P 4s <sup>1</sup> ( <sup>2</sup> S) <sup>4</sup> P <sub>1.5</sub>	839*	83.819	4	3s <sup>0</sup> 3p <sup>5</sup> ( <sup>2</sup> P) <sup>2</sup> P 3d <sup>2</sup> ( <sup>3</sup> P) <sup>2</sup> P <sub>1.5</sub>
10	16.562	2	3p <sup>4</sup> ( <sup>3</sup> P) <sup>3</sup> P 4s <sup>1</sup> ( <sup>2</sup> S) <sup>4</sup> P <sub>0.5</sub>	840*	84.456	6	3s <sup>0</sup> 3p <sup>5</sup> ( <sup>2</sup> P) <sup>2</sup> P 3d <sup>2</sup> ( <sup>3</sup> F) <sup>2</sup> D <sub>2.5</sub>
11	16.866	1	3p <sup>4</sup> ( <sup>3</sup> P) <sup>3</sup> P 4s <sup>1</sup> ( <sup>2</sup> S) <sup>2</sup> P <sub>1.5</sub>	841*	84.477	4	3s <sup>0</sup> 3p <sup>5</sup> ( <sup>2</sup> P) <sup>2</sup> P 3d <sup>2</sup> ( <sup>3</sup> F) <sup>2</sup> D <sub>1.5</sub>

**Table 3.4:** Ar+1 atomic levels found in the LANL database.

Listed here are the range of levels considered, corresponding energies, degeneracy, and structure of the 2 outermost subshells in LS (Russell-Saunders) notation. The ‘\*’ indicates 3 of the outermost subshells have been described for the level’s structure.

these methods are very sensitive for neutral and near-neutral atoms. A brief investigation of these rates will be conducted spectroscopically in Ch. 6. The cross sections obtained from the database were integrated over a Maxwellian distribution of electrons using equation 3.4. The rate calculation module yields a set of excitation rates, some of which can be seen in Fig. 3.1.

Lastly, for electron-impact ionization and photoionization, the cross sections have been

n	E(n) [eV]	$g_n$	$nl(^{2S+1}L_J)$	n	E(n) [eV]	$g_n$	$nl(^{2S+1}L_J)$
1	-2.654	5	[Mg]3p <sup>4</sup> ( <sup>3</sup> P) <sup>3</sup> P <sub>2.0</sub>	12	16.036	5	3p <sup>3</sup> ( <sup>4</sup> S) <sup>4</sup> S3d <sup>1</sup> ( <sup>2</sup> D) <sup>5</sup> D <sub>2.0</sub>
2	-2.527	3	[Mg]3p <sup>4</sup> ( <sup>3</sup> P) <sup>3</sup> P <sub>1.0</sub>	13	16.038	7	3p <sup>3</sup> ( <sup>4</sup> S) <sup>4</sup> S3d <sup>1</sup> ( <sup>2</sup> D) <sup>5</sup> D <sub>3.0</sub>
3	-2.474	1	[Mg]3p <sup>4</sup> ( <sup>3</sup> P) <sup>3</sup> P <sub>0.0</sub>	14	16.041	9	3p <sup>3</sup> ( <sup>4</sup> S) <sup>4</sup> S3d <sup>1</sup> ( <sup>2</sup> D) <sup>5</sup> D <sub>4.0</sub>
4	-0.990	5	[Mg]3p <sup>4</sup> ( <sup>1</sup> D) <sup>1</sup> D <sub>2.0</sub>	15	17.518	7	3p <sup>3</sup> ( <sup>2</sup> D) <sup>2</sup> D3d <sup>1</sup> ( <sup>2</sup> D) <sup>3</sup> D <sub>3.0</sub>
5	1.177	1	[Mg]3p <sup>4</sup> ( <sup>1</sup> S) <sup>1</sup> S <sub>0.0</sub>	16	17.519	5	3p <sup>5</sup> ( <sup>4</sup> S) <sup>4</sup> S3d <sup>1</sup> ( <sup>2</sup> D) <sup>3</sup> D <sub>2.0</sub>
6	12.280	5	3s <sup>1</sup> ( <sup>2</sup> S) <sup>2</sup> S 3p <sup>5</sup> ( <sup>2</sup> P) <sup>3</sup> P <sub>2.0</sub>	..	.....	..	.....
7	12.395	3	3s <sup>1</sup> ( <sup>2</sup> S) <sup>2</sup> S 3p <sup>5</sup> ( <sup>2</sup> P) <sup>3</sup> P <sub>1.0</sub>	1384*	87.525	3	3s <sup>2</sup> 3p <sup>2</sup> ( <sup>3</sup> P) <sup>3</sup> P 3d <sup>2</sup> ( <sup>1</sup> S) <sup>3</sup> P <sub>1.0</sub>
8	12.455	1	3s <sup>1</sup> ( <sup>2</sup> S) <sup>2</sup> S 3p <sup>5</sup> ( <sup>2</sup> P) <sup>3</sup> P <sub>0.0</sub>	1385*	87.538	1	3s <sup>0</sup> 3p <sup>4</sup> ( <sup>3</sup> P) <sup>3</sup> P 3d <sup>2</sup> ( <sup>3</sup> P) <sup>3</sup> P <sub>0.0</sub>
9	15.964	3	3s <sup>1</sup> ( <sup>2</sup> S) <sup>2</sup> S 3p <sup>5</sup> ( <sup>2</sup> P) <sup>1</sup> P <sub>1.0</sub>	1386*	88.094	7	3s <sup>0</sup> 3p <sup>4</sup> ( <sup>3</sup> P) <sup>3</sup> P 3d <sup>2</sup> ( <sup>3</sup> F) <sup>3</sup> G <sub>3.0</sub>
10	16.034	1	3p <sup>3</sup> ( <sup>4</sup> S) <sup>4</sup> S 3d <sup>1</sup> ( <sup>2</sup> D) <sup>5</sup> D <sub>0.0</sub>	1387*	93.557	5	3s <sup>2</sup> 3p <sup>2</sup> ( <sup>2</sup> D) <sup>2</sup> D 3d <sup>2</sup> ( <sup>1</sup> D) <sup>1</sup> D <sub>2.0</sub>
11	16.035	3	3p <sup>3</sup> ( <sup>4</sup> S) <sup>4</sup> S 3d <sup>1</sup> ( <sup>2</sup> D) <sup>5</sup> D <sub>1.0</sub>	1388*	97.817	1	3s <sup>0</sup> 3p <sup>4</sup> ( <sup>3</sup> P) <sup>3</sup> P 3d <sup>2</sup> ( <sup>3</sup> P) <sup>1</sup> S <sub>0.0</sub>

**Table 3.5:** Ar+2 atomic levels found in the LANL database.

Listed here are the range of levels considered, corresponding energies, degeneracy, and structure of the 2 outermost subshells in LS (Russell-Saunders) notation. The ‘\*’ indicates 3 of the outermost subshells have been described for the level’s structure.

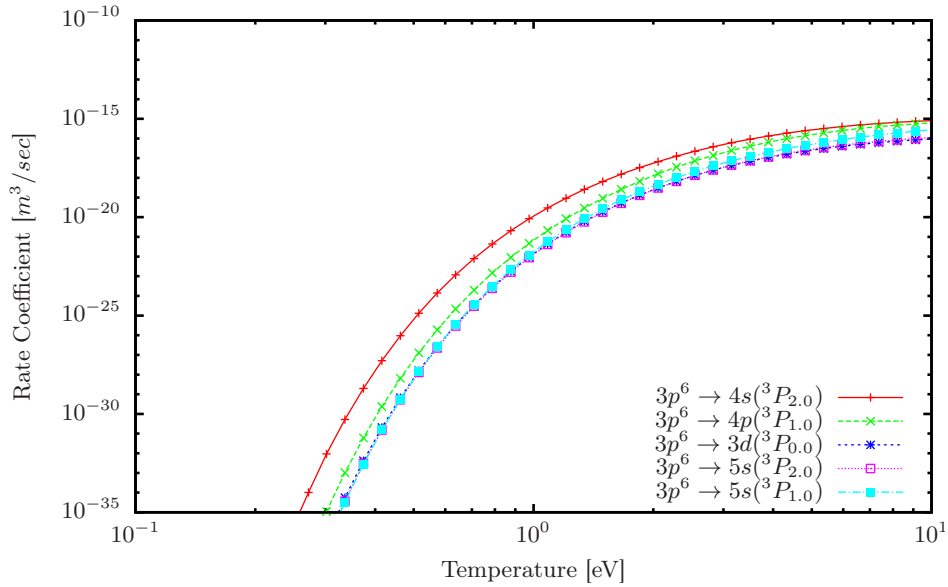


**Figure 3.1:** Excitation rates from the ground state of Ar+0 to the 5 next subshells, calculated using a Maxwellian distribution.

produced using either the scaled hydrogenic method, the distorted wave method, or the binary encounter method. For ionization processes, the transition between a bound and free state requires proper treatment of the continuum states’ wavefunction, unlike the bound-bound processes in which wavefunctions prescribing each bound-state is clearly defined. The previously methods for solving this transition addresses this issue. References regarding the

theory and implementation of calculating relevant cross sections and rates are included for further details. [27–29, 33] A sample set of ionization rates from the ground state of Ar+0 to the first 3 levels of Ar+1 are shown in Fig. 3.2 using the same rate calculation in the excitation scenario with a Maxwellian electron distribution.

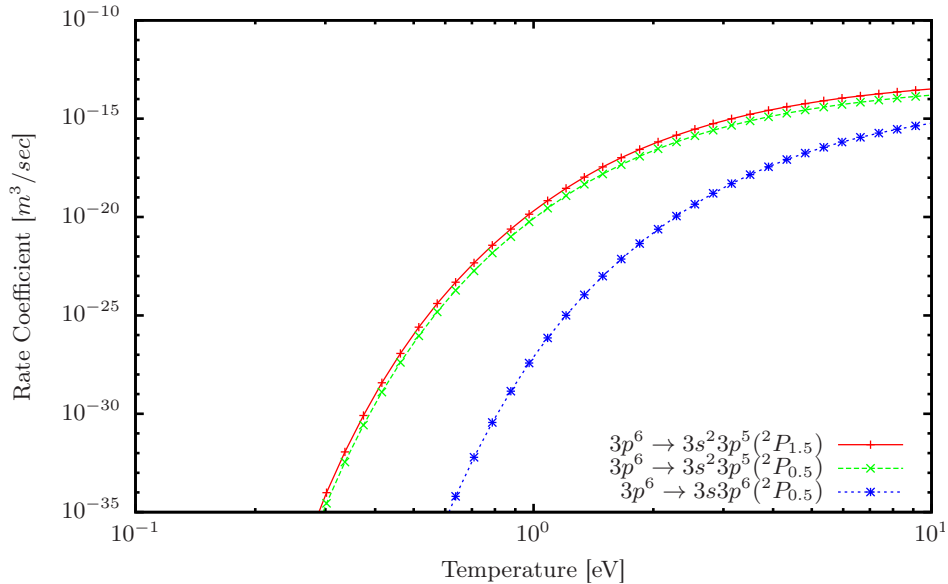


**Figure 3.2:** Sample ionization rates from the ground state of Ar+0 to the first 3 levels of Ar+1 are shown here, using a Maxwellian distribution.

### 3.4 Chlorine Atomic Data Sets

In addition to the argon data, published chlorine data was also extracted for their use in the collisional-radiative model. The chlorine data was generated using the same set of LANL codes described in the prior section. Despite being considered as a potential impurity in fusion devices at the time of the data’s generation, there is a lack of extensive experimentation solely on Cl and its transitions because of the element’s toxicity. [27, 34] Nonetheless, atomic data can be generated for Cl with analyses conducted mainly against other computationally-generated data. A table listing the number of levels and transitions for Cl is shown in table 3.6.

As a contrast to the listing of argon levels, highly ionized chlorine levels are shown in

Ion Level	Levels	CE	PI/CI	Ion Level	Levels	CE	PI/CI
Cl +0	841	106079	123445	Cl +9	554	5485	40154
Cl +1	1388	252121	240084	Cl +10	668	9900	35935
Cl +2	1472	284696	217850	Cl +11	564	11070	17682
Cl +3	1104	173763	99049	Cl +12	291	4245	4265
Cl +4	2003	195867	68550	Cl +13	98	925	916
Cl +5	283	9032	3289	Cl +14	97	285	780
Cl +6	258	1273	3310	Cl +15	31	30	73
Cl +7	89	88	3563	Cl +16	16	15	16
Cl +8	279	831	19990	————	—	—	—

**Table 3.6:** Chlorine atomic data sets found in the LANL database.

Argon sets include information about the atomic levels and the cross sections relevant for state to state transitions. CE: electron-impact (collisional) excitation; PI/CI: photo/electron-impact (collisional) ionization.

tables 3.7 and 3.8. These Li-like and He-like ions are pertinent to fusion conditions. As the atomic structure becomes more H-like, the data is expected to become more accurate since the potential becomes more increasingly dependent on the nuclear core instead of the electron shells. This data will be used primarily for spectroscopic construction and validation of experiments, the results of which may be found in chapter 6.

n	E(n) [eV]	$g_n$	$nl(^{2S+1}L_J)$	n	E(n) [eV]	$g_n$	$nl(^{2S+1}L_J)$
1	-0.849	2	$1s^2 2s^1(^2S)^2S_{0.5}$	12	618.43	4	$1s^2 4d^1(^2D)^2D_{1.5}$
2	29.854	2	$1s^2 2p^1(^2P)^2P_{0.5}$	13	618.53	6	$1s^2 4d^1(^2D)^2D_{2.5}$
3	32.302	4	$1s^2 2s^1(^2P)^2P_{1.5}$	14	618.66	6	$1s^2 4f^1(^2F)^2F_{2.5}$
4	457.15	2	$1s^2 3s^1(^2S)^2S_{0.5}$	15	618.70	8	$1s^2 4f^1(^2F)^2F_{3.5}$
5	465.43	2	$1s^2 3p^1(^2P)^2P_{0.5}$	16	2735.5	2	$1s^1(^2S)^2S 2s^2(^1S)^2S_{0.5}$
6	466.16	4	$1s^2 3p^1(^2P)^2P_{1.5}$	..	.....	..	.....
7	469.15	4	$1s^2 3d^1(^2D)^2D_{1.5}$	93*	3256.5	6	$1s^1(^2S)^2S 2p^1(^2P)^2P 3d^1(^2D)^2D_{2.5}$
8	469.38	6	$1s^2 3d^1(^2D)^2D_{2.5}$	94*	3258.0	8	$1s^1(^2S)^2S 2p^1(^2P)^2P 3d^1(^2D)^2F_{3.5}$
9	613.47	2	$1s^2 4s^1(^2S)^2S_{0.5}$	95*	3258.6	6	$1s^1(^2S)^2S 2p^1(^2P)^2P 3d^1(^2D)^2F_{2.5}$
10	616.87	2	$1s^2 4p^1(^2P)^2P_{0.5}$	96*	3260.6	2	$1s^1(^2S)^2S 2p^1(^2P)^2P 3d^1(^2D)^2P_{0.5}$
11	617.18	4	$1s^2 4p^1(^2P)^2P_{1.5}$	97*	3261.1	4	$1s^1(^2S)^2S 2p^1(^2P)^2P 3d^1(^2D)^2P_{1.5}$

**Table 3.7:** Cl+14 atomic levels found in the LANL database.

Listed here are the range of levels considered, corresponding energies, degeneracy, and structure of the 2 outermost subshells in LS (Russell-Saunders) notation. The ‘\*’ indicates 3 of the outermost subshells have been described for the level’s structure.

n	E(n) [eV]	$g_n$	$nl(^{2S+1}L_J)$	n	E(n) [eV]	$g_n$	$nl(^{2S+1}L_J)$
1	-0.835	1	$1s^2$	12	3270.3	5	$1s^1(^2S)^2S 3p^1(^2P)^3P_{2.0}$
2	2758.6	3	$1s^1(^2S)^2S 2s^1(^2S)^3S_{1.0}$	13	3272.7	3	$1s^1(^2S)^2S 3d^1(^2D)^3D_{1.0}$
3	2775.7	1	$1s^1(^2S)^2S 2p^1(^2P)^3P_{0.0}$	14	3272.8	5	$1s^1(^2S)^2S 3d^1(^2D)^3D_{2.0}$
4	2776.5	1	$1s^1(^2S)^2S 2s^1(^2S)^1S_{0.0}$	15	3273.1	7	$1s^1(^2S)^2S 3d^1(^2D)^3D_{3.0}$
5	2776.6	3	$1s^1(^2S)^2S 2p^1(^2P)^3P_{1.0}$	16	3273.2	5	$1s^1(^2S)^2S 3d^2(^2D)^1D_{2.0}$
6	2778.8	5	$1s^1(^2S)^2S 2p^1(^2P)^3P_{2.0}$	..	.....	..	.....
7	2790.9	3	$1s^1(^2S)^2S 2p^1(^2P)^1P_{1.0}$	27	3442.7(94)	5	$1s^1(^2S)^2S 4f^1(^2F)^3F_{2.0}$
8	3264.7	3	$1s^1(^2S)^2S 3s^1(^2S)^3S_{1.0}$	28	3442.7(95)	7	$1s^1(^2S)^2S 4f^1(^2F)^3F_{3.0}$
9	3269.4	1	$1s^1(^2S)^2S 3p^1(^2P)^3P_{0.0}$	29	3442.8(56)	9	$1s^1(^2S)^2S 4f^1(^2F)^3F_{4.0}$
10	3269.5	1	$1s^1(^2S)^2S 3s^1(^2S)^1S_{0.0}$	30	3442.8(57)	7	$1s^1(^2S)^2S 4f^1(^2F)^1F_{3.0}$
11	3269.7	3	$1s^1(^2S)^2S 3p^1(^2P)^3P_{1.0}$	31	3442.87	3	$1s^1(^2S)^2S 4p^1(^2P)^1P_{1.0}$

**Table 3.8:** Cl+15 atomic levels found in the LANL database.

Listed here are the range of levels considered, corresponding energies, degeneracy, and structure of the 2 outermost subshells in LS (Russell-Saunders) notation.

### 3.5 Preliminary Code Validation and Analysis

With the atomic data on hand and a collisional-radiative model, initial validation of the CR model must be performed to ensure proper utilization of the atomic data. One of the ways to validate the CRM is to investigate the plasma parameters under various applied conditions. This involves implementing a 0-dimensional, steady-state solver in the CRM. A steady state CRM consists of a system of equations that expresses the dependencies between each of the atomic states through the constructed rates. This entire system of atomic states is constrained by enforcing the conservation of mass or by quasineutrality. The constraint in this model is quasineutrality. The inputs for the CRM's steady-state configuration are electron temperature and electron density.

A variety of results can be obtained from the CR model such as Boltzmann distributions, radiation emission losses, and mean ion charge. With many available CR models in the community, the mean ion charge is one of the readily-available ways to compare the CR model. Therefore, the mean ion charge was chosen as the parameter to compare with other models and results in the literature. Results such as Boltzmann distributions and radiation emission in the form of spectra certainly present much more accurate comparisons and provide greater scrutiny of the CR model. However, these values are often subject to the accuracy

of the atomic data which is also generated by computational models that complement the collisional-radiative modeling field. Studies of the atomic data require a completely different knowledge set that goes beyond the aim of this current work, despite being relevant to CR modeling. [29,35–38] Therefore, it is much more beneficial to address the comparisons of mean ion charge, a plasma parameter that is used across all forms of plasma physics research.

Initial comparisons of the mean ion charge will be compared against FLYCHK. Extended from the spectroscopic model called FLY, FLYCHK is a collisional-radiative code written primarily by H. K. Chung to study hot dense plasmas, such as those found in fusion devices. [37] Some of the code’s results, which are steady-state results, are publicly available on the International Atomic Energy Agency’s (IAEA) Atomic Molecular Data Services website. [39] Results include steady-state charge state distributions and radiative power loss rates for elements up to gold (Au). Due to the website’s ease of accessibility, experimentalists have taken advantage of its provisions and used the results on the website for comparisons. Similarly, the availability of this data allowed the CR model to be validated as a first pass.

The first set of data compared between FLYCHK and the CRM is the charge state distribution for argon as a function of temperature in Fig. 3.3. Both of the data were generated by assuming an initial electron density of  $10^{22} \text{ m}^{-3}$  for temperatures of 10, 52, 100, 475, and 1000 eV. At steady state, predominant charge fractions that are normalized to the total number density are displayed. For  $10^{22} \text{ m}^{-3}$ , most of the charge state distributions follow the FLYCHK results shown as dashed plots. However, there are readily-visible errors between both of the results in some of the cases. At 10 eV, the CSD shows that there is a larger concentration of Ar+5 ions than that predicted in the CR model. In the 475 eV plot, the CR model is unable to capture the presence of Ar+11 to Ar+15 ions in a predominantly Ar+16 ion-filled plasma. The biggest disparity in the model is shown for an electron temperature of 100 eV where mean charge of 8 was determined by FLYCHK as opposed to a 10.6 value by this CR model. There are several reasons that are attributed to these discrepancies, but a glance at the  $10^{25} \text{ m}^{-3}$  CSD will also maintain some of these discrepant features.

Fig. 3.4 shows the charge state distribution for the case of  $N_e = 10^{25} \text{ m}^{-3}$ . In this

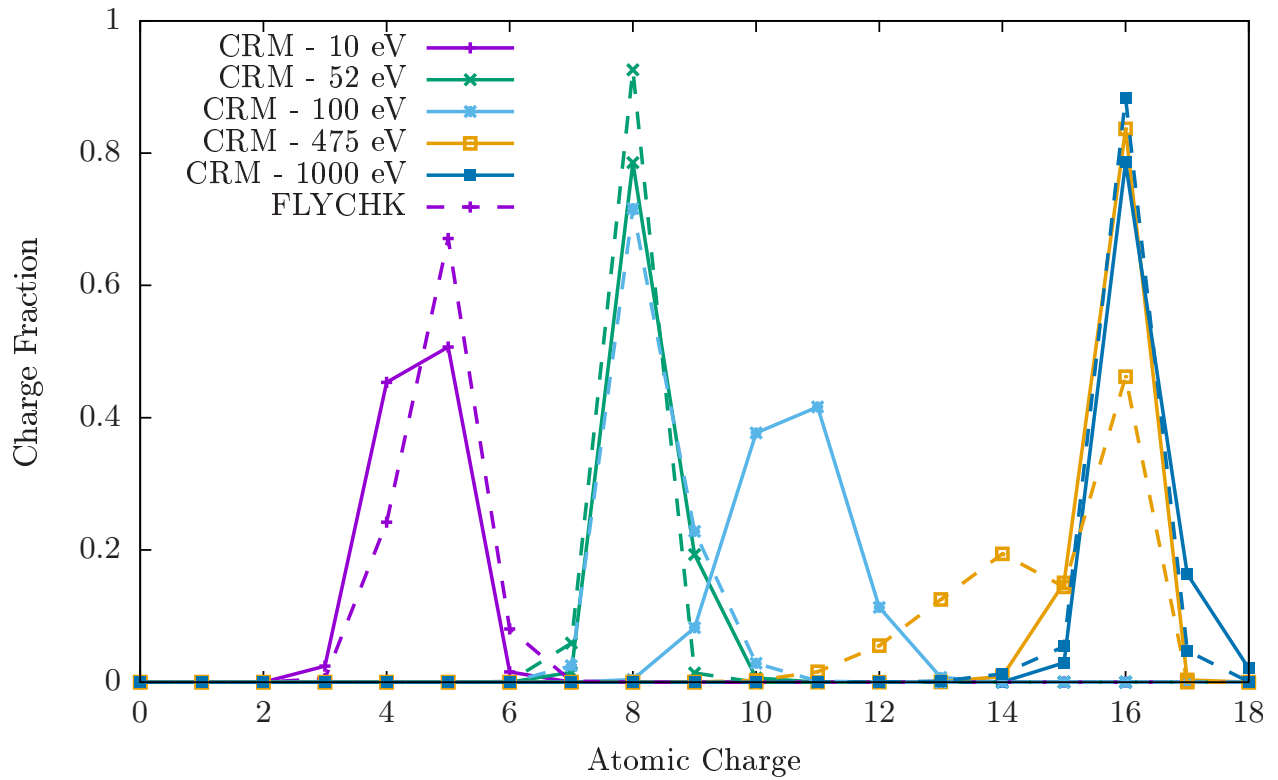


**Figure 3.3:** Comparison of argon charge fraction between FLYCHK and this work's collisional radiative model for  $N_e = 10^{22} \text{ m}^{-3}$  at multiple electron temperatures.

figure, most of the results are more closely aligned with the FLYCHK results. For instance, the CSDs for the 10 eV case do not have the mismatch as previously seen in the  $10^{22} \text{ m}^{-3}$  case and the FLYCHK CSD for 475 eV is less pronounced from Ar+11 to Ar+15. A quick explanation for this more accurate representation of the CSD is the increasing role of electron density in the rate equations: reactions involving electron densities become more dominant in both CR models, showing the accuracy of the rates in this CR model. However, the results for 52 eV and 100 eV still show a slight mismatch with the FLYCHK model. Although the average charge values are within one charge state of each other, the FLYCHK results show a distinguishable lean towards a higher charge state for 10 eV and a more balanced distribution in the 100 eV scenario.

The FLYCHK model has been around for many years and accounts for several more features that are not captured in the current iteration of the CR model. One of those features is the lack of autoionization and dielectronic recombination processes in this CR model. Autoionization is the process of spontaneous ionization to an upper charge state due to the presence of at least a doubly-excited state. In these events, one electron seeks to deexcite, which leads to the emission of radiation that is captured by the other excited electron. Sometimes, the total energy of the electron is enough to exceed the energy gap and leads to ionization. In dielectronic recombination, not to be confused with 3-body recombination although being very similar, electron capture occurs by an ionized atom that leads to a doubly-excited state. Subsequently, this overly excited atom seeks a more stable state, therefore emitting a photon in the process. The absence of these two processes is partly the reason for the mismatch in the FLYCHK charge fractions.

Another reason relates directly to the atomic data which was published by LANL. The maximum number of shells in this CR model is either 4 or 5, depending upon the ion in question. However, there may easily be more atomic shells that are relevant in the atomic model. In Fig. 3.5, a comparison of CSDs from CRETIN for a different number of shells considered are shown for the electron density of  $10^{25} \text{ m}^{-3}$  and a temperature of 52 eV. By increasing the number of shells from 4 to 10, the charge state distribution shifts towards a higher Z value. These results are very similar to the CSDs shown in Fig. 3.4. Therefore, the

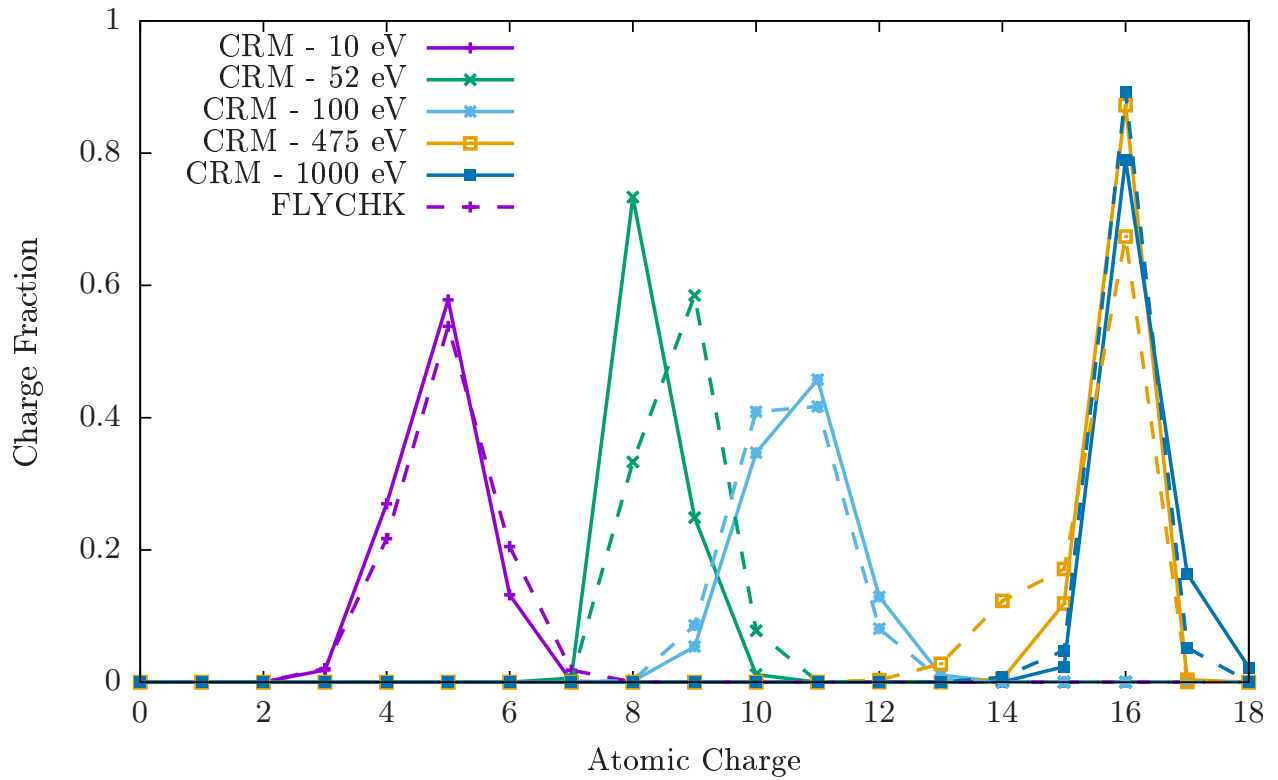


**Figure 3.4:** Comparison of argon charge fraction between FLYCHK and this work's collisional radiative model for  $N_e = 10^{25} \text{ m}^{-3}$  at multiple electron temperatures.

combination of missing AI/DR rates and high-n shells leads to the discrepancies observed between FLYCHK and the CRM.

The next plot shown in Fig. 3.6 is a set of CSDs obtained at a higher electron density of  $10^{28} \text{ m}^{-3}$ . At this density, the plasma is considered to be more tightly-packed and dense. This particular test and comparison is interesting because the collisional-radiative model does not account for dense-plasma modifications. In the figure, there is a mismatch that is consistently observed for several of the low-temperature CSDs. At high temperatures, the distributions closely match one another as the atomic state densities push towards the hydrogen-like ions. For the cases of 10, 52, and 100 eV, the trends are very similar between FLYCHK and the CRM, but shifted by 1 ionization stage. At this density, the effect of continuum lowering becomes significant. In dense plasmas, continuum lowering occurs such that the continuum limit moves closer to the ion's nucleus, making ionization much more feasible than before. In addition to continuum lowering, the CSDs display slightly broader distributions than shown in the  $10^{22} \text{ m}^{-3}$  and  $10^{25} \text{ m}^{-3}$  cases. One can conclude that this CRM must account for dense plasma effects if this solver is to be used for high-density applications such as inertial fusion.

Lastly, Fig. 3.7 shows a comparison of mean ion charge values generated for multiple electron temperatures at a density of  $10^{18} \text{ m}^{-3}$ . The NLTE workshops are dedicated towards validation and verification of CR models in the community by supplying information for ongoing experiments while comparing the CR models. [40, 41] Several of the workshops involved obtaining mean ion charge values for argon which are shown in the figure. The vertical bars indicate the amount of separation in calculated mean ion charge values of the participating codes. For the results without DR produced at NLTE-7, the CRM performs very well by landing within the bounds of the data. However, the data clearly shows that the CRM is outside of the bounds generated from NLTE-4, where dielectronic recombination is considered. There are certainly multiple improvements that can be implemented in the CR model. But, these results are sufficient for the studies to be shown in the following chapters.

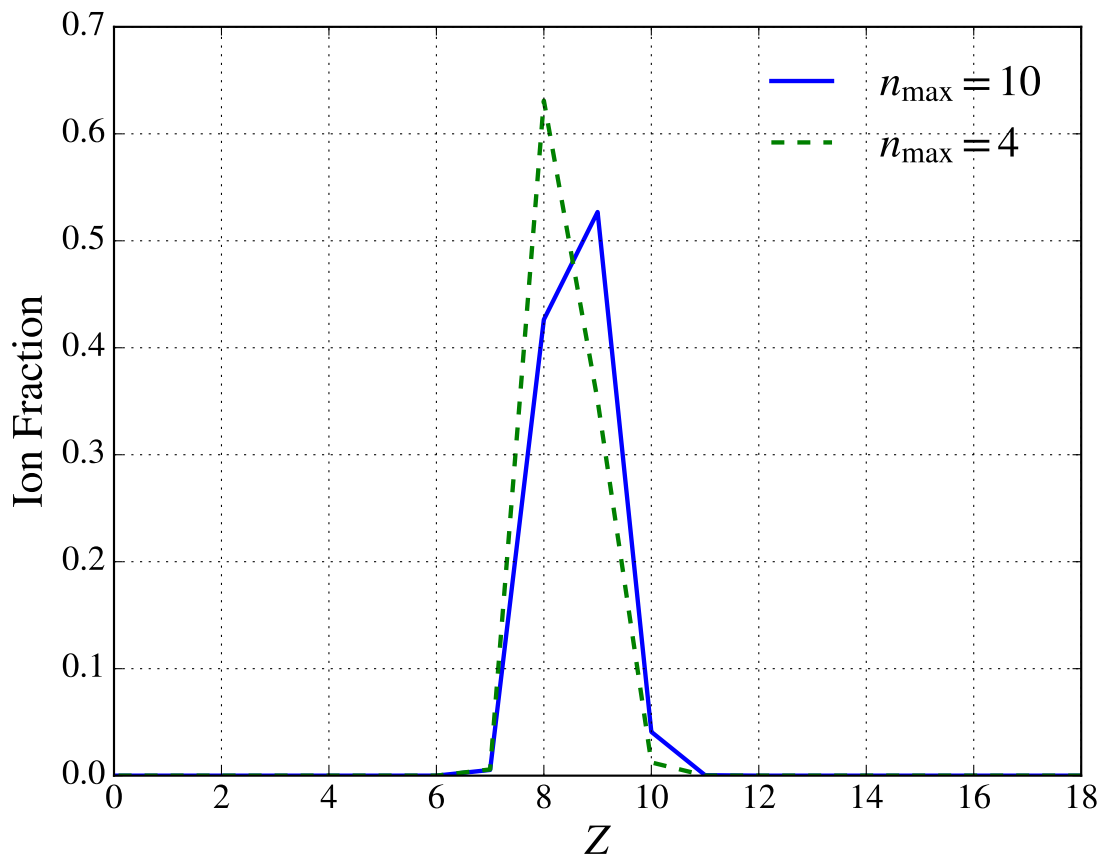


**Figure 3.5:** Effect of increasing number of n shells in CRETIN simulations from 4 to 10. The overall charge distribution shifts to higher Z for a sufficient number of shells in the simulation. (Courtesy of H. Le and H. Scott from LLNL)

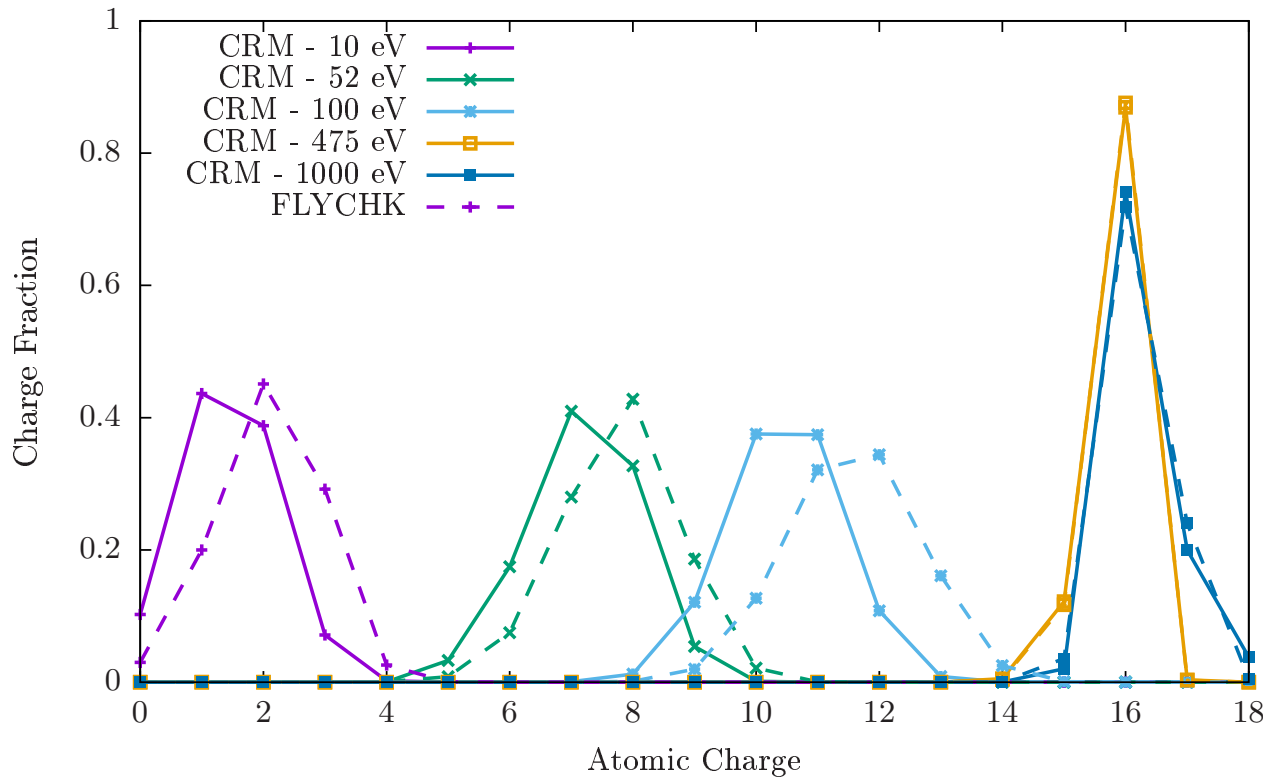


**Figure 3.6:** Comparison of argon charge fraction between FLYCHK and this work's collisional radiative model for  $N_e = 10^{28} \text{ m}^{-3}$  at multiple electron temperatures.

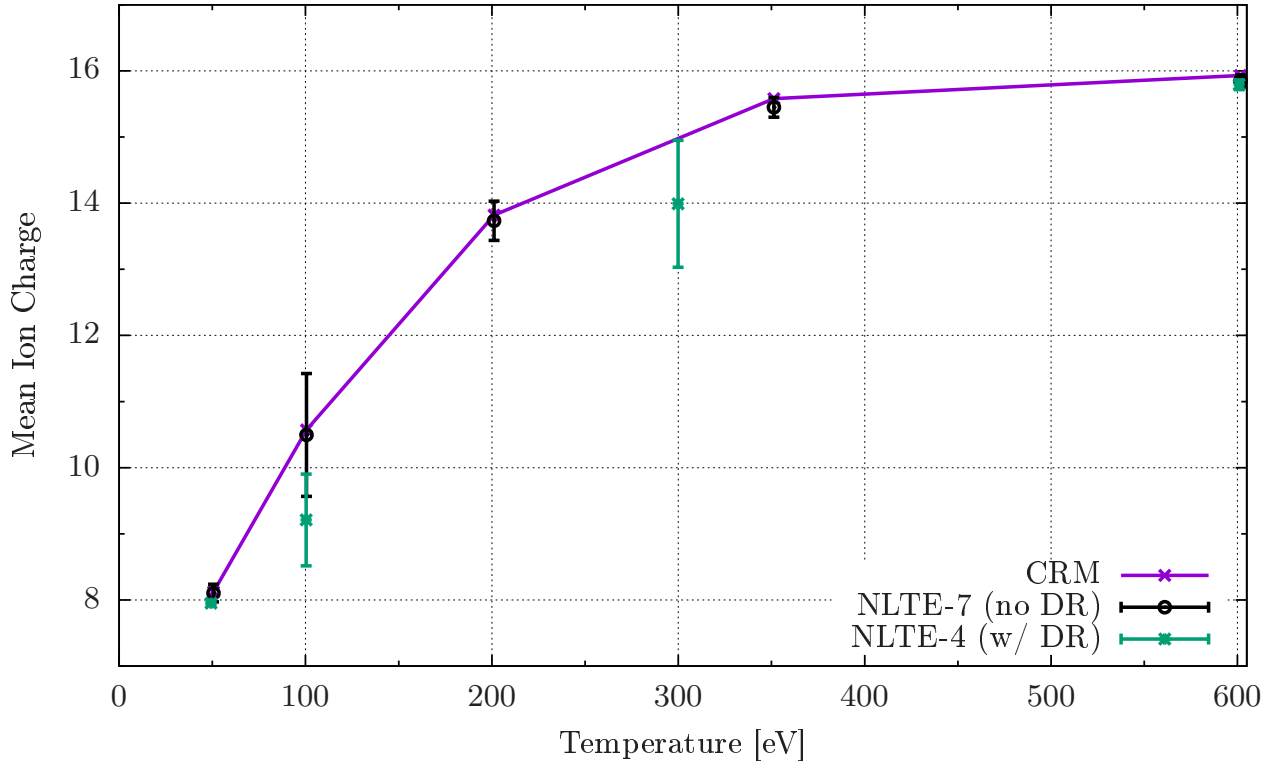


**Figure 3.7:** Comparison of mean Ar charge with NLTE-4 and 7 results for various temperatures with an electron density of  $10^{18} \text{ m}^{-3}$ . The bars refer to the spanned set of mean ion charges by multiple CR models at the NLTE workshops. Without dielectronic recombination, the collisional-radiative model compares very well with the NLTE-7 data. However, the inclusion of NLTE-4 data leads to a more inaccurate representation of the mean charge by the CR model.

## CHAPTER 4

# Laser-Induced Breakdown Modeling of Argon

### 4.1 Introduction

The breakdown of particulates through lasers involves multiple physical phenomena such as particle and radiation kinetics, as well as fluid flows. This makes the simulation of laser-induced breakdown (LIB) a fulfilling objective since it encompasses many physical interactions that can be modeled with today's numerical tools including chemical kinetics, radiation transport, and fluid solvers. To address the chemical kinetics aspect of LIB, the focus of this chapter will be directed primarily towards the collisional-radiative model. As the CRM is developed, LIB becomes a particularly useful subject when employed as a spectroscopic tool (LIBS) to diagnose particulates of interest. Before using the CRM as a LIBS tool, however, the atomic data must be assessed to determine whether the data is capable of producing accurate spectroscopic data (see Chapter 6). This uncertainty is related to the atomic data which was discussed in Ch. 3. Generating atomic data to remedy these inaccuracies involves studies that go beyond this work. Instead, the overall impact of the kinetics on the macroscopic parameters will be investigated. This analysis will not only scrutinize the variations of the 0-D plasma, but will also lead towards the coupling of the CRM to a plasma fluid solver.

A typical laser-induced breakdown setup is shown in Fig. 4.1. A laser beam is generated from the laser head which is then focused onto the material in question with a converging lens. Laser parameters such as spot size and beam divergence are important when attempting to replicate these experiments. This simple setup may easily be extended into a LIBS tool by adding a spectrometer for material analysis. The ease of constructing a

LIBS diagnostic platform as well as its functionality makes its applicability far-reaching and goes beyond the physical sciences. LIBS is a diagnostic tool currently used across many

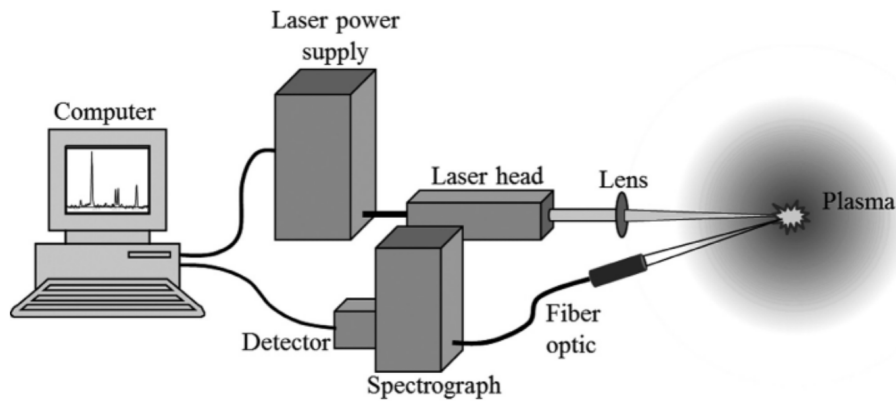


**Figure 4.1:** A generic setup for laser-induced breakdown with spectroscopy capabilities is shown. The sample under investigation may fall under any phase of matter. (Figure taken from Radziemski and Cremers [42])

facets within the research community. As an engineering application, LIBS has been used to quantify variations caused by air-fuel mass ratios for combustion systems under different injection configurations. [43] More recently, the ChemCam Instrument Suite onboard the Mars Science Laboratory (MSL) Rover deployed its LIBS functionality for the first time on a planetary mission. [44] Beyond engineering, LIBS is also used in environmental studies, where determining soil composition is vital for potential farming exploits, and in archaeology to analyze samples dating many centuries ago. [45, 46] While the relevance and impact of LIB(S) has grown as evidenced by the proliferation of these experiments, the dynamics of the LIB phenomenon is unraveling itself with access to high-speed cameras and large-scale computations, the latter being the pursuit of this work. [42]

Although most of the examples presented above, as well as experiments in the field, are preferentially applied to solid and liquid specimens, there are still experiments devoted towards breakdown of gases such as the aforementioned combustion study. Shown in Fig. 4.2 is the laser breakdown of a solid material; breakdown of solids and liquids require additional transitions to be modeled, such as vaporization or sublimation, making such a simulation resource-demanding. Therefore, a gaseous breakdown will be pursued for the meantime,

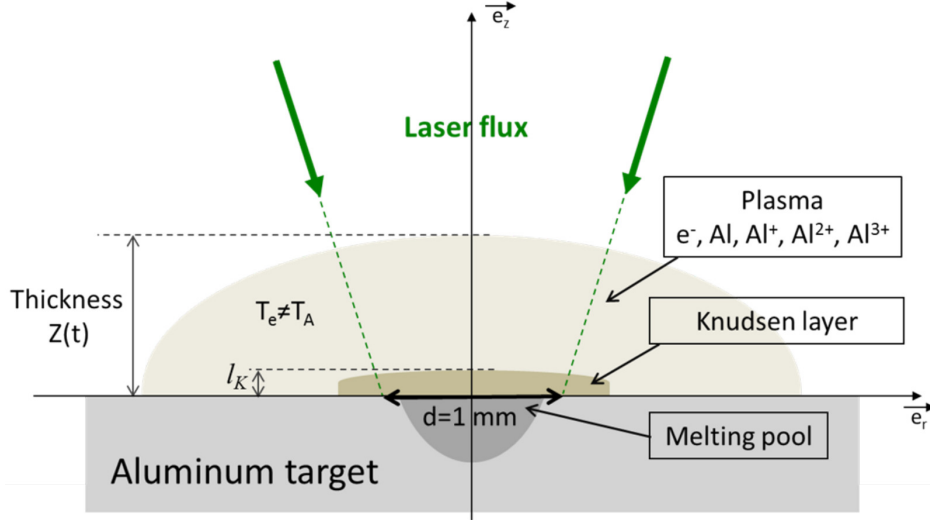


**Figure 4.2:** Schematic of layers present during laser-induced breakdown of aluminum target. The incoming laser flux interacts with the generated plasma and solid aluminum. The presence of a solid aluminum presents a computational challenge in modeling the Knudsen layer formed from the melting aluminum target. (Figure taken from Morel et al. [47])

using the LANL argon data to model an argon gas breakdown. Details to model the 0-D breakdown of any gaseous system as provided in the following section.

## 4.2 Modeling the Breakdown

The collisional-radiative model will be used to simulate the gaseous breakdown in a 0-dimensional setting. Being 0-D, no fluid equations will be used to capture the plasma flows that are typically present in breakdown. Instead of using detailed-level accounting (DLA) states, detailed-configuration averaged (DCA) states were used to compute the breakdown without any loss of information pertaining to the results shown in this study. The computation and expense associated with solving the non-Maxwellian electron distribution and radiation transport will not be considered in the model. Therefore, this argon breakdown will simulate an incoming laser pulse for an optically-thin plasma under Maxwellian conditions. The breakdown model will be solved in a multi-temperature manner as well, allowing an exchange of energy between the electrons and atoms. A similar model was developed by Morel et al. for laser interactions with an aluminum slab with a slight difference. [47] Since

the authors were modeling the plasma with a metal slab, a source term was introduced in their model that accounts for the influx of aluminum gas .

The key event associated with the gaseous breakdown is the impulsive deposition of energy into the focal volume of the laser. This requires modeling the laser terms leading to the ionization of the atoms. The processes considered for this injection of energy are multi-photon ionization (MPI) and inverse Bremsstrahlung (IB), which will be discussed in detail in the following subsections. First, a quick discussion of the laser parameters and pulse shape is needed to include the laser source terms in the simulation.

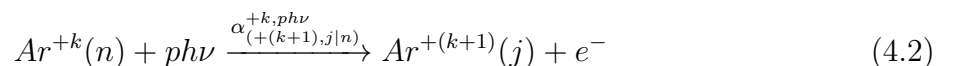
To model the laser in time, a Gaussian form has been assumed to model the laser intensity,  $\phi_L$ , as a function of time,

$$\phi_L(t) = \phi_{L,max} e^{-(t-t_c)^2/2\sigma^2} = \phi_{L,max} e^{-2\sqrt{2\ln 2}(t-t_c)^2/\Gamma^2} \quad (4.1)$$

where  $\phi_{L,max}$  is the maximum laser intensity during the laser pulse,  $t_c$  is the time at which the laser's intensity reaches  $\phi_{L,max}$ , and  $\sigma$  is defined to be the standard deviation of the pulse. The equation may also be written in terms of more conventionally-known parameters. In the rewritten equation,  $\Gamma$  is defined as the full-width half-maximum (FWHM) duration of the pulse; this value is also commonly known to be the pulse duration. As most lasers are defined according to this value, this will be the terminology associated with the duration of the pulse.

#### 4.2.1 Multiphoton Ionization

In the case where one photon does not have the required energy to free a bound electron, there is a possibility where photoionization still occurs due to multiple, simultaneous photon interactions, which is to say  $p(h\nu) \geq \Delta E$ , where  $\Delta E$  is the energy required to ionize an atom and  $p$  implies a sufficient number of photons for such a process to proceed. This process is known as multiphoton ionization and is captured in the following reaction equation.



Considering the photo-ionizing scenario, the corresponding rate,  $\alpha_{+(k+1),j|n}^{+k,ph\nu}$ , was derived by Ireland et al. [48] This photoionization rate has been used for metallic particles by Müsing, along with gaseous particles by Morel, in their respective models. [47] [49]. The effective MPI cross section for the multiple photon interaction is prescribed by the following equation.

$$\sigma_{MPI}^{(p)} = \frac{\sigma_1^p}{(p-1)! \nu^{p-1} (h\nu)^p} \quad (4.3)$$

In previous studies, the cross section,  $\sigma_1$ , was assumed to be a constant  $10^{-20} m^2$ . Although this value was a mere assumption, the value has shown its reliability in several experiments and simulations. [50] [49] [51] In this work, however, the photoionization cross sections can be immediately obtained by interpolating from the LANL set of photoionization data and will therefore be used in this model.

The reaction rate for multi-photon ionization is then related to the MPI cross section through the laser energy flux density as follows:

$$\alpha_{+(k+1),j|n}^{+k,ph\nu} = k_{MPI}(p) = \sigma_{MPI}^{(p)} \phi_E^p \quad (4.4)$$

One should also note that for single-photon ionization events, the effective cross section above still holds and reduces to the entire rate coefficient to the single-photon case.

The rate of change in species density due to MPI is provided by the following expression.

$$\dot{\omega}_n^{+k} = \sum_{j,p} \alpha_{(n|+(k-1),j)}^{+(k-1),ph\nu} N_{+(k-1),n} - \sum_{n,p} \alpha_{+(k+1),j|n}^{+k,ph\nu} N_{+k,n} \quad (4.5)$$

Since the electron energy is also being simulated through the entire system of equations, the rate of electron energy change due to MPI must be supplied:

$$\dot{\omega}_{E_e} = \sum_{k,n,p} \alpha_{+(k+1),j|n}^{+k,ph\nu} N_{+k,n} (ph\nu - \Delta E) \quad (4.6)$$

Note that an inverse process for MPI was not taken into account in the reaction equation

due to the assumption that multiple photons emitted at low energies is highly unlikely. However, radiative recombination events are still present in these simulations; these processes, while not direct inverses of MPI, will complement the MPI events during the lasing duration.

#### 4.2.2 Inverse Bremsstrahlung

The Bremsstrahlung process was described previously as the loss of radiation due to an acceleration event during an electron-atom interaction. Consider a scenario where the electron-atom interaction also involves a photon: it becomes possible that the electron absorbs the photon energy due to the resonance between the radiation frequency and electron motion. This process is called inverse Bremsstrahlung (IB).

$$e^-(\varepsilon_1) + h\nu \longrightarrow e^-(\varepsilon_2) \quad (4.7)$$

Recall that  $\varepsilon_2 > \varepsilon_1$ .

The associated absorption coefficients from the ionic contribution is given by the following equation, taken from Rosen et al. [52] The electron-neutral absorption rates, however, are extrapolated from a tabulated set of rates taken from McEachran and Stauffer. [53]

$$K_{IB}(k) = \frac{4}{3} \sqrt{\frac{2\pi}{3m_e k_B T_e}} \frac{G}{hc\nu^3 m_e} \frac{e^6}{(4\pi\epsilon_0)^3} k^{2(1-\delta_{k,0})} \quad (4.8)$$

Here, the Gaunt factor is taken as unity. The rate of energy change due to IB is then as follows:

$$\dot{\omega}_{E_e, IB} = N_e \phi_E \left( 1 - e^{-h\nu/k_B T_e} \right) \sum_{k,n} K_{IB}(k) N_{+k,n} \quad (4.9)$$

This process is balanced by the Bremsstrahlung emission process mentioned in Chapter 3. Therefore, there are 2 heating processes in this breakdown model: multiphoton ionization involves “leftover” radiation energy that is deposited on the recently-liberated electron, while the other process of inverse Bremsstrahlung injects energy directly into the electrons.

### 4.3 Comparative Results and Analysis

The collisional-radiative model (CRM) was used to simulate gas breakdown at several pressure values. The target of interest will be argon gas for which there is plenty of breakdown data for various combinations of laser parameters, such as lenses and pulse widths. While holding some laser parameters constant for the simulation, breakdown trends as a function of pressure were obtained to compare between the CRM and the experiments. Multiple experimental data points were compared with the CRM’s breakdown interpretation to draw conclusions without bias towards any experimental setup. The time-dependent aspect of the collisional-radiative model also permits analysis beyond determining the sufficient laser breakdown intensity. Therefore, the results of this study will be used to extract information which will attempt to explain the nature of the breakdown trend.

The experimental data used to compare with the CRM’s results are shown in Table 4.1. Listed in the table are each of the experiment’s laser pulse width and lens focal length used to breakdown the gas. These are the parameters deemed significant when comparing with simulation results. Although the CR simulation is only 0-D, the spot sizes and focal length are also important when considering the amount of radiation being absorbed upstream of the breakdown region. Therefore, these aspects should be carefully considered when comparing the breakdown trends between the CRM and the experiments.

Experiment	Pulse Width (ns)	Lens Focal Length
Chylek et al. (1990)	6.5	10 cm
Davis et al. (1991)	7.5	10 cm
Rosen et al. (1987)	15	7.5, 20, 30 cm
Sircar et al. (1996)	6	11 cm

**Table 4.1:** Argon LIB Parameters from Several 532 nm Experiments

Pulse widths and lens focal lengths from several laser-induced breakdown experiments for argon are shown here. The collisional-radiative model will be compared against these experiments.

The experiments chosen for comparisons in this work have laser wavelengths of 532 nm and laser pulse widths on the nanosecond timescale. A laser wavelength of 532 nm is fairly

common, leading to many LIB experiments in the literature to use this parameter. This wavelength is equivalent to an energy of 2.33 eV, which would require at least 7 photons to ionize argon with multiphoton ionization. The presence of nanosecond LIB studies is also abundant; but, the use of nanosecond lasers in the CRM also helps avoid the complications of using EEDF solvers when investigating laser-induced breakdown with, for example, picosecond lasers where non-Maxwellian electron distributions become much more likely and have a significant impact on the breakdown process.

While the wavelengths of the lasers are similar and the pulse widths are within an order of magnitude, there are some aspects of the experiments that must be acknowledged when comparing the results with the simulations. The spot size is one beam parameter that varies between the experiments. For a smaller spot size, a lower threshold intensity may be needed to ionize the gas, while a larger spot size leads to a higher threshold intensity. In Chylek et al.'s experiment, a beam focal diameter of 33  $\mu\text{m}$  was reported [54]. However, in Sircar et al.'s experiment, no spot size was reported aside from indicating a  $<0.5$  mrad laser beam divergence [55].

The experiments between Rosen et al. and Davis et al. provided a few more details regarding their laser-induced breakdown setup, as well as the relevant optics used. The experiment by Rosen et al. used a variable area aperture to modulate the beam diameter [56]. By using a variable area aperture prior to the lens, the intensity at the focus can also be altered by apodizing the beam, whereas before, a straightforward method of changing the laser intensity can be performed by varying the laser pump energy. In conjunction with this experimental methodology, the f-numbers were chosen to minimize lens aberration as guided by Ireland and Morgan [57]. At low densities, an f-number of  $f/10$  was used with a focal diameter of 13  $\mu\text{m}$  and an f-number of  $f/30$  using a focal diameter of 39  $\mu\text{m}$  was used at higher densities. This particular technique was also used by Davis et al. where a similar lens with a 10 cm focal length was used. [58] Their laser specifications include a pulse length that is half of the Rosen setup and a spot size of 85.2  $\mu\text{m}$ .

The collisional-radiative model's simulations were conducted to match each of the experimental conditions. These conditions include the initial pressure and the pulse width of the

lasers. Since the experiments are breakdown experiments, the heavy atoms were initialized to temperatures close to room temperature (0.035 eV). The initial conditions of the electrons were made small enough so as to have a negligible effect on the macroscopic parameters when breakdown occurs. Therefore, an electron density of  $10^{10} \text{ m}^{-3}$  and an initial electron temperature of 0.05 eV were chosen. It was also noted that altering the initial atomic temperature by 1/100ths of an eV impacted the electron temperature evolution due to the atomic species acting as a heat source. Results of the threshold breakdown trends between the CRM and the experiments are shown in Fig. 4.3.

The ionization fraction is generally used as the quantitative indicator for a plasma's formation. The value used for the simulations is 0.1% (0.001). Other values of merit may be used to signify breakdown; for instance, Rosen et al. uses the electron number density to theoretically justify the gaseous breakdown. [52] In the experimental case, the instance of a flash is often deemed sufficient for the formation of a plasma in a laser-induced breakdown setting. [59] [60] But, the sufficient detection of a flash becomes a somewhat subjective issue when intensity requirements become involved, especially with different detectors operating at various resolutions. For the moment, the use of the ionization fraction threshold as the defining breakdown event will be used to draw similarities between the experiment and simulations.

There are several features to note when comparing the CRM results with the experiments. Despite the different pulse widths, the simulated breakdown trends are very similar to one another. By changing the simulated pulse width for each experiment, a mere vertical shift in the profile is observed. Also, the pressure at which the slope of each profile changes is consistent between all of the pulse widths, being between 100 and 1,000 Torr. This change in slope is identified in the literature to be a transition from an MPI-dominated process to a electron-avalanche-dominated process, which will be shown. This is a contrast to the experiments where different trends are observed as the pressure is decreased in each of the independent studies. In the results of Chylek and Davis, one can perform a linear regression and observe that intensity decreases as a function of pressure. However, Rosen and Sircar present particularly different trends as the pressure decreases.

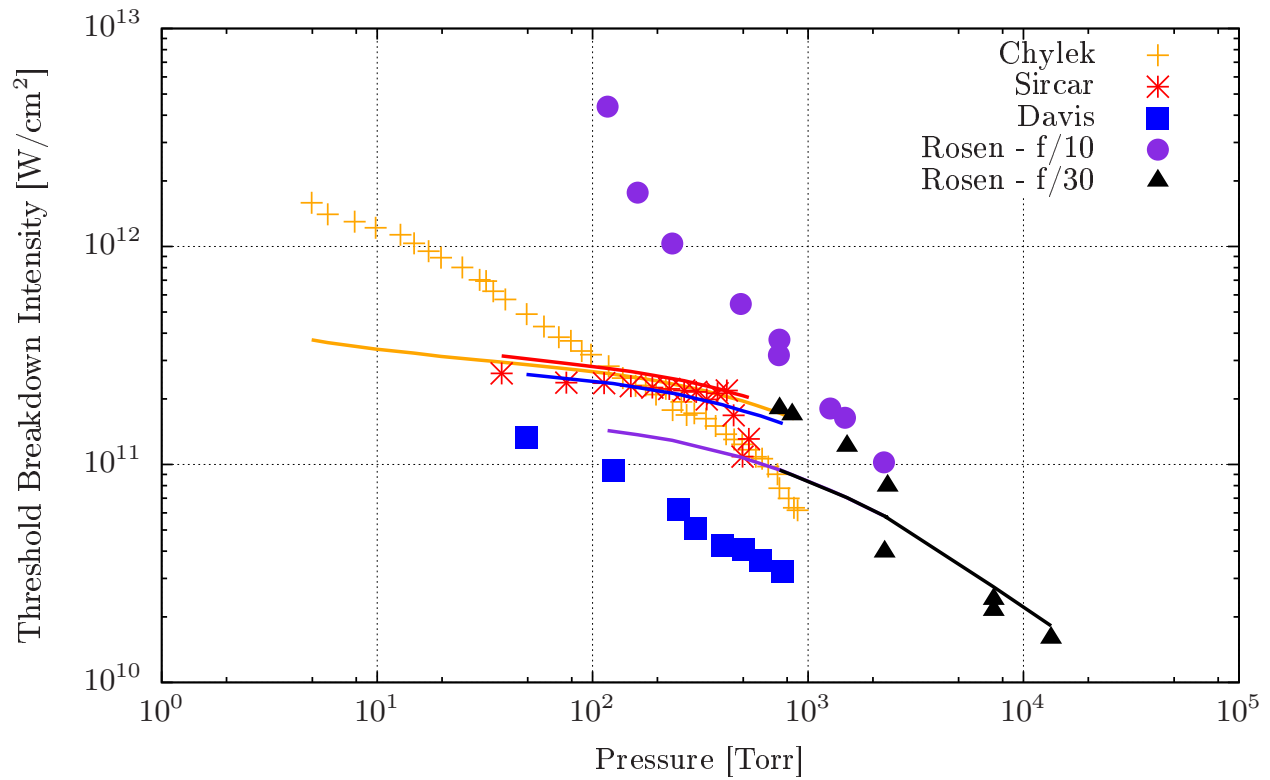


**Figure 4.3:** Comparisons of threshold breakdown intensities for argon between several experiments and the CR model shown by the solid lines, with colors corresponding to the experiments under a 532 nm laser. The experiments were conducted using nanosecond-scale laser pulse widths. Note the different slope trends amongst the experiments, all of which have some degree of variation in the experimental setup.

In Rosen et al.'s experiment, a linear extrapolation can be made from 10,000 Torr to 2,000 Torr. However, a jump occurs in the f/30 data at  $\leq 2,500$  Torr. Despite changing lens specifications, the f/10 data maintains this profile and increases exponentially as the pressure decreases. The collisional-radiative model's trend fits through the f/30 data; however, the simulated trend for f/10 shows a plateauing region as the pressure is reduced. Overall, a linear trend can still be ascertained from the Rosen data points. This leads to the speculation that breakdown in these experiments tends to follow the relationship between intensity, pressure, and pulse width below, where  $m$  provides the best fit based on the experimental data. [61]

$$I \propto (p \times \tau_p)^{-1/m} \quad (4.10)$$

The fit assumes that the laser frequency is larger than the electron-neutral collisional frequency. However, the important observation here is the inverse relationship between the intensity and pressure. This is apparent in the experimental data, along with the electron-avalanche region in the simulation results. In the Sircar et al. experiment, a majority of their data points indicate breakdown that is weakly dependent on pressure until a value of 450 Torr where the trend drops steeply. Here, the CRM contrasts the other experiments and matches the Sircar experiment very closely in magnitude and in trend, indicating an MPI-dominated region.

In the CRM, a sweep in pressure on the breakdown threshold plot highlights two different regimes: the MPI-dominated breakdown regime and the cascade ionization regime. At low pressures or densities, where collisional effects are negligible, the gas breakdown process into the plasma state is governed mainly by multiphoton ionization. The sparsity of particles means that the ionization of atoms depends increasingly on the interactions between the laser field and the particles, rather than the particle-particle interactions. At sufficiently higher pressures, breakdown effects coming from inverse Bremsstrahlung become more apparent in the form of cascade ionization or electron avalanches. The events leading to the avalanche initially involves electron heating. As the electrons are heated, the rate at which electrons are liberated from the neutral and ion species increases because of the heightened collisional interactions between the electrons and atoms. Subsequently, a runaway process occurs as

freed, but cold, electrons are heated, continuing the avalanche process.

This aspect of laser-induced breakdown for gases is contentious because of the different trends towards lower densities. In the electron avalanche-dominated case, the multiphoton ionization processes still exist. But, due to the number of bound electrons that can be potentially ionized in the high density case, the MPI rate may be comparable at most to the inverse Bremsstrahlung heating that leads to further ionization. This divide also persists at lower pulse widths. Fig. 4.4 and 4.5 show two threshold breakdown intensity profiles for argon using lasers operating at picosecond timescales. In Krasnyuk et al.'s experiment, a highly distinguishable pressure-independent profile can be seen at low pressures. Experiments conducted by Dewhurst shows a significant difference in the profile, despite operating in a similar range of pressures. Dewhurst makes an explicit point that no transition region was observed leading to the MPI-dominated range of pressures.

The absence of an MPI-dominated range of pressures warrants the question of whether inverse Bremsstrahlung was sufficient to capture the threshold breakdown intensity trends in the experiments. The multiphoton ionization source terms were suppressed in the CR model in an attempt to capture the electron avalanche caused mainly by heating due to inverse Bremsstrahlung. The Rosen et al. data was the comparison for this study since an analysis involving the theory of breakdown due to inverse Bremsstrahlung with and without MPI was performed (see Fig. 4.6).

A simplified, analytical equation used to monitor the rate of electron density change by Weyl is given by Eq. 4.11. [61] This equation was used in multiple references, at times with further simplifications, to quantify the breakdown threshold. The equation consists of source and sink terms due to multiphoton ionization, electronic ionization, attachment, recombination, and diffusion.

$$\frac{dN_e}{dt} = \alpha^{ph\nu} N + \nu_i N_e - \nu_a N_e - \nu_R N_e + \nabla(D\nabla N_e) \quad (4.11)$$

In Rosen et al.'s paper, attention was directed primarily to the multiphoton ionization and inverse Bremsstrahlung terms. The inverse Bremsstrahlung term was modified to account

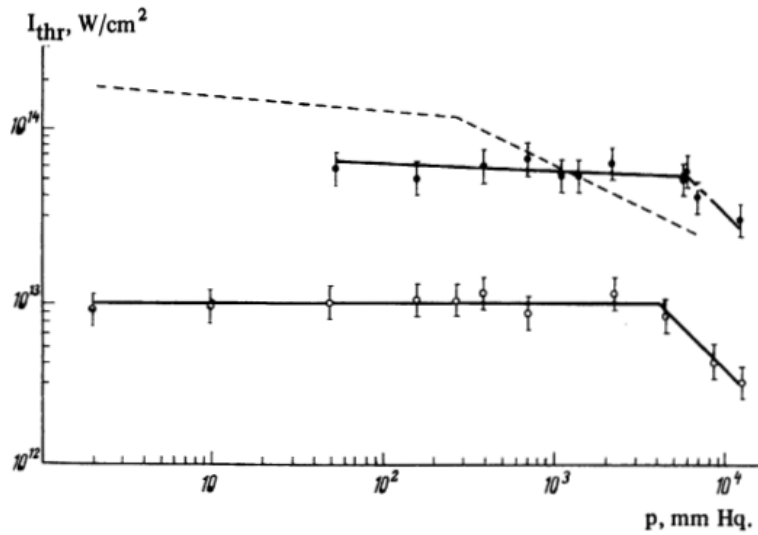


**Figure 4.4:** Threshold breakdown intensity for the case of a picosecond laser taken from Krasnyuk et al. [62]. The dashed lines correspond to nitrogen data taken from a previous experiment by the same authors, the filled data points to helium, and the open data points to argon. Note that the threshold intensity plateaus as the pressure is reduced, a contrast to several of the nanosecond experiments.

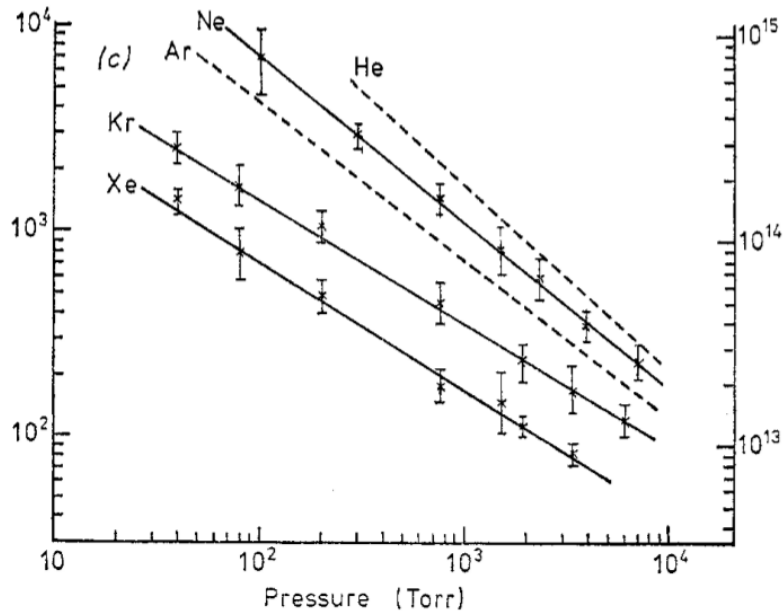


**Figure 4.5:** Threshold breakdown intensity for the case of a picosecond laser from Dewhurst [63]. In this study, the threshold intensity does not plateau as the pressure is reduced.

for diffusive processes, yielding the following equation.

$$\frac{dN_e}{dt} = \alpha^{ph\nu} N + \nu_{eff} N_e \quad (4.12)$$

Using an effective cross section characterizing the neutral argon atom's ionization, the results are shown Fig. 4.6. The results from the plot shows that the breakdown trend from Rosen follows the electron avalanche trend instead of the MPI-dominant trend.

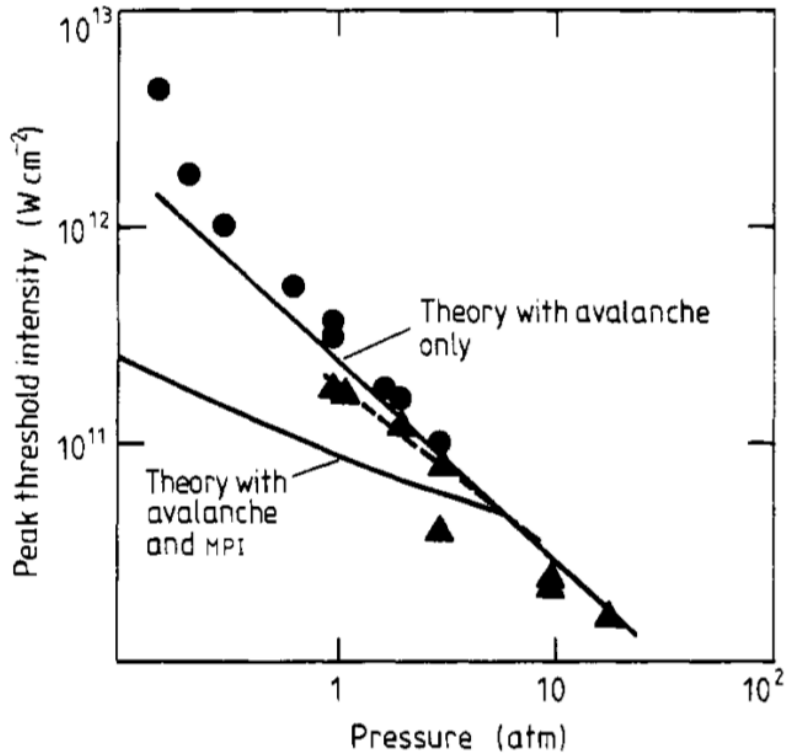


**Figure 4.6:** Original plot of breakdown intensity from Rosen et al. (1989) for argon breakdown with a 532 nm laser. The theory-based plot from Rosen et al. resembles the trend generated with the CR model.

When comparing the master equation to the Eq. 4.11, many of the terms are modeled in the collisional-radiative model with the exception of the diffusion term. As shown previously, the presence of multiphoton ionization dominates electron heating when used at low pressures. But, the CRM yields a different result when used without MPI as shown in Fig. 4.7. With inverse Bremsstrahlung as the main electron heating mechanism, the CRM trend

follows a profile resembling the Rosen experiments and theoretical analysis. The authors implicated a particular series of events for electron avalanche to become the dominant ionization mechanism in their experiment. The amount of energy required to ionize a ground, neutral argon atom requires 7 photons under the specified laser conditions. But, as the number of electrons increases, the upper excited states becoming increasingly populated which becomes easier to ionized, whether by (multi)photoionization or electron-impact ionization.

The authors also cite the “chaotic” nature of electron avalanches. From the experimental standpoint, the observation of a flash or spark was used to dictate the presence of a breakdown phenomenon. This, as mentioned, is highly subjective to the experimentalist when, in Rosen’s experiments, a glow will sometimes persist instead of a flash. The “chaotic” attribute which the authors used to describe the electron avalanche involves a certain synergy between the number of electrons available to liberate other bound electrons and the amount of energy available to break the energy gap. Therefore, it becomes difficult to define a numerical breakdown in their simulation. Unfortunately, this does not answer the prevalence of a supposed MPI-dominant regime in some of the other experiments as an all-encompassing theory would suggest.

By removing the MPI processes in the collisional-radiative model, the model becomes more increasingly dependent on the initial electron density and temperatures. By assuming a highly neutral argon gas, the initial ramp-up of electron density is primarily motivated by MPI rather than inverse Bremsstrahlung where an avalanche cannot effectively take place. Without MPI, IB becomes the source term that guides the evolution of the electrons through the course of the simulation. Since the electron avalanche process is highly dependent on the presence of electrons, the simulation becomes sensitive to the initial electron density and temperature. Several plots compared with the original simulation are shown in Fig. 4.8. The two initial conditions which were separately altered to compare are electron density, which was increased by 2 orders of magnitude, and electron temperature, which was increased to 0.2 eV instead of 0.05 eV. The increases in both cases led to increased peak ionization fractions; for the case with increased electron density, the parameter tends to persist longer rather than exhibit the decline seen in the other plots. Despite this brief study, the initial electron

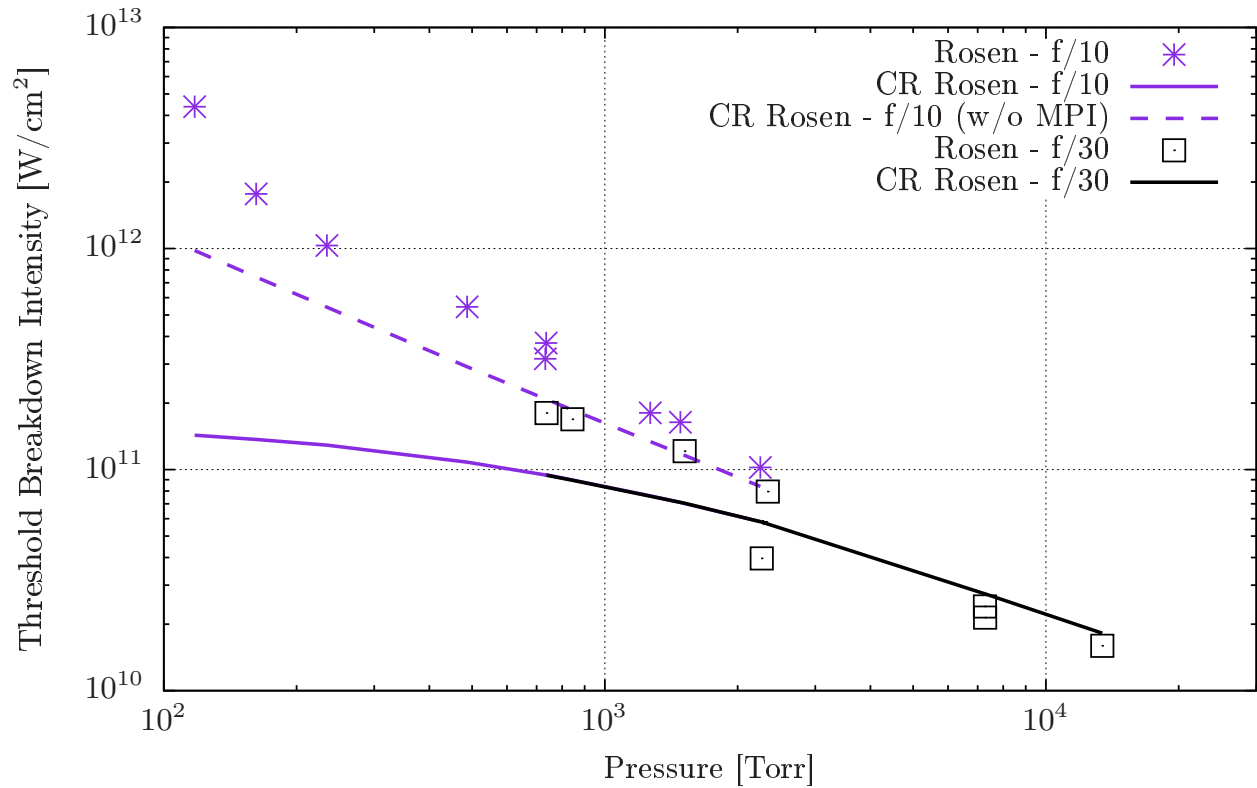


**Figure 4.7:** Comparison of CR results for Rosen et al.'s experimental conditions with and without multiphoton ionization. When MPI is enabled, the trend plateaus as one moves to lower densities. However, when inverse Bremsstrahlung is the sole heating source, the breakdown trend more closely resembles the results of Rosen et al.

density was set to the original value to remain consistent with the other simulations, which is also numerically sufficient to instantiate the electron avalanche.

The time-dependent simulations used to model the breakdown of argon provides additional information pertaining to the growth of the plasma. For each of the simulations on the breakdown plot, the laser pulse was shifted by two pulse widths in order to capture prepulse phenomenon. In Fig. 4.9, the density evolution of the Ar neutral atoms and ions are shown for the 736 Torr case from Rosen’s experiment. Note that while this simulation was conducted for the case with MPI, little variation was observed for the case without MPI.

One can see that the excited states of Ar+1 and all of Ar+2 are small relative to the rest of the atomic states. Also, a double hump feature can be seen in the excited states of Ar+0 and Ar+1. The first hump is attributed to the increasing population of the excited states due to the presence of the laser. The second hump is a consequence of the upper ionization stage’s recombination into the lower ionization stage. More interestingly, the growth of Ar+1 atoms is almost synonymous with the growth of neutral excited states of argon at early time. This would make an interesting case for Rosen et al.’s purported electron avalanche theory, but these profiles were observed in both cases with and without MPI.

The next parameter shown in Fig. 4.10 is the evolution of the electron temperature. The atomic temperature is not shown because the heavy species do not appreciably heat during the course of the simulation. In this plot, the simulations for Rosen’s 736 Torr case with and without MPI are shown. Both simulations show an electron temperature of approximately 2.2 eV. As a comparison, Weyl reports measuring electron temperatures of several eV when measuring breakdown for 0.35  $\mu\text{m}$  lasers, while Davis et al. reports roughly 1 eV from the experiments. [58, 64] The MPI profile shows two humps: the first hump is attributed to the multiphoton ionization ramp-up while the following hump is attributed to continued heating caused by inverse Bremsstrahlung and the electron avalanche.

Without MPI, there are small numerical difficulties associated with capturing the electron avalanche. At early times of the electron temperature’s increase, several temperature spikes can be seen. The reason for the spike stems from the exponential growth in electron density:

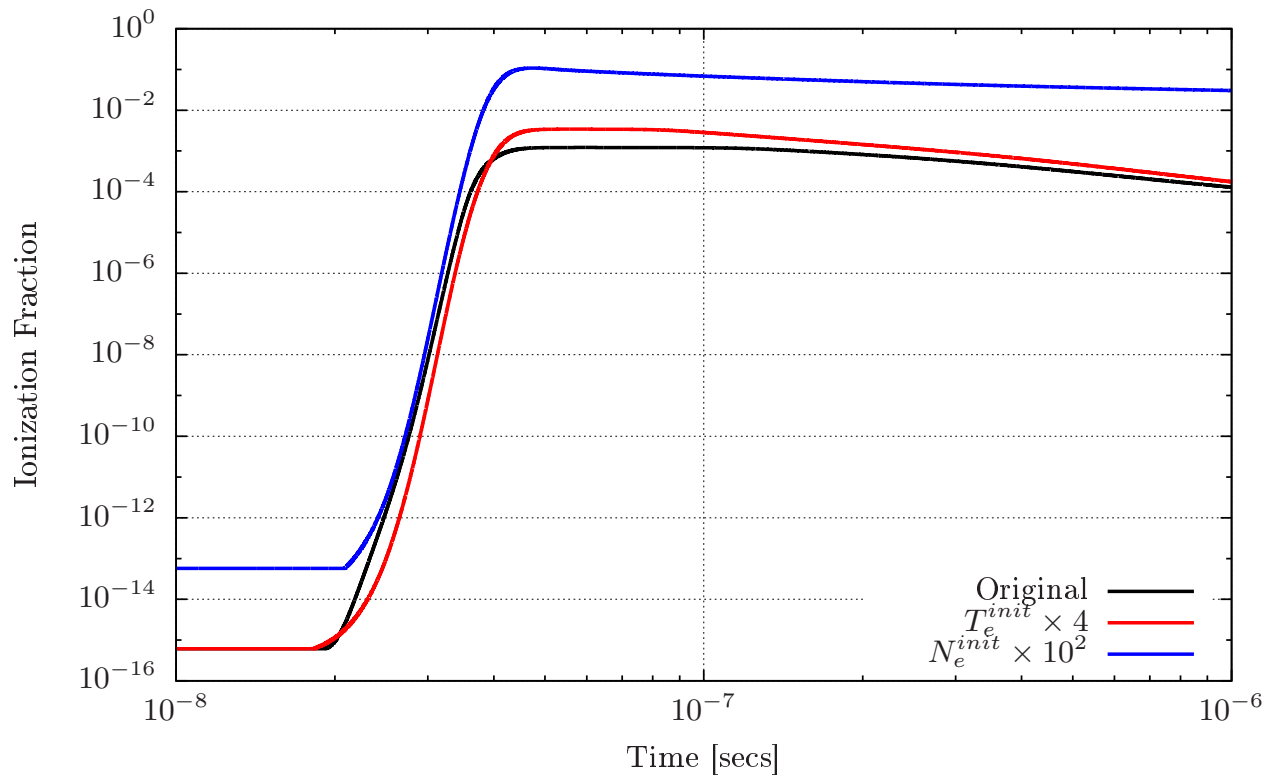


**Figure 4.8:** The sensitivity of the ionization fraction is shown for simulations where multi-photon ionization is absent. Increases in initial electron temperature and electron densities are shown to impact the results relative to the breakdown criterion.

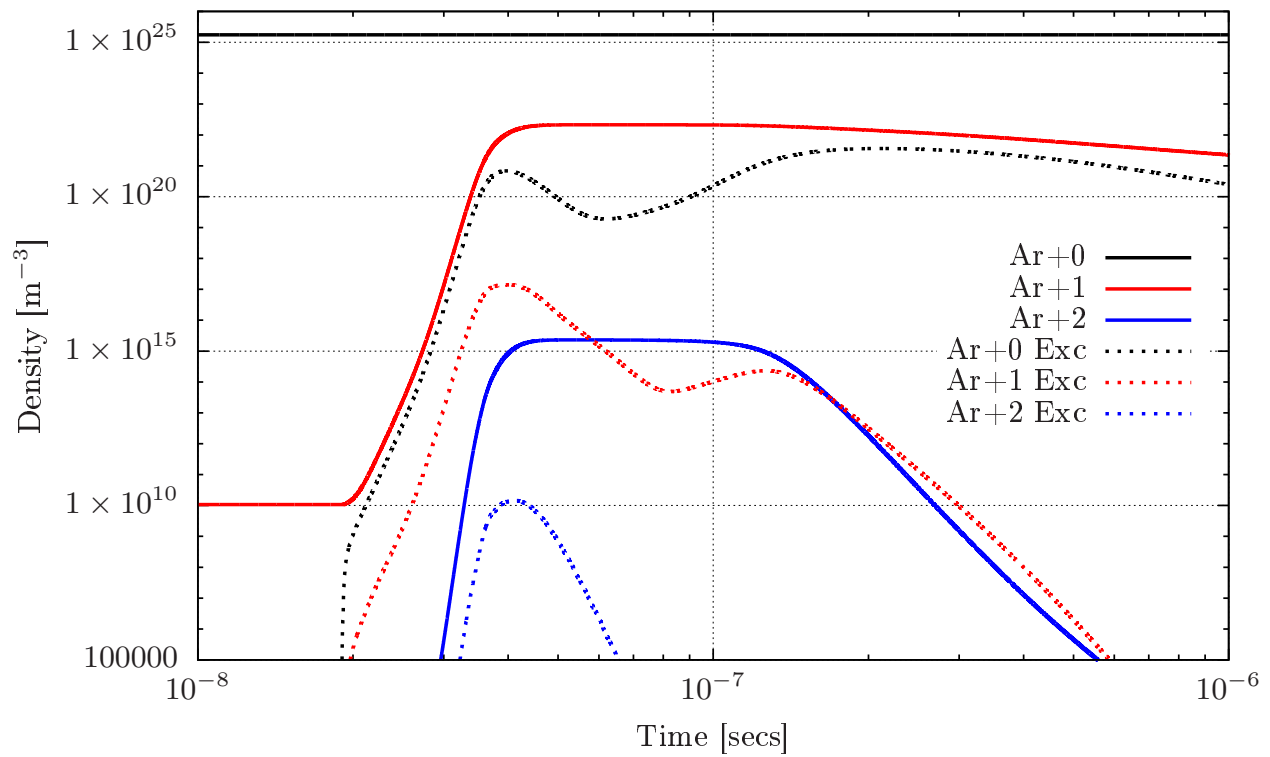


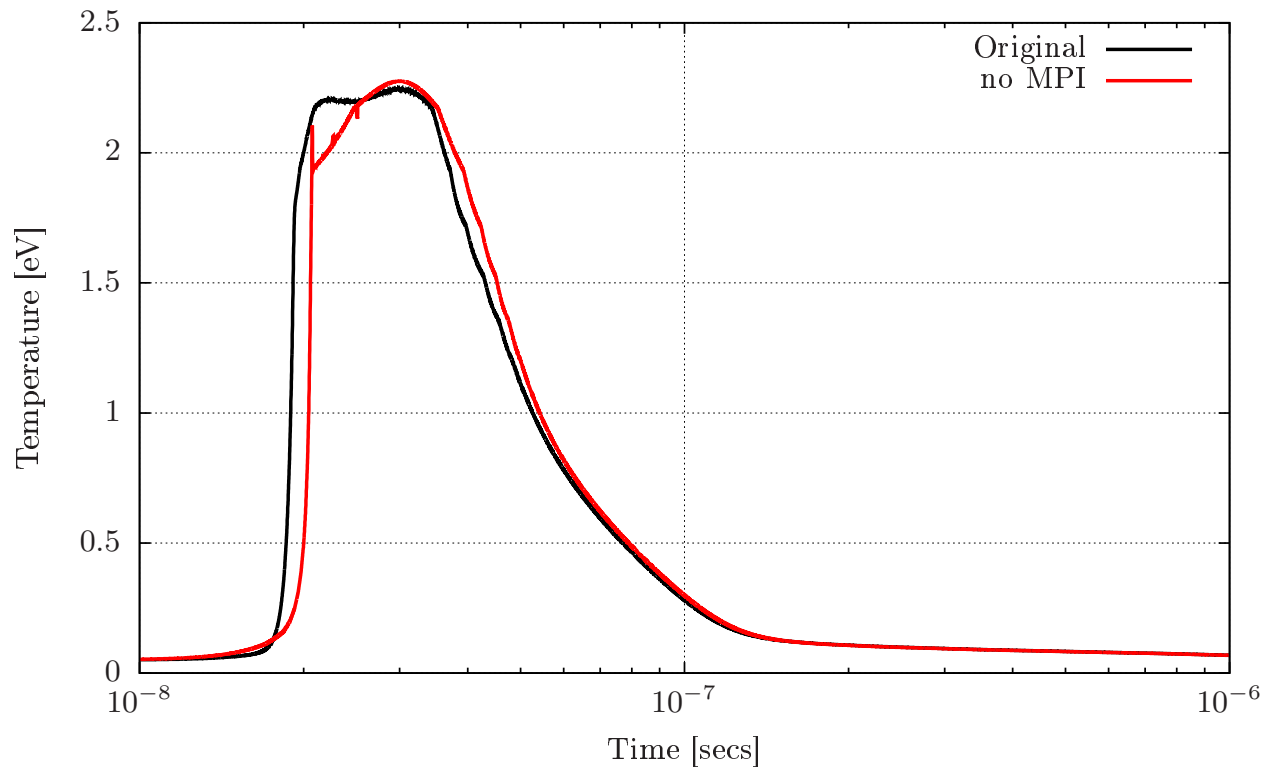
**Figure 4.9:** Evolution of total ion and ions' excited state densities for the 736 Torr Rosen case. The electron density (not shown here) closely matches the Ar+1 total density.

the deposition of energy complemented by the rapid growth of electrons means that the energy must be redistributed across the Maxwellian distribution of electrons. Note that these jumps occur primarily where the multiphoton ionization process would have surpassed that attributed to inverse Bremsstrahlung. This is a condition that may potentially be alleviated should an electron energy distribution solver be used to capture the transfer between electrons with different kinetic energies.

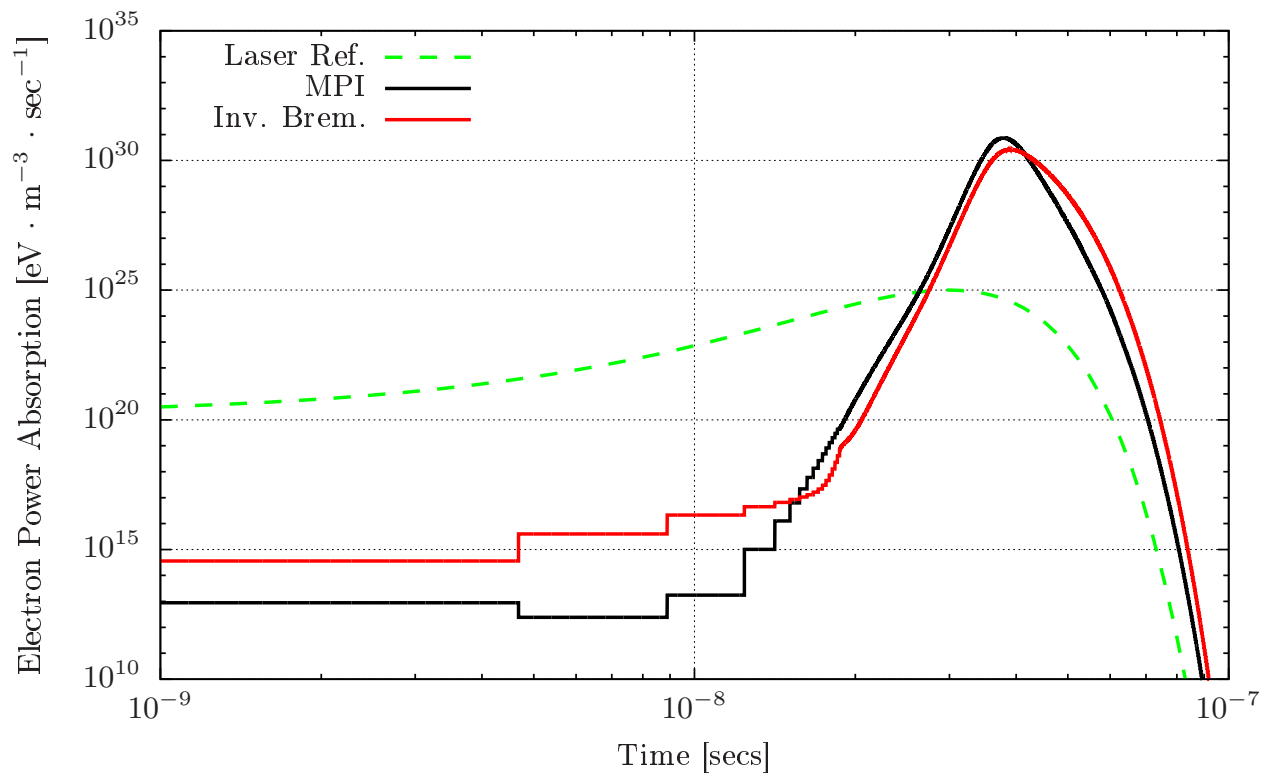
The following figures will show the rate of energy transfer to and from the electrons. The first set of these figures will be used to show the difference in energy transfer rate caused by multiphoton ionization and inverse Bremsstrahlung heating. For the case without MPI, the heat profile resembles the IB heating profile and therefore will not be shown. Fig. 4.11 shows the amount of heating contribution for one of Rosen et al.'s low density cases for a  $P = 117$  Torr. In this scenario, one can see that MPI is the more dominant heating mechanism during the laser ramp-up. As the laser diminishes, one finds that IB begins to surpass the MPI rate. The MPI and IB plots are observed to peak shortly after the laser peak as well, which can also explain the initial excited state density hump in Fig. 4.9. The MPI and IB rates also exhibit some temporal staircasing which occurs in roughly the first 20 nsecs of the simulation. This is caused by the adaptive nature of the numerical scheme, indicating that the early increase in laser intensity has a negligible effect on the atomic densities of the simulation.

Fig. 4.12 shows the laser energy transfer rate for a higher pressure of 1276 Torr from Rosen's simulation. Most of the features observed in the prior low-pressure case are visible in this plot, with the exception of the peaks. Instead of a dominant MPI trend towards the beginning of the simulation, the IB process competes with MPI and provides a larger heating source at its peak. Again, this is consistent with the theoretical understanding of breakdown when recognizing that the electron avalanche process is more significant when more atoms are present and therefore having more electrons. This is a contrast to the previous case where an insufficient amount of atoms leads to a weaker electron avalanche process relative to the presence of MPI.

With the population of excited and ionized states, the plasma can emit radiation via



**Figure 4.10:** Electron temperature plot as a function of time for the 736 Torr Rosen case with and without multiphoton ionization. Two features for the case without MPI can be observed. First, a delay in the electron heating is a result of the multi-step nature of the avalanche sequence. Second, the jumps in the case without MPI is a result of the rapid production of electrons under a Maxwellian assumption.



**Figure 4.11:** Power absorption by electrons shown for a pressure of 117 Torr. In this relatively low-density case, the multiphoton ionization process dominates the inverse Bremsstrahlung rates.

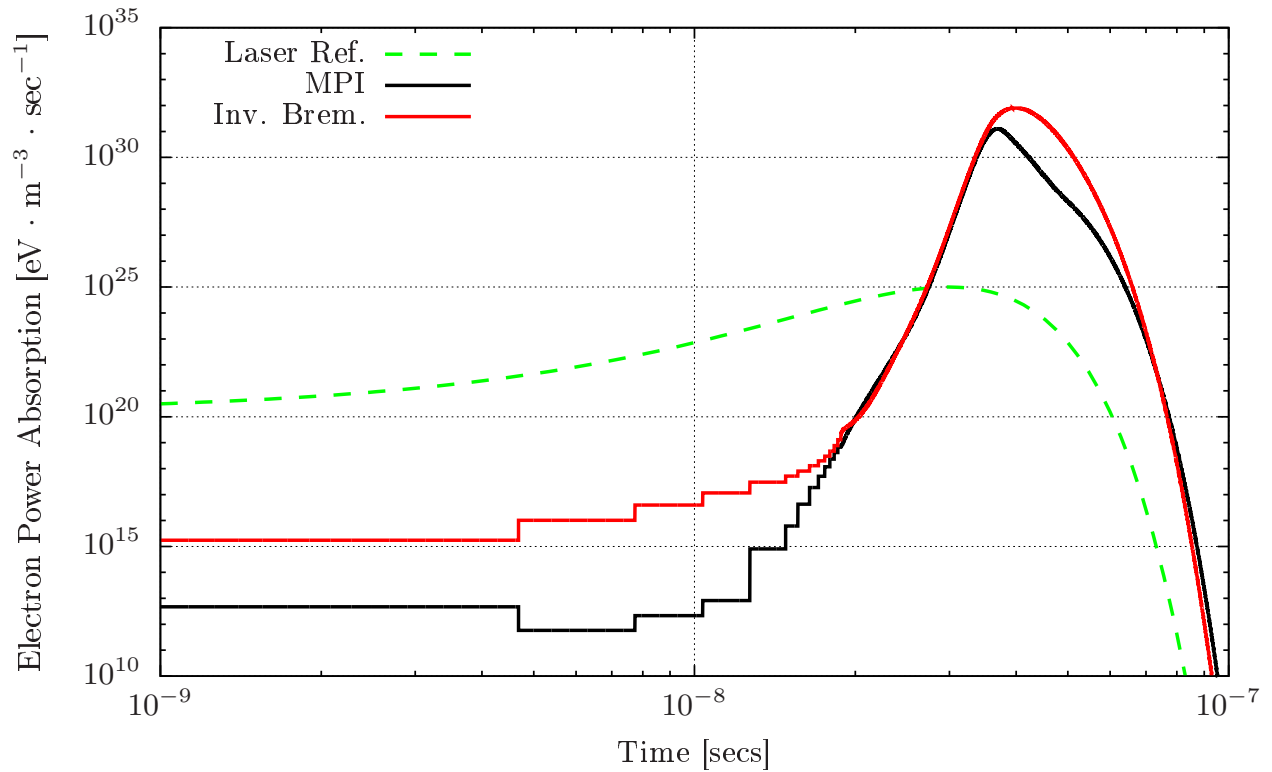


**Figure 4.12:** Power absorption by electrons shown for a pressure of 1276 Torr. In this relatively high-density case, the multiphoton ionization process competes with inverse Bremsstrahlung rates at early times. As the simulation proceeds, the avalanche heating surpasses the MPI power absorption.

spontaneous emissions, radiative recombination, and Bremsstrahlung. Fig. 4.13 shows the radiation losses from the LIB plasma for the 1276 Torr case. The result shows that most of the radiation comes from spontaneous emissions rather than radiative recombination or Bremsstrahlung. The spontaneously emitted radiation from the excited states also resembles the profile of the Ar+0 excited states in Fig. 4.9. With most of the excited states attributed to the neutral atom, most of the spontaneously emitted radiation stems from the Ar+0 excited states.

The last plot shown for Fig. 4.14 is the electron power transfer due to electron-impact excitation, deexcitation, electron-impact ionization, and 3-body recombination. Since the gas is relatively cold and neutral, most of the electron-impact processes remain dormant until approximately 20 nsecs. The plasma begins its electron-impact excitations and ionizations once a sufficient number of electrons are present. These two processes dominate the inverse processes until the laser begins to diminish, after which the deexcitation and 3-body recombination processes begin to cool the plasma.

## 4.4 Summary

The laser breakdown experiments used to compare with the collisional-radiative model's results in this chapter show some differences in the breakdown trends. The results by Rosen, Chylek, and Davis showed predominantly linear trends in the breakdown plots on a log-log scale, with the exception of the Rosen data's slight exponential increase in breakdown intensity for lower pressures. In contrast, Sircar's data exhibits the multiphoton ionization-dominant regime that the other experiments were unable to capture. The CRM was used to generate breakdown trends to capture the experimental observations. When MPI was included in the model, the breakdown plot tends to plateau towards low pressure values. However, when the model omits MPI, thereby relying solely on inverse Bremsstrahlung and the ensuing electron avalanche, the trend captures the avalanche-dominant trend deduced by Rosen et al. The community's division based on whether MPI is major contributor to breakdown at lower densities was also observed in picosecond experiments, as exemplified

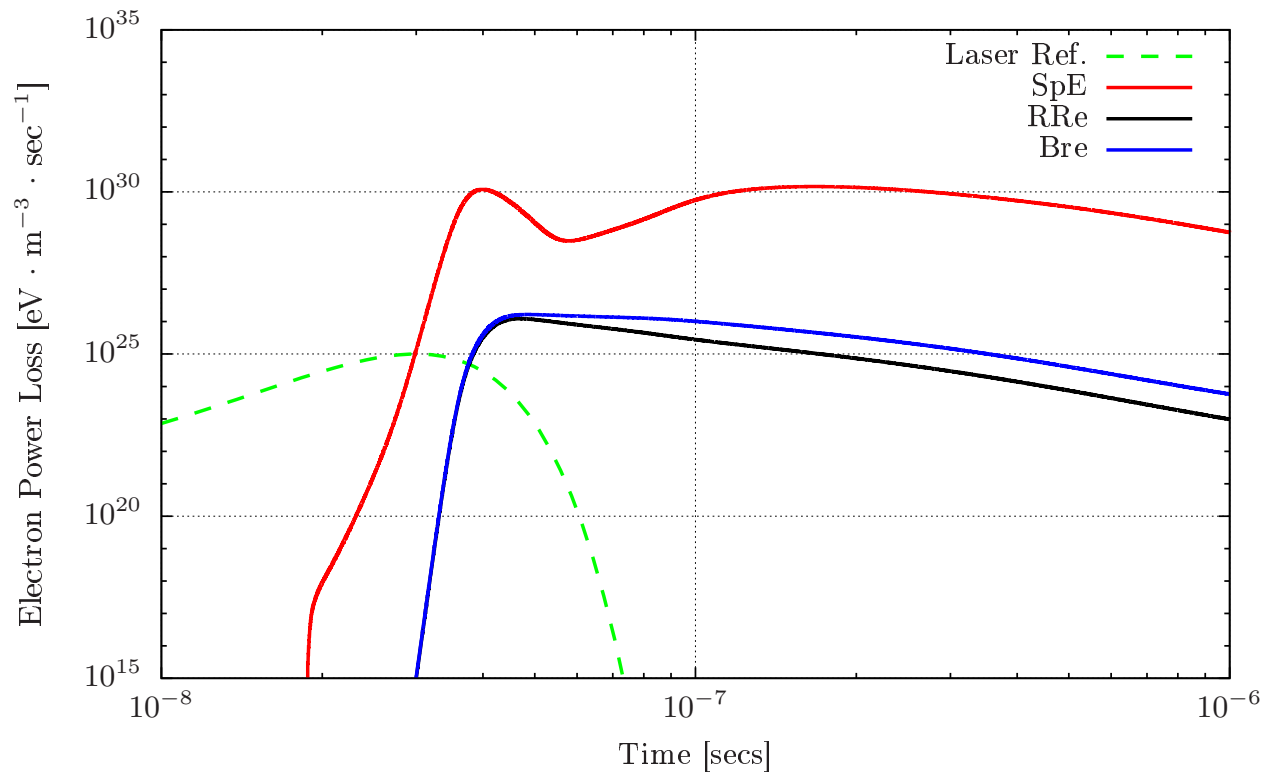


**Figure 4.13:** Plasma radiation loss for the 1276 Torr Rosen case. SpE: Spontaneous Emission; RRe: Radiative Recombination; Bre: Bremsstrahlung Emission.

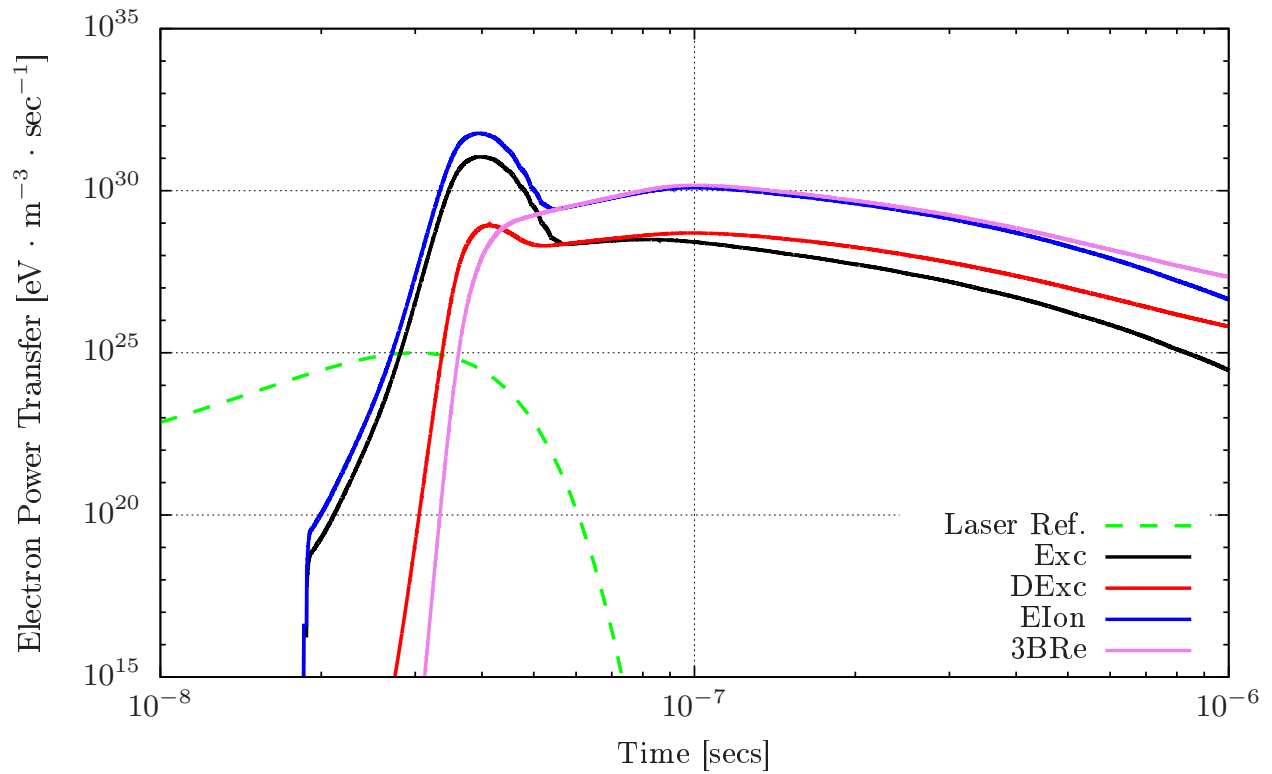


**Figure 4.14:** Electron power transfer due to various mechanisms for the 1276 Torr Rosen case. The plasma begins to cool once the laser energy diminishes as shown by the larger deexcitation and 3-body recombination rates compared with excitation and ionization. Exc: Electron-impact excitation; DExc: Electron-impact deexcitation; EIon: Electron-impact ionization; 3BRe: 3-Body Recombination.

by Krasnyuk and Dewhurst. While this remains as a subject that needs investigation, the numerical model was capable of replicating the two breakdown trends, one in which a transition from MPI-dominant to electron avalanche-dominant exists and another that shows a trend that is purely based on an electron avalanche.

Despite being able to capture the trends using this CR model, there many aspects of the laser-induced plasma that cannot be elucidated solely from a CR simulation. As hinted before, more accuracy can be obtained from the simulations by implementing a coupled electron energy distribution solver, especially for lasers operating at lower timescales. The plasma expansion in these simulations was also not modeled, which requires a coupled fluid solver. There are already works in the modeling community for laser-induced plasmas to capture these plasma dynamics. Morel et al. [65] have constructed a fluid-coupled argon model to simulate laser-induced plasma shock expansions, while Shabanov et al. [66] have constructed a laser-induced plasma model that also accounts for radiation transport. While these works show promise for full laser-induced plasma simulations, there are still many computational challenges in pursuing a full model due to computational time and memory requirements. Due to the many atomic states present in the CR model, one possible avenue to explore is the complexity reduction of the state-to-state model. If successful, the number of equations that must be solved in the fully-coupled system will be reduced through atomic state groupings. The use of complexity reduction in CR models and their implications for coupled systems are discussed in the following chapter.

## CHAPTER 5

# Complexity Reduction Techniques for Atomic Plasmas

This chapter was taken with modifications from the article Complexity Reduction Effects on Transient, Atomic Plasmas, currently under review in Journal of Quantitative Spectroscopy and Radiative Transfer (JQSRT).

### 5.1 Introduction

Simulations of plasmas under non-local thermodynamic equilibrium (non-LTE) conditions involves several computational challenges due to the multitude of time and length scales that must be considered. These time and length scales may be associated with the flow dynamics of the plasma down to the reactive processes between particles. Microscopic processes due to atomic transitions, such as excitation and ionization, can transcend these relevant scales and affect macroscopic properties, e.g., opacities and the equation of state. Collisional-radiative (CR) models are often employed to simulate non-LTE plasmas by numerically solving a set of rate equations for the solution of the atomic population. Unfortunately, simulating CR systems in a coupled environment can become computationally burdensome when one considers the number of levels and transitions that must be represented in the atomic kinetics. This challenge limits the applicability of detailed CR models in large-scale hydrodynamic simulations. The most common solution for this problem is to use compact, highly-averaged atomic models that can run efficiently and inline with hydro codes [37, 67]. Another approach is to employ complexity reduction techniques via grouping of atomic levels [68–70]. These techniques have successfully found applications in simulating partially ionized plasmas including molecular transitions and chemical reactions.

In this chapter, we consider applying the complexity reduction techniques to the case of an atomic plasma with multiple ionization stages. Several reduction schemes have been proposed in the past to deal with multiscale problems which include simulating CR kinetics. These schemes vary in the level of details one chooses to retain after the reduction, which directly affects the accuracy of the method. The common end goal for all of these methods, therefore, is to strike a balance between accuracy and computational cost.

The goal of this work is to assess the accuracy of a variety of complexity reduction techniques from the literature based on level grouping. The techniques we examined include the quasi-steady-state (QSS) solution [16, 71], uniform grouping, and Boltzmann grouping [68–70]. The effects of these methods will be explored through isothermal and Planckian irradiation test cases, from which various plasma parameters can be monitored. The isothermal test cases are designed to assess the ability of the grouping schemes to accurately capture the ionization/recombination kinetics, as well as the time evolution of the atomic states. The Planckian irradiation cases require an additional coupling to the energy equation of the free electrons, which mimics the source term of the material energy equation in a radiation hydrodynamics calculation [21].

## 5.2 Collisional-Radiative Model

### 5.2.1 Atomic and Cross-Sectional Data

The atomic data used for this work are the LANL argon atomic data. Some details regarding the atomic data were discussed in Section 3.3, while the entirety of the data may be found on the IAEA website [25]. For the purposes of this study, the atomic states were consolidated into detailed configuration-averaged (DCA) levels, which are comprised of states with similar occupation numbers in each subshell to focus on the grouping effects. Similar averaging methods have been applied in multiple collisional-radiative model studies [67, 72, 73]. The data includes cross sections for collisional excitation, ionization, and photoionization, as well as oscillator strengths for atomic bound-bound transitions. The macroscopic rates are

determined by averaging over a thermal distribution of free electrons (or photons), which will be described in the next sub-section.

### 5.2.2 Kinetic Processes and Rates

The first group of rates to be included in the model are the electron-impact collision rates. For a collisional excitation process from  $n$  to  $m$  ( $n < m$ ), the rate is given by:

$$\alpha_{(m|n)}^e(T_e) = \frac{\bar{v}}{(k_B T_e)^2} \int_{E_{nm}}^{\infty} \sigma_{(m|n)}^e(E) E e^{-E/k_B T_e} dE \quad (5.1)$$

where  $\bar{v} = \sqrt{\frac{8k_B T_e}{\pi m}}$  and  $E_{nm}$  is the energy gap between two levels. The rate coefficient corresponding to the collisional excitation event is denoted by  $\alpha$  with a superscript,  $e$ , indicating an electron-impact event and a subscript denoting the initial (right) and final (left) states. The deexcitation rate is computed from detailed balance as follows:

$$\frac{\alpha_{(m|n)}^e}{\beta_{(n|m)}^e} = \frac{g_m^{+k}}{g_n^{+k}} e^{-E_{nm}/k_B T_e} \quad (5.2)$$

where  $g_m^{+k}$  denotes the degeneracy for level  $m$  of ion  $+k$ .

For the case of collisional ionization and recombination between  $n$  and  $m$  ( $n < m$ ), the ionization rate, denoted as  $\alpha_{(+,m|n)}^e$ , can be similarly obtained using Eq. 5.1 and the corresponding ionization cross section. The additional '+' subscript in this variable indicates that the final state is an ionized state, i.e.,  $Z_m = Z_n + 1$ . The three-body recombination rate follows directly from detailed balance:

$$\frac{\alpha_{(+,m|n)}^e}{\beta_{(n|+,m)}^e} = \frac{2g_m^{+(k+1)}}{g_n^{+k}} \lambda^{-3} e^{-E_{nm}/k_B T_e} \quad (5.3)$$

where  $\lambda = \frac{h}{(2\pi m_e k_B T_e)^{1/2}}$  is the thermal deBroglie wavelength of the electrons and  $E_{nm}$  is the ionization energy from  $n$  to  $m$ .

The next group of rates to be included in the collisional-radiative model are the radiative rates. For a bound-bound transition between a pair of levels  $n$  and  $m$  ( $n < m$ ), the total

emission and absorption rates are:

$$R_{(n|m)} = A_{(n|m)} + \bar{J}_{\nu,nm} B_{(n|m)} \quad (5.4)$$

$$R_{(m|n)} = \bar{J}_{\nu,nm} B_{(m|n)} \quad (5.5)$$

where  $A$  and  $B$  are the Einstein coefficients for absorption and emission and  $\bar{J}_{\nu,nm}$  is the line intensity. The first and second terms on the right hand side of Eq. 5.4 correspond to spontaneous and stimulated emission, respectively. The right hand side of Eq. 5.5 is due to stimulated absorption. The line intensity is defined as  $\bar{J}_{\nu,nm} = \frac{1}{4\pi} \int I_{\nu} \phi_{nm}(\nu) d\nu d\Omega$  where  $\phi_{nm}(\nu)$  is the line shape. For simplicity, we assume here that the line shape is a delta function centered at the transition energy. We also assume that the photons have a thermal distribution, i.e., Planckian distribution, so that all of the radiative rates can be tabulated as a function of the radiation temperature. The Einstein coefficients are also related via detailed balance:

$$g_n^{+k} B_{(m|n)} = g_m^{+k} B_{(n|m)} \quad (5.6)$$

$$\frac{A_{(n|m)}}{B_{(n|m)}} = \frac{2h\nu^3}{c^2} \quad (5.7)$$

Lastly, the photoionization rate is obtained from:

$$\alpha_{(+,m|n)}^p = \int_{\nu_0}^{\infty} \int_0^{4\pi} \frac{I_{\nu}}{h\nu} \sigma_{(+,m|n)}^p \left[ 1 - \frac{N_m^{+(k+1)}}{N_n^{+k}} \left( \frac{N_n^{+k}}{N_m^{+(k+1)}} \right)^* e^{-h\nu/k_B T_e} \right] d\Omega d\nu \quad (5.8)$$

where  $\sigma_{(+,m|n)}^p$  is the photoionization cross section and  $\left( \frac{N_n^{+k}}{N_m^{+(k+1)}} \right)^*$  denotes the population ratio in LTE. The second term in the square bracket in Eq. 5.8 is the correction due to stimulated emission. The radiative recombination is obtained using Eq. 5.1 with the cross section  $\sigma_{(n|m,+)}^p$  obtained from detailed balance:

$$g_n^{+k} (h\nu)^2 \sigma_{(+,m|n)}^p(h\nu) = 2g_m^{+(k+1)} m_e c^2 E \sigma_{(n|m,+)}^p(E) \quad (5.9)$$

In the isothermal scenario, the electron temperature does not vary with time. But, for the test case where the plasma is irradiated with a Planckian field, the electron energy equation must also be included, where the energy transfer rates can be obtained in a similar manner.

## 5.3 Level Grouping Strategies

### 5.3.1 Quasi-Steady-State (QSS) Solution

Introduced by Bates et al., the quasi-steady-state (QSS) solution was first used to condense the set of rate equations and study recombinative plasma effects [74]. The first of the QSS method's two assumptions is the following:

$$\frac{\partial N_n^{+k}}{\partial t} = 0 \text{ for } n > 1 \quad (5.10)$$

This condition implies that the excited state densities are known if the densities of the ionic ground states and electrons, as well as the electron temperature, are known. Therefore, effective rates based on the electron density and temperature must be formulated to construct a system of ionic ground state ODEs that accounts for excited state transitions. The formulation of these effective rates was implemented and is well described by van der Mullen [16]. The second assumption states that the diffusion or plasma decay's timescales are longer than the excited states' lifetimes. Since this study operates in a 0-D, constant energy source framework, the validity of this condition will not be assessed for this work.

This method drastically reduces the detailed CR systems of equations to representative ion density equations by allowing each ion's excited states to take a quasi-steady-state solution. While the QSS method offers itself as a great reduction strategy considering its lower expense in computational resources, inaccuracies can be expected because of its underlying assumptions: by populating the  $n > 1$  states equivalently, the method neglects the more deeply coupled nature of the ground states to the excited states during the temporal evolution. This reduction method also breaks down when excited states evolve beyond the aforementioned plasma parameters, producing macroscopic errors when modeling highly-

transient plasma systems.

### 5.3.2 Uniform Grouping

Since the excited state evolution in the QSS method are too constrained based on other macroscopic parameters, a simple solution is to free several of the atomic states into variables in the collisional-radiative model. In the uniform grouping formulation, excited states evolve in an independent, but coupled, manner to other relevant atomic states. The construction of these uniform groups requires averaging in the atomic states and the rates which are shown below.

$$N_i = \mathcal{N}_n \frac{g_i}{g_n} \quad \text{where} \quad g_n = \sum_{i \in n} g_i \quad (5.11)$$

$$\tilde{\alpha}_{(m|n)} = \sum_{i \in n} \sum_{j \in m} \frac{g_i}{g_n} \alpha_{(j|i)} \quad (5.12)$$

The issue with this formulation is the strict representation of atomic state densities when observed on a Boltzmann plot. The normalized atomic state densities when extracted from the uniform group lies on a horizontal line, which has no possibility of resolving the Boltzmann line at equilibrium. Due to this limitation, uniform grouping in the past has been primarily used to consolidate detailed levels into DCA levels and as far as superconfiguration levels [29, 75]. When uniform grouping spans more and more levels, the plasma parameters severely deviate from the truth solution. Therefore, the uniform groups are chosen in this work so that parametric deviations are limited, while sufficiently demonstrating the impact of the formulation. However, the problem concerning the rigidity of the atomic state distribution within the group persists and should be ameliorated.

### 5.3.3 Boltzmann Grouping

Le et al.'s Boltzmann grouping strategy assumes a Boltzmann equilibrium distribution over the ensemble of grouped states using a temperature description [68]. This method is very similar to the effective temperatures concept introduced by Bauche et al. [75–77]. Although similar, Bauche's technique uses a root-mean-square fit across the grouped levels while the

technique here utilizes an interpolative means to determine the group temperature. When applied to the entire ion distribution, the group temperature becomes synonymous with the “ionic excitation temperature” defined by Bauche et al. One should note that the Boltzmann grouping formulation here when applied under an entire ion distribution also bears some similarity to the ionization temperature concept by M. Busquet [78].

In order to determine the Boltzmann distribution’s fit, the group is partitioned between the base, or lowest lying, level of the group,  $n_0$ , and the rest of the excited subgroup,  $n'$ . The parameter used to describe group  $n$ ’s Boltzmann distribution using  $n_0$  and  $n'$  is known as the group temperature,  $T_n$ , which is conceptually synonymous with Bauche’s defined “effective temperature”;  $T_n$  enters the Boltzmann weights which are used to extract the individual states’ densities in the effective rate:

$$N_i = \frac{\mathcal{N}'_n}{\mathcal{Z}'_n} g_i e^{-\Delta E_i/T_n} \quad \text{where} \quad \mathcal{Z}'_n = \sum_{i \in n'} g_i e^{-\Delta E_i/T_n} \quad (5.13)$$

$$\tilde{\alpha}_{(m|n')} = \sum_{i \in n'} \sum_{j \in m} \frac{g_i e^{-\Delta E_i/T_n}}{\mathcal{Z}'_n} \alpha_{(j|i)} \quad (5.14)$$

As discussed, the interpolation between  $n_0$  and  $n'$  to determine  $T_n$  is a necessary step to characterize any Boltzmann group. One should note that the limit of  $T_n$  approaching infinity reduces the Boltzmann method to the uniform grouping strategy. Therefore, to reap the benefits from this method, one suggestion is to select a group such that the base level maintains a nominally larger  $N/g$  value than the subgroup,  $n'$ , or its individual states. As a first pass, the group temperature can be determined using the following equation:

$$\frac{\mathcal{N}'_n{}^{(k)}}{N_{n_0}{}^{(k)}} g_{n_0} = \mathcal{Z}'_n(T_n) \quad \longrightarrow \quad T_n^{(k)} \simeq - \frac{\overline{\Delta E'_n}}{\ln \left[ \frac{\mathcal{N}'_n g_{n_0}}{g'_n N_{n_0}} \right]} \quad (5.15)$$

Unfortunately, the initial group temperature is not necessarily the best approximation since the degeneracies, exclusively, are insufficient to describe the Boltzmann statistics. A finer group temperature evaluation requires the use of Newtonian iterations to determine

in-situ a more precise value of the group's partition function:

$$T_n^{(k)} - T_n^* = \frac{\ln \mathcal{Z}'_n(T_n^{(k)}) - \ln \mathcal{Z}'_n(T_n^*)}{\left[ \frac{d \ln \mathcal{Z}'_n}{dT_n} \right] (T_n^*)} \quad \text{where} \quad \mathcal{Z}'_n(T_n^{(k)}) = g_{n_0} \frac{\mathcal{N}'_n^{(k)}}{N_{n_0}^{(k)}} \quad (5.16)$$

By refining the temperature, a line-of-best-fit can be obtained that describes the distribution across the grouped states based on the weighting of each level. Also, the extra degree of freedom introduced by the method's group temperature allows each grouped distribution to relax towards Boltzmann equilibrium should the conditions permit. In contrast, uniform grouping is unable to relax towards Boltzmann equilibrium because of its formulation.

Although major reductions in the CR system of ODEs can be attained, the computational penalty associated with this method still persists due to the required Newtonian iterations for each Boltzmann group. Future efforts may be directed towards more efficient calculations of group temperatures such as by Munafó et al. [70] Instances may also exist where using uniform grouping is sufficient to influence the plasma's macroscopic variations. However, Boltzmann grouping incentivizes coupled plasma simulations with more accurate atomic state distributions. Therefore, finer and more accurate details, such as emission spectra, can be extracted with minimal post-processing, making Boltzmann grouping a premier reduction candidate for its formulation and flexibility.

## 5.4 Isothermal Heating

The first set of comparisons between the complexity reduction schemes were performed using isothermal heating simulations to monitor the evolution of the plasma parameters. Isothermal heating, in the form of a constant electron temperature, constrains the variations of the rate coefficients in the CR model. By allowing all level densities to vary based on the rates, one can make judgments more directly tied between the groupings, reduction mechanisms, and plasma conditions without the additional complications introduced by a varying electron temperature.

Before using the reduction methods, level grouping must be applied to the levels in the collisional-radiative model. As implicated, the choice of whether to agglomerate or retain detailed levels for grouping is not a trivial matter. For instance, shown in Fig. 5.1 are the Ar+9 Boltzmann plots at steady state for multiple total argon densities, each at a fixed electron temperature of 50 eV. At high argon densities, one could construct a Boltzmann group spanning the entire ion distribution caused by high collisionality leading to near-Boltzmann distributions. However, as one approaches low densities leading to the coronal limit, the decision to prescribe a group temperature across the entire distribution is not necessarily appropriate as evidenced by the plot. Therefore, results from two sets of imposed Boltzmann groupings will be presented to show the effect of the grouping selection on the plasma parameters: one set of groupings is based on the ionic excitation (IE) concept, where one Boltzmann group is applied across an entire ionic distribution, and another is a more conservative set of groupings chosen by scrutinizing the truth simulation's Boltzmann plot evolution. Meanwhile, the set of uniform groups will be confined to upper excited state groupings because of the method's restrictive rate-averaging. These groups will be applied persistently for the duration of each simulation.

The first set of results was obtained from a relatively collisional case: a total argon atomic density of  $10^{19} \text{ cm}^{-3}$  and an electron temperature of 100 eV. Each of the cases in this work was seeded with a sufficient number of electrons to instantiate the electron-impact processes that will ionize the argon gas at early time. Boltzmann plots obtained at steady state are shown in Fig. 5.2, where features characteristic of each grouping scheme can be observed.

The QSS method in this plot follows the truth solution's distribution in spite of several excited states. This is easily explained by the QSS method's presumption of the excited state densities based on aforementioned plasma variables. For the more conservative Boltzmann groups, the method well captures the lower-lying excited states, while drawing well-fitted profiles through the upper excited states, all of which is expected of this scheme. However, the ionic excitation case poorly represents the DCA solution; a poor decision of selecting the entire distribution for kinetics averaging in the entire simulation led to a depleted representation of the Ar+8 distribution. More insight into the effect of the IE Boltzmann grouping

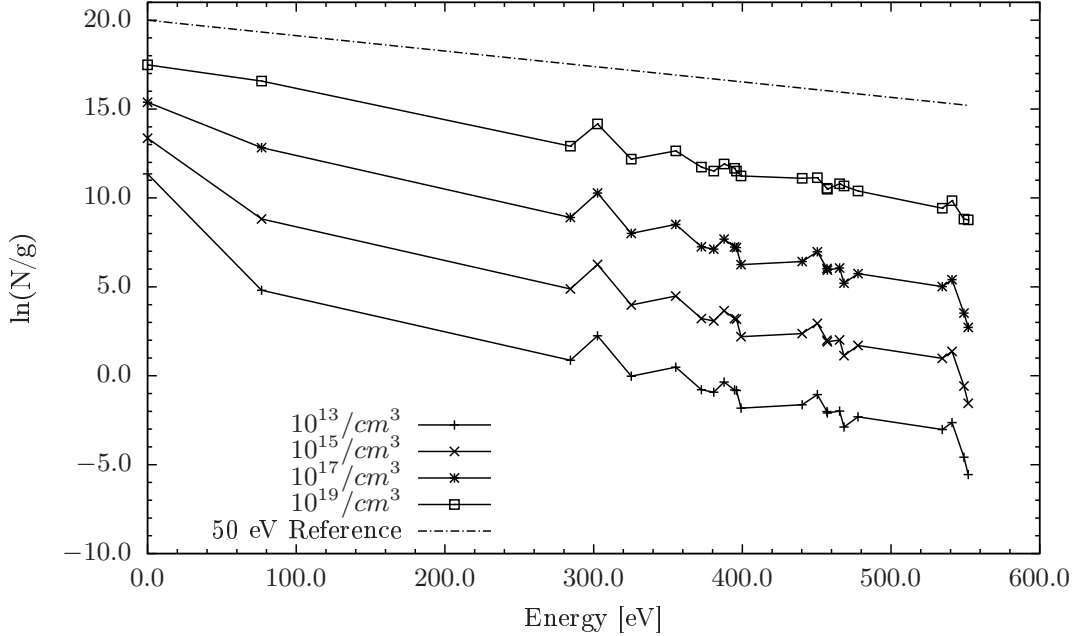


**Figure 5.1:** Boltzmann plots of Ar+9 for different  $N_{Ar}$  at steady state, for  $T_e = 50$  eV. Different plasma conditions, such as density, may require different sets of level grouping, even for similar electron temperatures.

can be seen in the next figure.

Although groupings were preferentially applied to the excited states, these states clearly played a role in the evolving plasma parameters, such as the mean ionic charge seen in Fig. 5.3. The figure shows two particular timeframes of interest: the transient growth of the ionizing plasma and the approaching steady state domain. During the transient stage, the plasma traverses multiple ionic stages within the first 100 psecs of the simulation. Despite the QSS method’s slow ionization phase, QSS plateaus more quickly relative to the other methods, which is a result of the excited states’ decoupling from the ODE.

Between all of the reduction methods, the Boltzmann method captures the mean ionic charge more accurately than its ionic excitation comparison and the uniform grouping method during the transient. However, as the simulation approaches the steady state solution, each of the grouping methods converge to mean charge values with a small amount of error relative to the DCA solution. These errors may either be corrected with finer groupings or unaltered once the variations are deemed inconsequential. The IE configuration’s higher mean ionic charge also explains the depleted Ar+8 distribution seen in Fig. 5.2. By forc-

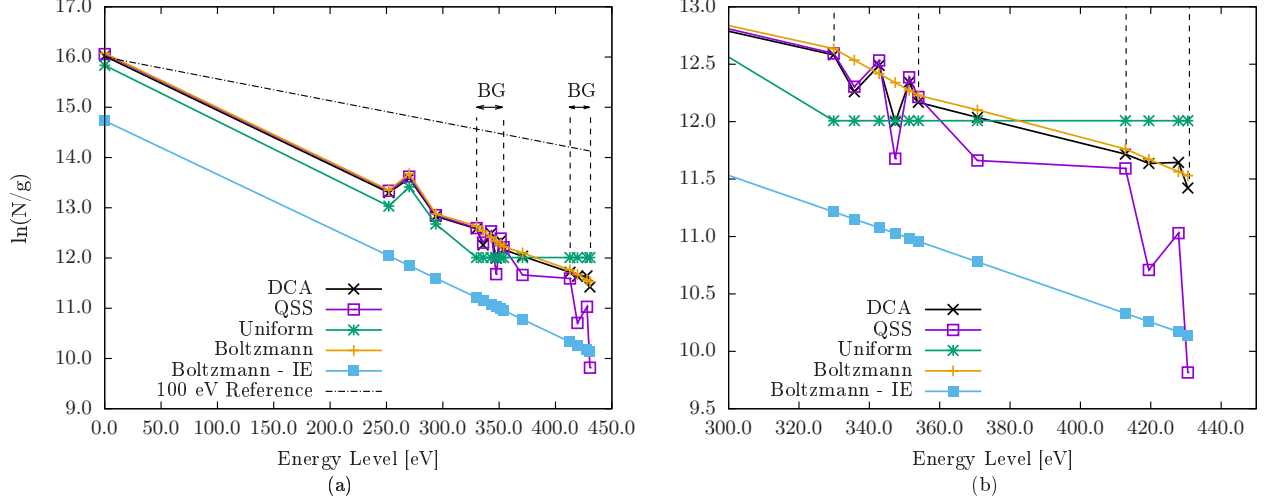


**Figure 5.2:** (a) Boltzmann plots for Ar+8 under various reduction schemes at steady state,  $N_{Ar} = 10^{19} \text{ cm}^{-3}$  and  $T_e = 100 \text{ eV}$ . A 100 eV Boltzmann line is shown for reference. (b) Zoomed image of upper excited state distribution. Grouped states capture distributions characteristic of each reduction scheme. The parts of the distribution spanned by the double-ended arrows indicate the Boltzmann groups (BG). The single uniform group is clearly shown by the horizontal profile amongst the excited states. (color)

ing entire ionic distributions to lie on Boltzmann equilibrium distributions, the IE steady state solution exhibits the largest deviation from the exact, DCA model. Unfortunately, the uniform and QSS methods also overestimate the mean ionic charge values. The more conservative Boltzmann grouping method, however, closely preserves the mean charge for the duration of the simulation.

The next figure depicts the radiation rates for spontaneous emission (SE) and radiative recombination (RR) as a result of the reduction methods. These rates were determined by reconstructing the DCA levels and calculating all of the state-to-state radiative losses. As the argon plasma develops, QSS shows an overestimation of the SE rates during the ionization process and an underestimation of the RR rates resulting from the lack of the transitions from the upper ion's excited states to the lower ion's excited states. In contrast, the IE configuration has a more accurate representation of the total emission rates than QSS. Closer inspection shows that error still persists between the IE and DCA spontaneous emission rates for the entire simulation. Despite the similar trend in the total spontaneous emission rate, recall that this rate was extracted from a reduction mechanism which produced an erroneous average ionic charge. Therefore, if one were to pursue more detail in the

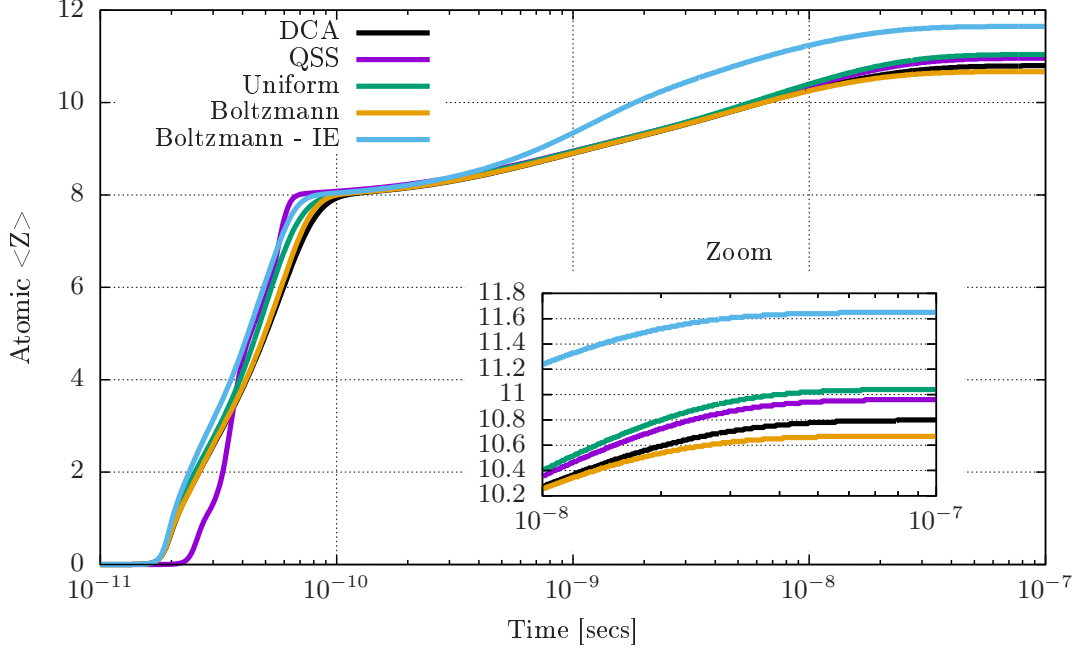


**Figure 5.3:** Mean ion charge evolution for multiple reduction schemes,  $N_{Ar} = 10^{19} \text{ cm}^{-3}$  and  $T_e = 100 \text{ eV}$ : (a) Early transient region, (b) Approach to steady state. Boltzmann outperforms uniform grouping and QSS during the transient duration. All reduction schemes converge with slight errors seen in the zoomed figure. (color)

emissions, i.e. spectroscopic data, the disparity becomes increasingly apparent. In this analysis, the uniform and Boltzmann methods accurately captured the total radiation trend of the DCA solution.

Lastly, unique to the Boltzmann grouping method is the assignment of a temperature description for each group. A plot of the group temperatures was constructed for the Boltzmann cases shown above; but, due to the number of groups constructed for the more conservative Boltzmann scheme, the group, or ionic-excitation, temperatures for the IE case will only be shown (Fig. 5.5). For a  $T_e = 100 \text{ eV}$ , none of the IE temperatures equilibrate to the electron temperature. This is attributed to the balances in the kinetics: excitation is balanced by deexcitation and by spontaneous emission, while ionization is balanced by both three-body and radiative recombination. This means each set of detailed balances is disrupted by a radiative process that has no inverse process, leading to the lower IE temperatures.

The next set of results was produced for conditions that tend more towards the coronal limit, with  $N_{Ar} = 10^{12} \text{ cm}^{-3}$  and a similar  $T_e = 100 \text{ eV}$ . There was increased difficulty in se-

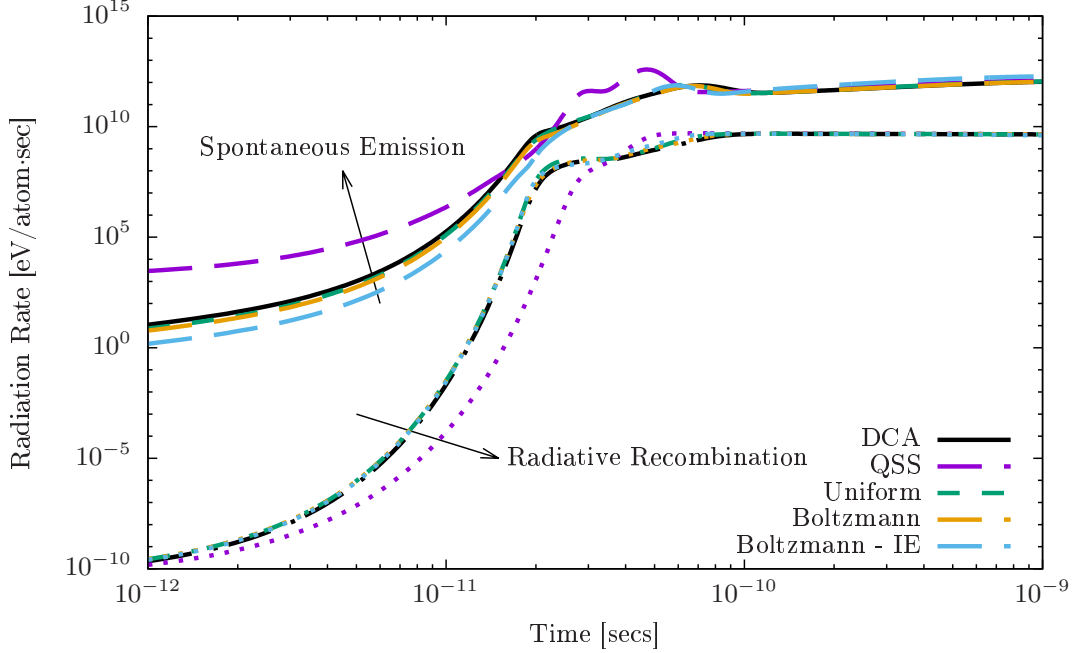


**Figure 5.4:** Spontaneous emission and radiative recombination energy rates for multiple reduction schemes,  $N_{Ar} = 10^{19}\text{cm}^{-3}$  and  $T_e = 100\text{ eV}$ . QSS does not accurately capture the true radiation rate prior to approaching steady state. Uniform and Boltzmann grouping, however, are better-aligned to the true solution. (color)

lecting new Boltzmann groups due to the rates' sensitivity to the low density conditions. Fig. 5.6 shows a snapshot of the Boltzmann plots of Ar+2 during the plasma's ionization phase. Several disparate features can be ascertained from comparisons of the reduction techniques and the DCA solution. Although the QSS method shows the most promise in capturing the shape of the distribution, the population density is underestimated across the entire distribution. For the Boltzmann cases, the conservative Boltzmann method captures the ion distribution much more closely than the ionic excitation case, where significant weighting is placed on the lower states. In the uniform grouping case, several upper excited state populations were overestimated, the impact of which can also be observed in the radiation emissions.

Fig. 5.7 shows the total spontaneous emission energy rate for the entire simulation. The impact of the reduction techniques on the ion distribution can be observed on the plot. For instance, the underestimated QSS densities effectively lowers the spontaneously emitted radiation, which shows in the emission profile for QSS. Despite assigning upper excited state

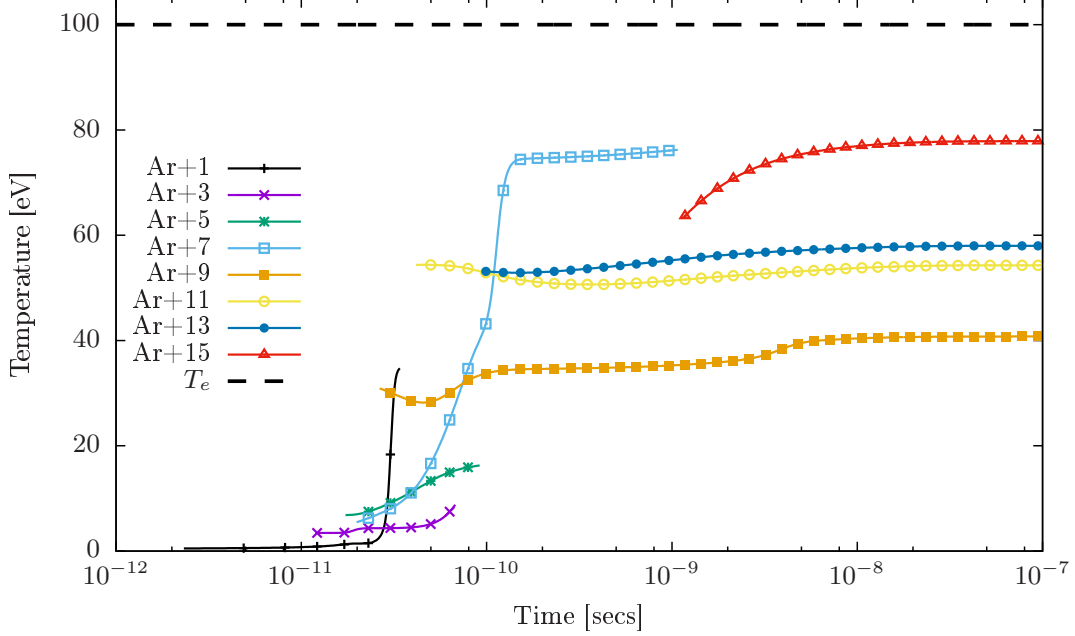


**Figure 5.5:** Group temperature evolution for multiple argon ion distributions using ionic excitation-based groups for target  $T_e = 100\text{eV}$ . Group temperatures were only plotted once the densities attain a threshold value. Note that none of the IE temperatures approach the electron temperature of 100 eV due to the presence of radiation terms. (color)

groupings for the uniform method, this led to overestimations of the individual level densities, producing an unexpected double-hump feature in the uniform method’s emission profile. The emissions are only slightly underestimated in the case of the Boltzmann methods. In the collisional scenario, the overall trends were mostly captured by the reduction mechanisms. However, for low densities, the plasma parameters are especially sensitive which quickly becomes an issue when grouping selection or reduction techniques are being chosen.

A flat profile can also be observed in the first 10  $\mu\text{secs}$  of the QSS simulation. One should recall that by using the QSS method, effective ionization rates are calculated for the entire ion distribution. This means that the eigenvalues of the QSS rate matrix are dependent on effective rates of the reduced CR model. In this scenario, the ionization timescales are pushed towards a later time. The other reduction techniques differ with open and decoupled ionization channels from excited states, leading to a cycle where more electrons are liberated and excited state densities become increasingly populated from electron collisions. Increased collisionality would also explain why variations in the spontaneous emission can be observed

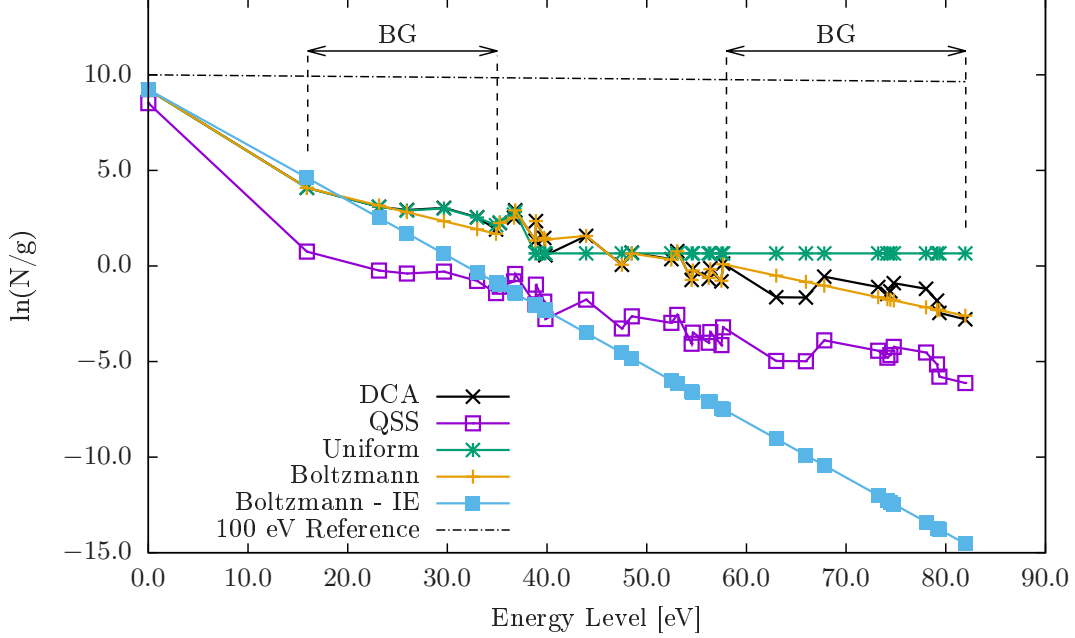


**Figure 5.6:** Boltzmann plots for Ar+2 under various reduction schemes as the plasma ionizes ( $t \sim 90 \mu\text{secs}$ ),  $N_{Ar} = 10^{12} \text{ cm}^{-3}$  and  $T_e = 100 \text{ eV}$ . Again, the Boltzmann groups (BG) are indicated by the double-ended arrows. The uniform group is easily distinguished by the horizontal distribution amongst the upper excited states. (color)

at early times in the QSS radiation rate of Fig. 5.4: the significant increase in the atomic density meant an increased likelihood in the liberation of bound electrons into a free state for more ionic interactions, increasing the upper excited state densities and subsequent radiation emission.

A large discrepancy can also be seen between the ionic-excitation's spontaneous emission energy rate in Fig. 5.7, which suggests good correspondence with the detailed configuration-averaged emission results, and its Boltzmann plot in Fig. 5.6, which would imply erroneous emission values based on the upper excited state densities. This mismatch can be explained by examining the configuration-based spectral lines generated solely for Ar+2 in Fig. 5.8. Many of the Boltzmann ionic-excitation lines are faint due to the method's suppression of the excited state densities. However, in both scenarios, the main contributions to the total Ar+2 spontaneous emission stem from 3 particular lines: the transitions from the  $3s^1 3p^5$ ,  $3s^2 3p^3 3d^1$ , and  $3s^2 3p^3 4p^1$  subshells down to the  $3s^2$  ground state. The order of magnitude of these transitions' intensities overshadow other spontaneous emission transitions, which

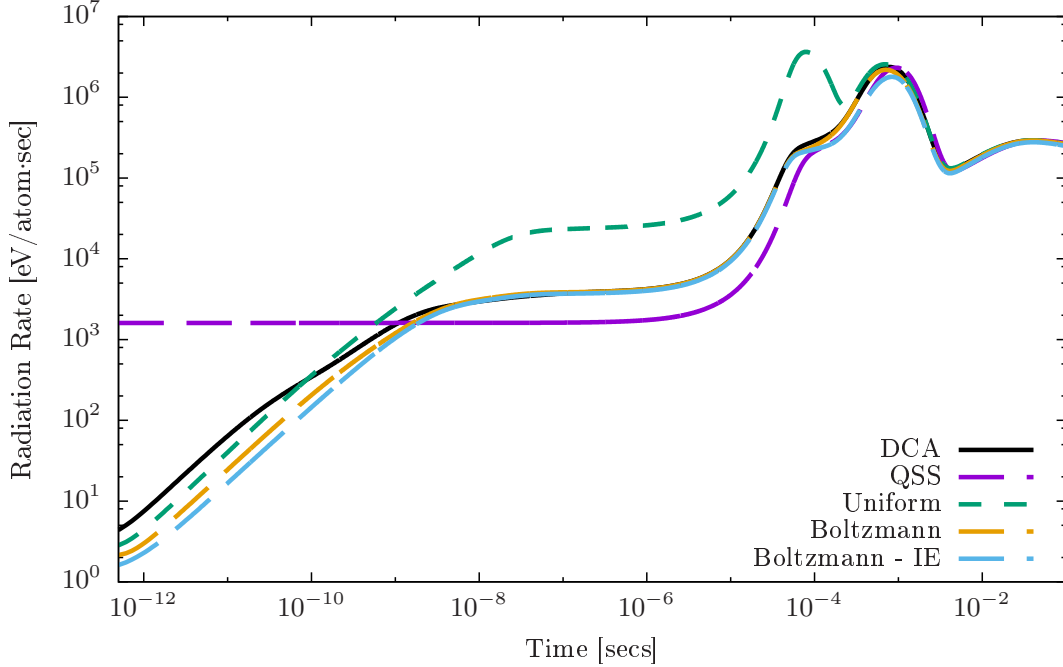


**Figure 5.7:** Spontaneous emission energy rates for multiple reduction schemes,  $N_{Ar} = 10^{12}\text{cm}^{-3}$  and  $T_e = 100\text{ eV}$ . The Boltzmann grouping schemes capture the spontaneous emission energy rates more accurately than the QSS and uniform grouping schemes. (color)

explains the small role played by the Ar+2 upper excited states in the total calculated emission.

Each of the reduction schemes showed several advantages and disadvantages based on several parametric observations in the plasma’s evolution. Boltzmann grouping, in particular, displayed multiple qualitative benefits in addition to the method’s flexibility in level grouping choices. The technique may potentially traverse multiple plasma regimes as well because of its flexibility observed in cases shown thus far. However, the other grouping schemes can still contend with Boltzmann grouping when considering benefits such as wall-clock accelerations associated with solving the CR system of equations. The plasma regime also extends beyond the conditions shown above. Therefore, there are potential scenarios where the other grouping methods may suffice for certain applications of interest.

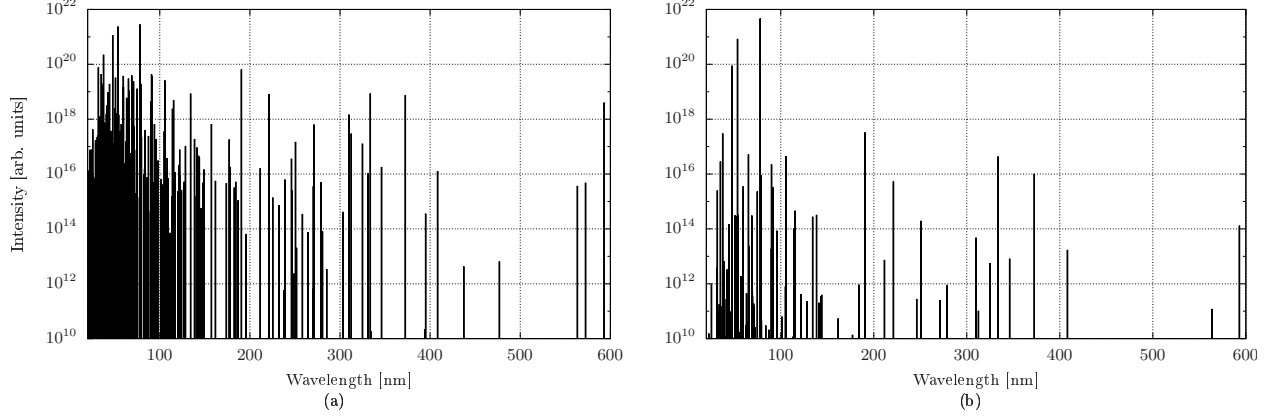


**Figure 5.8:** Configuration-based spectral plots for Ar+2 at  $t \sim 90 \mu\text{s}$  under conditions  $N_{Ar} = 10^{12} \text{ cm}^{-3}$  and  $T_e = 100 \text{ eV}$ : (a) Detailed configuration-averaged solution (b) Boltzmann ionic-excitation solution.

## 5.5 Planckian Irradiation

The Planckian field introduces photoexcitation, photoionization, stimulated emission, and stimulated recombination in the set of atomic processes through the specification of a radiation temperature,  $T_{rad}$ . These new source and sink terms allow each set of plasma processes within the CR model to become microscopically balanced. The photon-based processes not only verify the proper application of detailed balance, but also tests the effectiveness of the reduced models by varying the electron temperature as a contrast to the previous test cases. In this section, only the Boltzmann grouping technique will be studied since the reduction technique lends itself well to capturing potential Boltzmann equilibrium distributions. The impact of the grouping selection on the plasma parameters, in particular, will be assessed through the coarse and fine groupings. Therefore, the ionic-excitation Boltzmann groups and a more conservative set of Boltzmann groupings will be used to represent the coarse and fine solutions, respectively.

The addition of the radiation source and sink terms for the reduced model requires the formulation of the Boltzmann-weighted rates. Eq. 5.14 was similarly applied to the Planckian-based rates to be consistent with the previous Boltzmann-weighting procedure for electron-impact excitation and ionization. These terms also involve complementary energy rates which enters the electron energy equation. This involves identifying the Boltzmann-

grouped transitions of interest and formulating the energy source or sink terms using reconstructed DCA levels. Note that while Le et al.'s conservative energy rate formulation was not included for this study, the method here is sufficient to monitor the impact of grouping on the plasma parameters [68]. Future work will expand on using the corrected energy rates.

The conditions chosen for this Planckian-irradiated case are  $N_{Ar} = 10^{19} \text{ cm}^{-3}$  and  $T_{rad} = 50 \text{ eV}$ . The detail-balanced collisional and radiative rates led to the steady state, linear Boltzmann distributions for the DCA simulation shown in Fig. 5.9. Each of the Ar+5 to Ar+14 Boltzmann plots are not only linear, but also display similar slopes, or temperatures. The ionic distributions obtained from the coarse and fine Boltzmann-grouped simulations are also identical to the DCA Boltzmann distributions shown here. This implies that the group temperatures converge towards a target temperature of 50 eV, which is this case's specified radiation temperature.

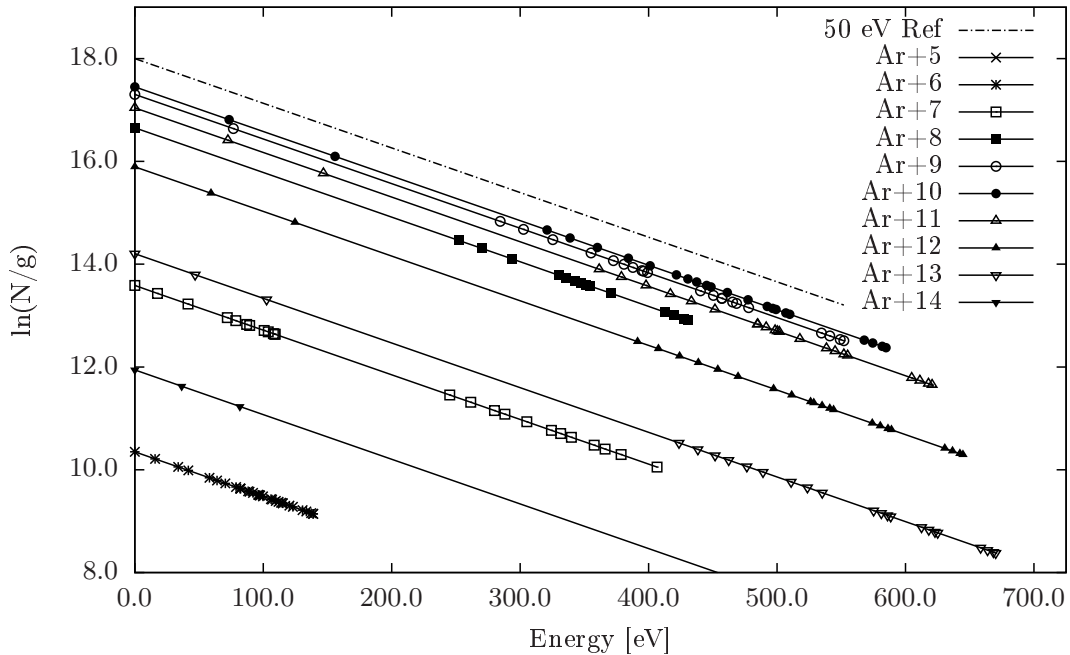


**Figure 5.9:** DCA-based Boltzmann plots of Ar+5 to Ar+14 at steady state for  $N_{Ar} = 10^{19} \text{ cm}^{-3}$  irradiated with a Planckian field at  $T_{rad} = 50 \text{ eV}$ . Each of the Boltzmann plots have similar slopes and compare well against the 50 eV reference, implying convergence to the radiation temperature.

The evolution of the group and electron temperatures can also be monitored as the plots converge towards the steady state value. These temperatures are shown in Fig. 5.10. The

plot only shows the ionic excitation temperature evolution since the number of conservative Boltzmann groups exceeds the number of ionic excitation groups. However, similar trends seen in the IE temperatures plot were also observed from the temperatures plot obtained from the more conservative Boltzmann groupings. At steady state, the group temperatures clearly converge to 50 eV as a result of the balanced kinetics.

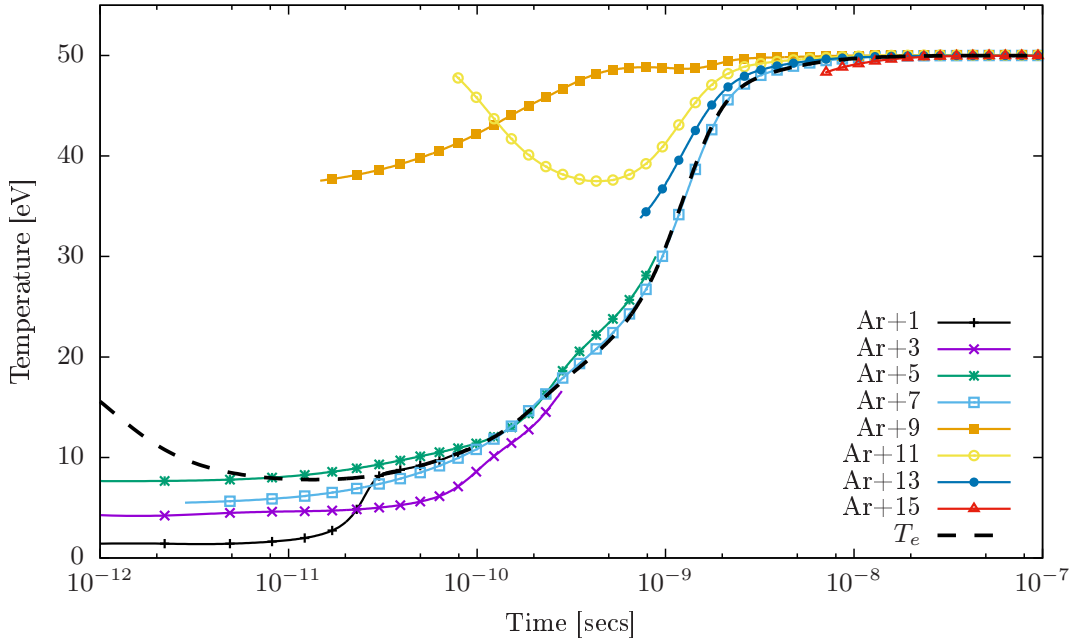


**Figure 5.10:** Temporal evolution of electron (black, dashed) and group temperatures for  $N_{Ar} = 10^{19} \text{ cm}^{-3}$  irradiated with a Planckian field at  $T_{rad} = 50 \text{ eV}$ . All temperatures converge to 50 eV at steady state. (color)

Additional remarks can also be made about the plasma from the temperatures plot. First, the initial electron temperature of  $\sim 15 \text{ eV}$  should be addressed: the calculated ratio of the photoionization energy rate coefficient to the photoionization rate coefficient exceeds unity because of the rate integration over a Planckian field. The initial jump is simply a mere numerical byproduct before the increasing electron density reengages with the ions through radiative and 3-body recombination, lowering the electron temperature before rising again. This phenomenon was also observed through very similar simulations conducted by Abdallah et al. [17]. However, their simulations differ from this study since their electron energy distribution was allowed to change in time. Second, the IE temperatures are observed to trend towards the electron temperature for the duration of the plasma as the system ionizes

and develops. Finally, higher-stage ions are observed to instantiate at a higher temperature, suggesting simultaneous population of the upper ions' excited states as the plasma ionizes.

The next quantities of interest are the spontaneous emission and radiative recombination energy loss rates. The presence of the Planckian field increases the population of upper stage ions and excited states through the photon-based processes. In Fig. 5.11, the separation in the radiation rates is much more apparent. Based on the SE rates, the ionic excitation case has an approximate order-of-magnitude difference in the rates before matching the DCA simulation near steady state. The more conservative Boltzmann grouping method produces a more accurate result for the entire simulation, matching the DCA result well before reaching the emission peak.

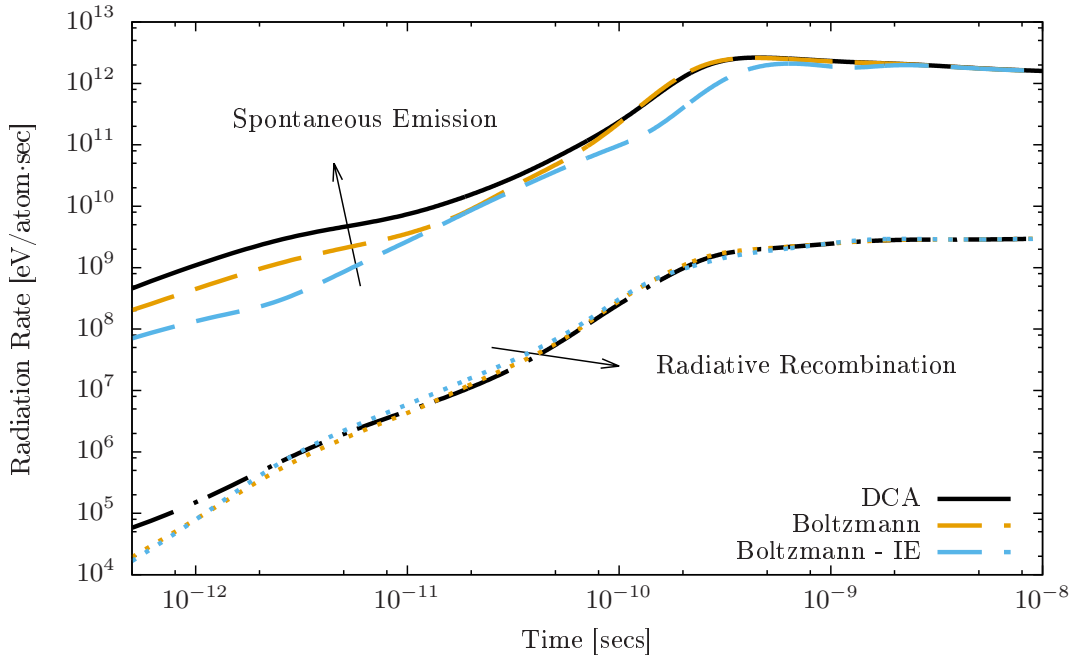


**Figure 5.11:** Spontaneous emission and radiative recombination rates for DCA levels, Boltzmann with finer groupings, and Boltzmann under an ionic excitation description,  $N_{Ar} = 10^{19} \text{ cm}^{-3}$  and  $T_{rad} = 50 \text{ eV}$ . The coarse groupings associated with Boltzmann IE leads to larger errors in spontaneous emission rates in this irradiation case. (color)

Several studies in the past have highlighted the presence of emission peaks in ionizing plasmas. The existence of these peaks in plasmas are known to depend on several factors, such as the final ionization state, the number of outer, open shell electrons, and the overall collisionality of the system [79, 80]. In Fig. 5.11, the conservative Boltzmann-grouped sim-

ulation well-matches the timestamp associated with the peak spontaneous emission of the DCA result, in contrast to the late and less-pronounced IE case's peak. Plots of the spontaneous emission rates for the same grouping scenarios are shown in Fig. 5.12 to explain this feature of ionizing plasmas. Spontaneous emissions will be the focus in the analysis since the largest source of emissions observed in the previous test cases stem from spontaneous emission.

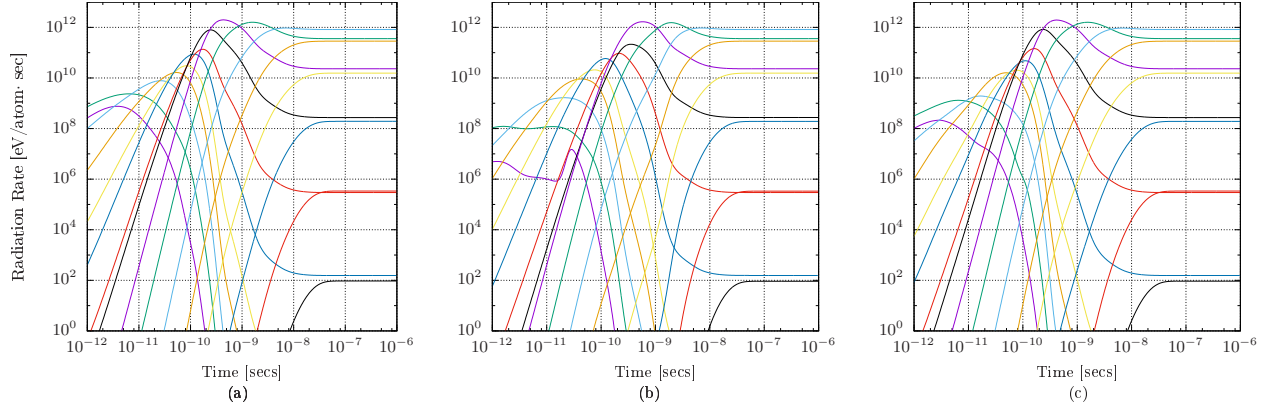


**Figure 5.12:** Total spontaneous emission rates under different grouping conditions: (a) DCA levels, (b) Boltzmann - IE, (c) Boltzmann (finer groupings). By refining the groupings, i.e. from (b) to (c), the plasma gradually recovers the emission profile shown under the DCA simulation. From left to right in each subplot, the peaks correspond to each ion from Ar+0 to Ar+17. (color)

The ionic excitation case, (b), shows several differences in each of the ion's total spontaneous emissions when compared with the DCA results in (a). As the plasma transitions through the ion stages, several of the ions' peak in spontaneous emission rates are either suppressed in magnitude or delayed in time when compared with the truth, DCA solution. By forcing the excited states to lie on a Boltzmann distribution for these conditions, important contributing transitions are hindered through the Boltzmann weighting, leading to the changes in the spontaneous emission rate. But, by refining the grouping selections and increasing the number of independent atomic levels, important line emissions are elucidated and the finer Boltzmann groupings in (c) more closely resemble the emissions seen in (a).

The results shown here are unique to Planckian field effects where all simulations, with or without Boltzmann grouping, converge to identical, Boltzmann ionic distributions at steady state. However, simulations involving radiation sources in the form of lasers or opaque

plasmas present a greater challenge for complexity reduction since specific frequencies, and therefore transitions, are activated by these sources. Alternatively, large errors in a hydrodynamic simulation can manifest because of unsuitable groupings that can magnify at the macroscopic level when considering the total energy losses in spontaneous emission. Therefore, groups must be carefully selected to mitigate these errors in the ion distribution, leading to greater fidelity in detailed and coupled plasma simulations.

## 5.6 Summary

Various complexity reduction techniques have been introduced through the decades in an attempt to curtail computations involving a plethora of atomic levels and relevant transitions. The techniques shown here included quasi-steady-state (QSS), which assumes an equilibrated set of excited states population, uniform grouping, which conserves number density but imposes a rigid distribution profile, and Boltzmann grouping, which grants extra flexibility in the distribution profile through group temperature iterations. However, each reduction technique has unique effects on the macroscopic plasma properties.

In this work, the effects from model reduction and grouping selection was investigated through the isothermal and Planckian irradiation test cases. Although the QSS method was able to capture the general profile of the atomic state distribution, the supposition of the excited states based on the macroscopic plasma parameters ( $N_0^{+k}, N_e, T_e$ ) led to the errors observed in the collisional and coronal isothermal studies. On the other hand, uniform grouping provides extra degrees of freedom by increasing the number of atomic state variables; despite restricting the construction of uniform groups to the excited states, the impact of the excited states on the rest of the ionic distribution and the entire plasma are still distinguishable.

Boltzmann grouping ameliorates several of these errors by accurately capturing the group distributions through the temperature descriptions. The accuracy was not only observed in the isothermal studies, but also in the Planckian test case where the atomic state distribution converged to the Boltzmann distribution. Despite having several advantages over previous

reduction techniques through the choice of groups and flexibility in the group distributions, Boltzmann groups can still be optimized to yield accurate time-dependent simulations through proper group construction. Numerical capabilities need to be explored in the future to adaptively construct more accurate groupings during the course of the simulation, such as the work by Sahai et al. [81] A collisional-radiative model with such capabilities would enable accurate plasma simulations across many scales once limited by computational time and resources.

## CHAPTER 6

### Spectroscopic Modeling

The wide range of plasma conditions that exists in nature or are artificially produced necessitates different types of methodologies to assess these systems. Diagnostic techniques are especially important because plasma assessment can, for example, help achieve performance objectives in electric propulsion devices or attain high-temperature, high-density conditions desired in fusion devices. Diagnoses of these plasma systems are either intrusive through the use of probes such as Langmuir probes or non-intrusive by relying on light emissions captured by spectrometers. Unfortunately for intrusive diagnostic tools, it is well-known that the interactions between the plasma and the tool cause proximal perturbations that can affect the nominal state of the plasma. [82] One way to avoid these effects is by using non-intrusive methods such as laser diagnostics, which limits their interactions directly with the plasma, leading to higher confidence in the information determined from these instruments. [83]

A popular, non-intrusive way to determine plasma conditions is by obtaining and analyzing spectral images from a plasma. There are several ways to determine the plasma conditions from the experimentally-obtained spectra. But, a comparison with spectra generated from a collisional-radiative model provides a robust method of analyzing plasmas because of the access to a broad range of spectral energies or frequencies. Given the reliability of the atomic data, these analyses may be performed upon the entirety of the spectral range or down to the characteristics of prominent line intensities, ratios, or widths. Therefore, the CR model was extended to supply spectroscopic information from its calculations to compare with experimental results. This chapter will discuss the implementation of such spectroscopic calculations followed by analysis of spectra images derived from the collisional-radiative model and two experiments. The two experiments will differ in plasma conditions,

one of which is high in temperature and density and the other being on low-temperature and low-density regime.

## 6.1 Spectroscopic Construction

The spectra can be constructed from the collisional-radiative model by isolating the radiation emission processes from the complete set of reactions in the master equation. These radiative emissions can be grouped into several categories based on whether the initial and final states of the radiative transition are bound or continuum/free states. These emission categories are known as bound-bound, bound-free, and free-free emissions. In this work, the bound-bound emissions correspond to the spontaneous emission events, the bound-free to the radiative recombination events, and the free-free to the electron Bremsstrahlung emissions. Certainly, other types of emission processes may occur, such as the stimulated forms of the aforementioned emissions, but the formulation discussed here easily extends to such processes.

A few assumptions must be made when generating spectra from the current iteration of the collisional-radiative model. The first assumption is that the ions are rendered quasistatic, whereas the electrons are dynamic. This is consistent with the rate calculations mentioned in Chapter 3, where the electrons are assumed to catalyze the reactions. Even though the reactions are driven by all participating reactants through their relative velocities, this assumption is applicable in many scenarios. Also, the computations associated with calculating bin-to-bin ( $f_e(v_e^j) \leftrightarrow f_i(v_i^k)$ ) reaction rates is very expensive, which is the reason the CR model as well as many concurrent models have abstained from performing such calculations. Another assumption pertains to the broadening of spectral lines: for each isolated line, the Baranger formalism dictates that the contributions to the broadened width stems from the levels' transitions and their corresponding rate coefficients. [84] Unfortunately, the “isolated line assumption” is only an approximation and becomes highly inaccurate when lines begin to influence each other, or, as a rule of thumb, when the width becomes comparable to the transition energy's width. The reader is encouraged to view the references

regarding ongoing work for improvements in computationally-generated spectra. [85–87]

The first spectroscopic feature which will be considered is the bound-bound (BB) set of emissions that form the spectral lines. The emission formula for each bound-bound transition per frequency,  $\nu$ , is as follows

$$j_\nu = \frac{1}{4\pi} A_{mn} N_m \Delta E \phi_\nu \quad (6.1)$$

where the units of the spectra will be in [eV / m<sup>3</sup> sec Hz ster]. [88] The variables here are slightly altered from the previously-used notation, where  $A_{mn}$  is the Einstein A for the transition between  $m$  and  $n$ ,  $N_m$  is the density of the upper state, and  $\Delta E$  is the transition energy. The  $1/4\pi$  factor corresponds to a line-of-sight measurement from the 0-D plasma. Finally, these line strengths must also account for line shapes,  $\phi_\nu$ , because of broadening effects that result from atomic physics and collective plasma dynamics. Three primary broadening mechanisms (Doppler, Natural, and Stark) will be considered for spectroscopic construction.

Doppler broadening of the spectral lines results from the motion of ions in the plasma. Since the simulations are 0-D, the ion motion referred to here is a consequence of the Maxwellian distribution assumption of the ions. The ion motion causes the expected line from bound-bound emissions to exhibit red and blue shifts, resulting in a broadened line distribution. This broadening effect is concretely characterized by an effective ion temperature,  $T_{ion}$ , which is representative of the kinetic motion of the ions. The formula for the Doppler half-width at half-maximum (HWHM) is given below

$$\Delta\nu_{Dopp}^G = \nu_0 \sqrt{\frac{2 \ln(2) T_{ion}}{Mc^2}} \quad (6.2)$$

Contributing variables to Doppler broadening also include the frequency of the transition,  $\nu_0$ , and the rest energy of the ion,  $Mc^2$ .

The next broadening effect, natural broadening, is a result of Heisenberg’s uncertainty principle on the reaction rates in the master equation, where  $\delta\nu \cdot \delta t \geq 1/4\pi$ . More precisely, if one takes the uncertainty in time to be the mean lifetime of a particular level, then the

uncertainty in the transition frequency, or energy, results from the principle resulting in a broadened line distribution on the spectra. The natural broadening HWHM is calculated from the following equation

$$\Delta\nu_{Nat}^L = \frac{1}{4\pi} \left( \sum_n A_{upp,n} + \sum_n A_{low,n} + \sum_n k_{upp,n} + \sum_n k_{low,n} \right) \quad (6.3)$$

where all radiative and collisional processes depopulating the upper and lower states of the transitions are considered in the formulation.

Lastly, the effect of Stark broadening is also considered especially for plasma conditions involving from high-density and/or large electric field effects. Stark broadening is a result of transitional perturbations that result from electric (micro)fields, whether applied externally or induced by charged particle or collective plasma effects. Proper treatment of Stark broadening is highly intricate since the electric field can lead to splitting of energy levels that varies based on the field strength. Calculations that ensue from modifications of energy levels and transitions become increasingly expensive as a result. Although there exists a sizable community pursuing accurate, and hopefully generalized, Stark calculations, the current methods can be computationally involved, cumbersome, or time-consuming. [86, 89] Instead, expedient and sufficient approximations are desired and implemented for the CR model's current spectroscopic capabilities.

The quasistatic assumption highlighted by Griem to characterize Lyman- $\alpha$  was therefore used as the foundation to construct Stark broadening widths. [90] Following S. Hansen's (Sandia Natl. Lab.) suggestion, the HWHM for Stark is

$$\Delta\nu_{Stark}^L = 2.15(n_{upp}^2 - n_{low}^2) \left( \frac{N_e}{1 \cdot 10^{28} \text{ m}^3} \right)^{0.58} \quad \text{for even } \Delta n \quad (6.4)$$

$$\Delta\nu_{Stark}^L = 2.15 \frac{n_{upp}^2 - n_{low}^2}{6^{2.5} Z_{nuc} / n_{upp}^2} \left( \frac{N_e}{1 \cdot 10^{28} \text{ m}^3} \right)^{0.58} \quad \text{for odd } \Delta n \quad (6.5)$$

In the case that the transitions are K-shell emissions,  $n_{low}$  should be set to 0. While the formula has been used beyond K-shell transitions, careful scrutiny should still be exercised when considering its generalization, i.e. wing broadening, nonlinear Stark, lightly-ionized/heavy

elements, etc. But, this formula will be employed in the model until a more thorough and/or quicker rendition of Stark calculations is found.

With the Doppler, natural, and Stark widths on hand, the appropriation of specific line profiles for each broadening effect must be performed. The Doppler effect corresponds to a Gaussian line profile, while the natural broadening width is assigned to the Lorentzian profile. The quasistatic approximation of the Stark broadening effect requires the Holtsmark distribution; however, the inclusion of this distribution goes beyond a straightforward implementation due to the wide range of phenomena that must also be considered, i.e. emitter source, ion dynamics, etc. [89,91] Therefore, the Lorentz profile will be provisionally applied. Employing the Lorentz profile for Stark broadening also translates to the impact approximation, which is an averaged collisional treatment of the Stark broadening effect. [83] Altogether, the contributions from all of the broadening mechanisms must be convolved, leading to the Voigt profile. Numerically, the Voigt profile is expensive to calculate; several methods have been developed to efficiently calculate the distribution. The approximation used by Whiting was ultimately chosen and implemented to calculate the broadened spectral lines. [92] Fig. 6.1 shows the characteristic differences of the Gaussian, Lorentz, and Voigt profiles.

Next, the bound-free (BF) emissions resulting from radiative recombination events were incorporated into the spectral calculations. These spectral features are highly distinguishable because of the continuum edge that results from the recombination energy threshold. The bound-free emissions can be calculated using the following representation. [88]

$$j_\nu = \frac{h^2\nu}{2^{3/2}\pi m_e^{1/2}} E^{1/2} N_m N_e f_e(E) \sigma(E) \quad (6.6)$$

The cross section in this equation,  $\sigma$ , is the radiative recombination cross section which can be computed from detailed balanced with the photoionization cross section as mentioned in Chapter 3. Although various distribution functions can take hold in this equation, the distribution function here is taken to be the Maxwellian distribution (Eq. 2.16).

As distinct as the continuum edge may be for bound-free emissions, the edge is not a pure

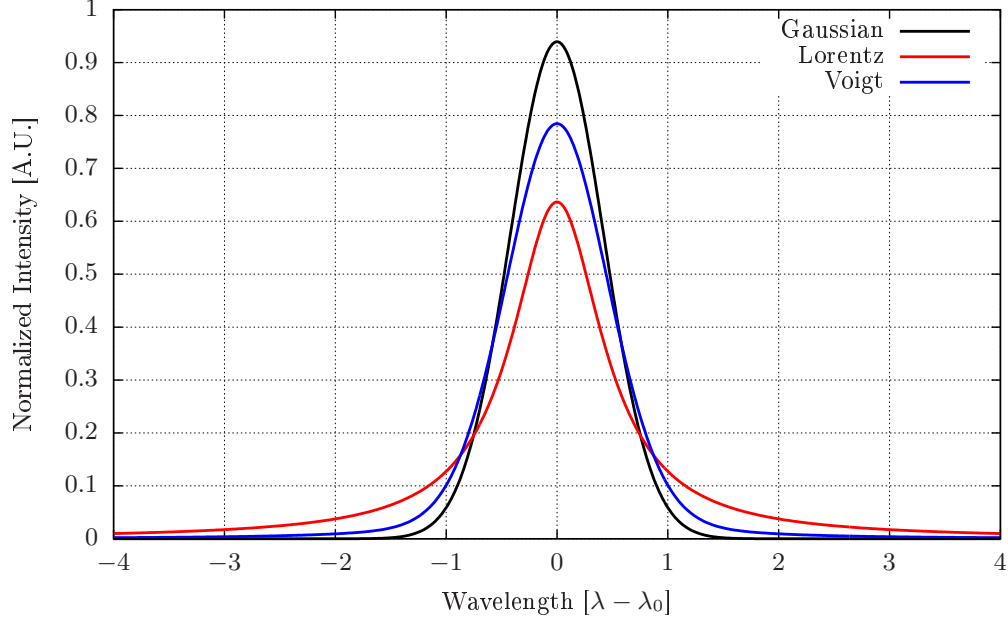


**Figure 6.1:** Sample plots of the Gaussian, Lorentz, and Voigt profiles. The Voigt profile approximation by Whiting was used in this work. [92]

discontinuity in plasma systems. Instead, the atomic-scale effects mentioned for the bound-bound emissions (Doppler, natural and Stark broadening) also apply to the continuum edge. Contrary to the bound-bound emissions where the transition is between states with the same ionization level, the transition is between two different ion stages for the continuum edge. Therefore,  $n_{upp}$  will be approximated as being one shell higher than the ionizing level,  $n_{low}$ , as a recommendation by H. Scott (Livermore Natl. Lab.). The edge modifications were then performed by convolving the “raw” continuum BF emissions with the line profiles derived from the broadening mechanisms. Again, this is only an approximation and will be used until a more accurate method is found.

The last emission feature to be included in the spectral calculations is the free-free (FF) emission. In this work, the free-free emissions result from Bremsstrahlung, inelastic collisions between colliding electrons where energy is lost through radiation. The emission is given by the following equation.

$$j_\nu = \frac{1}{4\pi} N_e N_m h\nu \int_{h\nu}^{\infty} \frac{d\sigma}{d\omega} \left( \frac{2E}{m_e} \right)^{1/2} f_e(E) dE \quad (6.7)$$

Again, one assumes that each of the emissive electrons fall within a Maxwellian distribution. However, the differential cross section describing the probability at which these electrons collide and produce photons is required. The Kramers cross section with the Gaunt factor correction,  $G$ , which accounts for non-relativistic quantum effects, is used in the emission formula. [93]

$$\frac{d\sigma}{d\omega} = \frac{16\pi}{3\sqrt{3}} \frac{Z^2}{h\nu} \left( \frac{e^2}{4\pi\epsilon_0} \right)^3 \frac{1}{m_e^2 c^3} \left( \frac{m_e}{2\varepsilon} \right) G \quad (6.8)$$

An analytical form of the Gaunt factor which encompasses a wide range of conditions is not currently known. If one were to integrate the formula for FF emission, the process would not be analytical unless the Gaunt factor is replaced by a Maxwell-averaged value,  $\langle G \rangle$ . And so, the formula is modified to use the Maxwell-averaged Gaunt factor taken from Hutchinson, where there are two predominant regions shown below. [82]

$$\text{Low frequency Kramers } (T \ll Z^2 Ry) : \quad \langle G \rangle = \frac{\sqrt{3}}{\pi} \ln \left[ \left( \frac{2T_e}{1.78m_e} \right)^{3/2} \frac{2m_e}{1.78\nu} \frac{2\epsilon_0}{Ze^2} \right] \quad (6.9)$$

$$\text{Born } (T \gg Z^2 Ry) : \quad \langle G \rangle = \frac{\sqrt{3}}{\pi} K_0 \left( \frac{h\nu}{2T_e} \right) \exp \left( \frac{h\nu}{2T_e} \right) \quad (6.10)$$

$K_0$  is the modified Hankel function, which is now more commonly known as the modified Bessel function. [95] These functions are related to the regular Bessel functions through purely imaginary arguments. [96] The algorithms for these functions may be found in *Numerical Recipes*, which was implemented for calculation of the Gaunt factors. [97] These Gaunt factor approximations were calculated in plotted in Fig. 6.2 and compared against the exact solutions obtained numerically by Karzas. [94] Numerical calculations of the Gaunt factors would not be appropriate considering the extensive computational time needed to generate Gaunt factor values for detailed computationally-generated spectra.

## 6.2 Chlorine Spectra from the ORION laser facility

The spectral reconstruction module in the CR model was used to generate results for The 10<sup>th</sup> NLTE Code Comparison Workshop held in San Diego, California on November 28 to

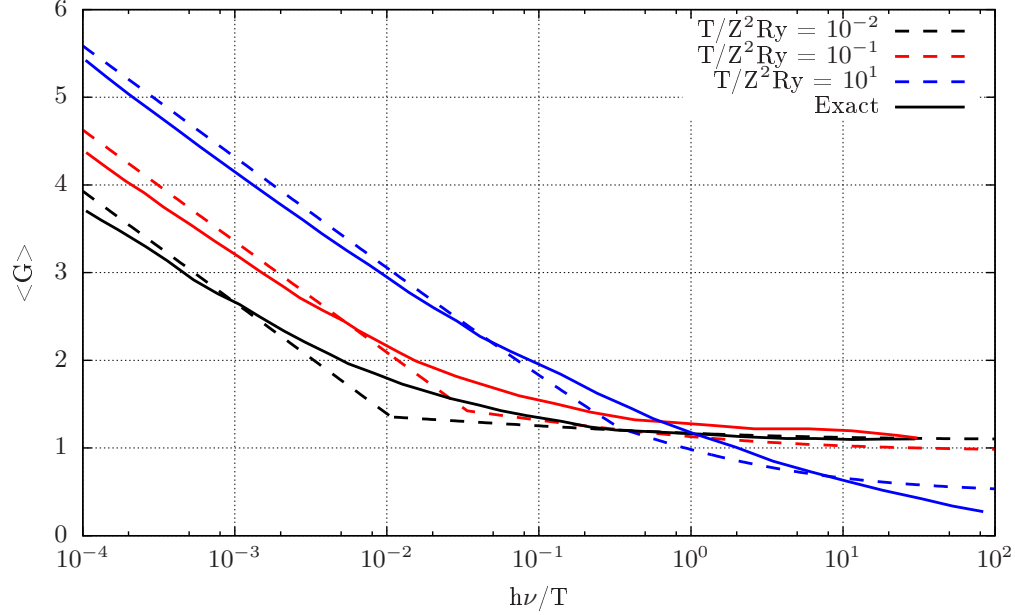


**Figure 6.2:** Approximation of Gaunt factors for Maxwellian electron distribution. Results were compared against the results of Karzas, which were calculated numerically. [94]

December 1, 2017. The aim of the workshop is not strictly to compare spectra generated from collisional-radiative models, but also to perform verification and validation of plasma conditions from experimental spectra. Amongst the list of suggested atomic plasma simulations for this workshop, the chlorine test cases were chosen for this collisional-radiative model. Before comparing with the experimental results, multiple spectral images under different plasma conditions were first generated as a “calibration” step against other computationally-generated spectra. This comparison helps verify that the spectral calculations were properly implemented in the model.

Figure 6.3 shows one of the sets of chlorine spectra generated for the workshop. The conditions used to produce the spectra involved setting the temperatures to 400 eV and the electron number density to  $10^{21} \text{ cm}^{-3}$ . The spectra shows that the most dominant spectral features stem from bound-bound and bound-free emissions; the BF emissions form the floor of the photon emissions while the BB emissions lead to the line emissions seen in the spectra. One can see from the spectra that the BB spectra has many lines in the photon energy range, some of which falls below the floor of the spectra. As such, the lines are suppressed and

hardly distinguishable from the rest of the BB emissions.

A preliminary comparison of this code's spectra in black with multiple spectra from the NLTE-10 workshop in gray can be seen in figure 6.4. Immediately, one can see that there are some differences between this code's spectra against the rest. The first feature which was previously highlighted in the discussion of the collisional-radiative model is the lack of lines, or bound-bound radiative transitions. This can be mended by increasing the size of the atomic data and the respective transitions. The second is the variability of the edges at higher photon energies: some of the bound-free edges instantiate at different values, with other continua plateauing within an order of magnitude of one another. Since the bound-free continua are dependent on the radiative recombination cross sections, the source of this variation can come from the atomic codes' methodologies in solving the atomic structure and the transition properties. It should also be noted that without the presence of sufficient data, along with autoionization and dielectronic recombination, the quality of the edges produced by this code may alter under additional modifications. Despite such hindrances, the code was able to produce the important spectral features which are highly comparable to data produced by other CR models.

Chlorine spectra were generated for several temperatures and electron densities, using all possible combinations between 400, 500, 600 eV and  $10^{21} \text{ cm}^{-3}$ ,  $10^{22} \text{ cm}^{-3}$ ,  $10^{23} \text{ cm}^{-3}$ . Spectra for all electron densities at 400, 500, and 600 eV can be seen in figures 6.5, 6.6, and 6.7, respectively. In the 400 eV plot, one can see that the lines broaden into the spectrum floor as the density increases. As the temperature is increased, the lines become much stronger at higher densities despite the corresponding increase in broadening widths. The edge broadening effect can also be observed as one increases the density in each scenario. A zoomed view of the edge broadening effect on the spectral reconstruction can be seen in figure 6.8.

The edge broadening effect for the 600 eV and  $10^{23} \text{ cm}^{-3}$  electron density conditions is shown in figure 6.8. Two scenarios where edge broadening was active and inactive was plotted for this figure. There are multiple edges spanning the entire photon energy range as seen in the spectra. However, without knowledge of the raw spectra in which no edge broadening

was applied, it becomes more difficult to discern the locations of all the edges. There are two phenomenological instances where the edges becomes indistinguishable. First, over the span from 3600 to 3640 eV, the contribution from multiple broadened edges hides 3 apparent edges. Secondly, the prominent broadened edge at approximately 3555 eV suppresses the smaller edges in its proximity.

After assessing the broadband chlorine spectra, an attempt to replicate experimental spectra from the ORION laser facility followed. The experimental spectra from the ORION laser was generated to test the capabilities of OHREX, an acronym for Orion high-resolution X-ray spectrometer. One of the measurements made from the experiment is focused on the  $\beta$  emission ( $n = 3 \rightarrow n = 1$ ) of chlorine. More specifically, long-pulse irradiation with a duration of 2 ns and 315 J of energy was incident upon a foil of parylene dichlorine, from which the chlorine spectra can be observed. Further details regarding the experiment and the spectrometers are found in the following references. [98,99]

Before attempting to recreate the Cl spectra, the experimental spectra shown in figures 6.9 to 6.12 will be discussed to highlight the key features to be computationally pursued. The first aspect to highlight begins with the set of BB lines seen in the experimental spectra: the lines seen in the spectra involve transitions in the Li-like and He-like ions of Cl, or Cl+14 and Cl+15, respectively. For Cl+15, there are two lines that lie between 3260 and 3280 eV; these lines correspond to the He- $\beta$  ( $n = 3 \rightarrow n = 1$ ) emissions. The higher energy resonance line is an emission from a singlet state ( $3p^1(^2P)^1P_{1.0}$ ), while the lower energy intercombination line is an emission from the triplet state ( $3p^1(^2P)^3P_{1.0}$ ). The resonance line refers to a  $\Delta S = 0$ , while the intercombination line results from a  $\Delta S = 1$  transition. The distinct Stark broadening effect on the lines and the resulting “shoulder” structure of the intercombination line make these lines highly sought-after in the reconstruction.

In the set of Cl+14 lines, there are multiple, observable BB transitions, but none as prominent as the set of He- $\beta$  lines. The most readily observable set of Cl+14 transitions come are the  $1s2p3p \rightarrow 1s^22p$  and  $1s2s3p \rightarrow 1s^22s$  emissions. While an attempt will be made to reproduce the spectra across the entire spectral range, one should note that the Cl+14 lines are highly sensitive to dielectronic recombination events as shown in Beiersdorfer et

al’s investigation. DR processes, more specifically, leads to a higher population density of Cl+14 excited states, leading to higher intensity emissions. Therefore, because of the lack of autoionization (AI) and inverse DR rates in this model, the fit produced in this work will likely lead to an overestimation in electron density with an increased uncertainty in the temperature.

Several iterations were then conducted before achieving a best fit of the Cl spectra from OHREX. Since one can acknowledge that the Cl+14 lines residing between 3200 and 3220 eV will not achieve a perfect fit to the experiment, the focus was redirected towards capturing the Cl+15 lines, along with the  $1s2s3p \rightarrow 1s^22s$  transition at  $\sim 3230$  eV. Using the Cl+15 resonance and intercombination lines, the electron density was first matched since the Stark broadening width is highly sensitive to the electron density ( $\sim N_e^{0.58}$ ). While a value of  $3.0 \times 10^{21} \text{ cm}^{-3}$  was deemed to be the best fit to the Stark-broadened lines as shown in figure 6.9, the imperfect fit along the high energy wing of the He- $\beta$  profile is a likely indicator of the overestimated electron density due to a lack of DR processes. Without Stark broadening, the best fit to the lines requires an order-of-magnitude increase in the electron density at the cost of losing the “shoulder” structure in the He- $\beta$  lines as seen in figure 6.10. In the case of the electron and atomic temperatures, a temperature of 450 eV was found to reasonably capture the spectral characteristics of the experiment. Reconstructed spectra for 400 and 500 eV are shown in figures 6.11 and 6.12. At 400 eV, the lines associated with the Cl+14 lines begin to increase in strength, suggesting an increase in the Cl+14 excited state densities. However, at 500 eV, the increased temperature results in slightly depleted line strengths, especially in the  $1s2s3p \rightarrow 1s^22s$  transition. Both observations led to the 450 eV compromise shown in the first figure. The reader is encouraged to view results from other CR models, where all of the spectra generated in the calibration step as well as the best fit from this model were compiled and submitted for the NLTE-10 Code Comparison workshop.

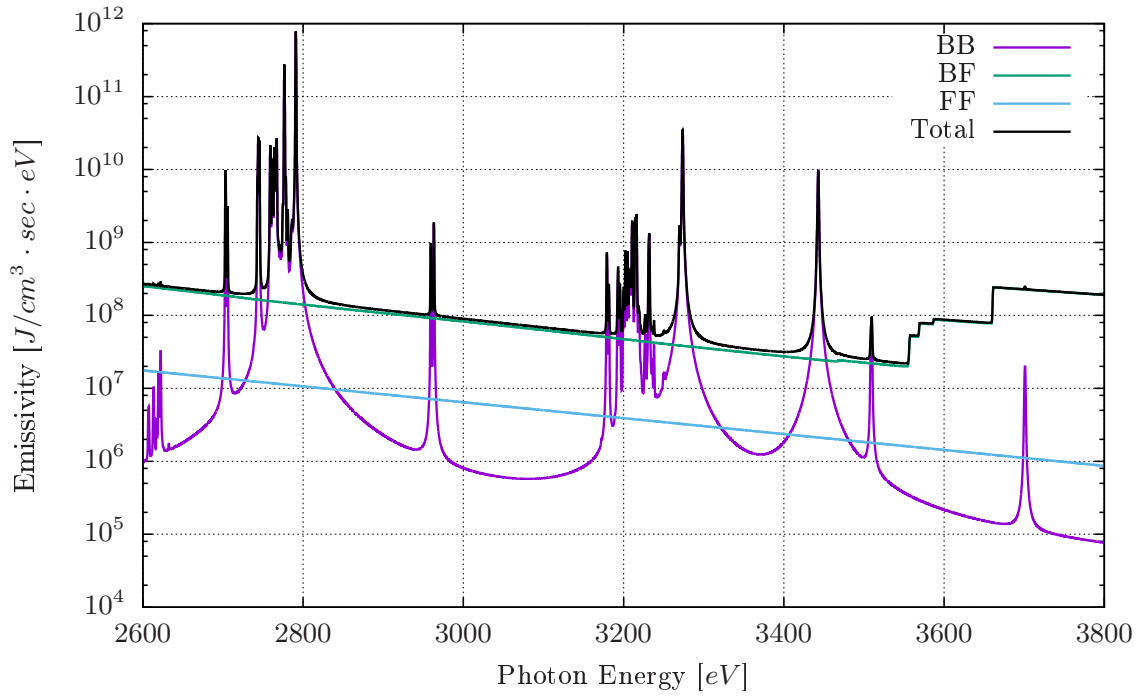


**Figure 6.3:** Contributions of bound-bound (BB), bound-free (BF), and free-free (FF) emissions to the total reconstructed spectra generated for the NLTE-10 Code Comparison Workshop. Spectra were generated at conditions of  $T_e = T_h = 400$  eV and  $N_e = 1.0 \times 10^{21}$  cm<sup>-3</sup>.

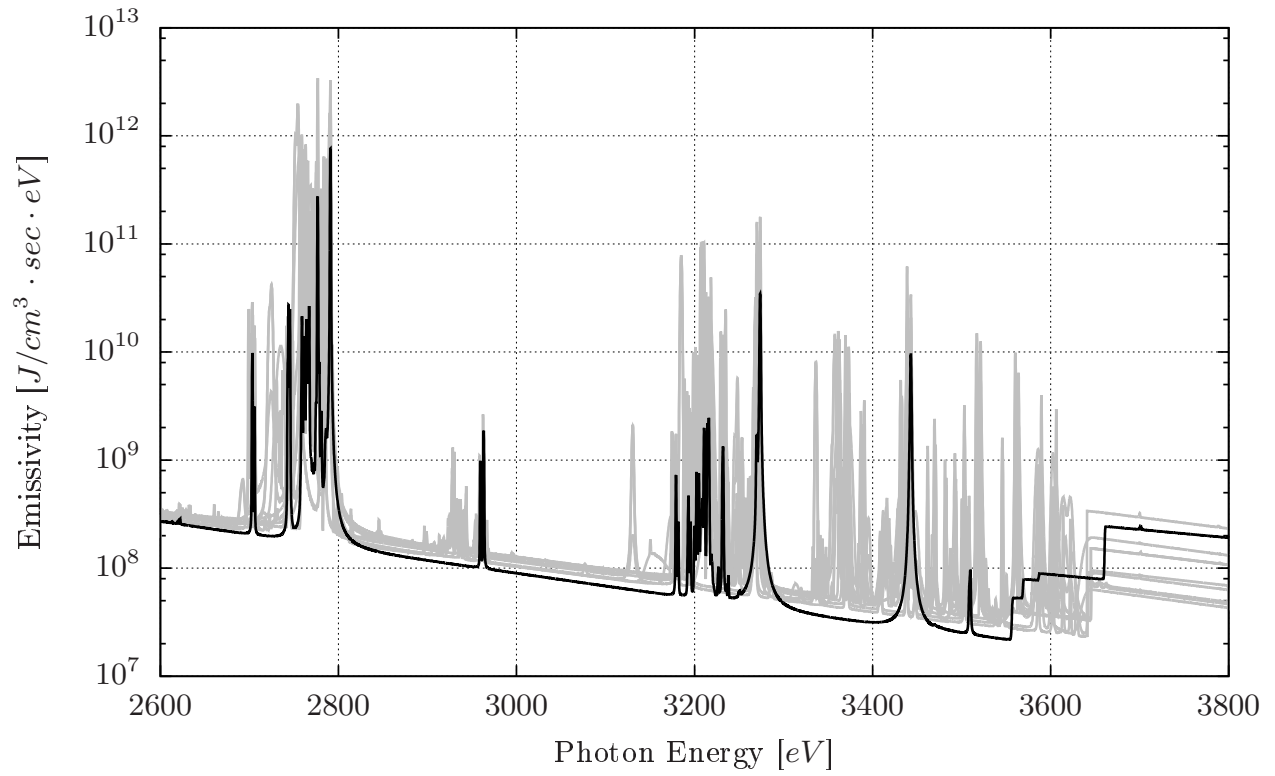


**Figure 6.4:** Comparison of Cl spectra at 400 eV and  $10^{21} \text{ cm}^{-3}$  (present code, black) against other generated spectra (gray) for the NLTE-10 workshop.

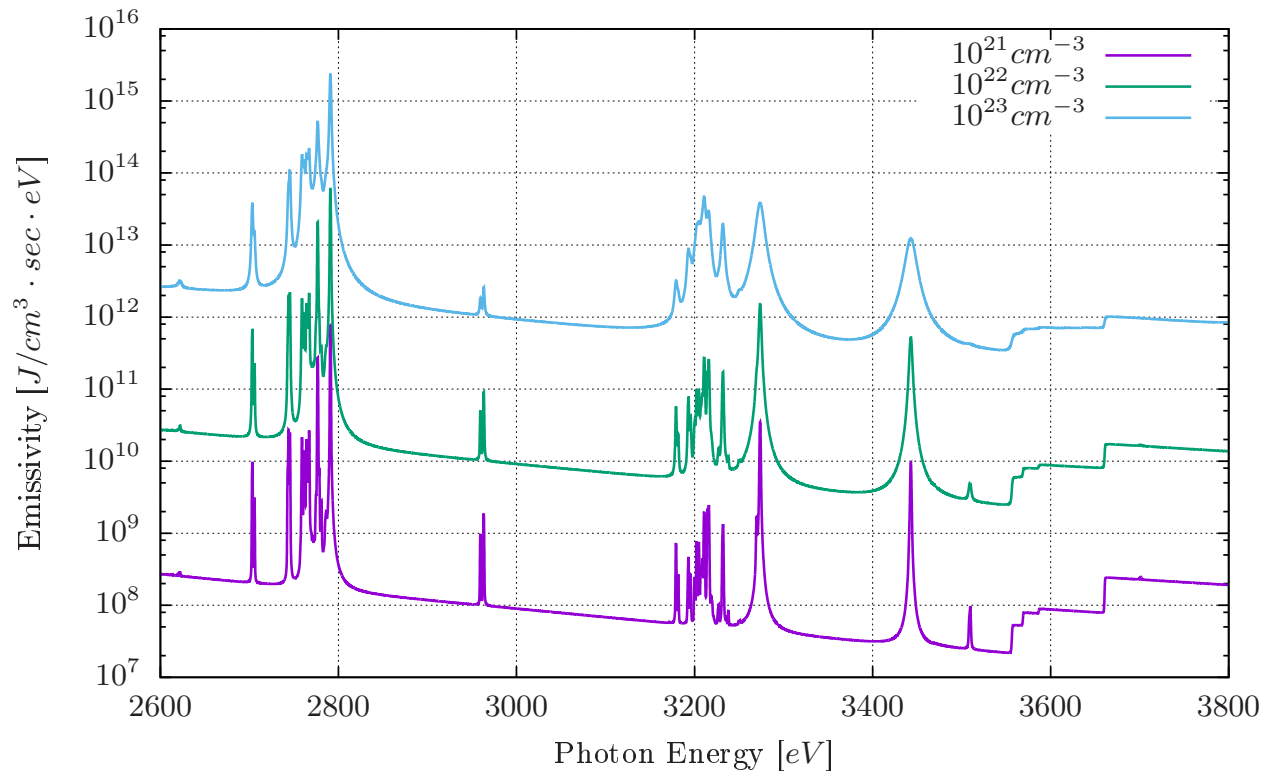


**Figure 6.5:** Generated spectra for Cl at 400 eV with  $N_e = 10^{21} \text{ cm}^{-3}$ ,  $10^{22} \text{ cm}^{-3}$ ,  $10^{23} \text{ cm}^{-3}$

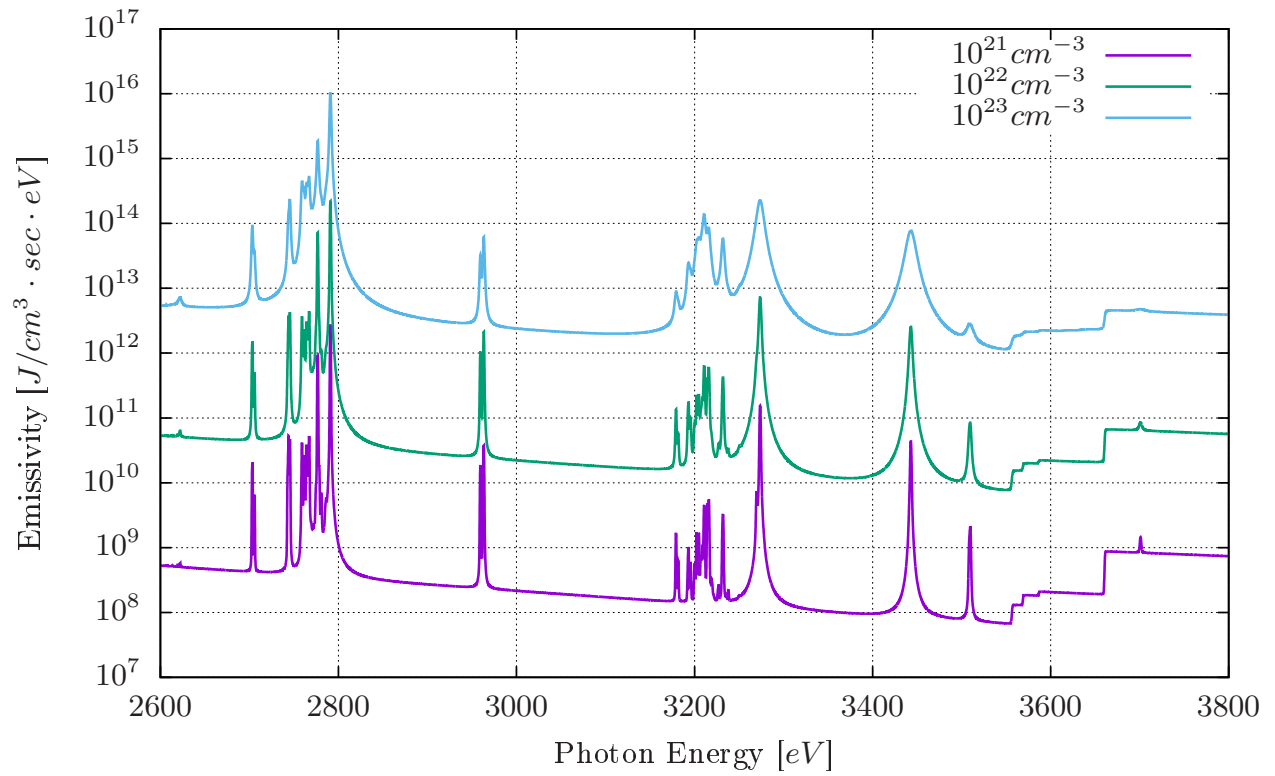


**Figure 6.6:** Generated spectra for Cl at 500 eV with  $N_e = 10^{21} cm^{-3}$ ,  $10^{22} cm^{-3}$ ,  $10^{23} cm^{-3}$

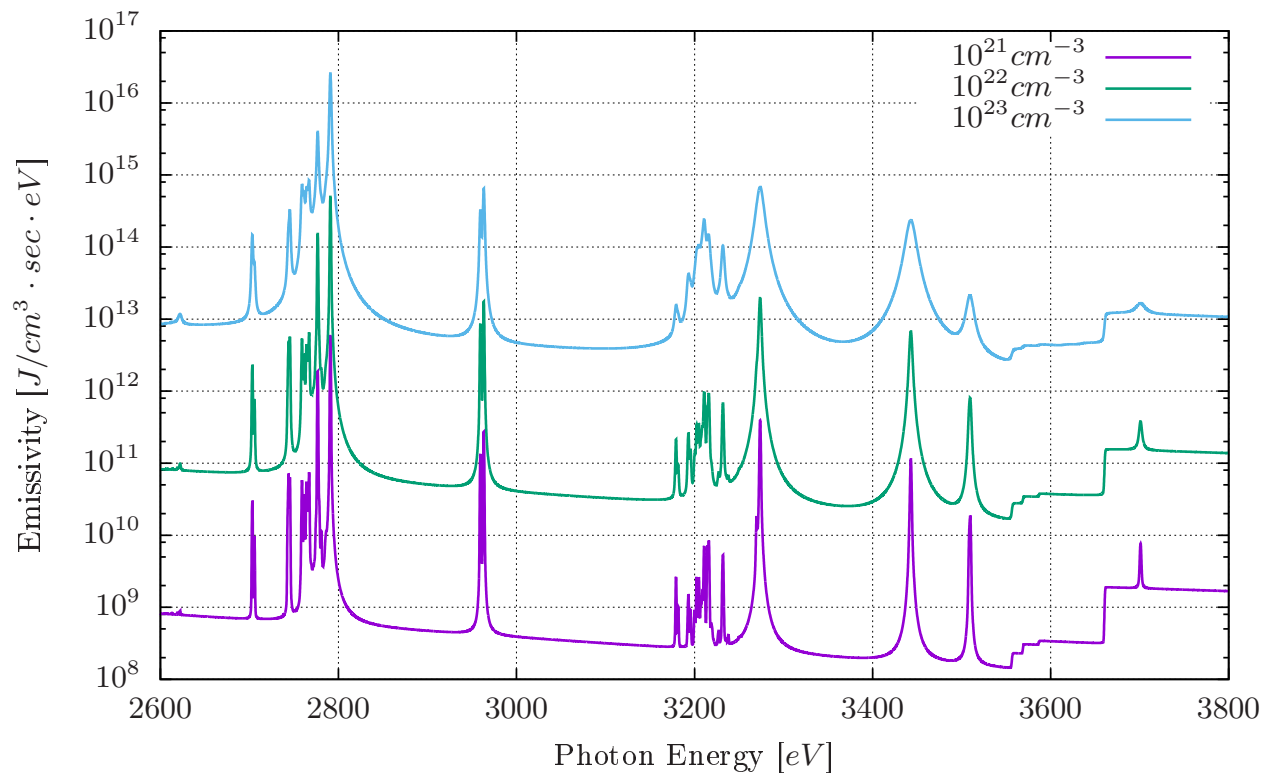


**Figure 6.7:** Generated spectra for Cl at 600 eV with  $N_e = 10^{21} \text{ cm}^{-3}$ ,  $10^{22} \text{ cm}^{-3}$ ,  $10^{23} \text{ cm}^{-3}$

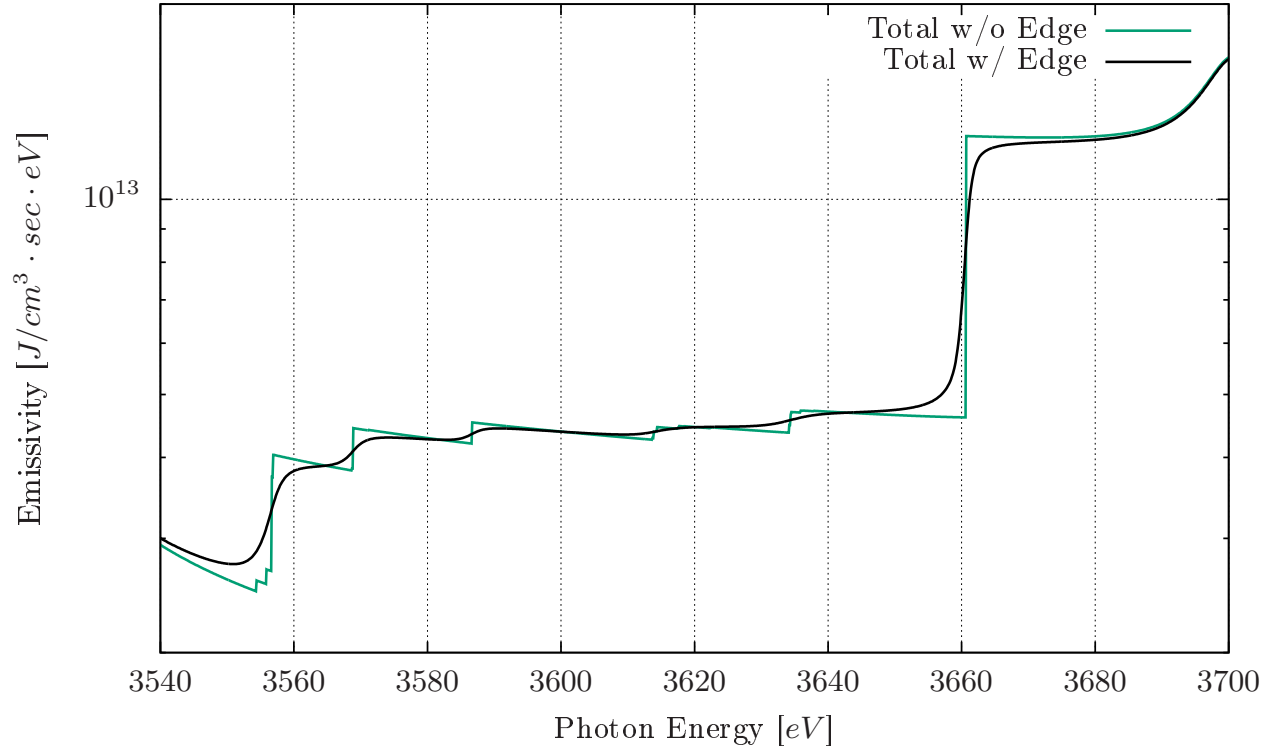


**Figure 6.8:** Effect of edge broadening on the Cl Spectra for conditions of 600 eV and  $N_e = 10^{23} \text{ cm}^{-3}$ . The introduction of edge broadening makes the bound-free transitions indistinguishable in two particular ways seen in this spectra. First, over the span of photon energies from 3600 to 3640 eV, the multiple edges are indiscernible because of the overlapping, broadened edges. Secondly, broadening at the more prominent  $\sim 3555$  eV edge hides the multiple edges present at energies below this feature.

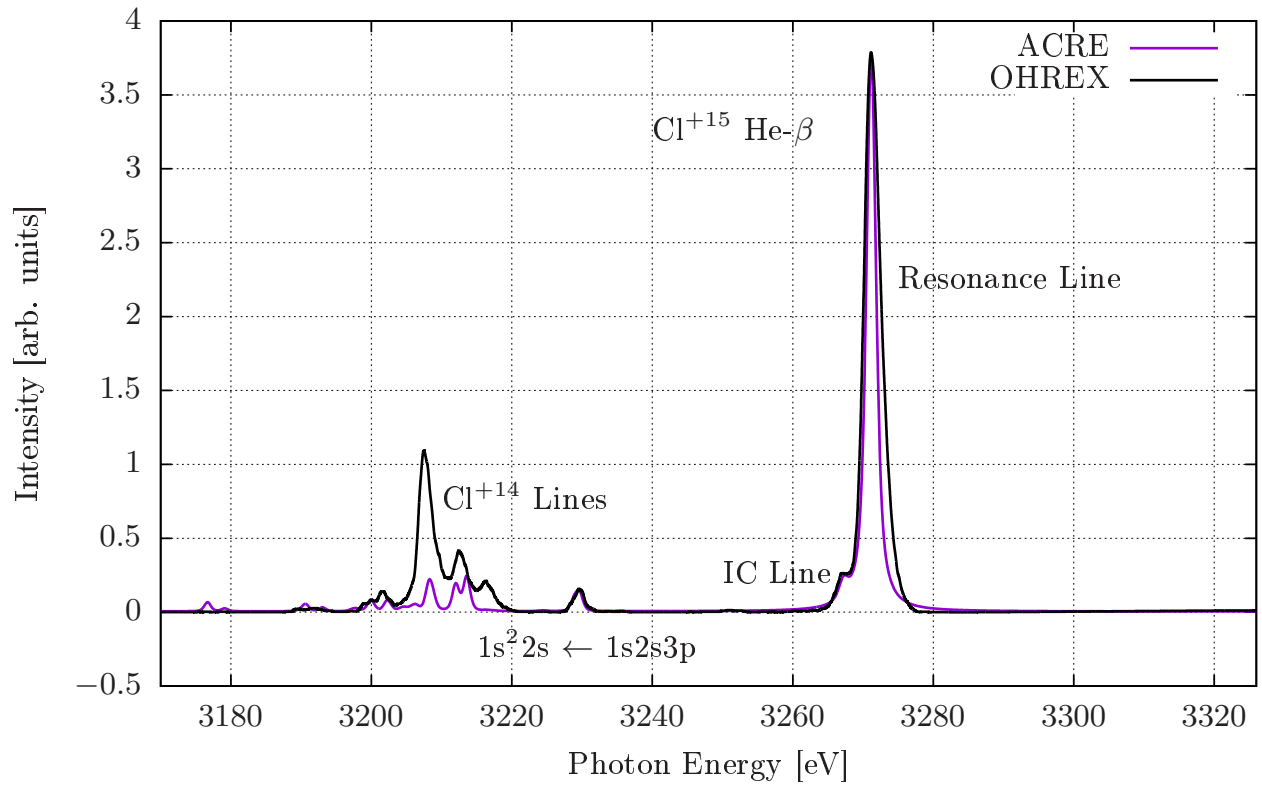


**Figure 6.9:** Numerically-generated chlorine spectra at 450 eV and  $N_e = 3.0 \times 10^{21} \text{ cm}^{-3}$  compared against OHREX data. (Submitted Spectra)

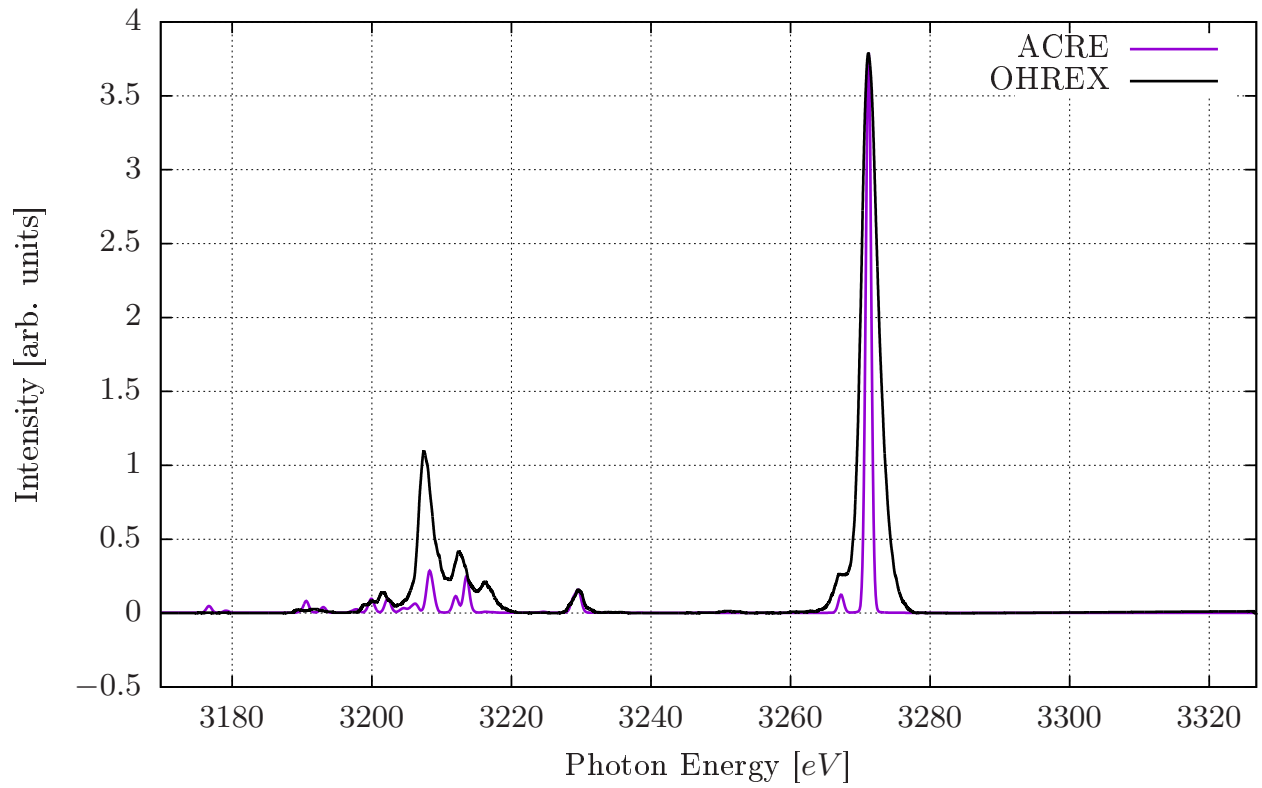


**Figure 6.10:** Numerically-generated chlorine spectra without Stark broadening at 450 eV and  $N_e = 2.8 \times 10^{22} \text{ cm}^{-3}$  compared against OHREX data. An increase in electron density was necessary to equate the lines at  $\sim 3230 \text{ eV}$ .

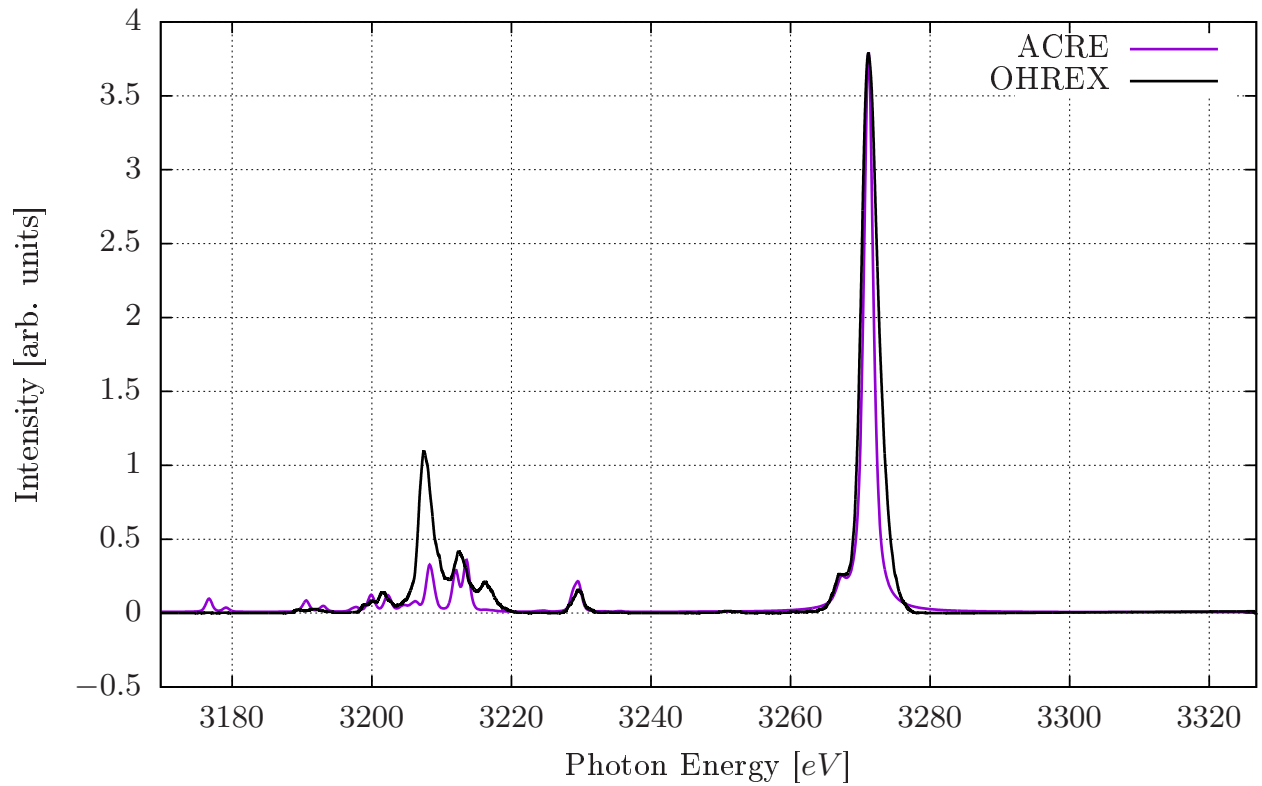


**Figure 6.11:** Numerically-generated chlorine spectra at 400 eV and  $N_e = 3.0 \times 10^{21} \text{ cm}^{-3}$  compared against OHREX data. Lowering the electron temperature increases the line strengths in the Cl+14 ions.

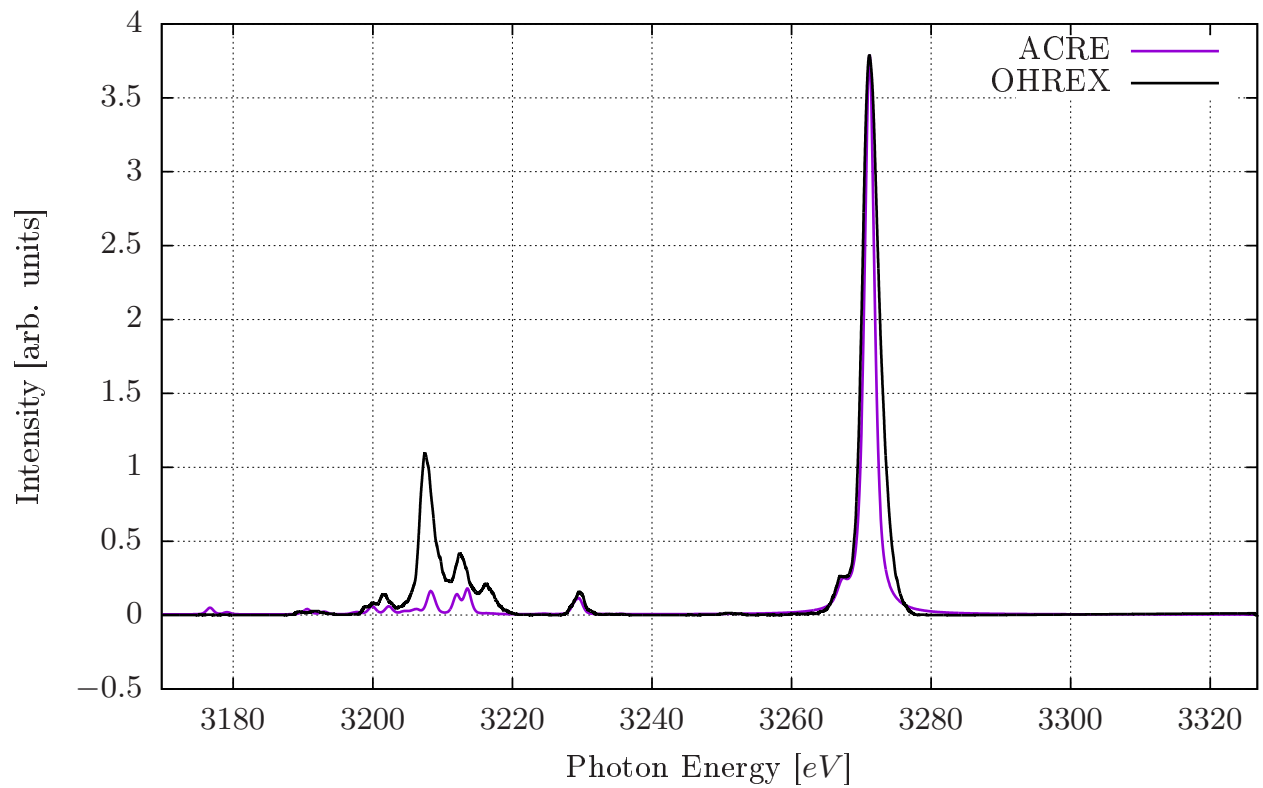


**Figure 6.12:** Numerically-generated chlorine spectra at 500 eV and  $N_e = 3.0 \times 10^{21} \text{ cm}^{-3}$  compared against OHREX data. Increasing the electron temperature decreases the line strengths in the Cl+14 ions, making reproduction of the spectral peaks more difficult.

## 6.3 Inductively-coupled Argon Spectra from the Bell Jar Device

The spectra shown in this section will be from an inductively-coupled plasma generated from the Bell Jar at the Air Force Research Laboratory. The Bell Jar is a simple device that is used to test other components or instruments under vacuum conditions. Besides this functionality, adjacent to the Bell Jar is a port that has been modified into an inductively-coupled system that can be used to generate a plasma. This setup provides an experimental means to assess the validity of the previously-used argon atomic data for low- $Z$  plasmas. In addition, this experiment will also be a gateway to spectroscopically analyze low- $Z$  plasmas generated from other systems, such as propulsion devices. Therefore, the goal in this section will be to perform spectral line identification of the inductively-coupled plasma and determine some of the shortcomings of using the atomic data for low- $Z$  applications.

### 6.3.1 Experimental Setup

The Bell Jar device used to study instrument operation in vacuum conditions is capable of producing plasmas using inductive coupling. This device's dual functionality may be elaborated upon through the schematic shown in Fig. 6.13. The Bell Jar is capable of dropping to sub-mTorr vacuum conditions through a sequence of steps involving the use of the roughing pump and turbo pump. The roughing pump is typically used for initial ventilation of the chamber gas, while the turbo pump is used to drive the bell-shaped chamber further towards vacuum conditions.

Once the chamber attains sufficient or desirable vacuum conditions, during which the pumps are allowed to remain in operation, argon gas may then flow into the vacuum chamber by adjusting the flow meter. The flow meter setting correlates to the flow rate of the argon gas which eventually reaches a tube wound by a coil with alternating currents. The supplied AC-based power to the coil is controlled by a Parallax Serial Terminal, which is a microprocessor that controls the current, voltage, and frequency of the current. The generation of an ICP relies strongly on these coil parameters. Due to the alternating current from the induction coil, electromagnetic fields are generated as a consequence of Faraday's

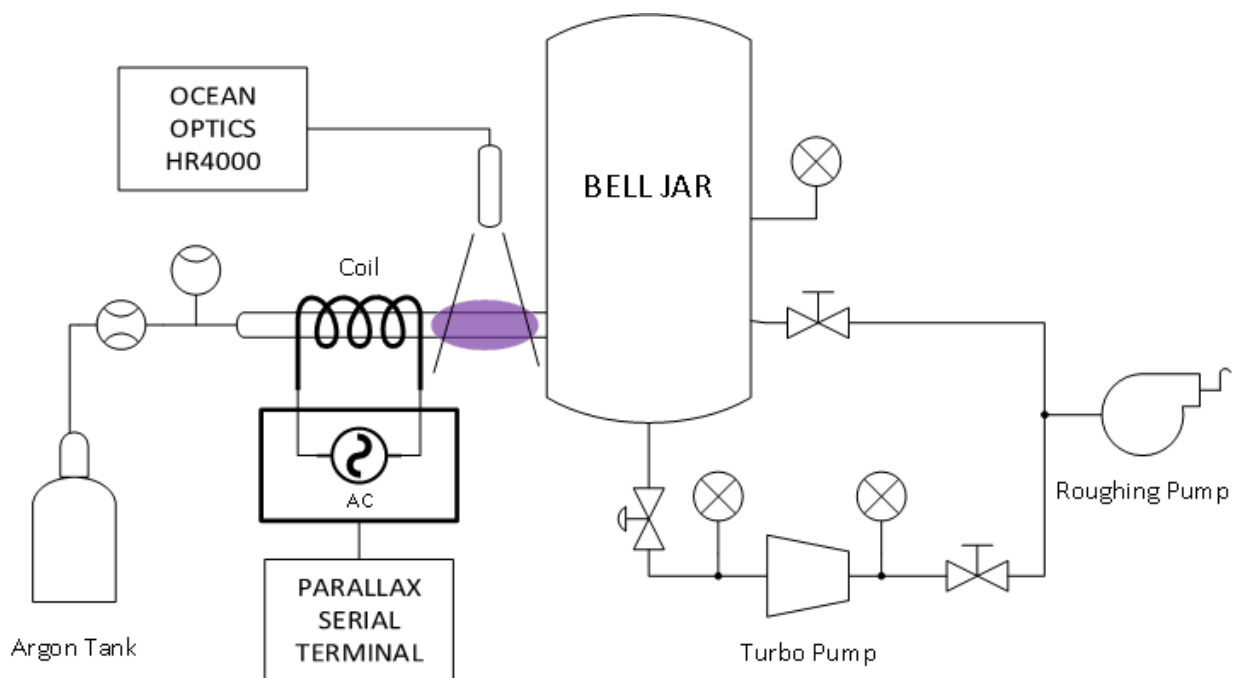


**Figure 6.13:** Schematic of the Bell Jar device used for instrumental validation and generation of inductively-coupled plasmas (ICP).

Law and Lenz's Law. These electromagnetic fields interact with the electrons and ions in the system which ultimately lead to the gaseous breakdown and increased ionization. Two pictures of the inductively-coupled plasma are shown in Figs. 6.14 and 6.15.

The ICP shown in Fig. 6.14 develops partway through the coil. This feature can also be observed in ICP torches where the plasma develops downstream of the coil's first ring. [100] This is easily explained by the argon gas blowing into the ICP tube. However, one can also see the striations in the plasma caused by low intensity emissions. If one looks downstream of the induction coil close to the chamber, the plasma has neither formed a distinct plume in ICP torches nor has the plasma relaxed to more neutral and cooler conditions as seen in Fig. 6.15. Instead, the plasma remains persistent. This can be explained if one considers that the Bell Jar's base and port material are from aluminum, which allows for the coupling of electromagnetic forces between the port and the induction coil through Lenz's law. This causes the argon plasma to reheat, repopulate the excited states, and possibly reionize, thereby increasing the emission intensities downstream of the induction coil.

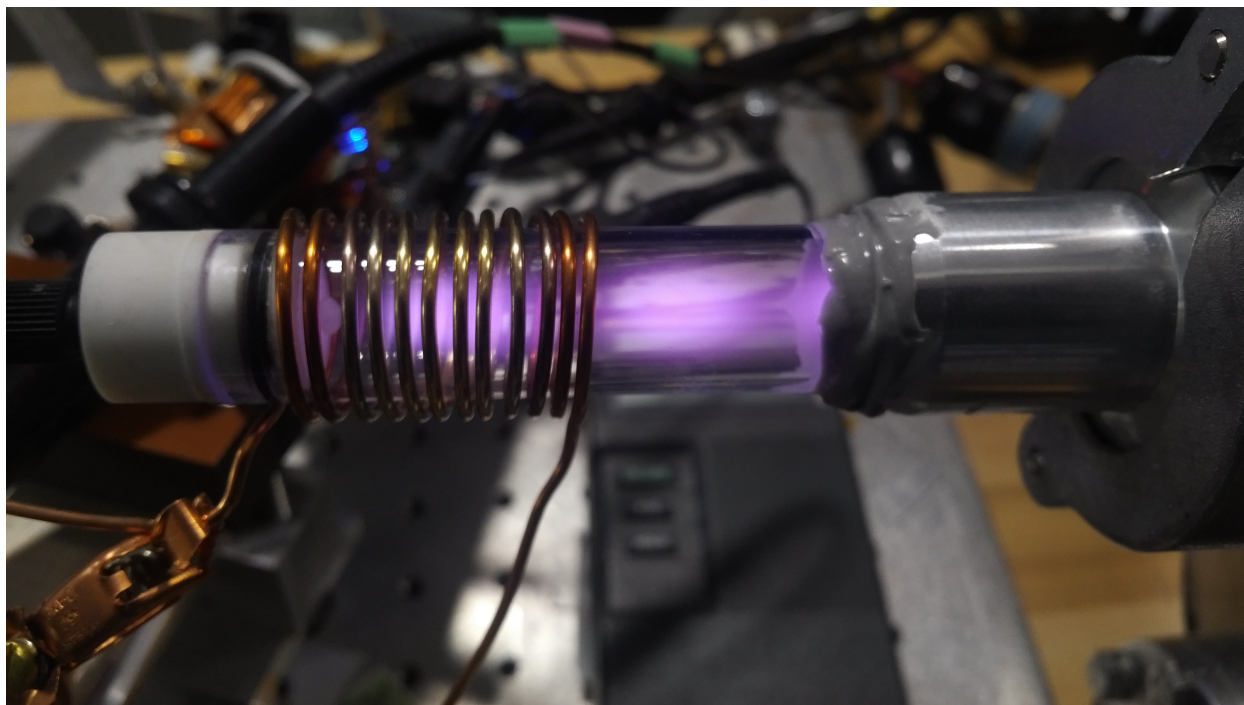


**Figure 6.14:** Inductively-coupled plasma generated using the Bell Jar’s induction coil. Some features may be observed including the generation of the plasma partway through the coil and the striations caused by low intensity emissions.

For the spectra obtained in this work, the experiment’s parameters were set to operate at steady-state conditions. Parameters were chosen to prevent overheating of the coil while providing reliable plasma emission intensities. The target AC frequency in this work is set to 8.470 MHz. The nominal voltage and current readings were approximately 28 V and 0.5 A through the coil. Although strong enough to sustain the plasma, an initial spark was still provided to instantiate the plasma’s formation. The emitting plasma was then spectroscopically monitored using the Ocean Optics HR4000, which records over a wavelength range from 195 to 1125 nm. A few spectral images of the inductively-coupled plasma downstream of the induction coil follow.

### 6.3.2 Spectral Comparisons and Analysis

The spectra shown in this section involves a representative set of images from an experimental sweep in gas pressure. Two spectral images under different pressure conditions of 50 mTorr

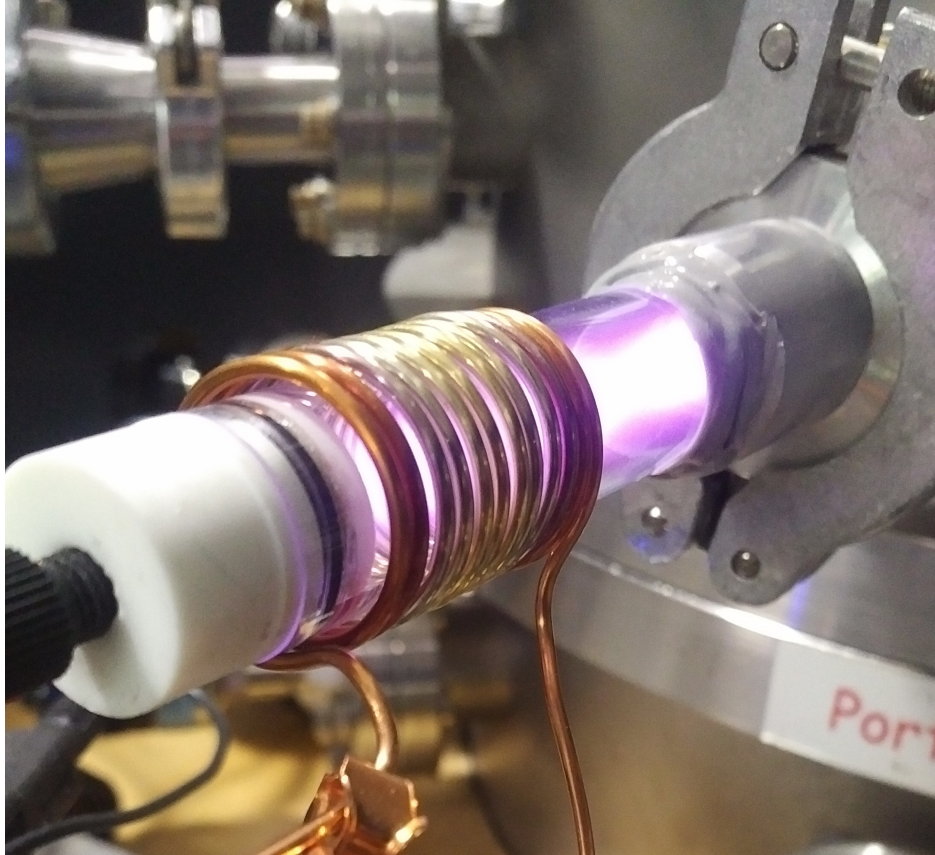


**Figure 6.15:** More plasma emission can be observed further downstream of the induction coil. This plasma formation may be due to the coupling between the induction coil and the Bell Jar's port, which would explain the striations seen in the Fig. 6.14.

and 75 mTorr will be analyzed. Figs. 6.16 and 6.17 show the spectra obtained for the two pressure conditions. The spectral range in the figures are restricted between 650 nm to 950 nm as it contains most of the relevant lines for these plasma conditions. These lines were observed to primarily be neutral Ar lines which will be discussed later. An additional comparison was performed with NIST data as a cross-validation set for the experiment and CR model. [101]

The NIST spectra in Fig. 6.16 were generated with conditions of  $T_e = 0.80$  eV and  $N_e = 1 \cdot 10^{13}$  cm<sup>3</sup>. For larger  $T_e$ , Ar+1 lines were much more apparent in the NIST lines, while for lower  $T_e$ , the line strengths became much more dominant for larger wavelengths. Therefore, the choice in 0.80 eV as the electron temperature was appropriate to match the experimental spectra. Assuming that the argon gas is at standard temperature ( $\sim 300$  K),

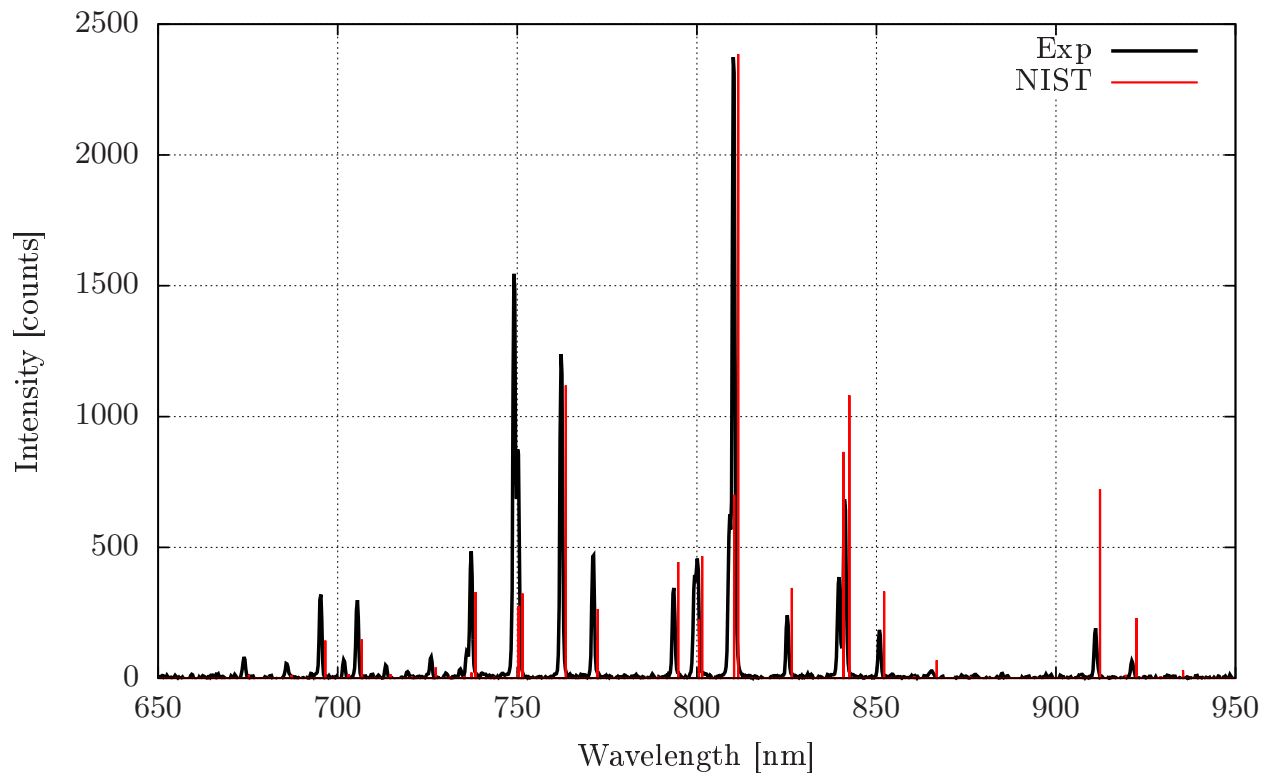


**Figure 6.16:** Experimental spectra obtained from the Bell Jar's inductively-coupled argon plasma. Gas pressure for this spectra was set to 75 mTorr. NIST spectra obtained for 0.80 eV and  $1 \cdot 10^{13} \text{ cm}^3$  is superimposed for reference.

the density of the atomic species based on the pressure gauge readings is roughly  $2 \cdot 10^{15}$   $\text{cm}^3$ . Since the gas is weakly ionized, an electron density below this value may be assumed; however, an electron density value below  $2 \cdot 10^{15}$   $\text{cm}^3$  does not vary considerably in the NIST-generated spectra, leading to an assumption of 1% ionization fraction at best. One should also bear in mind that the spectra generated from NIST assumes Saha-LTE, meaning that the atomic state densities used to generate the plasma are under Saha and Boltzmann equilibria assumptions between ionic and excited states, respectively. This means that any NLTE phenomenon, such as non-Maxwellian electron distributions which are pervasive in ICPs, are not captured. [100]

The non-Maxwellian characteristic of the electrons can be observed on the 75 mTorr spectra. The heightened intensities of lines with wavelength smaller than 800 nm suggests that the higher energy portion of the electron distribution is being utilized to drive the transitions with larger energy gaps which contrasts with the intensities of lines beyond 800 nm. It should also be noted that at low temperatures, the high energy portion or tail of the electron distribution would be the main catalyst in populating atomic states, leading to these high intensity values at lower wavelengths. At a lower atomic density shown in Fig. 6.17, the lower wavelengths (<775 nm) are driven to even larger intensities relative to the lines at higher wavelengths. This implies that the relative contribution of the tail from the electron distribution makes for a more depleted tail. This analysis may mean that the ideal lines to compare between the experiment and NIST spectra should be at a higher wavelength; the line intensities between 780 nm and 860 nm would be lowered which is consistent with the observation of tail depletions. This simple progression in pressure exemplifies the importance of electron energy distributions in non-Maxwellian systems. Further studies involving the impact of non-Maxwellian electron energy distributions would be necessary to examine the coupling of the electrons to the collisional-radiative set of kinetics.

Next, an attempt to generate similar spectra using the CR model for 0.8 eV and  $1 \cdot 10^{13}$   $\text{cm}^3$  was performed. The spectra obtained from the CR model was compared with the NIST data, the results of which are shown in Fig. 6.18. The NIST spectra were scaled to match with the largest peak of the CR model. At first glance, one can immediately see

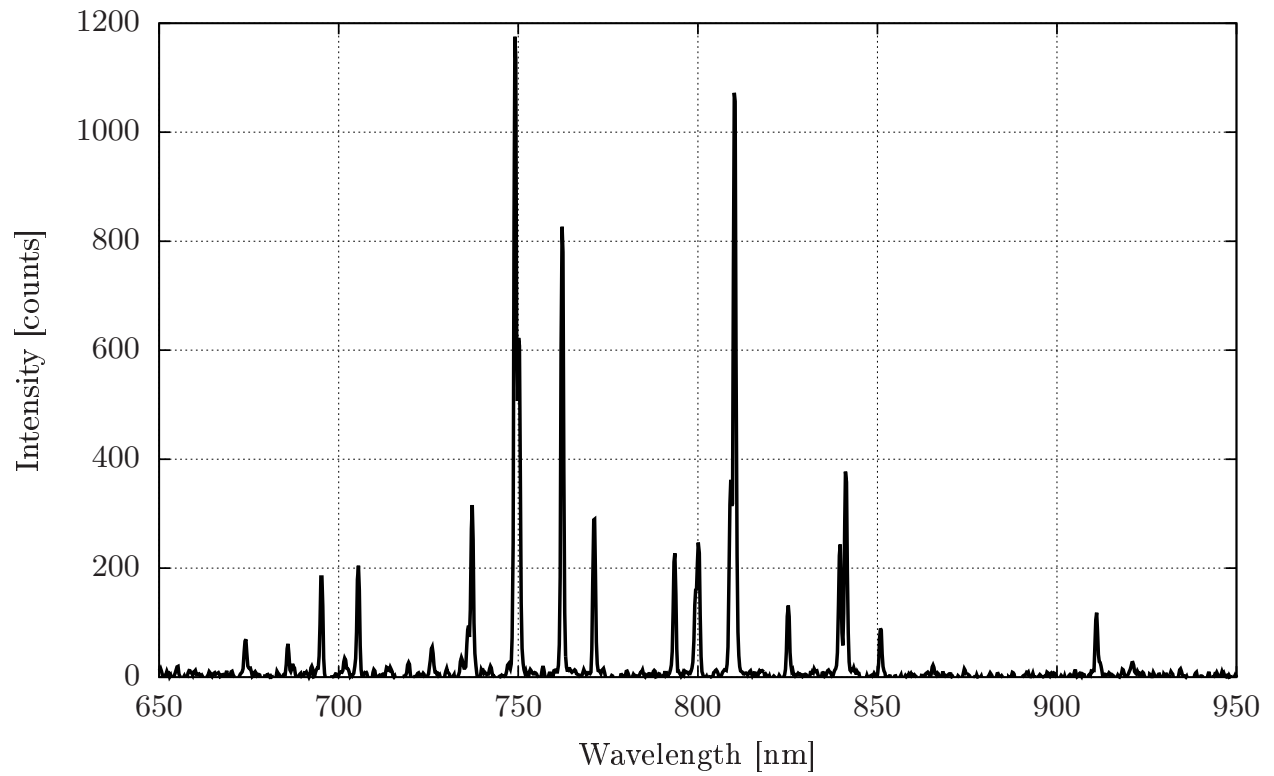


**Figure 6.17:** Experimental spectra obtained from the Bell Jar's inductively-coupled argon plasma. Gas pressure for this spectra was set to 50 mTorr.

that the line separations are large in comparison to the experimental data. The collisional-radiative model has 4 particular lines indicated on the spectra that are separated by several nanometers. Several of these lines thought to match the most prominent lines in the NIST data also do not match. Also, the  $2 \leftarrow 12$  transition is almost nonexistent in intensity on the NIST spectra. Altogether, the number of distinguishable lines from the CR model is fewer compared to the number of distinct NIST lines. These inaccuracies have several causes which can explain the CR model's inability to match the line positions and intensities of the NIST and experimental spectra.

Before proceeding to explain the sources of error in the spectral mismatch, it should be noted that the error observed in the spectra is not necessarily specific to the atomic database used in this model. Many atomic codes used in the collisional-radiative modeling field are used for fusion studies, where the nominal operation of these studied devices rely on high-Z atomic species. That being said, the LANL data used in this study is not an isolated feature. Instead, the data shown here is representative of the results one might obtain should such atomic codes be utilized for low-Z applications. [29,35–38] The NIST data shown in this work is not susceptible to such errors because the atomic data used to generate the results involved rates and cross sections which have been empirically determined for many years. Users of atomic codes or data should therefore exercise careful scrutiny when exploring atomic codes for their applications of interest.

One source of error in these atomic models begins with the calculated energy levels. In Table 6.1, information regarding the first 15 levels of Ar+0 from NIST and LANL are shown. Between the LANL and NIST energy levels, errors by as much as approximately 2% can be observed. The reason for this error is caused by the atomic structure calculations. The atomic structure calculations require an effective central potential which interacts with the surrounding electron clouds that are expressed by wavefunctions in their radial orbitals. For near-neutral atoms, the potential from the nucleus is effectively counterbalanced by a neutralizing number of electrons. This makes the calculations highly sensitive in this regard and explains why the chlorine spectra shown for much higher temperatures is more accurate. In high-Z situations, the forces between the electrons and nucleus becomes increasingly

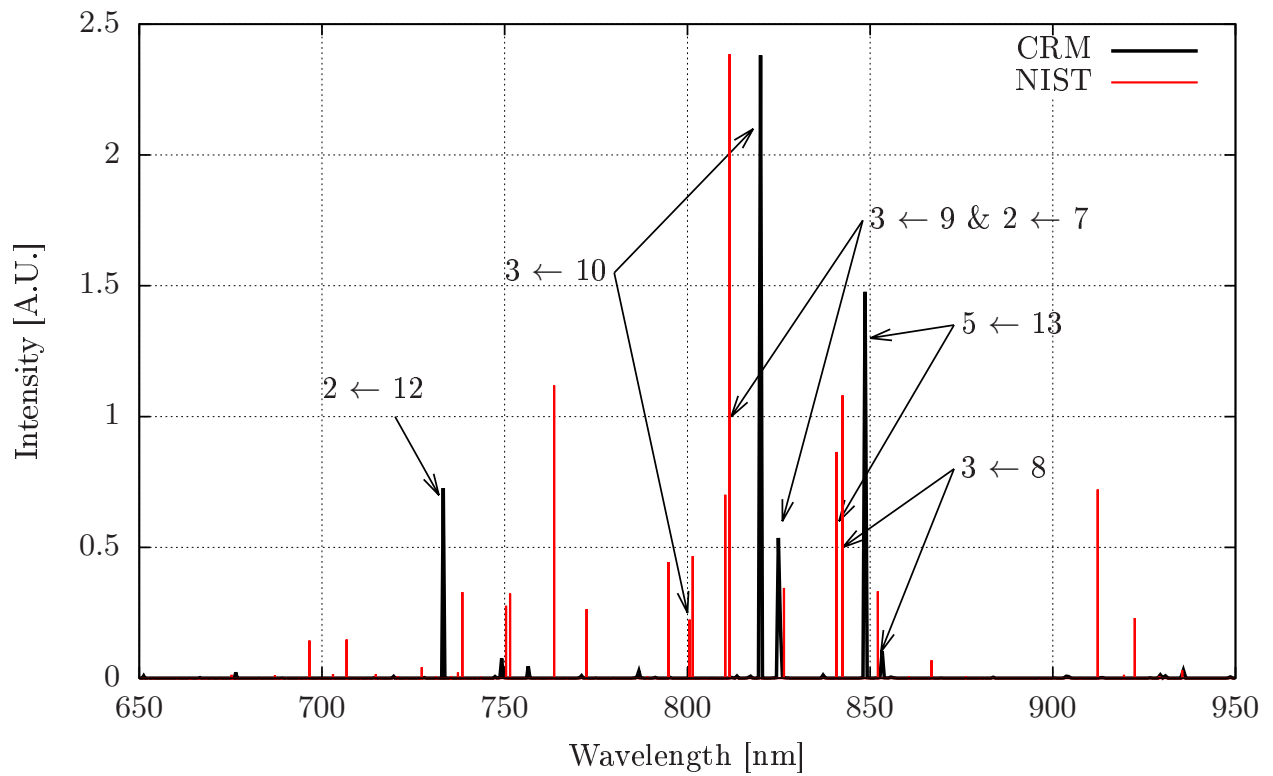


**Figure 6.18:** Experimental spectra obtained from the Bell Jar's inductively-coupled argon plasma. Gas pressure for this spectra was set to 75 mTorr. CR spectra obtained for 0.80 eV and  $1 \cdot 10^{13} \text{ cm}^3$  is superimposed for reference.

dominated by the nucleus, causing these electromagnetic interactions to overcome sensitive effects such as LS-coupling.

n	$nl(^{2S+1}L_J)$	E(n) [eV] (LANL)	E(n) (NIST)	Rel. Error
1	[Mg]3p <sup>6</sup>	0.0	0.0	N/A
2	3p <sup>5</sup> ( <sup>2</sup> P) <sup>2</sup> P 4s <sup>1</sup> ( <sup>2</sup> S) <sup>3</sup> P <sub>2.0</sub>	11.740	11.548	1.66%
3	3p <sup>5</sup> ( <sup>2</sup> P) <sup>2</sup> P 4s <sup>1</sup> ( <sup>2</sup> S) <sup>3</sup> P <sub>1.0</sub>	11.805	11.624	1.56%
4	3p <sup>5</sup> ( <sup>2</sup> P) <sup>2</sup> P 4s <sup>1</sup> ( <sup>2</sup> S) <sup>3</sup> P <sub>0.0</sub>	11.905	11.723	1.55%
5	3p <sup>5</sup> ( <sup>2</sup> P) <sup>2</sup> P 4s <sup>1</sup> ( <sup>2</sup> S) <sup>1</sup> P <sub>1.0</sub>	11.983	11.828	1.31%
6	3p <sup>5</sup> ( <sup>2</sup> P) <sup>2</sup> P 4p <sup>1</sup> ( <sup>2</sup> P) <sup>3</sup> S <sub>1.0</sub>	13.112	12.907	1.59%
7	3p <sup>5</sup> ( <sup>2</sup> P) <sup>2</sup> P 4p <sup>1</sup> ( <sup>2</sup> P) <sup>3</sup> D <sub>3.0</sub>	13.242	13.273	0.23%
8	3p <sup>5</sup> ( <sup>2</sup> P) <sup>2</sup> P 4p <sup>1</sup> ( <sup>2</sup> P) <sup>3</sup> D <sub>2.0</sub>	13.258	13.076	1.39%
9	3p <sup>5</sup> ( <sup>2</sup> P) <sup>2</sup> P 4p <sup>1</sup> ( <sup>2</sup> P) <sup>3</sup> D <sub>1.0</sub>	13.308	13.095	1.63%
10	3p <sup>5</sup> ( <sup>2</sup> P) <sup>2</sup> P 4p <sup>1</sup> ( <sup>2</sup> P) <sup>3</sup> P <sub>2.0</sub>	13.317	13.153	1.24%
11	3p <sup>5</sup> ( <sup>2</sup> P) <sup>2</sup> P 4p <sup>1</sup> ( <sup>2</sup> P) <sup>3</sup> P <sub>0.0</sub>	13.413	13.172	1.83%
12	3p <sup>5</sup> ( <sup>2</sup> P) <sup>2</sup> P 4p <sup>1</sup> ( <sup>2</sup> P) <sup>1</sup> P <sub>1.0</sub>	13.431	13.283	1.12%
13	3p <sup>5</sup> ( <sup>2</sup> P) <sup>2</sup> P 4p <sup>1</sup> ( <sup>2</sup> P) <sup>1</sup> D <sub>2.0</sub>	13.444	13.302	1.06%
14	3p <sup>5</sup> ( <sup>2</sup> P) <sup>2</sup> P 4p <sup>1</sup> ( <sup>2</sup> P) <sup>3</sup> P <sub>1.0</sub>	13.464	13.328	1.02%
15	3p <sup>5</sup> ( <sup>2</sup> P) <sup>2</sup> P 4p <sup>1</sup> ( <sup>2</sup> P) <sup>1</sup> S <sub>0.0</sub>	13.638	13.480	1.17%

**Table 6.1:** Listing of energy levels for the first 15 states of Ar+0 from LANL atomic data and NIST.

The energy levels are subsequently used to calculate many of the relevant transitions in the atomic codes, such as radiative decay. Several of the significant spontaneous emission transitions between the levels shown in the previous table are displayed in Table 6.2. The transitions which are listed in the table are lines which are visible between 650 nm and 950 nm for the ICP conditions in this work. As seen previously, the line positions for the experiment show very little variation in comparison to the lines obtained from NIST, without accounting for the 0.25 nm bin resolution of the spectrometer. However, the errors from the previous energy levels have accumulated in the atomic data calculation, resulting in errors between 0.18% to 6.88%. These errors translate themselves into the misrepresentation of lines observed in the spectra. It is possible that one might alter the energy levels to derive much more accurate transitions in the atomic data; however, this impacts the other transitions, such as excitation and the energy gap necessary for ionization, making this simple alteration insufficient.

Transition	$\lambda_{nm}$ (NIST)	$\lambda_{nm}$ (LANL)	$\lambda_{nm}$ (Exp.)
2 $\leftarrow$ 14	696.73	719.50 (3.27%)	695.30 (0.21%)
2 $\leftarrow$ 13	706.92	727.86 (2.96%)	705.48 (0.20%)
3 $\leftarrow$ 13	738.60	756.42 (2.41%)	737.17 (0.19%)
5 $\leftarrow$ 15	750.59	749.24 (0.18%)	749.05 (0.21%)
3 $\leftarrow$ 11	751.67	770.90 (2.56%)	750.06 (0.21%)
2 $\leftarrow$ 10	763.72	786.55 (2.99%)	762.18 (0.20%)
2 $\leftarrow$ 9	772.59	791.07 (2.39%)	770.99 (0.21%)
4 $\leftarrow$ 14	772.63	719.50 (6.88%)	771.24 (0.18%)
4 $\leftarrow$ 12	795.04	812.16 (2.15%)	793.62 (0.18%)
3 $\leftarrow$ 10	800.84	820.00 (2.39%)	799.39 (0.18%)
2 $\leftarrow$ 8	801.70	817.08 (1.92%)	800.14 (0.19%)
3 $\leftarrow$ 9	810.59	824.91 (1.77%)	809.16 (0.18%)
2 $\leftarrow$ 7	811.75	825.57 (1.70%)	810.16 (0.20%)
5 $\leftarrow$ 14	826.68	837.28 (1.28%)	825.17 (0.18%)
5 $\leftarrow$ 13	841.05	848.63 (0.90%)	839.64 (0.17%)
3 $\leftarrow$ 8	842.70	853.24 (1.25%)	841.13 (0.19%)
5 $\leftarrow$ 12	852.38	855.89 (0.41%)	850.85 (0.18%)
2 $\leftarrow$ 6	912.55	904.00 (0.94%)	911.05 (0.16%)
5 $\leftarrow$ 10	922.70	929.49 (0.74%)	921.15 (0.17%)

**Table 6.2:** Listing of prominent radiative transition wavelengths from the first 15 Ar+0 states spanning from 650 nm to 950 nm. Errors in the transitions have compounded from errors previously observed in the listing of energy levels.

The oscillator strengths between the transition states are also shown in Table 6.3. Based on the mismatch in the spectra, the rates and cross sections are also called into question. The table is an attempt to find similarities between the LANL atomic code and NIST data regarding the transitions. Unfortunately, the relative scale, in addition to the order of magnitudes between the data, are highly inconsistent throughout all of the spectral transitions. Since the atomic codes rely immensely on the calculated energy levels, the rate and cross section calculations have an even smaller likelihood of capturing the numerics of the low-Z plasma's kinetics. This combination of inaccurate energy levels and compounded errors in the rates ultimately leads to a CR-generated spectra which cannot replicate the experimental spectra. Until accurate low-Z atomic data can be numerically generated under reasonable computational times, empirical data may be the best option to perform CR calculations in these conditions. [20]

Transition	$f_{nm}$ (LANL)	$f_{nm}$ (NIST)	Rel. Scale
2 ← 14	0.0279	0.1334	3.78
2 ← 13	0.0285	0.1059	2.72
3 ← 13	0.1150	0.3267	1.84
5 ← 15	0.1250	0.4483	2.59
3 ← 11	0.1140	0.4031	2.54
2 ← 10	0.2140	1.4101	5.59
2 ← 9	0.0278	0.1799	5.47
4 ← 14	0.3140	0.3445	0.10
4 ← 12	0.5290	0.7491	0.42
3 ← 10	0.0785	0.2833	2.61
2 ← 8	0.0894	0.4946	4.53
3 ← 9	0.2500	0.9199	2.68
2 ← 7	0.4580	2.8783	5.28
5 ← 14	0.1570	0.6904	3.40
5 ← 13	0.3940	1.5832	3.02
3 ← 8	0.3810	1.4173	2.72
5 ← 12	0.1510	0.4501	1.98
2 ← 6	0.1420	0.8890	5.26
5 ← 10	0.1070	0.3093	1.89

**Table 6.3:** Listing of prominent radiative transition oscillator strengths from the first 15 Ar+0 states spanning from 650 nm to 950 nm. Inconsistent scalings are observed across all of the transitions.

## 6.4 Summary

In this chapter, the construction of spectral images for plasma applications was developed. Using the radiation losses caused by emissions due to bound-bound, bound-free, and free-free processes, a full spectral image can be constructed and used as a tool to compare, validate, and verify with experiments and other collisional-radiative models. Many other features are also present in the spectra including line widths due to Doppler, natural, and Stark broadening, as well as edge broadening effects caused by similar phenomena in the bound-bound cases. This spectral construction module was used for the NLTE-10 workshop where chlorine-based spectra was produced. The Cl-based spectra allowed cross-validation between multiple CR models presented at the workshop and also led to the investigation of experimental spectra from OHREX, which was used on a plasma formed from laser-impinged parylene dichloride. The results were very promising, making the CR model a

possible investigation tool for more high-density, high-temperature plasma applications.

The spectral construction module was also used to generate argon spectra for low-density, low-temperature conditions. The use of an argon-based ICP motivated the examination of the argon atomic data for these conditions that contrast the previous CI spectra. The results show that the spectra do not match with the experimental and NIST spectra as a consequence of inaccurate near-neutral atomic calculations. The atomic data's inaccuracies stem from errors in the energy levels which are also used in the rate/cross-section calculations. As these errors originate from these atomic data calculations, these types of errors are also found in other atomic codes that similarly and primarily used for fusion applications. It is possible to generate more accurate energy levels using a many-body calculation for low- $Z$  species; but, these calculations are computationally expensive and are not currently practical for full plasma simulations. [102, 103] Since the simulation of fusion plasmas can span many plasma regimes and scales, quick calculations for atomic data are highly-desired which leaves the pursuit of more efficient, accurate low- $Z$  atomic calculations an open field for research.

# CHAPTER 7

## Conclusions & Future Work

Many modern plasma applications are becoming increasingly complex through their design and functionality. Some of these modern applications may depart significantly from equilibrium such that a simple fluid or kinetic description of the plasma is insufficient. Other applications can be highly transient where multiple plasma regimes are traversed, such as the plasmas found in FRC thrusters or laser-plasma systems. In these situations, atomic processes must be resolved in order to determine the impact of the particle collisions and photon interactions on the overall kinetics of these plasmas. Therefore, a collisional-radiative model was developed to capture the set of atomic kinetics that may ultimately affect the operation of these plasma applications.

The collisional-radiative model is a set of ordinary differential equations modeling the growth of the relevant atomic state densities in the plasma. Information about the particle states in the plasma include the atomic structure of each state and the transitional data, such as cross sections, that lead from one state to another. The data used primarily for this study are the argon and chlorine atomic data sets from Los Alamos National Laboratory. These rates were then calculated from the cross sectional data to be validated through some steady state calculations. After being deemed satisfactory, this intermediary data was used to explore various capabilities of the collisional-radiative model.

One of the first modifications made to the collisional-radiative model is the inclusion of energy rate equations. These energy rate equations were implemented in the form atomic and electron temperatures, both of which can vastly differ due to the differences in particle mass and velocity. An application explored with this multi-temperature model is the field of laser-induced breakdown. By using laser-induced sources via multiphoton ionization and

inverse Bremsstrahlung, the achievement of breakdown through the competition of these two terms were investigated. At low densities, it was numerically observed that MPI became the dominant mechanism in the breakdown of argon gas. At higher densities, IB became a much more comparable and efficient breakdown mechanism. Unfortunately, experimental results provide conflicting evidence between MPI being the dominant breakdown source as opposed to an electron avalanche caused by IB at low densities. Nonetheless, the model was able to capture both trends under the assumptions posed by both ideas.

The multi-temperature CR model can easily extend to a 2-fluid plasma model comprised of heavy-species (atomic/ionic) and electron fluids. But, the number of equations in the CR model can range from 100s to 1,000,000s based on the number of atomic states that are resolved. Complexity reduction techniques were compiled and developed to address the issue of solving such a large number of equations. Three methodologies, the quasi-steady-state solution, uniform grouping, and Boltzmann grouping, were explored as potential reduction strategies for the CR model. In addition to the acceleration of the CR calculations, the impact of the reduction techniques on the plasma parameters is equally important. These effects were explored through two test cases: one being isothermal via constant  $T_e$  and the other involving plasma irradiation with a constant Planckian field. Although the QSS and uniform grouping techniques show benefits under certain conditions, the Boltzmann grouping method has flexibility that extends to many plasma conditions, which is beneficial for transitory, non-equilibrium conditions.

Another capability added to the collisional-radiative model is spectroscopic construction. The availability of atomic codes that can resolve many transitions easily lends to the numerical generation of spectroscopic data. The first set of spectral images of chlorine were generated for the NLTE-10 workshop. The conditions typically sought at the NLTE workshops are high in density and temperature, i.e. fusion conditions. The results extracted from the CR model for the workshop closely matched many of the other models' results, which implies that the CR code may be readily applicable for several high-density, high-temperature studies. Another set of spectral comparisons were performed for low-density, low-temperature argon ICP. For near-neutral ions, the atomic codes were designed to capture

enough of the macroscopic plasma parameters before transitioning to the high- $Z$  species; this may be considered as the tradeoff for having efficient atomic structure calculations in place of having accurate calculations for low- $Z$  atoms. In this regard, the model failed to accurately replicate the line intensities observed from the Bell Jar’s inductively-coupled system.

In this work, the collisional-radiative model was extended for multiple features by including energy equations to model transient plasmas, complexity reduction techniques for more efficient plasma simulations, and spectroscopic capabilities to assess plasma conditions. However, these aspects of the CR model either need improvement or further development of other physical models to capture highly-coupled plasma simulations. One coupling scheme involving the CR model is the connection between atomic kinetics and the plasma’s fluid evolution. For example, Cambier has discussed the coupling of processes using lower-order methods that can nowadays be achieved with greater order and accuracy. [104] Nearly two decades after Cambier’s initial work, Kapper and Cambier developed a coupled fluid and kinetics solver to investigate argon shocks. [20] This is one example of a benchmark that can be used to generate codes with kinetics-fluid coupling. When modeling an FRC plasma, which is a future endeavor of this model, the simulations will rely on this same framework to numerically replicate the FRC plasmoid.

A plasma involves many radiative and kinetic processes that can lead to many complicated instabilities or structures. In a numerical framework, this leads to an increasing set of physics modules that are crucial in capturing these plasma dynamics. An example of a heavily-coupled plasma simulation is shown in Fig. 7.1. The network formed between atomic kinetics, radiation transport, an electron distribution solver, and a fluid system means that a large information set is necessary to fulfill the simulation objective.

The complexity reduction techniques explored in this work would help alleviate the intensive memory requirements in a CR-coupled simulation. However, the groupings explored in this work were determined manually and may be optimized even further to more accurately represent the atomic state distributions. Therefore, adaptive level grouping for atomic species must be explored to fully capitalize on the benefits of Boltzmann grouping. Works by Munafò et al. and Sahai et al. explored the use of machine learning to cluster molecular

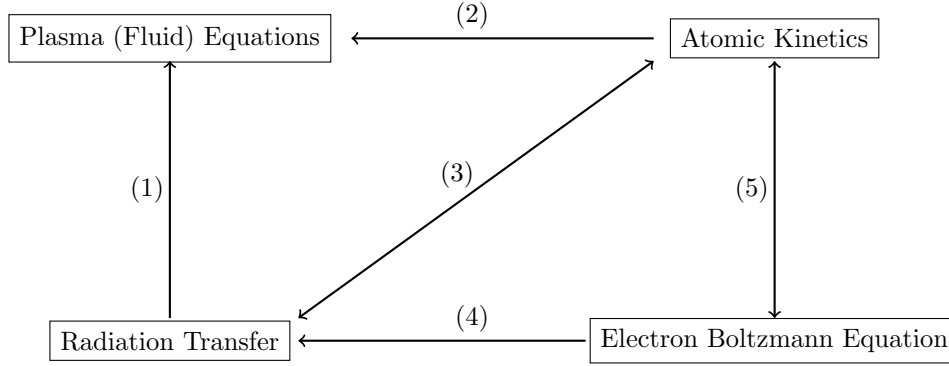


**Figure 7.1:** Adapted schematic of physical models that may be necessary and coupled for a plasma fluid simulation. [105] (1) Radiative energies are supplied to the fluid solver. (2) Kinetics-based changes to mass and energy alter the fluid solver. (3) Emission and absorption coefficients are supplied by the kinetics, while radiative rate coefficients are transferred to the radiation solver. (4) Electron energy distribution functions are supplied to the radiative transfer module. (5) Electron energy distribution also given to the chemical kinetics and electron impact rate coefficients are provided by the kinetics solver.

states for their applications. [70,81] It may be possible to extend their work to atomic states due to the absence of rovibrational modes that are present in the molecular species. The robustness of these groupings may be further tested with coupling to the previously-mentioned EEDF and RT solvers.

Lastly, the spectroscopic module also needs improvement whether one seeks spectral data for low- $Z$  or high- $Z$  applications. In the low- $Z$  scenario, we observed that the atomic codes that are primarily used for high-temperature, high-density studies were not entirely applicable for low- $Z$  studies. More accurate atomic codes for low- $Z$  plasma applications would be required; such codes exist in the community as many-body atomic theory-based codes that may appease these low- $Z$  calculations. For higher- $Z$  ions that push towards such extreme conditions, atomistic-density effects such as continuum lowering must be considered in these spectroscopic models. [106, 107] Approximations used to model continuum lowering have been shown to be inconsistent in a wide range of studies. [40, 108] Additionally, plasmas that are dynamically impacted by continuum lowering phenomenon would require inline atomic calculations that ultimately require tremendous amounts of memory and computational time. Therefore, much work is also needed to accurately calculate atomic structures for various ranges in the plasma regimes.

The scope of applications tackled in this work is a testament to the range of services offered by collisional-radiative models and atomic physics codes. Even though the collisional-radiative model can fulfill many objectives by modeling atomic kinetics in plasma simulations or by supplying experimentalists with extra means of validation, many opportunities remain for improvement in a wide range of plasma regimes, whether for low- $Z$  applications such as electric propulsion or high- $Z$  studies through various high-temperature, high density plasma devices. In the future, as numerical capabilities continue to increase through faster calculations, better numerical algorithms, and increased resource management, one can hope that collisional-radiative modeling will be at the center of many plasma simulations.

## APPENDIX A

### Rate Calculation Adjustment: Change of Variable

Implementing the forward rate calculation with the rate equation as is, seen in equation A.1, leads to divergent values for high  $\Delta E_{ij}/T$  cases when calculating the inverse rates. Therefore, a change of variable is conducted for the forward rate calculation in order to relax away from these scenarios.

Rate equation:

$$k(T) = \frac{\bar{v}}{(kT)^2} \int_0^\infty \sigma(E) E e^{-E/kT} dE \quad (\text{A.1})$$

Change of variable:

$$E = E^* + E_{ij} \quad \rightarrow \quad dE = dE^* \quad (\text{A.2})$$

Modified rate equation:

$$k(T) = \frac{\bar{v}}{(kT)^2} e^{-E_{ij}/kT} \int_0^\infty \sigma(E^* + E_{ij}) \cdot (E^* + E_{ij}) e^{-E^*/kT} dE^* \quad (\text{A.3})$$

This change of variable is valid because a sufficient amount of energy is needed for the transitions to occur. The assumption then that the cross-sectional values are 0 until a sufficient energy needed for transition is achieved permits this change of variable. This alteration's benefit can be seen below.

$$k_{inv} \sim k_{for} \cdot e^{E_{ij}/kT} \quad (\text{A.4})$$

Therefore:

$$k_{inv}(T) \sim \frac{\bar{v}}{(kT)^2} \int_0^\infty \sigma(E^* + E_{ij}) \cdot (E^* + E_{ij}) e^{-E^*/kT} dE^*$$

A finite inverse rate value is calculated here, whereas implementation on an “as-is” basis, causes subsequent calculations of the inverse rate to lead to infinity values because of the exponential term,  $e^{E_{ij}/kT}$

## APPENDIX B

### Construction of the Source Terms and Jacobian Matrix

#### B.1 Terms due to change in species density

For Argon, the following equation is valid for  $k = 0, \dots, 16$ . For the value  $k = 17$ , the last 2 terms are omitted since further ionization is not possible.

In these equations, assumptions are made that only single jumps in ionization levels are permitted at a time. Also, the plasma is defined to be optically thin to radiative processes for simplicity.

$$\begin{aligned}
 \dot{\omega}_n^{+k} = & - \sum_{m>n} \alpha_{(m|n)}^{+k,e} N_e N_{+k,n} + \sum_{m>n} \beta_{(n|m)}^{+k,e} N_e N_{+k,m} + \sum_{m>n} A_{(n|m)}^{+k} N_{+k,m} \\
 & + \sum_{m<n} \alpha_{(n|m)}^{+k,e} N_e N_{+k,m} - \sum_{m<n} \beta_{(m|n)}^{+k,e} N_e N_{+k,n} - \sum_{m<n} A_{(m|n)}^{+k} N_{+k,n} \\
 & - \sum_j \alpha_{+(k+1),j|n}^{+k,e} N_e N_{+k,n} + \sum_j \beta_{(n|+(k+1),j)}^{+k,e} N_{+(k+1),j} N_e^2 \\
 & - \sum_j R_{(-,j|n)}^{+k} N_{+k,n} N_e + \sum_j R_{(n|+,j)}^{+(k+1)} N_{+(k+1),n} N_e
 \end{aligned} \tag{B.1}$$

Let's now look at the Jacobian terms.

Begin with the terms pertaining to derivatives with species density.

$$\begin{aligned} \frac{\partial \dot{\omega}_n^{+k}}{\partial N_{+k,n}} = & - \sum_{m>n} \alpha_{(m|n)}^{+k,e} N_e - \sum_{m<n} \beta_{(m|n)}^{+k,e} N_e - \sum_{m<n} A_{(m|n)}^{+k} \\ & - \sum_j \alpha_{+(k+1,j|n)}^{+k,e} N_e - \sum_j R_{(-,j|n)}^{+k} N_e \end{aligned} \quad (\text{B.2})$$

$$\frac{\partial \dot{\omega}_n^{+k}}{\partial N_{+k,m}} = \sum_{m>n} \beta_{(n|m)}^{+k,e} N_e + \sum_{m>n} A_{(n|m)}^{+k} + \sum_{m<n} \alpha_{(n|m)}^{+k,e} N_e \quad (\text{B.3})$$

$$\begin{aligned} \frac{\partial \dot{\omega}_n^{+k}}{\partial N_{+(k+1),j}} = & - \sum_{m>n} \alpha_{(m|n)}^{+k,e} Z_{+(k+1),j} N_{+k,n} + \sum_{m>n} \beta_{(n|m)}^{+k,e} Z_{+(k+1),j} N_{+k,m} \\ & + \sum_{m<n} \alpha_{(n|m)}^{+k,e} Z_{+(k+1),j} N_{+k,m} - \sum_{m<n} \beta_{(m|n)}^{+k,e} Z_{+(k+1),j} N_{+k,n} \\ & - \sum_j \alpha_{+(k+1,j|n)}^{+k,e} Z_{+(k+1),j} N_{+k,n} \\ & + \sum_j \beta_{(n|+(k+1),j)}^{+k,e} (N_e^2 + 2Z_{+(k+1),j} N_{+(k+1),j} N_e) + \sum_j R_{(n|+,j)}^{+(k+1)} N_e \end{aligned} \quad (\text{B.4})$$

Terms with derivatives with respect to energy:

$$\frac{\partial \dot{\omega}_n^{+k}}{\partial E_h} = 0 \quad (\text{B.5})$$

$$\begin{aligned}
\frac{\partial \dot{\omega}_n^{+k}}{\partial E_e} &= \frac{\partial \dot{\omega}_n^{+k}}{\partial T_e} \frac{\partial T_e}{\partial E_e} = \frac{2}{3k_b} \left[ - \sum_{m>n} \frac{\partial \alpha_{(m|n)}^{+k,e}}{\partial T_e} N_{+k,n} + \sum_{m>n} \frac{\partial \beta_{(n|m)}^{+k,e}}{\partial T_e} N_{+k,m} \right] \\
&\quad + \frac{2}{3k_b} \left[ \sum_{m<n} \frac{\partial \alpha_{(n|m)}^{+k,e}}{\partial T_e} N_{+k,m} - \sum_{m<n} \frac{\partial \beta_{(m|n)}^{+k,e}}{\partial T_e} N_{+k,n} \right] \\
&\quad + \frac{2}{3k_b} \left[ - \sum_j \frac{\partial \alpha_{+(k+1),j|n}^{+k,e}}{\partial T_e} N_{+k,n} + \sum_j \frac{\partial \beta_{n|+(k+1),j}^{+k,e}}{\partial T_e} (N_{+(k+1),j} N_e) \right] \\
&\quad + \frac{2}{3k_b} \left[ - \sum_j \frac{\partial R_{(-,j|n)}^{+k}}{\partial T_e} N_{+k,n} + \sum_j \frac{\partial R_{(n|+,j)}^{+(k+1)}}{\partial T_e} N_{+(k+1),n} \right]
\end{aligned} \tag{B.6}$$

The coefficient rates are numerically estimated within the code.

## B.2 Terms due to change in energy of heavy species

For a system where one assumes that is electron-impact dominated due to high temperature dynamics, atom-impact processes are ignored, reducing to the following equations.

$$\dot{\omega}_{E_h} = 0 \tag{B.7}$$

$$\frac{\partial \dot{\omega}_{E_h}}{\partial N_n^{+k}} = 0 \tag{B.8}$$

$$\frac{\partial \dot{\omega}_{E_h}}{\partial E_h} = 0 \tag{B.9}$$

$$\frac{\partial \dot{\omega}_{E_h}}{\partial E_e} = 0 \tag{B.10}$$

However, in the scenario where the heavy atom temperature is accounted for, it becomes more appropriate to consider elastic collisions due to the exchange in energy between electrons and atoms.

$$\dot{\omega}_{E_h} = \frac{2m_e}{m_{Ar}} \sum_k \alpha^{+k,e} [E_e N^{+k} - N_e E_h] = \frac{2m_e}{m_{Ar}} N_e \frac{3}{2} k_B (T_e - T_h) \sum_{k,j} \bar{\alpha}^{+k,e} N^{+k},$$

$$N^{+k} = \sum_j N_j^{+k}$$
(B.11)

The Jacobian terms are defined in the following equations, beginning with the species terms. Bear in mind that conserved variables are utilized within the code; therefore, the derivatives are specifically applied to the variable alone.

$$\frac{\partial \dot{\omega}_{E_h}}{\partial N_n^{+k}} = \frac{2m_e}{m_{Ar}} \left[ \alpha^{+k,e} E_e - \sum_k \alpha^{+k,e} Z_{+k} E_h \right]$$
(B.12)

$$\frac{\partial \dot{\omega}_{E_h}}{\partial E_h} = -\frac{2m_e}{m_{Ar}} \sum_{k,j} \alpha^{+k,e} N_e$$
(B.13)

$$\frac{\partial \dot{\omega}_{E_h}}{\partial E_e} = \frac{2m_e}{m_{Ar}} \sum_k \alpha^{+k,e} N^{+k} + \frac{2m_e}{m_{Ar}} \sum_k \frac{\partial \alpha^{+k,e}}{\partial T_e} \frac{2}{3k_B N_e} [E_e N^{+k} - N_e E_h]$$
(B.14)

### B.3 Terms due to change in electron energy

$E_{nm}$  is defined as the energy needed to proceed from a lower state,  $n$ , to a higher state,  $m$ .

$$\begin{aligned}
\dot{\omega}_{E_e} = & \sum_n \sum_{m>n} E_{nm}^{+k} \left( -\alpha_{(m|n)}^{+k,e} N_{+k,n} N_e + \beta_{(n|m)}^{+k,e} N_{+k,m} N_e \right) \\
& + \sum_n \sum_j I_{n,j}^{+k} \left( \beta_{(n|+(k+1),j)}^{+k,e} N_{+(k+1),j} N_e^2 - \alpha_{(+(k+1),j|n)}^e N_{+k,n} N_e \right) \\
& - \frac{2m_e}{m_{Ar}} \sum_k \alpha^{+k,e} [E_e N^{+k} - N_e E_h] - T_e \sum_n \sum_{k,j} R_{E;(n|+,j)}^{+(k+1)} N_{+(k+1),n} N_e
\end{aligned} \tag{B.15}$$

Note that including the following term is redundant as double counting the energy transfer will occur if it is included:

$$\sum_n \sum_{m<n} E_{mn}^{+k} \left( +\alpha_{(n|m)}^{+k,e} N_{+k,m} N_e - \beta_{(m|n)}^{+k,e} N_{+k,n} N_e \right)$$

Jacobian Terms:

$$\begin{aligned}
\frac{\partial \dot{\omega}_{E_e}}{\partial N_{+k,n}} = & -N_e \sum_{m>n} E_{nm}^{+k} \alpha_{(m|n)}^{+k,e} - N_e \sum_j I_{n,j}^{+k} \alpha_{(+(k+1),j|n)}^e - \\
& \frac{2m_e}{m_{Ar}} \sum_k \alpha^{+k,e} [E_e - Z_{+k} E_h]
\end{aligned} \tag{B.16}$$

$$\frac{\partial \dot{\omega}_{E_e}}{\partial N_{+k,m}} = N_e \sum_{m>n} E_{nm}^{+k} \beta_{(n|m)}^{+k,e} \tag{B.17}$$

$$\begin{aligned}
\frac{\partial \dot{\omega}_{E_e}}{\partial N_{+(k+1),j}} = & \sum_n \sum_j I_{n,j}^{+k} [\beta_{(n|+(k+1),j)}^{+k,e} (N_e^2 + 2N_e N_{+(k+1),j} Z_{+(k+1),j}) \\
& - \alpha_{(+(k+1),j|n)}^e N_{+k,n} Z_{+(k+1),j}] - T_e \sum_n \sum_{k,j} R_{E;(n|+,j)}^{+(k+1)} N_e
\end{aligned} \tag{B.18}$$

$$\frac{\partial \dot{\omega}_{E_e}}{\partial E_h} = \frac{2m_e}{m_{Ar}} \sum_{k,j} \alpha^{+k,e} N_e \quad (\text{B.19})$$

$$\begin{aligned} \frac{\partial \dot{\omega}_{E_e}}{\partial E_e} &= \frac{\partial \dot{\omega}_{E_e}}{\partial T_e} \frac{\partial T_e}{\partial E_e} = \frac{2}{3k_b} \sum_n \sum_{m>n} E_{nm}^{+k} \left( -\frac{\partial \alpha_{(m|n)}^{+k,e}}{\partial T_e} N_{+k,n} + \frac{\partial \beta_{(n|m)}^{+k,e}}{\partial T_e} N_{+k,m} \right) \\ &+ \frac{2}{3k_b} \sum_n \sum_j I_{n,j}^{+k} \left( \frac{\partial \beta_{(n|+(k+1),j)}^{+k,e}}{\partial T_e} N_{+(k+1),j} N_e - \frac{\partial \alpha_{+(k+1),j|n}^e}{\partial T_e} N_{+k,n} \right) \\ &- \frac{2m_e}{m_{Ar}} \sum_k \alpha^{+k,e} N^{+k} - \frac{2m_e}{m_{Ar}} \sum_k \frac{\partial \alpha^{+k,e}}{\partial T_e} \frac{2}{3k_B N_e} [E_e N^{+k} - N_e E_h] \\ &- T_e \sum_n \sum_{(k,j)} \frac{\partial R_{E;(n|+,j)}^{+(k+1)}}{\partial T_e} N_{+(k+1),j} N_e \end{aligned} \quad (\text{B.20})$$

## APPENDIX C

### Ordinary Differential Equation (ODE) Solvers

#### C.1 Backward Euler

In order to develop a sound understanding of the Radau5 scheme, the backward Euler method will be elaborated upon as a basis for the multi-stage implicit RK method. The model ODE is provided as follows, from which the time-marching backward Euler scheme is extracted.

$$\frac{dy}{dt} = f(t, y) \tag{C.1}$$

The LHS of the equation is then discretized in time to allow incrementation in  $\Delta t$ . For a first-order, backward Euler scheme, the function's inputs on the RHS are solved based on the next timestep's result.

$$y^{n+1} = y^n + \Delta t \cdot f(t^{n+1}, y^{n+1}) \tag{C.2}$$

Alternatively, using function inputs on the RHS based on the current timestep leads to the first-order, forward Euler scheme. Unfortunately, the large range of timescales associated with solving the system of ODEs, especially for chemical kinetics as will be observed in the chapter discussing the CR model, leads to a very restrictive timestep in using forward Euler. To further explore the stability properties of the implicit Euler scheme, we alter the equation such that the model equation marches according to the eigenvalue of the system:

$$y^{n+1} = y^n + \Delta t \lambda y^{n+1} \tag{C.3}$$

Reorganizing the equation to isolate the terms involving the previous and current timesteps of the equation above, the equation becomes the following, from which the stability domain

may also be determined.

$$y^{n+1} = R(\Delta t \lambda) y^n \quad \text{where } R(z) = \frac{1}{1-z} \quad (\text{C.4})$$

$R$  gives the stability, or growth, function pertaining to the temporal algorithm here; other implicit and explicit schemes can lead to different stability functions based on their implementation. One can already see that a sufficiently small  $z$  leads to a stable solution in successive timesteps, whereas a large  $z$  value can easily lead to stability issues in the forward Euler scheme. The term “*large*” refers to the stability domain mapped by the growth function: unless a value of  $z$  is chosen such that it lands outside a circle of radius 1 with a center at +1 according to the stability function, the backward Euler scheme will be unstable.

However, the large stability domain covered by the backward Euler scheme is very attractive for problems with large separation of timescales. This property is similarly observed with the Radau5 solver. With the foundations of the backward Euler scheme at hand, one may now proceed to explore the Radau5 scheme and other associated advantages and disadvantages of bringing the method into the reaction kinetics solver.

## C.2 Radau5

Having discussed the numerics behind the backward Euler scheme, one can now extend to the multistage, implicit RK method, where the focus will be concentrated on the Radau5 scheme. Important details regarding the use of the scheme with the chemical kinetics will be discussed here. Further details of the scheme have been comprehensively noted by Hairer and Wanner. [24] The implicit Euler scheme is very simple in that its single-stage, single-step feature makes the scheme quick to implement. In order to extend to the multistage scenario, one needs to generalize the set of implicit RK equations.

$$g_i = y^n + \Delta t \sum_{j=1}^s a_{ij} f(x^n + c_j \Delta t, g_j) \quad i = 1, \dots, s \quad (\text{C.5})$$

$$y^{n+1} = y^n + \Delta t \sum_{j=1}^s b_j f(x^n + c_j \Delta t, g_j) \quad (\text{C.6})$$

where  $\mathbf{b}$  corresponds to the coefficients associated with solution propagation to the next timestep and  $\mathbf{A}$ , where  $\mathbf{A} = (a_{ij})_{i,j=1}^s$ , is comprised of coefficients that determine each of the implicit Runge-Kutta stages. The equations correspond to the stage-wise and step-wise results of the Radau5 scheme, respectively. In other words, each subsequent stage must be calculated in order to determine the following timestep's result. The Radau5 scheme is a 3-stage, 5<sup>th</sup> order scheme, thus requiring  $i = 1, 2, 3$  for  $g_i$ .

The stability function and stability domain corresponding to the Radau5 scheme are also provided below. The backward Euler scheme's stability domain has also been included for comparison. A scale factor increase of approximately 5 in the instability circle can be seen going from backward Euler to Radau5. Despite this increase in the instability region, the timesteps chosen for this simulation are such that they lie in the vast, stable region for Radau5. Additionally, the choice in timestep is also supplemented by the 5<sup>th</sup> order nature of the scheme, which leads to reduced numerical error with increasing timestep, unlike the 1<sup>st</sup> order, backward Euler scheme.

$$R(z) = \frac{1 + 2z/5 + z^2/20}{1 - 3z/5 + 3z^2/20 - z^3/60} \quad (\text{C.7})$$

### C.2.1 Implementation

The increased complexity in using a multistage, implicit Runge-Kutta method also requires a discussion of various techniques brought together for this time-marching algorithm. The first step taken to implement Radau5 involves reformulating the system such that a system of equations are solved using the incremental value between the previous timestep's value and the stage result, i.e.  $z_i = g_i - y^n$ . This effectively alters equations C.5 and C.6 giving

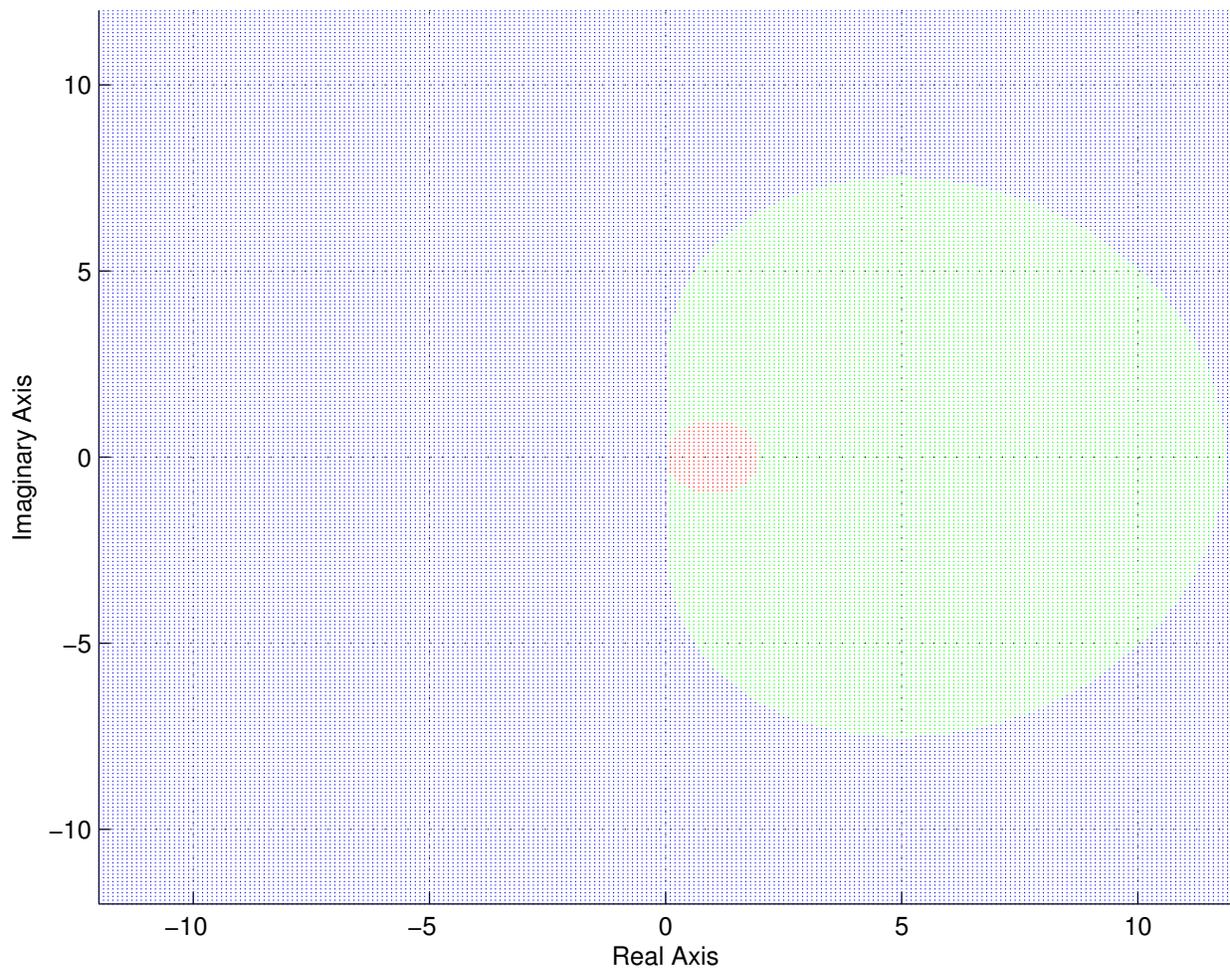


**Figure C.1:** Stability regions corresponding to the schemes used in this work: ● Backward Euler; ● Radau5; ● Stable. The area enclosed by the schemes lead to numerical instabilities and cause solutions to diverge.

the following set of equations.

$$z_i = \Delta t \sum_{j=1}^s a_{ij} f(x^n + c_j \Delta t, z_j) \quad i = 1, \dots, 3 \quad (\text{C.8})$$

$$y^{n+1} = y^n + \sum_{j=1}^s d_j z_j \quad \text{where } \mathbf{d} = \mathbf{bA}^{-1} \quad (\text{C.9})$$

There are immediately two advantages in using this formulation. First, the occurrence of round-off errors becomes confined to the incremental value, rather than the absolute value of the sought-after variable after the timestep. This is important as the stopping criterion for the iterations to be performed are based on tolerance values. This will soon become clear when discussing the iterative method used to solve the system. Second, the errors associated with the timestep iterations accrue based on the numerical scheme, but are also amplified based on the Lipschitz constant associated with the RHS of the solver. Therefore, looking at the incremental value of  $z_i$ , instead of the derivatives found in  $f(x^n + c_j \Delta t, z_j)$ , have more benign effects in the accumulation of numerical error.

As mentioned, the values corresponding to subsequent timesteps are solved iteratively. This iterative solve is conducted using Newtonian iterations. The Newtonian solves are performed on equation C.8. To perform a Newtonian solve, a Taylor expansion around the set of variables after the  $k^{th}$  iteration, which is used to determine the viability of the variable set,  $\mathbf{z}$ , is given by equation C.10. Additionally, the equation for  $\mathbf{F}$  giving the measure of accuracy in the temporally-discretized form and its derivative are given by equations C.11 and C.12.

$$\mathbf{F}(\mathbf{z}) = \mathbf{F}(\mathbf{z}^k) + \frac{\partial \mathbf{F}}{\partial \mathbf{z}}(\mathbf{z} - \mathbf{z}^k) \quad (\text{C.10})$$

$$\mathbf{F}(\mathbf{z}) = \mathbf{z} - \Delta t \mathbf{A} \mathbf{f}(t, \mathbf{z}) \quad (\text{C.11})$$

$$\frac{\partial \mathbf{F}}{\partial \mathbf{z}} = \mathbf{I} - \Delta t \mathbf{A} \frac{\partial \mathbf{f}}{\partial \mathbf{z}}(t, \mathbf{z}) \quad (\text{C.12})$$

In these set of equations,  $\mathbf{z}$  is the set of variables being solved for in the system, equivalent to the number densities sought after in the CR model,  $\mathbf{A}$  is the matrix set of Runge-Kutta coefficients, and  $\mathbf{f}$  is the vector of RHS evaluations, which corresponds to the net rates of

each state. One then combines the equations above to produce the equation used for the Newtonian iterations.

$$\begin{aligned}
 (\mathbf{I} - \Delta t \mathbf{A} \times \mathbf{J}) \Delta \mathbf{z}^k &= -\mathbf{z}_n^k + \Delta t (\mathbf{A} \times \mathbf{I}) \mathbf{f}(\mathbf{z}^k) \\
 \mathbf{z}^{k+1} &= \mathbf{z}^k + \Delta \mathbf{z}^k
 \end{aligned}
 \tag{C.13}$$

In this equation,  $\mathbf{J}$  is approximated to  $\frac{\partial \mathbf{f}}{\partial \mathbf{y}}(t_n, z_n)$  as a simplification, lest we utilize more memory for the multiple stages involved in the scheme.

Finally, in order to proceed to the next timestep, there must be a stopping criterion dictating the acceptance of the estimated value for the current set of iterations. The stopping criterion is based on the following set of formulas:

$$\begin{aligned}
 \eta_k \|\Delta Z^k\| &\leq Tol_{eff} \quad \text{where} \quad \eta_k = \frac{\Theta_k}{1 - \Theta_k}, \\
 \Theta_k &= \|\Delta Z^k\| / \|\Delta Z^{k-1}\|
 \end{aligned}
 \tag{C.14}$$

If the solution diverges or the stopping criterion is not satisfied, the algorithm restarts with a smaller step size. These smaller step sizes are described by Hairer and Wanner as the standard step size controller and a predictive controller, both of which are used depending on whichever provides the smaller time step, albeit in keeping with the stability domain.

## REFERENCES

- [1] National Research Council, ed., *Plasma Science: Advancing Knowledge in the National Interest*. Washington, DC: The National Academies Press, 2007.
- [2] D. M. Goebel and I. Katz, *Fundamentals of Electric Propulsion: Ion and Hall Thrusters*. 2008.
- [3] J. Slough, D. Kirtley, and T. Weber, “Pulsed Plasmoid Propulsion: The ELF Thruster,” No. 265 in 31, International Electric Propulsion Conference, 2009.
- [4] L. C. Steinhauer, “Review of field-reversed configurations,” *Physics of Plasmas*, vol. 18, no. 7, 2011.
- [5] D. Kirtley, A. Pancotti, J. Slough, and P. Chris, “Steady Operation of an FRC Thruster on Martian Atmosphere and Liquid Water Propellants,” *48th AIAA/ASME/SAE/ASEE Joint Propulsion Conference & Exhibit*, 2012.
- [6] K. M. Velas, “Investigation of the Three-Dimensional Structure of a Rotating Magnetic Field Driven Field-Reversed Configuration using Internal Magnetic Field Measurements,” 2013.
- [7] F. Albert, A. G. R. Thomas, S. P. D. Mangles, S. Banerjee, S. Corde, A. Flacco, M. Litos, D. Neely, J. Vieira, Z. Najmudin, R. Bingham, C. Joshi, and T. Katsouleas, “Laser wakefield accelerator based light sources: potential applications and requirements,” *Plasma Physics and Controlled Fusion*, vol. 56, 2014.
- [8] V. Malka, J. Faure, Y. A. Gauduel, E. Lefebvre, A. Rousse, and K. T. Phuoc, “Principles and applications of compact laser-plasma accelerators,” *Nature physics*, vol. 4, pp. 447–453, jun 2008.
- [9] R. Betti, “Hot Spot Dynamics and Hydrodynamic Instabilities,” *HEDP Summer School Presentations*, 2015.
- [10] R. S. Craxton, K. S. Anderson, T. R. Boehly, V. N. Goncharov, D. R. Harding, J. P. Knauer, R. L. McCrory, P. W. McKenty, D. D. Meyerhofer, J. F. Myatt, A. J. Schmitt, J. D. Sethian, R. W. Short, S. Skupsky, W. Theobald, W. L. Kruer, K. Tanaka, R. Betti, T. J. Collins, J. A. Delettrez, S. X. Hu, J. A. Marozas, A. V. Maximov, D. T. Michel, P. B. Radha, S. P. Regan, T. C. Sangster, W. Seka, A. A. Solodov, J. M. Soures, C. Stoeckl, and J. D. Zuegel, “Direct-drive inertial confinement fusion: A review,” *Physics of Plasmas*, vol. 22, no. 11, pp. 0–153, 2015.
- [11] J. Lindl, “Development of the indirect-drive approach to inertial confinement fusion and the target physics basis for ignition and gain,” *Physics of Plasmas*, vol. 2, no. 11, pp. 3933–4024, 1995.
- [12] J. Maxwell, “On the dynamical theory of gases,” *Philosophical Transactions of the Royal Society of London*, vol. 157, pp. 49–88, 1867.

- [13] S. I. Braginskii, “Transport Processes in a Plasma,” in *Reviews of Plasma Physics*, pp. 205–311, New York: Consultants Bureau, 1965.
- [14] C. Kittel, “Elementary Statistical Physics,” *John Wiley & Sons Inc*, vol. 27, no. 2, pp. 169–183, 1959.
- [15] W. G. Vincenti and C. H. Kruger, *Introduction to Physical Gas Dynamics*. Krieger Pub Co, 1975.
- [16] J. A. M. van der Mullen, “Excitation equilibria in plasmas; a classification,” *Physics Reports*, vol. 191, no. 2-3, pp. 109–220, 1990.
- [17] J. Abdallah and J. Colgan, “Time-dependent calculations of electron energy distribution functions for cold argon gas in the presence of intense black-body radiation,” *Journal of Physics B: Atomic, Molecular and Optical Physics*, vol. 45, no. 3, 2012.
- [18] T. B. Petrova, H. D. Ladouceur, and A. P. Baronavski, “Numerical modeling of the electrical breakdown and discharge properties of laser-generated plasma channels,” *Physical Review E*, vol. 76, no. 066405, 2007.
- [19] A. C. Genz and A. A. Malik, “Remarks on algorithm 006: An adaptive algorithm for numerical integration over an N-dimensional rectangular region,” *Journal of Computational and Applied Mathematics*, vol. 6, no. 4, pp. 295–302, 1980.
- [20] M. G. Kapper and J. L. Cambier, “Ionizing shocks in argon. Part I: Collisional-radiative model and steady-state structure,” *Journal of Applied Physics*, vol. 109, no. 11, 2011.
- [21] D. Mihalas and B. W. Mihalas, “Foundations of radiation hydrodynamics,” *Oxford University Press*, pp. 366–386, 1984.
- [22] M. Mitchner and C. H. Kruger, *Partially Ionized Gases*. New York: John Wiley & Sons Inc, 1st ed., 1973.
- [23] Y. B. Zeldovich and Y. P. Raizer, “Physics of Shock Waves and High-Temperature Hydrodynamic Phenomena,” *Dover Publications*, p. 258, 2002.
- [24] E. Hairer and G. Wanner, “Solving Ordinary Differential Equations II: Stiff and Differential - Algebraic Problems,” *Springer-Verlag Berlin Heidelberg*, pp. 118–127, 1991.
- [25] Los Alamos National Laboratory T-4 Group, “Argon Atomic Data Sets.” <https://www-amdis.iaea.org/LANL/argon/>.
- [26] R. E. H. Clark, “Atomic data for heavy element impurities in fusion reactors,” in *Summary Report of the Final Research Coordination Meeting 0552*, (International Atomic Energy Agency, IAEA Headquarters, Vienna, Austria), 2009.
- [27] J. Colgan, H. L. Zhang, and C. J. Fontes, “Electron-impact excitation and ionization cross sections for the Si, Cl, and Ar isonuclear sequences,” *Phys. Rev. A: At., Mol., Opt. Phys.*, vol. 77, no. 062704, 2008.

- [28] R. E. H. Clark, J. J. Abdallah, and J. B. Mann, “Integral and Differential Cross Sections for Electron Impact Ionization,” *The Astrophysical Journal*, vol. 381, pp. 597–600, 1991.
- [29] R. D. Cowan, “The theory of atomic structure and spectra,” *Los Alamos Series in Basic and Applied Sciences, Berkeley: University of California Press*, pp. 176–212, 1981.
- [30] J. J. Abdallah, R. E. H. Clark, and R. D. Cowan, “Theoretical Atomic Physics Code Development I CATS: Cowan Atomic Structure Code,” *Los Alamos National Laboratory Manuals*, vol. 1, 1988.
- [31] R. E. H. Clark, J. J. Abdallah, and S. P. Kramer, “Theoretical Atomic Physics Code Development III TAPS: A Display Code for Atomic Physics Data,” *Los Alamos National Laboratory Manuals*, vol. III, 1988.
- [32] J. B. Mann, “Excitation collision strengths for iron ions calculated with a distorted wave method,” *Atomic Data and Nuclear Data Tables*, vol. 29, pp. 407–465, 1983.
- [33] B. J. Archer, R. E. H. Clark, C. J. Fontes, and H. Zhang, “Ionization : GIPPER User Manual,” vol. 836, 2000.
- [34] C. W. White and J. G. Martin, “Chlorine Gas Inhalation Human Clinical Evidence of Toxicity and Experience in Animal Models,” *Proceedings of the American Thoracic Society*, vol. 7, no. 4, 2010.
- [35] K. A. Berrington, W. B. Eissner, and P. H. Norrington, “RMATRX1: Belfast atomic R-matrix codes,” *Computer Physics Communications*, vol. 92, no. 2-3, pp. 290–420, 1995.
- [36] M. Gu, “The flexible atomic code,” *Canadian Journal of Physics*, vol. 86, no. 5, pp. 675–689, 2008.
- [37] H. K. Chung, M. H. Chen, W. L. Morgan, Y. Ralchenko, and R. W. Lee, “FLYCHK: Generalized population kinetics and spectral model for rapid spectroscopic analysis for all elements,” *High Energy Density Physics*, vol. 1, no. 1, pp. 3–12, 2005.
- [38] H. A. Scott, “Cretin - A radiative transfer capability for laboratory plasmas,” *Journal of Quantitative Spectroscopy and Radiative Transfer*, vol. 71, no. 2-6, pp. 689–701, 2001.
- [39] H. K. Chung, “FLYCHK: Generalized Model of Atomic Processes in Plasmas.” <https://www-amdis.iaea.org/FLYCHK>.
- [40] H. K. Chung, C. Bowen, C. J. Fontes, S. B. Hansen, and Y. Ralchenko, “Comparison and analysis of collisional-radiative models at the NLTE-7 workshop,” *High Energy Density Physics*, vol. 9, no. 4, pp. 645–652, 2013.

- [41] J. Rubiano, R. Florido, C. Bowen, R. Lee, and Y. Ralchenko, “Review of the 4th NLTE Code Comparison Workshop,” *High Energy Density Physics*, vol. 3, no. 1-2, pp. 225–232, 2007.
- [42] D. A. Cremers and L. J. Radziemski, *Handbook of Laser-Induced Breakdown Spectroscopy*. John Wiley & Sons, Ltd, 2013.
- [43] M. Buschbeck, F. Büchler, T. Halfmann, and S. Arndt, “Laser-induced breakdown spectroscopy for lambda quantification in a direct-injection engine,” *Spectrochimica Acta - Part B Atomic Spectroscopy*, vol. 74-75, pp. 103–108, 2012.
- [44] R. C. Wiens, S. Maurice, B. Barraclough, M. Saccoccio, W. C. Barkley, J. F. Bell, S. Bender, J. Bernardin, D. Blaney, J. Blank, M. Bouyé, N. Bridges, N. Bultman, P. Caïs, R. C. Clanton, B. Clark, S. Clegg, A. Cousin, D. Cremers, A. Cros, L. Deflores, D. Delapp, R. Dingler, C. D’Uston, M. Darby Dyar, T. Elliott, D. Enemark, C. Fabre, M. Flores, O. Forni, O. Gasnault, T. Hale, C. Hays, K. Herkenhoff, E. Kan, L. Kirkland, D. Kouach, D. Landis, Y. Langevin, N. Lanza, F. Larocca, J. Lasue, J. Latino, D. Limonadi, C. Lindensmith, C. Little, N. Mangold, G. Manhes, P. Mauchien, C. McKay, E. Miller, J. Mooney, R. V. Morris, L. Morrison, T. Nelson, H. Newsom, A. Ollila, M. Ott, L. Pares, R. Perez, F. Poitrasson, C. Provost, J. W. Reiter, T. Roberts, F. Romero, V. Sautter, S. Salazar, J. J. Simmonds, R. Stiglich, S. Storms, N. Striebig, J. J. Thocaven, T. Trujillo, M. Ulibarri, D. Vaniman, N. Warner, R. Waterbury, R. Whitaker, J. Witt, and B. Wong-Swanson, “The ChemCam instrument suite on the Mars Science Laboratory (MSL) rover: Body unit and combined system tests,” *Space Science Reviews*, vol. 170, no. 1-4, pp. 167–227, 2012.
- [45] D. A. Cremers, M. H. Ebinger, D. D. Breshears, P. J. Unkefer, S. A. Kammerdiener, M. J. Ferris, K. M. Catlett, and J. R. Brown, *Measuring total soil carbon with laser-induced breakdown spectroscopy (LIBS)*. PhD thesis, 2001.
- [46] K. Melessanaki, M. Mateo, S. C. Ferrence, P. P. Betancourt, and D. Anglos, “The application of LIBS for the analysis of archaeological ceramic and metal artifacts,” in *Applied Surface Science*, vol. 197-198, pp. 156–163, 2002.
- [47] V. Morel, A. Bultel, and B. G. Chéron, “Modeling of thermal and chemical non-equilibrium in a laser-induced aluminum plasma by means of a Collisional-Radiative Model,” *Spectrochimica Acta, Part B: Atomic Spectroscopy*, vol. 65, pp. 830–841, 2010.
- [48] C. L. Ireland and C. G. Morgan, “Gas breakdown by a short laser pulse,” *Journal of Physics D: Applied Physics*, vol. 6, no. 6, pp. 720–729, 1973.
- [49] A. Müsing, U. Riedel, J. Warnatz, W. Herden, and H. Ridderbusch, “Laser-induced breakdown in air and behind droplets: A detailed Monte-Carlo simulation,” *Proceedings of the Combustion Institute*, vol. 31 II, pp. 3007–3014, 2007.
- [50] C. G. Morgan, “Laser-induced breakdown of gases,” *Reports on Progress in Physics*, vol. 621, pp. pp 717 – 752, 1975.

- [51] Y. Choi, C. Zhou, P. Stoltz, S. Joshi, and A. Yalin, "Simulation and Measurement of the Laser Induced Breakdown in Air and Argon for Nanosecond Order Pulses," *Proceedings of the ASME 2012 Internal Combustion Engine Division Fall Technical Conference*, pp. 1–9, 2016.
- [52] D. I. Rosen, D. E. Hastings, and G. M. Weyl, "Coupling of pulsed 0.35- $\mu\text{m}$  laser radiation to titanium alloys," *Journal of Applied Physics*, vol. 53, no. 8, pp. 5882–5890, 1982.
- [53] R. P. McEachran and A. D. Stauffer, "Momentum transfer cross sections for the heavy noble gases," *European Physical Journal D*, vol. 68, no. 6, 2014.
- [54] P. Chylek, M. A. Jarzembki, V. Srivastava, and R. G. Pinnick, "Pressure dependence of the laser-induced breakdown thresholds of gases and droplets.," *Applied Optics*, vol. 29, no. 15, pp. 2303–6, 1990.
- [55] A. Sircar, R. K. Dwivedi, and R. K. Thareja, "Laser-induced breakdown of Ar, N<sub>2</sub>, and O<sub>2</sub> gases using 1.064, 0.53, 0.355, and 0.266  $\mu\text{m}$  radiation," *Applied Physics B: Lasers and Optics*, vol. 63, pp. 623–627, 1996.
- [56] D. I. Rosen and G. Weyl, "Laser-Induced Breakdown in Nitrogen and the Rare-Gases At 0.53 and 0.35  $\mu\text{m}$ ," *Journal of Physics D-Applied Physics*, vol. 20, pp. 1264–1276, 1987.
- [57] J. M. Aaron, C. L. M. Ireland, and C. Grey Morgan, "Aberration effects in the interaction of focused laser beams with matter," *Journal of Physics D: Applied Physics*, vol. 7, no. 14, pp. 1907–1917, 1974.
- [58] J. P. Davis, A. L. Smith, C. Giranda, and M. Squicciarini, "Laser-induced plasma formation in Xe, Ar, N<sub>2</sub>, and O<sub>2</sub> at the first four Nd:YAG harmonics.," *Applied optics*, vol. 30, no. 30, pp. 4358–64, 1991.
- [59] R. G. Meyerand and A. F. Haught, "Gas breakdown at optical frequencies," *Physical Review Letters*, vol. 11, no. 9, pp. 401–403, 1963.
- [60] A. J. Alcock, C. Demichelis, and K. Hamal, "Subnanosecond schlieren photography of laser-induced gas breakdown," *Applied Physics Letters*, vol. 12, no. 4, pp. 148–150, 1968.
- [61] G. M. Weyl, "Physics of laser-induced breakdown," in *Laser-induced plasmas and applications*, pp. 1–68, 1989.
- [62] I. K. Krasnyuk, P. P. Pashinin, and A. M. Prokhorov, "Investigation of breakdown in Argon and Helium produced by a picosecond ruby laser light pulse," *Soviet Physics JETP*, vol. 31, pp. 860–861, nov 1970.
- [63] R. J. Dewhurst, "Breakdown in the rare gases using single picosecond ruby laser pulses," *Journal of Physics D: Applied Physics*, vol. 283, pp. 1–8, 1977.

- [64] G. M. Weyl and D. Rosen, “Laser-induced breakdown in argon at  $0.35\ \mu\text{m}$ : Theory and experiments,” *Physical Review A*, vol. 31, no. 4, pp. 2300–2313, 1985.
- [65] V. Morel, A. Bultel, I. Schneider, and C. Grisolia, “State-to-state modeling of ultrashort laser-induced plasmas,” *Spectrochimica Acta - Part B Atomic Spectroscopy*, vol. 127, pp. 7–19, 2017.
- [66] S. V. Shabanov and I. B. Gornushkin, “Two-dimensional axisymmetric models of laser induced plasmas relevant to laser induced breakdown spectroscopy,” *Spectrochimica Acta - Part B Atomic Spectroscopy*, vol. 100, pp. 147–172, 2014.
- [67] H. A. Scott and S. B. Hansen, “Advances in NLTE modeling for integrated simulations,” *High Energy Density Physics*, vol. 6, no. 1, pp. 39–47, 2010.
- [68] H. P. Le, A. R. Karagozian, and J. L. Cambier, “Complexity reduction of collisional-radiative kinetics for atomic plasma,” *Physics of Plasmas*, vol. 20, no. 12, 2013.
- [69] Y. Liu, M. Panesi, A. Sahai, and M. Vinokur, “General multi-group macroscopic modeling for thermo-chemical non-equilibrium gas mixtures,” *Journal of Chemical Physics*, vol. 142, no. 13, 2015.
- [70] A. Munafò, N. N. Mansour, and M. Panesi, “A Reduced-order NLTE Kinetic Model for Radiating Plasmas of Outer Envelopes of Stellar Atmospheres,” *The Astrophysical Journal*, vol. 838, no. 2, p. 126, 2017.
- [71] T. Fujimoto, *Plasma Spectroscopy*. Oxford University Press, 2004.
- [72] S. B. Hansen, J. Bauche, C. Bauche-Arnoult, and M. F. Gu, “Hybrid atomic models for spectroscopic plasma diagnostics,” *High Energy Density Physics*, vol. 3, no. 1-2, pp. 109–114, 2007.
- [73] Y. Frank, E. Louzon, P. Mandelbaum, and Z. Henis, “SEMILLAC: A new hybrid atomic model of hot dense plasmas,” *High Energy Density Physics*, vol. 9, no. 3, pp. 594–600, 2013.
- [74] D. R. Bates, A. E. Kingston, and R. W. P. McWhirter, “Recombination between electrons and atomic ions I. Optically thin plasmas,” *Proceedings of the Royal Society of London*, vol. 268, p. 527, 1962.
- [75] S. B. Hansen, K. B. Fournier, C. Bauche-Arnoult, J. Bauche, and O. Peyrusse, “A comparison of detailed level and superconfiguration models of neon,” *Journal of Quantitative Spectroscopy and Radiative Transfer*, vol. 99, no. 1-3, pp. 272–282, 2006.
- [76] J. Bauche, C. Bauche-Arnoult, and K. B. Fournier, “Model for computing superconfiguration temperatures in nonlocal-thermodynamic-equilibrium hot plasmas,” *Physical Review E - Statistical, Nonlinear, and Soft Matter Physics*, vol. 69, no. 2 2, 2004.
- [77] J. Bauche, C. Bauche-Arnoult, and O. Peyrusse, “Effective temperatures in hot dense plasmas,” *Journal of Quantitative Spectroscopy and Radiative Transfer*, vol. 99, no. 1-3, pp. 55–66, 2006.

- [78] M. Busquet, “Radiation-dependent ionization model for laser-created plasmas,” *Physics of Fluids B*, vol. 5, no. 11, pp. 4191–4206, 1993.
- [79] P. G. Carolan and V. A. Piotrowicz, “The behaviour of impurities out of coronal equilibrium,” *Plasma Physics*, vol. 25, no. 10, p. 1065, 1983.
- [80] C. Keane and C. H. Skinner, “Radiative power and electron cooling rates for oxygen in steady-state and transient plasmas at densities beyond the coronal limit,” *Physical Review A*, vol. 33, no. 6, pp. 4179–4190, 1986.
- [81] A. Sahai, B. Lopez, C. O. Johnston, and M. Panesi, “Adaptive coarse graining method for energy transfer and dissociation kinetics of polyatomic species,” *The Journal of Chemical Physics*, vol. 147, no. 5, p. 054107, 2017.
- [82] I. H. Hutchinson, “Principles of Plasma Diagnostics,” *Cambridge University Press*, pp. 160–175, 1987.
- [83] H.-J. Kunze, *Introduction to Plasma Spectroscopy*. Springer-Verlag Berlin Heidelberg, 1 ed., 2009.
- [84] M. Baranger, “General impact theory of pressure broadening,” *Physical Review*, vol. 112, no. 3, pp. 855–865, 1958.
- [85] A. Calisti, A. Demura, M. Gigos, D. González-Herrero, C. Iglesias, V. Lisitsa, and E. Stambulchik, “Influence of Microfield Directionality on Line Shapes,” *Atoms*, vol. 2, no. 2, pp. 259–276, 2014.
- [86] E. Stambulchik and A. V. Demura, “Dynamic Stark broadening of Lyman- $\alpha$ ,” *Journal of Physics B: Atomic, Molecular and Optical Physics*, vol. 49, no. 3, 2016.
- [87] E. Stambulchik and A. V. Demura, “On nature of ion dynamics,” *IOP Conf. Series: Journal of Physics: Conf. Series*, vol. 810, no. 1, pp. 1–5, 2017.
- [88] J. Oxenius, “Kinetic Theory of Particles and Photons: Theoretical Foundations of Non-LTE Plasma Spectroscopy,” *Springer*, pp. 71–78, 2012.
- [89] M. A. Gigos, “Stark broadening models for plasma diagnostics,” *Journal of Physics D: Applied Physics*, vol. 47, no. 34, 2014.
- [90] H. R. Griem, “Principles of Plasma Spectroscopy,” *Cambridge University Press*, pp. 90–100, 2005.
- [91] J. Holtsmark, “Über die verbreiterung von spektrallinien,” *Annalen der Physik*, vol. 363, no. 7, pp. 577–630, 1919.
- [92] E. Whiting, “An empirical approximation to the Voigt profile,” *Journal of Quantitative Spectroscopy and Radiative Transfer*, vol. 8, no. 6, pp. 1379–1384, 1968.
- [93] I. I. Sobelman, “Atomic Spectra and Radiative Transitions,” *Springer-Verlag Berlin Heidelberg*, pp. 257–274, 1979.

- [94] W. Karzas and R. Latter, “Electron Radiative Transitions in a Coulomb Field,” *The Astrophysical Journal Supplement Series*, vol. 6, p. 167, 1961.
- [95] I. P. Shkarofsky, T. W. Johnston, and M. P. Bachynski, “The Particle Kinetics of Plasmas,” *Addison-Wesley Pub. Co.*, pp. 202–240, 1966.
- [96] M. Abramowitz and I. A. Stegun, “Handbook of Mathematical Functions: with Formulas, Graphs, and Mathematical Tables,” *Dover Publications*, pp. 374–375, 1965.
- [97] W. H. Press, S. a. Teukolsky, W. T. Vetterling, and B. P. Flannery, “Numerical Recipes: The Art of Scientific Computing,” *Cambridge University Press*, vol. 1, pp. 279–283, 2007.
- [98] N. Hell, P. Beiersdorfer, E. W. Magee, and G. V. Brown, “Calibration of the OHREX high-resolution imaging crystal spectrometer at the Livermore electron beam ion traps,” *Review of Scientific Instruments*, vol. 87, no. 11, 2016.
- [99] P. Beiersdorfer, G. V. Brown, R. Shepherd, P. Allan, C. R. Brown, M. P. Hill, D. J. Hoarty, L. M. Hobbs, S. F. James, H. K. Chung, and E. Hill, “Lineshape measurements of He-  $\beta$  spectra on the ORION laser facility,” *Physics of Plasmas*, vol. 23, no. 10, 2016.
- [100] A. Montaser and D. W. Golightly, eds., *Inductively Coupled Plasmas in Analytical Atomic Spectrometry*. Wiley-VCH Verlag GmbH, 1987.
- [101] A. Kramida, Y. Ralchenko, J. Reader, and N. A. TEAM, “NIST Atomic Spectra Database (ver. 5.5.3),” 2018.
- [102] I. Lindgren and J. Morrison, *Atomic Many-Body Theory*. Springer-Verlag Berlin Heidelberg, 2 ed., 1986.
- [103] T.-N. Chang, ed., *Many-Body Theory of Atomic Structure and Photoionization*. World Scientific Pub Co Inc, 1993.
- [104] J. L. Cambier, “Numerical simulations of a nonequilibrium argon plasma in a shock-tube experiment,” in *22nd Fluid Dynamics, Plasma Dynamics and Lasers Conference*, (Honolulu, HI, U.S.A.), pp. 1–20, 1991.
- [105] M. Capitelli, G. Colonna, L. D. Pietanza, and G. D’Ammando, “Coupling of radiation, excited states and electron energy distribution function in non equilibrium hydrogen plasmas,” 2013.
- [106] J. Stewart and K. Pyatt, “Lowering of ionization potentials in plasmas,” *The Astrophysical Journal*, vol. 144, p. 1203, 1966.
- [107] G. Ecker and W. Kroll, “Lowering of the ionization energy for a plasma in thermodynamic equilibrium,” *Physics of Fluids*, vol. 6, no. 1, p. 62, 1963.
- [108] H. A. Scott, “Non-LTE Modeling of Radiatively Driven Dense Plasmas,” in *AIP Conference Proceedings*, (Paris, France), 2016.